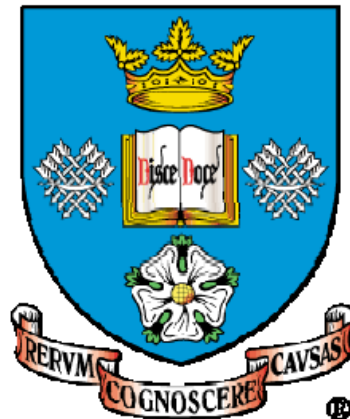

Development of Ultra High Strength Steels for Reduced Carbon Emissions in Automotive Vehicles

By

Alfonse Chamisa



Thesis submitted for the degree of Doctor of Philosophy

Department of Material Science & Engineering

The University of Sheffield

February 2014

Abstract

Automotive steels with enhanced strength and ductility beyond the current bounds can be engineered through microstructural strategies that take into account the benefits brought about by nanoprecipitates formed during the transformation from austenite to ferrite. Three multiphase steel compositions were initially studied. A patented Ti-Al-Mo steel composition was selected as the baseline for comparison with the other two steels. It is claimed that this steel has exceptional mechanical properties. The Ti and V microalloyed steels were selected to check whether interphase precipitates (IP), which can yield a high degree of precipitation strengthening, could be produced. Results showed that Ti-Al-Mo had superior microstructure and properties as compared to the other two. The microstructure was composed of ferrite, martensite, bainite and retained austenite. Unlike the other two steels, IP was also observed and the UTS of 780MPa and uniform elongation of 21% previously reported by other authors were also confirmed.

The V microalloyed steel composition was selected for the next part of the project since it would be commercially viable to produce for Tata Steel. The time/temperature/transformation behaviours of the V microalloyed steel were extensively studied. The microstructures developed were analysed and high precipitate number densities averaging $394 \text{ particles}/\mu\text{m}^2$ were recorded in the sample transformed at 700°C for 1200s. A high uniform elongation of 30.8% and the highest UTS of 627MPa were also reported on the same sample. The UTS value was attributed to the high precipitate number density which made an overall contribution to the yield strength of 270MPa. However, further studies need to be carried out, since the properties were not optimised and were inferior to some of the steels in current use for automotive applications. Questions were asked as to why IP was not observed. The low austenising temperature of 950°C was cited as the possible reason. Thermodynamic calculations using Thermo-Cal software had predicted that the optimum should have been 1050°C . As a result, 950°C was believed to be inadequate to effectively dissolve the carbides present to allow effective formation of interphase precipitates during the temperature hold in the $\alpha + \gamma$ temperature region.

The high N content was cited as another possible reason, but this was not conclusive and shown in itself not to be true by work in the next stage of the project.

It has since been established that Mo retards precipitate growth in both Nb and Ti alloyed steels. However, nothing has been reported on the effects of Mo on V microalloyed steels. As a result, the next stage of the project studied the effects of Mo on V microalloyed steels. Predominantly ferritic steels with Nb-V-Mo microalloying additions were produced and coiled at different temperatures. Samples microalloyed with Ti-Mo, Ti, V-Mo, V, Nb-Mo and Nb were also produced for comparison purposes. IP was observed in most of the Nb-V-Mo steels. IP with average interparticle distances of $8 \pm 2\text{nm}$ and row spacing of $22 \pm 3\text{nm}$ were observed in sample 10-630Nb⁺VMo. High YS of 925MPa, UTS of 1023MPa and total elongation of 16.8% were recorded for this sample. The exceptional mechanical properties were attributed to high number densities of fine IP averaging 1766 particles/ μm^2 . 82% of the precipitates had average sizes below 7nm and these made a contribution to YS of approximately 546MPa. It was then concluded that Mo additions were likely to have influenced the formation of fine precipitates that strengthened the ferritic steels. Hence Mo is likely to influence the high nucleation rate and slow precipitate growth in the same way that it influences Ti and Nb microalloyed steels. Since one of the steels studied at this stage had high N additions, it was also confirmed that the precipitate number densities in the previous V microalloyed steels batch had nothing to do with the N content; instead, it all had to do with the low austenising temperature which failed to put the carbides into solution.

Contents

<i>Abstract</i>	i
<i>Contents</i>	iii
<i>List of Figures</i>	viii
<i>List of Tables</i>	xxi
<i>Nomenclature and Abbreviations</i>	xxii
<i>Acknowledgements</i>	xxv
CHAPTER 1: INTRODUCTION	1
CHAPTER 2: LITERATURE REVIEW	5
2.1 Material Selection for Automotive Applications	5
2.1.1 Introduction	5
2.1.2 Aluminium	6
2.1.3 Magnesium.....	6
2.1.4 Polymers.....	7
2.1.5 Steel.....	7
2.1.6 High Strength Low Alloy Steels (HSLA)	7
2.1.7 Advanced High Strength Steels (AHSS).....	8
2.1.8 Mechanical Properties of DP, TRIP and HSLA Automotive Steels.....	9
2.1.8.1 Work Hardening and Yield Behaviour.....	10
2.1.9 Dual Phase Steels	12
2.1.10 Transformation Induced Plasticity Steels (TRIP steels)	13
2.1.10.1 Intercritical Annealing of Multiphase Steels	14
2.1.11 Twinning Induced Plasticity (TWIP) Steels	15
2.1.12 Ultra High Strength Steels	17
2.1.13 Martensitic Steels	18
2.1.14 Quench and Partition Steels	19
2.1.15 Bainite in Steels	20
2.1.15.1 Granular Bainite.....	20
2.1.15.2 Upper Bainite	21
2.1.15.3 Lower Bainite	22
2.1.15.4 Strengthening Mechanisms in Bainite	23
2.1.16 Ferrite-Pearlite Steels	25

2.1.16.1	Banding in Pearlitic Steels	26
2.1.17	The Role of Microalloying Elements	27
2.1.17.1	Carbon.....	27
2.1.17.2	Nitrogen	27
2.1.17.3	Silicon	28
2.1.17.4	Niobium	28
2.1.17.5	Vanadium.....	29
2.1.17.6	Titanium.....	29
2.1.17.7	Boron	30
2.1.18	Effects of Other Alloying Elements	30
2.1.18.1	Aluminium	30
2.1.18.2	Molybdenum.....	31
2.1.18.3	Manganese	31
2.2	<i>Strengthening Mechanisms in Microalloyed Steels</i>	32
2.2.1	Contributions to Yield Strength	32
2.2.2	Grain Refinement in Microalloyed Steels.....	33
2.2.2.1	Effects of Particle Pinning and Solute Drag on Grain Growth	34
2.2.2.2	Effects of Particle Pinning and Solute Drag on Recrystallization....	38
2.2.2.3	Effect of Coiling Temperature on Grain Size	38
2.2.3	Solid Solution Strengthening	39
2.2.4	Strengthening at High Interstitial Concentrations.....	39
2.2.5	Strain Hardening or Work Hardening	39
2.2.6	Dispersion Strengthening	40
2.3	<i>Precipitation Strengthening</i>	41
2.3.1	Precipitate Types	41
2.3.2	Nucleation in the Liquid Phase, During and after Solidification	41
2.3.3	Strain Induced Precipitates.....	41
2.3.4	Precipitates Contributing to Yield Strength	43
2.3.5	Nucleation on Dislocations	44
2.3.6	Nucleation at the Interphase Boundary	45
2.3.7	Solubility Products of the Carbide Formers.....	46
2.3.8	Coarsening of Precipitates.....	47

2.3.9	Precipitation Strengthening Mechanisms.....	48
2.3.10	Heat Treatments for Precipitation Hardening	51
2.3.11	Interphase Precipitates (IP)	53
2.3.11.1	Planar Interphase Precipitates.....	56
2.3.11.2	Random Interphase Precipitates.....	57
2.3.11.3	Irregular Banded Arrays	58
<i>CHAPTER 3: EXPERIMENTAL PROCEDURE</i>		<i>60</i>
3.1	Introduction	60
3.2	Stage 1 Materials - Multiphase Steels with Different Chemical Compositions.....	61
3.2.1	Thermomechanical Treatment of Multiphase Steel Samples.....	63
3.3	Stage 2 Materials - V Microalloyed Samples.....	65
3.3.1	Heat Treatments on the Thermomechanical Compression Machine (TMC) 67	
3.4	Stage 3 Materials - New Alloy Compositions Strengthened by Nanoprecipitates	69
3.5	Tensile Specimens	71
3.6	X-ray Diffraction (XRD).....	71
3.7	Retained Austenite Content Estimation	72
3.8	Optical and Scanning Electron Microscopy (SEM)	74
3.9	TEM Carbon Extraction Replicas	75
3.10	TEM Thin Foils	77
3.11	Grain Size Measurements.....	77
3.12	Quantification of Phases.....	78
3.13	Precipitate Sizes and Distribution	78
<i>CHAPTER 4: MULTIPHASE STEELS OF DIFFERENT CHEMICAL COMPOSITIONS</i>		<i>79</i>
4.1	Introduction	79
4.2	Tensile Properties	80
4.3	Retained Austenite Content.....	81
4.4	Characterization of the Microstructure.....	83
4.4.1	Optical Microscopy	83
4.4.2	Scanning Electron Microscopy (SEM)	85

4.5	Grain Size Measurements.....	87
4.6	TEM Thin Foils and Carbon Extraction Replicas.....	88
4.6.1	Ti-Al-Mo Alloyed Samples.....	88
4.6.2	Ti Microalloyed Samples.....	91
4.6.3	V Microalloyed Samples.....	94
4.7	Summary.....	99
<i>CHAPTER 5: TIME/TEMPERATURE/TRANSFORMATION BEHAVIOUR OF A VANADIUM MICROALLOYED STEEL.....</i>		100
5.1	Introduction.....	100
5.2	Tensile Properties.....	101
5.3	Vickers Hardness.....	102
5.4	Retained Austenite Content.....	103
5.5	The Microstructure - Optical Microscopy and SEM.....	104
5.6	Grain Sizes Measurements.....	109
5.7	TEM Carbon Extraction Replicas.....	110
5.8	Precipitate Morphology and Chemistry.....	113
5.9	Precipitate Sizes and Distribution.....	114
5.10	TEM Thin foil Analysis.....	118
5.11	Summary.....	122
<i>CHAPTER 6: FERRITIC V-Nb-Mo MICROALLOYED STEELS STRENGTHENED BY NANOPRECIPITATES.....</i>		124
6.1	Introduction.....	124
6.2	Tensile Properties.....	125
6.3	The Microstructure.....	126
6.4	Grain Sizes Distribution.....	148
6.5	Precipitate Analysis.....	151
6.5.1	Precipitate Size Distribution.....	182
6.6	Summary.....	187
<i>CHAPTER 7: DISCUSSION.....</i>		188
7.1	<i>Multiphase Steels with Ferrite Strengthened by Nanoprecipitates.....</i>	189
7.1.1	Retained Austenite Content.....	189
7.1.2	TiAlMo Microalloyed Steels.....	190

7.1.3	Ti microalloyed Steels.....	192
7.1.4	V microalloyed Steels	193
7.1.5	Summary and Introduction to V microalloyed Steels	195
7.2	<i>The Time/Temperature/Transformation Behaviour of a Vanadium Microalloyed Steel</i>	196
7.2.1	Microstructural Development	196
7.2.2	Grain Sizes Analysis	198
7.2.3	Phase Distribution	199
7.2.4	Precipitate Analysis.....	200
7.2.5	Mechanical Properties - Estimated versus Measured.....	204
7.2.6	Summary and Introduction to Ferritic Microalloyed Steels.....	207
7.3	<i>Ferritic V-Nb-Mo Microalloyed Steels Strengthened by Nanoprecipitates</i> ...	208
7.3.1	Yield Strength Estimation	208
7.3.2	Grain Refinement	212
7.3.3	Effects of Alloying Elements and Thermal History on Grain Coarsening	213
7.3.4	Grain Size Estimation – SEM and EBSD	215
7.3.5	Precipitate Analysis.....	216
7.3.6	Precipitate Morphology and Chemistry	217
7.3.7	Precipitate Size Distribution and Number Densities.....	219
7.3.8	Carbon Extraction Replicas – The Challenges.....	220
7.4	<i>Summary</i>	222
8.	<i>CHAPTER 8: FUTURE WORK</i>	224
9.	<i>CHAPTER 9: CONCLUSIONS</i>	225
9.1	Multiphase Steels with the Ferrite Strengthened by Nanoprecipitates.....	225
9.2	Time/Temperature/Transformation Behaviour of a Vanadium Microalloyed Steel	227
9.3	Ferritic V-Nb-Mo microalloyed Steels Strengthened by Nanoprecipitates 229	
	<i>REFERENCES</i>	231

List of Figures

Figure 2.1 – 2010 Light Vehicle Material Content adapted from Steelworks online [14].....	5
Figure 2.2 –Strength-Formability relationship for AHSS as compared to low strength steels and conventional HSS[23]	8
Figure 2.3 – Stress strain curve showing TRIP 350/600 with greater total elongation than DP350/600 and HSLA 350/450[23].....	11
Figure 2.4 - Schematic of the combined conventional thermomechanical process and continuous annealing cycle for cold rolled intercritically annealed TRIP steels[40] 14	
Figure 2.5 – Schematic diagram of total elongation vs strength for automotive steels. The region in orange represents future steels (UHSS), (adapted from WorldAutoSteel)[23].....	17
Figure 2.6 – Schematic of the Q and T heat treatments adapted from[59]	19
Figure 2.7 – Granular bainite in .06C-B-free Steels and 0.04C complex B-steel[60]	20
Figure 2.8 - TEM thin foil image showing upper bainite produced by carbon enrichment of austenite in a V microalloyed steel	22
Figure 2.9 - SEM images showing lower bainite type carbides in a Ti microalloyed steel	23
Figure 2.10 - Effects of 50% transformation temperature on tensile strength of bainite. Adapted from F.B. Pickering[62].....	24
Figure 2.11 – Effect of alloying elements on grain refinement in microalloyed steels adapted from [87].....	35
Figure 2.12 - Solubility products of carbides and nitrides as a function of temperature adapted from K. Narita[71].....	46
Figure 2.13 – Traditional heat treatment cycles for precipitation strengthening	51
Figure 2.14 – Modern heat treatment cycles for precipitation strengthening	52
Figure 2.15 - Schematic model of the interphase precipitation process adapted from Davenport and Honeycombe[141]	53

Figure 2.16 – Precipitate row spacing as a function of temperature [129]	54
Figure 2.17 – Bands of discrete particles (interphase precipitates) formed at the interphase boundary during transformation from γ to α [73].....	56
Figure 2.18 – Mechanism for nucleation and growth of precipitates on the γ/α interphase (adapted from Ricks and Howell)[70]	57
Figure 2.19 – Random interphase precipitates formed through the interphase boundary bowing around particles[70]	57
Figure 2.20 - Ledge formation through localised bulges[145]	59
Figure 2.21 – Curved sheets formation as result of localised bulges (Adapted from Ricks and Howell[145])	59
Figure 3.1 – Images of tensile test bar grip heads received from Tata Steel for characterisation	61
Figure 3.2 – a) Thermomechanical processing conditions for a) 2 steps cooled samples and b) continuously cooled samples.....	64
Figure 3.3 – Schematic diagram of the manufacturing process adopted by Tata Steel	65
Figure 3.4 – Purpose made holder used during heat treatment of samples in the TMC machine	67
Figure 3.5 – Actual heat treatment Cycle adopted from the TMC machine for sample 650-60s.....	68
Figure 3.6 – Schematic diagram of the process used to produce the samples by Tata Steels	70
Figure 3.7 – Tensile specimen prepared according to ASTM standard E8/E8M – 09[148].....	71
Figure 3.8 – Sample mounted in bakelite for optical microscopy, SEM and TEM carbon extraction replicas	74
Figure 3.9 - Schematic diagram of the carbon extraction replica process[154].....	76
Figure 4.1 – Summarised tensile test results.....	81
Figure 4.2 – XRD results for TiAlMo, Ti and V alloyed multiphase steels.	81

Figure 4.3 – Optical micrographs showing distinct ferrite grains and an unresolved second phase in TiAlMo-2S and TiAlMo-CC.	83
Figure 4.4 - Optical micrographs showing a fine unresolved microstructure in Ti-2S and Ti-CC.....	84
Figure 4.5 - Optical micrographs showing an unresolved 2 nd phase within the ferrite matrix in V-2S and a fine unresolved microstructure for V-CC.....	84
Figure 4.6 – Secondary electron SEM images showing similar features in TiAlMo-2S and TiAlMo-CC.....	85
Figure 4.7 - SEM images showing the bainitic microstructure in samples Ti-2S and Ti-CC	86
Figure 4.8 – SEM images showing the distribution of phases in V-2S and V-CC....	86
Figure 4.9 – TEM images for TiAlMo showing a) Random precipitates and high dislocation density within the ferrite in TiAlMo-CC and b) possible interphase precipitates in the ferrite in TiAlMo-2S.....	89
Figure 4.10 – TEM thin foil images showing a) region of fine ferrite within and in adjacent lower grain in TiAlMo-2S and b) Retained austenite located intragranularly within ferrite.....	89
Figure 4.11 – TEM thin foil images showing a) Local region of bainite in TiAlMo-2S and b) region of bainite and fine lath martensite in TiAlMo-CC.	90
Figure 4.12 – Carbon extraction replica images showing region with random and high precipitate number densities in TiAlMo-2S and TiAlMo-CC	90
Figure 4.13 – TEM thin foil images for Ti-2S showing a) Ferritic region with few precipitates and an unidentified feature (probably MnS) in Ti-2S and b) Bainitic region with high dislocation density	92
Figure 4.14 – TEM thin foil images for Ti-2S showing a) carbides within a bainite sheaf and b) upper bainite type carbides	92
Figure 4.15 – TEM thin foil images showing; a) region of fine martensite in Ti-2S and b) narrow ferrite with occasional precipitates in a bainitic region in Ti-CC.....	93
Figure 4.16 – TEM thin foil images for Ti-CC showing a) carbides within the grain boundary and b) irregular grain boundaries	93

Figure 4.17 – TEM carbon extraction replica images showing random and course precipitates in Ti-2S and finer precipitates in Ti-CC	94
Figure 4.18- TEM thin foil images a) odd morphologies in ferrite for V-CC and b) pearlitic features in V-2S	96
Figure 4.19 - TEM thin foil images showing the presence of pearlite V-2S	96
Figure 4.20 – TEM thin foil images for V-CC showing: a) retained austenite and b) curved grain boundaries	97
Figure 4.21- TEM thin foil images for V-2S showing: a) high angle grain boundary and b) precipitates in the grain boundary and in ferrite	97
Figure 4.22 TEM thin foil images for V-2S showing: a) carbides in grain boundary and b) bainite with carbides	98
Figure 4.23 – TEM carbon extraction replica images showing regions with random precipitates in V-2S and V-CC	98
Figure 5.1 – a) Stress-strain curves and b) comparison of mechanical properties...	101
Figure 5.2 – Vickers hardness test profiles for all the samples.....	103
Figure 5.3– Optical microscopy images showing unresolved fine microstructures for 950Q and 950-60Q	104
Figure 5.4– SEM images showing predominantly bainitic microstructures for samples 950Q and 950-60Q	104
Figure 5.5 – Optical microscopy images for 950-120Q and 750-60s	105
Figure 5.6 – SEM images for 950-120Q and 750-60s showing bainitic microstructures with few martensitic and ferritic regions.....	105
Figure 5.7 – Optical microscopy images for 750-1800s and 725-1800s showing a ferrite matrix with an unresolved second phase	106
Figure 5.8 – SEM images for V3 750-1800s and 725-1800s showing a mixed ferrite, bainite and martensite microstructure. The arrows in both show possible precipitates	106
Figure 5.9 – Optical microscopy images for 700-30s and 700-1200s showing a ferrite matrix with an unresolved 2 nd phase	107

Figure 5.10 – SEM images for 700-30s showing a ferrite matrix with bainite and martensite and 700-1200s showing the ferritic and martensitic microstructure. The arrows in both show possible precipitates.....	107
Figure 5.11 – Optical microscopy images for 650 – 60s and 650-600s showing ferrite with an unresolved 2 nd phase	108
Figure 5.12– SEM images showing ferrite and martensite in 650 – 60s and ferrite, martensite and bainite in 650-600s	108
Figure 5.13 – a) Optical microscopy image and b) SEM image for 625-300s pearlite within a ferrite matrix. The arrow shows possible precipitates	108
Figure 5.14 – TEM carbon extraction replica images showing lowing precipitate counts in 950Q and 950-60Q	110
Figure 5.15 - TEM carbon extraction replica images showing some of the precipitates in 950-120Q and 750-60s	111
Figure 5.16 - TEM carbon extraction replica images showing some of the precipitates in 750-1800s and 725-1800s.....	111
Figure 5.17 – TEM carbon extraction replica images showing a) region with high precipitate density and ordered array of precipitates in 700-30s and b) Region with high precipitate density and random distribution in 700-1200s.....	112
Figure 5.18 – TEM extraction replica images for 650-60s showing a) Random distribution of precipitates and b) circled region with precipitate cluster, dotted arrow pointing at a spherical precipitate and a solid arrow pointing at a cube type precipitate.....	112
Figure 5.19 – TEM extraction replica images showing regions with low precipitation number densities a) arrow pointing at a rod type precipitate in 650-600s and b) randomly distributed precipitates in 625-300s.....	113
Figure 5.20 – Energy loss spectra (EELS) for the various precipitates analysed	114
Figure 5.21 – Precipitate sizes and distribution curves for the various samples.....	115
Figure 5.22 – Precipitate Sizes distribution curves (contd) for the various samples	116
Figure 5.23 – Average precipitate sizes for the various samples.....	117

Figure 5.24 – TEM thin foil images for V6 showing a) region with high precipitate number densities and high dislocation density b) region of high precipitate density	119
Figure 5.25 – TEM thin foil images for V7 showing a) region of high precipitate density and b) course precipitates in ferrite	119
Figure 5.26 – TEM thin foil images for V8 showing a) region with high precipitate number density and arrow showing an ordered array of precipitates b) region with coherent precipitates in ferrite.....	120
Figure 5.27 - TEM thin foil images for V8 showing a) rod type precipitates b) region with high precipitate and dislocation densities	120
Figure 5.28 - TEM thin foil images for V9 showing a) randomly distributed precipitates and b) region with high precipitate and dislocation densities.....	121
Figure 5.29 - TEM thin foil images for V10 showing a) region with ordered array of precipitates and b) region with high precipitate density	121
Figure 6.1 – Summarised Tensile test results for the ferritic steels supplied by Tata Steels	126
Figure 6.2 – a) SEM images showing the microstructures of samples 01-630Nb ⁺ VMo and b) grain boundary misorientation distribution for the same sample.	128
Figure 6.3 – EBSD maps for 01-630Nb ⁺ VMo showing a) texture of the grains and b) low angle boundaries in blue and high angle boundaries in red	128
Figure 6.4 – a) SEM images showing the microstructures of samples 02-630Nb ⁺ VMo and b) grain boundary misorientation distribution for the same sample.	130
Figure 6.5 – EBSD maps for 02-630Nb ⁺ VMo showing a) texture of the grains and b) low angle boundaries in blue and high angle boundaries in red	130
Figure 6.6 - a) SEM images showing the microstructures of samples 06-600Nb ⁺ VMo and b) grain boundary misorientation distribution for the same sample.....	131
Figure 6.7 – EBSD maps for 06-600Nb ⁺ VMo showing a) texture of the grains and b) low angle boundaries in blue and high angle boundaries in red	131
Figure 6.8 - a) SEM images showing the microstructures of samples 07-630NbVMo and b) grain boundary misorientation distribution for the same sample.....	133

Figure 6.9 – EBSD maps for 07-630NbVMo showing a) texture of the grains and b) low angle boundaries in blue and high angle boundaries in red	133
Figure 6.10 – a) SEM images showing the microstructures of samples 10-630Nb ⁺ VMo and b) grain boundary misorientation distribution for the same sample	134
Figure 6.11 – EBSD maps for 10-630Nb ⁺ VMo showing a) texture of the grains and b) low angle boundaries in blue and high angle boundaries in red	134
Figure 6.12– a) SEM images showing the microstructures of samples 14-630Nb ⁺ VMo and b) grain boundary misorientation distribution for the same sample	135
Figure 6.13 – EBSD maps for 14-630Nb ⁺ VMo showing a) texture of the grains and b) low angle boundaries in blue and high angle boundaries in red	135
Figure 6.14 – a) SEM images showing the microstructures of samples 15-650TiMo with arrow showing banded ferrite and b) grain boundary misorientation distribution curve for the same sample.....	136
Figure 6.15 – EBSD maps for 15-650TiMo showing a) texture of the grains and b) low angle boundaries in blue and high angle boundaries in red	136
Figure 6.16 – a) SEM images showing the microstructures of samples 16-650Ti and b) grain boundary misorientation distribution curve for the same sample.....	137
Figure 6.17 – EBSD maps for 16-650Ti showing a) texture of the grains and b) low angle boundaries in blue and high angle boundaries in red	137
Figure 6.18 – SEM images for 17-650VMo showing a) the general microstructure and b) high resolution image showing to show the presents of pearlite within the grains.	139
Figure 6.19 – EBSD maps for 17-650NbMo showing a) texture of the grains and b) low angle boundaries in blue and high angle boundaries in red	139
Figure 6.20 – Grain boundary misorientation distribution curve for 17-650VMo ..	140
Figure 6.21– a) SEM images showing the microstructures of samples 18-650V and b) grain boundary misorientation distribution curve for the same sample.....	141
Figure 6.22 – EBSD maps for 18-650V showing a) texture of the grains and b) low angle boundaries in blue and high angle boundaries in red	141

Figure 6.23 – a) SEM images showing the microstructures of samples 19-650NbMo and b) grain boundary misorientation distribution curve for the same sample.....	142
Figure 6.24 – EBSD maps for 19-650NbMo showing a) texture of the grains and b) low angle boundaries in blue and high angle boundaries in red	142
Figure 6.25 – a) SEM images showing the microstructures of samples 20-650Nb and b) grain boundary misorientation distribution curve for the same sample.....	144
Figure 6.26– EBSD maps for 20-650Nb showing a) texture of the grains and b) low angle boundaries in blue and high angle boundaries in red	144
Figure 6.27 – a) SEM images showing the microstructures of samples 21-650TiMo and b) grain boundary misorientation distribution curve for the same sample.....	145
Figure 6.28 – EBSD maps for 21-650TiMo showing a) texture of the grains and b) low angle boundaries in blue and high angle boundaries in red	145
Figure 6.29 – a) SEM images showing the microstructures of samples 22-630N+and b) grain boundary misorientation distribution curve for the same sample.....	147
Figure 6.30 – EBSD maps for 22-630N+ showing a) texture of the grains and b) low angle boundaries in blue and high angle boundaries in red	147
Figure 6.31 – Measured average grain sizes for all the samples.....	148
Figure 6.32 – Grain size distribution curves for samples 01-630Nb ⁺ VMo to 18-650V	149
Figure 6.33– Grain size distribution curves for samples 19-650NbMo to 22-630N ⁺	150
Figure 6.34 – TEM thin foil images for 01-630Nb ⁺ VMo showing the existence of fine precipitates; some in slightly ordered arrays and the majority randomly distributed.....	153
Figure 6.35 – TEM Carbon extraction replica images showing the existence fine precipitates in 01-630Nb ⁺ VMo	153
Figure 6.36 - EELS spectras for 01-630Nb ⁺ VMo showing that some of the Spheres, rods and cube type precipitates	154
Figure 6.37 – EELS spectra for 01-630Nb ⁺ VMo showing that the fine sphere and rod shaped precipitates were mainly VC.....	154

Figure 6.38 –TEM thin foil images showing the existence of planar IP in sample 02-630Nb ⁺ VMo.....	155
Figure 6.39 – TEM carbon extraction replica images showing the morphologies and relative sizes and distribution of the precipitates	155
Figure 6.40 – EEL spectra for sample 02-630Nb ⁺ VMo showing that the rod and spherical precipitates were mainly VC	156
Figure 6.41 - EDX spectrum for spherical and rod shaped precipitates in samples 01-630Nb ⁺ VMo and 02-630Nb ⁺ VMo showing the presents of Mo in all fine precipitates	156
Figure 6.42 – TEM thin foil images for 06-600Nb ⁺ VMo showing regions with high precipitate number densities and some regions with planar IP	157
Figure 6.43- Carbon extraction replica image showing fine precipitates in a region of high precipitate density in 06-600Nb ⁺ VMo	157
Figure 6.44 - EELS spectra showing V(Mo)C for the finest (~5nm) sphere and rod shaped precipitates in steel 06-600Nb ⁺ VMo.....	158
Figure 6.45 - EELS spectra showing VCN for (~10nm) sphere and rod shaped precipitates and stringers in steel 06-600Nb ⁺ VMo	158
Figure 6.46 - EELS spectra showing the presence of Ti in some of the sphere and rod shaped precipitates, as well as stringers. This was common in coarser precipitates (>20nm).....	158
Figure 6.47 –EDX analysis revealed the presents of Mo and Nb in all precipitates analysed.....	158
Figure 6.48 – TEM carbon extraction replica images for 07-630NbVMo showing a) a mixture of coarse and fine precipitates and b) precipitate bands which seemed to have been captured along raised grain boundaries.....	159
Figure 6.49 – EELS spectra for 07-630NbVMo confirming that the precipitates were vanadium carbides.....	159
Figure 6.50 – EDX spectrum showing the presents of Mo in the fine precipitates .	160
Figure 6.51 – TEM thin foil images for 10-630Nb ⁺ VMo showing a) random distribution of fine precipitates and b) rows of precipitates which confirms planar IP in this sample	161

Figure 6.52 – Carbon extraction replica images for 10-630Nb ⁺ VMo showing a) region of planar IP and b) high resolution image showing the morphology of some of the precipitates	161
Figure 6.53 – EELS spectrum for spheres, strings, precipitate clusters, rods and cube type precipitates in 10-630Nb ⁺ VMo	162
Figure 6.54 – EDX spectra for spheres, strings precipitate clusters, rods and cube type precipitates in 10-630Nb ⁺ VMo`	162
Figure 6.55 – TEM thin foil images for 14-650Nb ⁺ VMo showing a) region of IP and b) region of high precipitate numbers randomly distributed.....	164
Figure 6.56 – TEM carbon extraction replica images showing fine precipitates, some of them in clusters, in sample 14-650Nb ⁺ VMo	164
Figure 6.57 - EELS spectra for steel 14-650Nb ⁺ VMo showing VCN for the fine sphere and rod shaped precipitates.....	165
Figure 6.58 - EELS spectra for steel 14-650Nb ⁺ VMo showing Ti(V)CN in some stringers and cube type precipitates	165
Figure 6.59 - EELS spectra for steel 14-650Nb ⁺ VMo showing TiCN mostly in cube type precipitates	165
Figure 6.60– EDX spectrum showing the presents of Nb and Mo in sphere, rod, stringer and cube type precipitates in 14-650Nb ⁺ VMo.....	165
Figure 6.61 – TEM thin foil images for 15-650TiMo showing 15a) region of high precipitate number density as well as possible IP along a tilted grain boundary and 15b) region with possible IP	167
Figure 6.62 – TEM carbon extraction replica images showing the distribution of fine precipitates within the sample in 15-650TiMo	167
Figure 6.63 - EELS spectra for steel 15-650TiMo showing that the majority of the fine carbides were TiC	168
Figure 6.64 - EELS spectra for steel 15-650TiMo showing that some of the round and square precipitates were VC.....	168
Figure 6.65 - EELS spectra for steel 15-650TiMo showing that some of the round and square precipitates were VC.....	168

Figure 6.66 – EDX spectrum showing the presents of Mo and Nb in all precipitates analysed.....	168
Figure 6.67 – TEM Carbon extraction replica images for spheres and stringers in sample 16-650Ti.....	169
Figure 6.68 – EELS spectrum for spheres and stringers in sample 16-650Ti	170
Figure 6.69 – EDX spectrum for spheres and stringers in sample 16-650Ti.....	170
Figure 6.70 – TEM thin foil images for 17-650VMo showing a) region of high rod shaped precipitate number densities and b) region with IP and grain boundary carbides shown by the arrows	171
Figure 6.71 – TEM carbon extraction replica images showing the low precipitation counts within the 17-650VMo	171
Figure 6.72 - EELS spectra for sphererical, stringers and rod type precipitates in 17-650VMo	172
Figure 6.73 – EDX analysis for 17-650VMo showing spectrum for a) the majority of round, stringers and rod type precipitates and b) a few rod type precipitates.....	172
Figure 6.74 – Carbon extraction replica images showing regions of high and low precipitate number densities in 18-650V	173
Figure 6.75 - EELS spectra for rod and sphere type precipitates in 18-650V	173
Figure 6.76 – EDX spectrum for rod shaped and spherical precipitates in 18-650V	173
Figure 6.77 – TEM thin foil images showing the location and morphology of precipitates in 19-650NbMo	174
Figure 6.78 – TEM carbon extraction replica images precipitate distribution in 19-650NbMo	174
Figure 6.79 – EELS spectrum for the sphere and cube type precipitates in 19-650NbMo	175
Figure 6.80 – EDX spectrum for the sphere and cube type precipitates in 19-650NbMo	175
Figure 6.81 – TEM carbon extraction replica images showing the distribution of precipitates in 20-650Nb	176

Figure 6.82 – EEL spectroscopy analysis showing the chemistry of the precipitates in 20-650Nb	176
Figure 6.83 – EDX analysis showing the chemistry of the precipitates in 20-650Nb	176
Figure 6.84 – TEM thin foil images for 21-650TiMo showing random distribution of fine precipitates within the sample.....	178
Figure 6.85 – TEM carbon extraction replica images for sample 21-650TiMo showing a) high resolution bright field image showing fine precipitates and b) dark field image confirming that the dark contrast were actual precipitates	178
Figure 6.86 – EELS spectrum for 21-650TiMo showing that the fine precipitates were TiC.....	179
Figure 6.87 – EDX spectrum confirming the presents of Mo (Ti(Mo)C) in the fine precipitates in 21-650TiMo.....	179
Figure 6.88 – TEM thin foils images for 22-630N ⁺ showing a) random distribution of precipitates and b) Interphase precipitates in some regions.....	180
Figure 6.89 – TEM carbon extraction replica images for 22-630N ⁺ showing a) region of low precipitation number densities and b) random distribution of precipitates in the sample.....	180
Figure 6.90 – EELS spectra showing that the spheres, rods and stringers in 22-630N ⁺ were mainly VCN	181
Figure 6.91 - EDX spectrum confirming the presents of Nb and Mo in the precipitates previously analysed by EELS above	181
Figure 6.92 – Precipitates counted per μm^2 for the various samples	183
Figure 6.93 – Average precipitate sizes for all the samples.....	183
Figure 6.94 – Precipitate size distribution curves for samples 02-630Nb ⁺ VMo to 18-650V	185
Figure 6.95 - Precipitate size distribution curves for samples 19-650NbMo to 22-630N ⁺	186
Figure 7.1 – Average grain sizes for the various samples	199
Figure 7.2 – Percentage ferrite in the various samples	199

Figure 7.3 - Precipitate count comparisons for the various samples.....	200
Figure 7.4 – Actual versus Estimated Yield Strength	205
Figure 7.5 – Calculated base and precipitate strengths contributions to estimated yield strength.....	210
Figure 7.6 – Comparison of yield strength measured through tensile testing (Actual YS) and the estimated yield strength	211
Figure 7.7 – Plot of estimated versus actual yield strengths showing that the two set of results were almost a perfect fit with most of the points on the trentline ($y = x$)	211
Figure 7.8 – Grain size comparisons for results obtained through EBSD and SEM	216

List of Tables

Table 2.1 – Tensile properties for automotive steels[25].....	10
Table 3.1 – Table of Chemical compositions [wt%].....	61
Table 3.2 – Thermal cycle schedule for V alloyed steel	66
Table 3.3- Table of Chemical Composition.....	69
Table 4.1 – Table of tensile properties.....	80
Table 4.2 – Table of Retained Austenite Content	82
Table 4.3 – Table of grain size measurements and phase summaries (B= bainite, M=martensite).....	87
Table 5.1 – Summarised Hardness and Tensile Test Results.....	102
Table 5.2 – Summary of grain sizes, volume fractions and phases	109
Table 5.3 – Precipitate Summary	117
Table 6.1 – Mechanical test results courtesy of Tata Steel (IJmuiden)	125
Table 6.2 – Summarised grain sizes and grain boundary misorientation data.....	150
Table 6.3 – Precipitate Counts Summary.....	182
Table 7.1– Estimated Yield Strength, UTS and Total Elongation.....	204
Table 7.2 – Yield Strength Estimation.....	209

Nomenclature and Abbreviations

Γ	Austenite
A	Ferrite
RA	Retained austenite
B	Bainite
M	Martensite
M/A	Martensite – austenite constituent
UHSS	Ultra High Strength Steels
AHSS	Advanced high strength steels
UHSS	Ultra High Strength Steels
TRIP	Transformation induced plasticity Steels
HSLA	High Strength Low Alloy steel
DP	Dual phase steel
UTS	Ultimate tensile strength (MPa)
YS	Yield strength (MPa)
σ_y	Yield strength
σ_{ss}	Solid Solution Strength
σ_{ppt}	Precipitation Strengthening
σ_{dis}	Dislocation Strengthening
σ_{trans}	Transformation Hardening
δ	Precipitation Strengthening
XRD	X-ray Diffraction
EBSD	Electron backscatter diffraction
MOD	Misorientation distribution
SE	Secondary Electrons
SEM	Scanning electron microscopy
TEM	Transmission Electron Microscopy
APT	Atom Probe Tomography
EELS	Electron Energy Loss Spectroscopy
EDS	Energy Dispersive X-ray Spectroscopy

GIF	Gatan image filter
FEG	Field emission gun
TMC	Thermomechanical compression
Bcc	Body centre cubic
Fcc	Face centre cubic
Ppt	Precipitates
IP	Interphase precipitates
Ms	Martensite-start temperature (°C)
Mf	Martensite-finish temperature (°C)
CC	Continuous cooling
2S	2 steps cooling
Ac1	Austenite formation start temperature on heating (°C)
Ac3	Austenite formation completion temperature on heating (°C)
A _{r3}	Transformation start temperature (°C)
El	Elongation (%)
T _R	Recrystallization temperature (°C)
P _z	Zener Pinning pressure exerted by particles on unit area of the boundary
F _v	Volume fraction spherical particles of radius r
R	Radius of the matrix grains as sphere
Γ	Specific energy of the boundary on the Zener pinning relationship
Å	Angstroms
μm	Microns
nm	nanometre
T	Temperature (°C or K)
H	Hour
S	second
MPa	Megapascals

mA	Milliamps
V	Voltage
KV	Kilo voltage
Vol.	Volume
wt. %	Weight percent
V_γ	Volume fraction of retained austenite (%)
L	Long (mm)
W	Wide (mm)
T	Thickness (mm)
A_g	Uniform elongation (%)
R_m	Ultimate tensile strength (MPa)
N_S	number of particles intersecting a unit area of the grain boundary
F_S	the force on the boundary
Γ	specific energy of the boundary
R	particle radius
V	Boundary velocity
M	Boundary mobility
C	Solute level or concentration
R	radius of the particles
r_c	Critical particle size
F_R	driving force for recrystallization
B	Burgers vector
M	shear modulus
P	Dislocation density
N_v	particle number density
D	interatomic spacing
λ	Wavelength
θ	Bragg angle

Acknowledgements

Firstly, I would like to express my sincere gratitude to the Advanced Metallic Systems CDT management team for giving me the opportunity to study metallurgy as well as the guidance and support that they dedicated to me over the past four years. I would also want to acknowledge the Engineering and Physical Science Research Council (EPSRC) for the financial support and Tata Steels for both financial support and providing the materials used in this project.

My sincere gratitude goes to Professor W. Mark Rainforth, my project supervisor for his patience, guidance and support during the course of the project. Without his help and attention to detail, this project would not have been successful. I would also want to thank Dr David Hanlon, Dr Theo Kop and Dr Arjan van Rijkenburg at Tata Steels (IJmuiden) for the helpful discussions during progress meetings as well as providing some of the experimental data that was reported in this thesis.

I must express my sincere gratitude to the staff and other research students in the Department of Material Science and Engineering and the Advanced Metallic Systems CDT both at Manchester and Sheffield Universities. In particular, I would like to thank Dr Peter Kogul, Dr Peng Zeng, Dr Cheryl Shaw and Dr Le Ma for all the training and facilitating the Electron Microscopy Laboratory sessions at Sorby Centre. Particular thanks go to Dr Joanne Sharp for facilitating and helping out with EELS and EDX on the 2010F. I would also want to thank Richard Kangley for all the help and support in the Met prep lab and Deano Haylock for the support on the TMC machine, tensile and hardness testing machines.

Last but not least, my sincere gratitude goes to my wife and children, for their unwavering support during the course of this project. Without their patience and understanding, this project would not have been a success.

CHAPTER 1: INTRODUCTION

The improvement of vehicle efficiency is now of paramount importance due to the recent prominence of natural resource conservation as well as global warming, with carbon emissions from automotive vehicles being a major contributor[1]. According to the national statistics report recently published by the UK Department of Energy and Climate Change, automotive vehicles accounted for 24% of the total carbon emissions in 2012. Hence, vehicle light-weighting, being one of the ways in which fuel efficiency can be improved, can play an important role in the overall carbon emissions reduction[2, 3]. Other benefits brought about by vehicle light weighting includes the driving performance which also improves as a result[3]. However, despite all these efforts over the past years, the introduction of advanced safety and comfort systems as well as customer's wishes to have more powerful vehicles has led to increased rather than reduced vehicle weight[2].

Weight reduction can be achieved through either material substitution or alternatively architectural changes[2, 4]. Even though aluminium has been used extensively in the top of the range vehicles where it can be afforded, the body in white is always made up of steel. The challenge still remains for aluminium to meet the strength requirements. As a result, technological advancements in steel automotive bodies seem to be the answer. The body of an automotive vehicle and the interiors accounts for approximately 40% of the vehicle's total weight. Therefore, it has the greatest potential for weight reduction[2]. It has been shown that a 100kg reduction in the weight of cars can reduce carbon emissions by approximately 130kg in a year[5]. The major challenge is that of reducing the body weight without compromising the strength of the vehicle.

Ever since Henry Ford introduced the mass production of cars in 1913, steel has always been the material of choice for the automotive industry and numerous studies have since been carried out have always proved that steel has the most competitive

advantage not only in terms of cost effectiveness, but also in production volumes over competing materials such as composites, aluminium and magnesium[4].

Even though Transformation Induced Plasticity (TRIP) steels with strengths in the region of 800MPa have since been developed (TRIP 450/800), it is most unlikely that TRIP and other high strength steels such as dual phase steels (DP) will be developed further with higher strength. A new approach is required, namely the development of Ultra High Strength Steels (UHSS) with improved mechanical properties. The term Ultra High Strength Steel (UHSS) is sometimes used interchangeably with Advanced High Strength Steels (AHSS). These steels are supposed to have superior strength-ductility balance as compared to conventional steels. Some authors have suggested that Twinning Induced Plasticity (TWIP) steels can offer a suitable alternative. Chung et al.[6] investigated the mechanical properties of TWIP940 and showed that a uniform elongation of more than 60% and a UTS close to 1000MPa can be achieved. However, high production costs as well as end splitting (a form of delayed fracture) are some of the major issues preventing manufacturers from adopting TWIP steels [7].

Recent work has suggested that so-called “nanoprecipitation” may provide a microstructural strategy that allows strength and ductility to be developed beyond the current bounds [8-10]. It has been claimed that nanoprecipitates can lead to both high strength and retain high ductility[7, 11, 12]. Where the precipitates are formed distinguishes between the different types of precipitates. Interphase precipitates are believed to be formed at the interphase transformation front during the transformation from austenite to ferrite, resulting in bands of precipitates that run parallel to, and following the direction of the interphase boundary[11]. Other precipitates are known to form on dislocations and grain boundaries (e.g. niobium carbide precipitated in austenite and vanadium carbides formed in the ferrite). Precipitates impede dislocation motion resulting in additional stresses being required to enable the dislocations to either shear the precipitates or loop between them; the preferred mechanism being dependent on the size, distribution and coherence of the precipitates. Funakawa et al.[7] proposed that the optimum is precipitation hardening of an otherwise purely ferritic microstructure, without pearlite or cementite, hence,

minimizing localised stress concentrations, which would give the best combination of ductility and strength. However, this approach tends to ignore benefits brought by other phases. The presence of martensite can greatly improve the strength while retained austenite can introduce the TRIP effect, which improves strength during straining. Recent work by JFE Steel[13] and Raabe et al.[10] confirms this approach. JFE steels[13] claims they have made a high strength low alloy steel (HSLAS) with a tensile strength of up to 780MPa and strengthened by nanoprecipitation, exhibiting a high yield ratio and high formability as well as good plating properties. Raabe et al.[10] reported that through a combination of the TRIP effect and the martensitic aging effect (maraging), they have developed a low alloy high strength steel hardened by heavily strained martensite. The maraging is believed to be responsible for nanoprecipitate formation which acts as an obstacle to dislocation motion enhancing the strength of the material.

This project was undertaken in collaboration with Tata Steels (IJmuiden – The Netherlands); the major objective being to develop a very high strength steel (“Ultra High Strength Steel”) with high uniform elongation for use as raw materials in press forming as well as stretch flanging processes such as body sheets for automotive vehicle manufacturing.

Two strategies were developed to achieve this goal:

- The first strategy involved developing a multiphase steel composition with the ferrite matrix strengthened by nano-sized interphase precipitates formed during the transformation from austenite to ferrite.

In this instance, different strengthening mechanisms were used, with the presence of martensite being an important one. The ductile low carbon α' and ϵ -martensite introduces strain hardening while retained austenite introduces the TRIP effect. The ductile ferrite phase was strengthened through the introduction of nano-sized interphase precipitates which are believed to have been formed at the interphase during the transformation from austenite to ferrite.

-
- The second strategy involved developing precipitation in a predominantly ferritic microstructure without pearlite, cementite or any other phases in order to minimise stress concentrations.

This approach takes advantage of the high ductility brought by the ferrite phase while grain refinement and precipitation strengthening can be adapted to strengthen the alloy.

The project was divided into three major components:

The first part of the project compared three steel alloys of different chemistries. The alloy composition reported by JFE Steels and Raabe et al.[10, 13], which contained Ti, Al and Mo, formed one of the three alloys examined at this stage. This was done in order to verify their claims as well as to verify whether similar or better results could be achieved from the other two alloy compositions. The second steel had vanadium while the third one had titanium as the microalloying additions.

The second part of the project focused on developing various thermal cycles to optimise the mechanical properties of the V microalloyed steel. The success of commercial steels for the automotive industry is heavily dependent on the cost of production and this was one of the main reasons why the V microalloyed steel was of great interest. The steels were heat treated at different thermal cycles after which samples were taken for both microstructural examinations as well as testing for mechanical properties. The results were compared to the TiAlMo steel developed by JFE steels in order to determine if and why TiAlMo was better.

The third and final part of the project looked at the development of a predominantly ferritic steel strengthened by a high number density of nanoprecipitates. The aim at this stage was to develop a new alloy that could be used commercially in automotive manufacturing process.

CHAPTER 2: LITERATURE REVIEW

2.1 Material Selection for Automotive Applications

2.1.1 Introduction

According to the March 2013 national statistics published by the UK Department of Energy and Climate change, 24% of carbon emissions is produced by automotive vehicles in the UK[1]. The use of lighter materials in the construction of automobiles bring about many benefits in terms of fuel efficiency, lowering carbon emissions and improving the overall driving performance of the automotive vehicles[3]. As a result, this chapter examines alternative materials with the potential to fulfil these goals, paying more attention to the role of steel; which is more widely used than any of the other materials. According to the American Iron and Steel Institute, the Life Cycle Assessment (LCA) on automotive materials shows that steel, which currently makes up approximately 60% of the average vehicle, is the most environmentally friendly as compared to other competing automotive material[14].

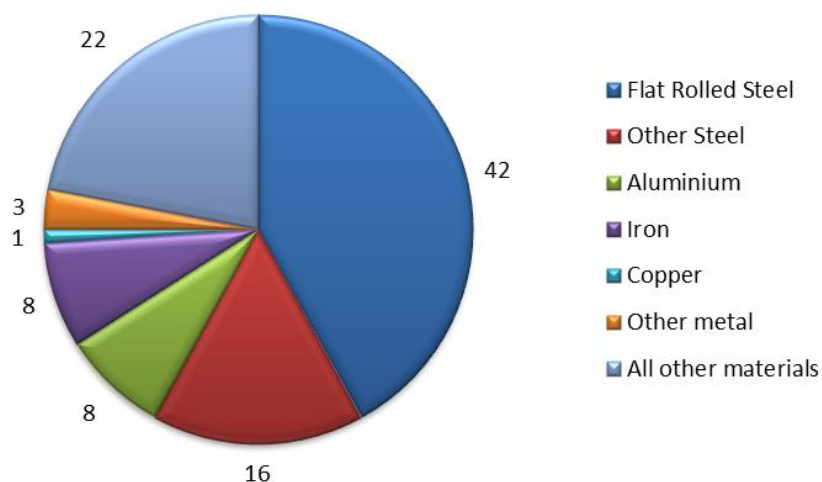


Figure 2.1 – 2010 Light Vehicle Material Content adapted from Steelworks online [14]

Three major strategies have been suggested for weight reduction in automotive vehicles [4, 15]. These includes making architectural changes to automotive body designs, the use of alternative lighter materials such as aluminium and magnesium and the use of new steel alloys with better material performances.

2.1.2 Aluminium

A lot of attention has recently been placed on aluminium as one of the most promising substitutions for steel. Mechanical properties of interest include its low density, which is most effective in weight reduction, as well as its good energy absorption capabilities. When exposed to air, Al forms an oxide layer at the surface which prevents further corrosion and this makes it easier to recycle in its pure form. Its applications have mainly been on body parts such as car bonnets, doors and crossbeams. However, total aluminium builds have been applied in some luxury cars including Audi A8 and BMW Z8[16]. The reasons why aluminium has not been fully adopted by the automotive industry are mainly two fold[2]. Firstly, its lower elastic modulus makes it impossible to substitute steel on a one to one basis. The second reason is its high production costs, which is the reason why it is limited to fewer parts compared to steel in low cost cars. However, it has been extensively used in high cost cars (e.g. Audi A8) not only because of its effectiveness in weight reduction which improves the fuel performance, but also due to emission control legislations.

2.1.3 Magnesium

Magnesium, being even lighter than aluminium, has also recently been used in automotive manufacturing processes. Magnesium alloys have been applied to components such as transmission housings, doors and bonnets for light-weighting. Stamping and forming Mg alloy parts is quite a complex process. Pressure die casting is often used, which brings about the advantage of integrating numerous diverse parts, resulting in further reduction in the overall weight of the automotive vehicle[2]. Unfortunately Mg alloy is expensive and this has also played a significant part in preventing Mg alloy from being adopted by the automotive industry.

2.1.4 Polymers

The use of unreinforced polymers has been limited to plastic bumpers as well as the interior such as the dashboard[2, 4]. This is widely due to their weak mechanical properties which makes it impossible for them to be used in regions where high strength is required. However, polymers reinforced with fibres (e.g. carbon fibres) have recently been used for energy absorption parts in few high value vehicles such as the Aston Martin due to the high cost of production[2].

2.1.5 Steel

Ever since the first automotive vehicle was invented, steel has always been the material of choice for the automotive industry. Besides the low carbon footprint as compared to other automotive materials, steels bring a whole range of other benefits including low cost of production, mass reduction capabilities, safety traits as well as greater recyclability capabilities [14]. Some of the grades commonly used in the current generations of automotive vehicles will be briefly discussed in the next section.

2.1.6 High Strength Low Alloy Steels (HSLA)

HSLA steels were designed to give better mechanical properties in terms of strength and ductility. They are generally low carbon sheet steels having C content ranging from 0.05 to 0.25wt. %[17]. They can be produced in the form of rolled products ranging in yield strength from 290-550MPa and UTS of 415-700MPa[18]. They are relatively cheap to produce due to the small alloying elements additions that are required to generate the desired mechanical properties. The role of the microalloying additions will be discussed in more detail later in this chapter. The resulting product is generally more resistant to corrosion as compared to other conventional carbon steels.

The contribution to strength in HSLA steels comes from several strengthening mechanisms including grain refinement, precipitation strengthening, dislocation strengthening, solid solution and strain aging[18]. The desired microstructure and mechanical properties can be attained through [18]:-

- Microalloying with strong carbide or nitride formers such as Ti, Nb, V and Mo.
- Controlled rolling coupled with controlled cooling and
- Controlling the shapes of the inclusions.

Even though several strengthening mechanisms have been suggested, the key feature that determines the strength-ductility balance in HSLA steels has been the refinement of the ferrite grains. The various strengthening mechanisms will be discussed later in this chapter.

2.1.7 Advanced High Strength Steels (AHSS)

In order to improve the fuel efficiency of vehicles through weight reduction of automotive vehicles, materials that offer high formability and high strength per mass ratios are now part of the automotive designs for improved crashworthiness and the forming of complex shapes associated with modern vehicles[19-21]. These steels are known as Advanced High Strength Steels (AHSS). The UltraLight Steel Autobody consortium (ULSAB)[22] defined high strengths steels as steels with yield strengths ranging from 210-550MPa. Ultra High Strengths steels were defined as having strengths greater than 550MPa while AHSS were defined as overlapping between HSS and UHSS. Figure 2.2 shows the strength-elongation relationship for mild, conventional HSS and AHSS.

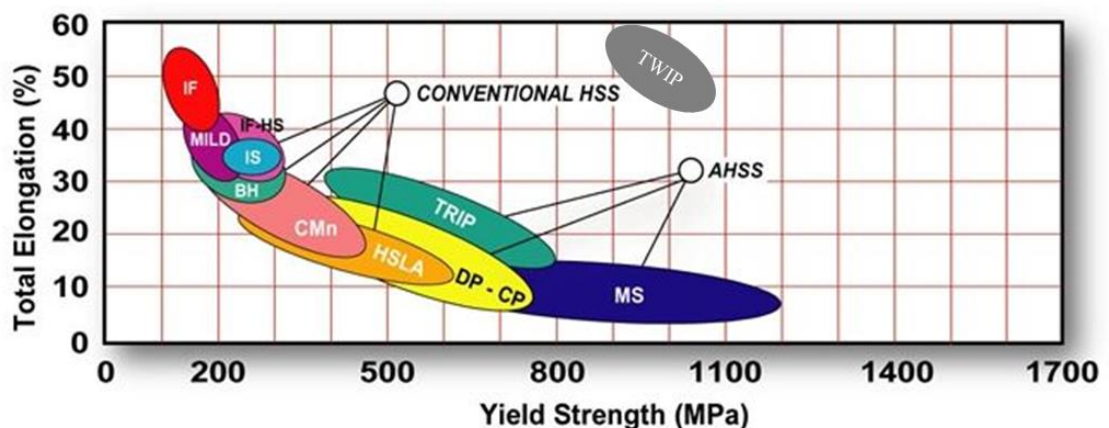


Figure 2.2 –Strength-Formability relationship for AHSS as compared to low strength steels and conventional HSS[23]

The major difference between conventional HSS and AHSS has always been attributed to the microstructure. HSS have a ferritic microstructure whereas AHSS are multiphase. AHSS also exhibits superior combinations of strengths and ductility, taking advantage of strength-ductility balance brought about through the introduction of other phases as compared to HSS. Current automotive steels falling into the AHSS category includes Dual Phase (DP) steels, Transformation Induced Plasticity steels (TRIP), Twinning Induced Plasticity steels (TWIP) and martensitic steels. The structure and distribution of the phases within AHSS steels is mainly a function of the chemical composition, annealing temperatures and quenching rates. For TRIP and DP steels, appropriate selection of the intercritical annealing parameters is crucial to get the desired microstructure[24]. Higher energy absorption capabilities have been one of the major advantages of using DP and TRIP steels with ferrite as the major phase[22, 23]. This has been attributed to the high work hardening rate and bake hardening which results in high UTS. The greater energy absorption capabilities of these steels are a result of the large area under the true stress-strain curve. Work hardening during the forming process also increases the area under the stress-strain curve, further improving energy absorption capabilities during car crushes.

2.1.8 Mechanical Properties of DP, TRIP and HSLA Automotive Steels

The mechanical properties for TRIP and DP steels for automotive applications as reported by Schaeffler[25] are listed in Table 2.1. DP steels have yield strengths (YS) ranging from 280 to 700MPa, maximum UTS of 1000MPa in DP700/1000 and total elongation ranging from 12 to 34% depending on the grade. TRIP steels compares very well with a YS of 450MPa, UTS of 800MPa and total elongation ranging from 26 – 32%. HSLA steels have YS of 350MPa, UTS of 450MPa and total elongation ranging from 23 – 27% which is comparably lower than both TRIP and DP steels.

Table 2.1 – Tensile properties for automotive steels[25]

Steel Grade	YS [MPa]	UTS [MPa]	Total Elong. [%]
DP 280/600	280	600	30 - 34
DP 300/500	300	500	30 - 34
HSLA 350/450	350	450	23 - 27
DP 350/600	350	600	24 - 30
DP 400/700	400	700	19 - 25
TRIP 450/800	450	800	26 - 32
DP 500/800	500	800	14 - 20
DP 700/1000	700	1000	12 - 17

2.1.8.1 Work Hardening and Yield Behaviour

DP steels do not show a yield point and this is due to the existence of high mobile dislocations and high residual stresses which promotes plastic flow[26]. Conditions favourable for plastic flow include fast cooling to transform austenite to martensite thereby creating residual stresses that results in the formation of incremental dislocations in the ferrite[27]. The first stage involves rapid work hardening due to the eradication of residual stresses and rapid accrual of back stresses in the ferrite due to plastic mismatch of the two phases. This high work hardening at the initial stages is believed to be responsible for the high formability of these steels[27, 28]. The reduction in work hardening in the second stage is attributed to the constrained plastic flow of the ferrite by the hard un-deformed martensite. In TRIP steels, this is the stage where the transformation of retained austenite to martensite is also likely to occur. The third and final stage involves the formation of dislocation cell structures. The dynamic recovery, cross slip and yielding of the martensite controls further deformation of the ferrite. Oliver et al.[28] showed that the tensile strength in both DP and TRIP steels increased with increasing hard second phase e.g. bainite and martensite. Figure 2.3 compares the flow behaviour for DP, TRIP and HSLA steels.

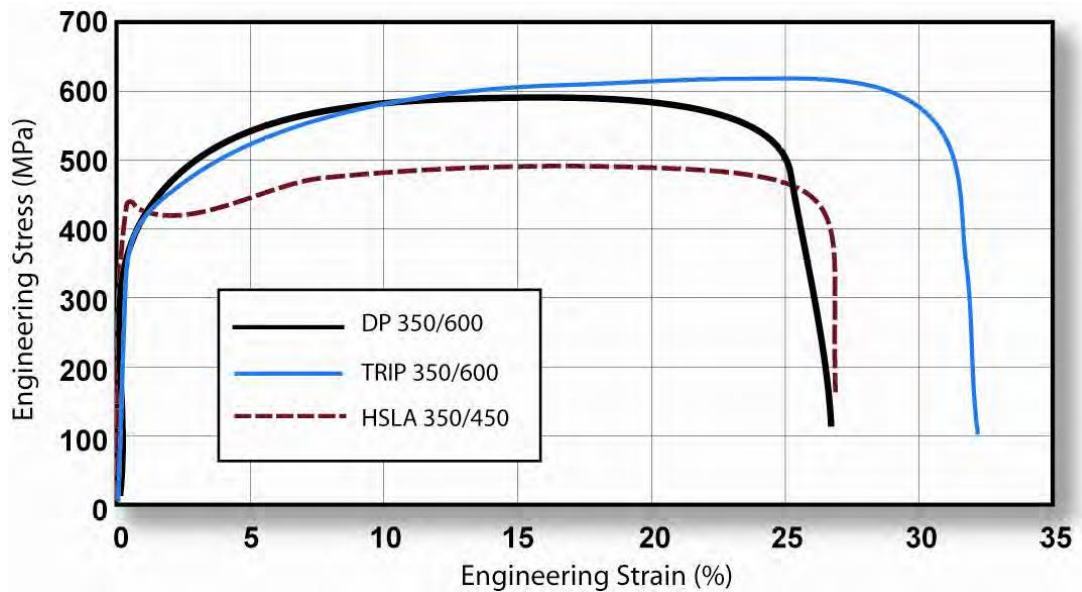


Figure 2.3 – Stress strain curve showing TRIP 350/600 with greater total elongation than DP350/600 and HSLA 350/450[23]

It is clear that even though HSLA steel has the highest yield point, DP and TRIP steels have high UTS and high uniform elongation. The work hardening behaviour of DP steels just after yielding is much higher than that of TRIP and HSLA steels. However, this tends to decrease with increasing strain. In contrast, work hardening seems to increase with strain for TRIP steels. Oliver et al.[28] showed that ferrite deformation was much higher in TRIP grades as compared to DP grades. The work hardening behaviour was attributed to additional stresses and dislocations in the ferrite and at the ferrite-bainite interface during the transformation of retained austenite to martensite. The volume expansion generated as a result of this transformation deforms the ferrite further, resulting in the creation of additional dislocations. The additional dislocations increases strain hardening, delaying necking and increasing the overall uniform elongation. Beynon et al.[26] observed deformed ferrite grains around martensite islands which increased the grain elongation measurements in a range of DP grades.

2.1.9 Dual Phase Steels

DP steels are a class of low alloy steels that exploit the microstructure which is composed mainly of martensite grains (hard phase for strength) within a ferrite matrix (softer phase for ductility) and having an ultimate tensile strength ranging between 600 to 800MPa. DP steels for automotive applications can be produced through cold rolling followed by continuous annealing. Rapid heating of the strip to annealing temperatures in the $\alpha + \gamma$ region above the A_{c1} results in the transformation of ferrite to a ferrite-austenite mixture. This temperature determines the volume fractions of the ferrite and austenite in the matrix. The strength of the final product is dependent on the volume fraction of the martensite, which in turn is dependent on the volume fraction of the austenite phase at the intercritical temperature[28, 29].

The temperature is kept constant in the intercritical region for a specified period and then quenched, the cooling rate providing the driving force for transformation from austenite to martensite. The cooling rate determines the level of strength. High cooling rates ensures that greater amounts of austenite are transformed to martensite. Alloying elements such as manganese, chromium and molybdenum are also added to ensure successful transformation from austenite to martensite during quenching. The processing of DP steels is similar to that for TRIP steels in Figure 2.4; the only difference being that there is no temperature hold in the bainitic transformation region for DP steels. Numerous studies have since been carried out to determine the effect of volume fraction of the phases as well as the tempering conditions on the steel mechanical properties [30-32]. Akbarpour et al.[30] investigated the dependency of phase compositions (volume fraction of ferrite and martensite) and mechanical properties on the annealing time as well as the work hardening behaviour of DP steels. They concluded that the strength decreased while the uniform elongation increased with increasing ferrite volume fraction. Kumar et al.[31] investigated the properties and structure of the phases in DP steels, paying attention to tensile and hardness properties as a function of the bainite and martensite volume fraction. A similar study was also conducted by Saeidi and Ekrami[33] and their

conclusion was that ferrite-bainite steels had lower strength and better formability as compared to ferrite-martensite steels.

2.1.10 Transformation Induced Plasticity Steels (TRIP steels)

TRIP steels rely on the presence of retained austenite; hence, they are mixtures of ferrite, retained austenite, bainite and martensite. It is well established that retained austenite in steels, after heat treatment, has the effect of improving both toughness and ductility[34]. Ductility and work hardening properties in TRIP steels have been shown to be superior in TRIP steels as compared to DP Steels of similar grades[28, 35]. Their microstructure is composed of mainly ferrite combined with 30 – 40% of harder regions which could be a combination of mixtures of bainite, martensite and carbon enriched retained austenite[13]. The retained austenite in TRIP steels is generally between 5 to 10% and this is normally brought about through the use of expensive austenite stabilizers such as nickel[36]. In order to improve the carbon enrichment into retained austenite, alloying elements which inhibit cementite formation are often used. Critical to the development of TRIP steels is the determination of the right mix of alloying elements for the attainment of the right properties. Conventional TRIP steels have compositions based on 0.12-0.55wt % C, 0.2 – 2.5 wt. % Mn and 0.4 – 1.8 wt.% Si.

During straining, the FCC structure of the retained austenite transforms to the martensitic BCT structure or bainite. The transformation to martensite and bainite during straining contributes to work hardening of the material and at higher strain rates; the large strain hardening rates tend to persist as compared to DP steels whose work hardening rate diminishes with strain rate. Huh et al.[37] compared the dynamic tensile properties of TRIP600 and DP600 and they observed that the flow stress increased with strain rate with the formability and total elongation being better in TRIP as compared to DP steels. The slow transformation delays necking, making a significant contribution towards the high uniform elongation and this is what is known as the TRIP effect. This is the particular reason why TRIP steels tend to be more formable compared to DP steels.

2.1.10.1 Intercritical Annealing of Multiphase Steels

The annealing cycles used to produce TRIP steels have a lot of similarities to those for DP steels. Just like DP steels, rapid heating of the strips to annealing temperatures in the intercritical region ($\alpha + \gamma$) above the A_{c1} are also required to transform the ferrite into a ferrite-austenite mixture. Figure 2.4 is a schematic representation of the continuous annealing process for TRIP steels. The strip is then quenched to temperatures in the bainitic transformation region and this is also known as austempering [38, 39]. At this stage, rapid cooling ($>30^{\circ}\text{C/s}$) is required in order to prevent cementite and pearlite formation. However, the initial cooling rate may be lower to further enrich the austenite with carbon and this can only be done when the temperature is still above the A_{r1} temperature[40]. Unlike DP steel production, an isothermal bainitic transformation hold stage is introduced in the region $400^{\circ}\text{C} - 500^{\circ}\text{C}$.

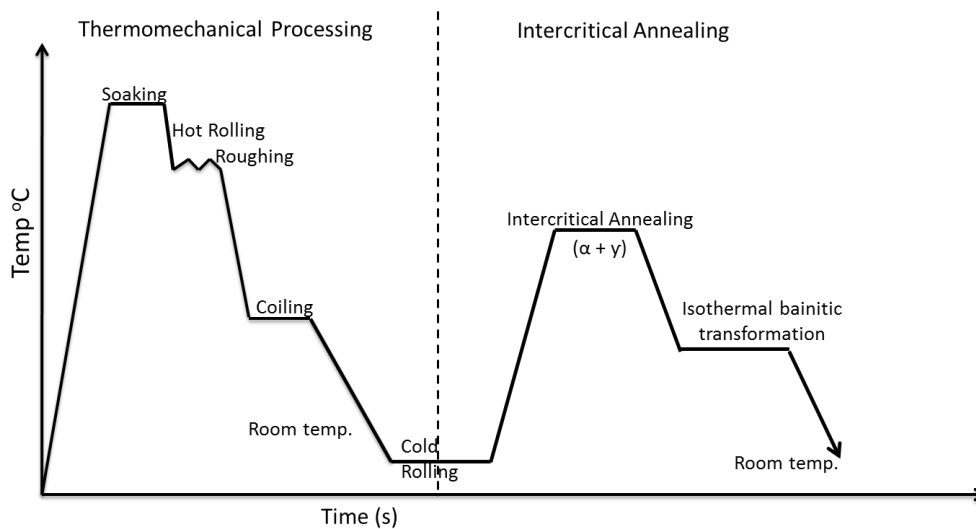


Figure 2.4 - Schematic of the combined conventional thermomechanical process and continuous annealing cycle for cold rolled intercritically annealed TRIP steels[40]

This stage depresses the martensite start temperature to below 0°C while encouraging bainite formation[28]. The carbon which is rejected by bainitic ferrite partitions into the remaining austenite. This carbon enriched austenite remains stable on further cooling to room temperature and this is what is known as retained austenite[39, 41-44]. During slow cooling to room temperature, some of the retained austenite might transform to martensite

Due to the existence of several phases within the microstructure, TRIP steels are sometimes referred to as multiphase steels. Critics have argued that the improved mechanical properties of these steels are a result of the contribution from the various phases. Bhadeshia, working on a steel of chemical composition Fe–0.15C–1.5Si–1.5Mn wt%, showed that retained austenite contributes approximately only 2.25% to the total elongation of the steel[45]. Jacques et al.[46] came to the same conclusion and they argued that the work hardening effect was a result of contributions made by each of the phases within the microstructure.

2.1.11 Twinning Induced Plasticity Steels (TWIP)

Among those recently developed and promising steels is high manganese austenitic steel with low stacking fault energy (SFE). A combination of high strength and ductility has been found to occur especially when mechanical twinning occurs. This is caused by the low stacking faulty energy (SFE) in face centered cubic (FCC) material which promotes mechanical twinning [47]. Most of the TWIP steels have manganese content in the region of 15 to 25% and this produces an austenite matrix (FCC structure)[11].The addition of manganese and other alloying elements stabilizes the austenite so that it becomes stable at room temperature. The deformation mechanisms of TWIP steels have been found to involves both twinning and dislocation slip[48]. Mechanical twinning is the dominant mechanism for high strain hardening rates. Austenite can have a high total elongation (>60%) attributed to its high strain hardening rate which is due to the mechanical twinning delaying necking[6]. These high strain hardening rates in Fe-Mn-C austenitic steels can be attributed to dynamic strain aging mechanisms which are a result of the interaction between C-Mn bonds and mobile dislocations[47].

Recent studies have shown that it is possible to produce TWIP steels with manganese content greater than 12% [34, 49]. Dini et al.[34] showed that grain refinement of Fe-31Mn-3Al-3Si submicron TWIP steel can give rise to UTS of 811MPa and an elongation of 52%. By extrapolating the Hall-Petch relationship, their conclusion was that TWIP steels with grain sizes of 210nm can yield strengths of over 1000MPa. The strengthening mechanisms were attributed to twin boundaries while the ductility was attributed to reduction in dislocation density. In general,

TWIP steels have very high ductility and very high work hardening which improves strength.

Bouaziz et al.[49] showed that the TWIP effect in Fe-22Mn-0.6Mn is mainly kinematic and that the mechanical twins have thermal stability which makes a significant contribution towards the strength (same mechanism as grain boundaries). Chung et al.[6] also investigated the mechanical properties of TWIP940, which is one of the few TWIP steels that have managed to make it into the commercial market. They concluded that it was possible to produce a TWIP steel with uniform elongation greater than 60% and a UTS close to 1000MPa.

Commercially, the market has been a bit hesitant in adopting TWIP steels partially due to forming issues which have remained unresolved. These includes poor hole expansion and stretch forming performances, low normal anisotropy and low strain sensitivity. Zn and Zn alloy coating remains a major issue and delayed fracture which causes splitting on the edges of the plate has also been one of the major issue preventing manufacturers from adopting TWIP steels [11]. Low yield strength is also one of the issues that needs addressing. The high costs of production associated with high alloying additions (e.g. Mn) also makes TWIP steels commercially non-viable. However, there is no doubt that TWIP steels have got a lot of potential and the possibilities are endless for them to be the material of choice for future automotive applications.

2.1.12 Ultra High Strength Steels

Steel components in automotive vehicles currently account for approximately 60% of the automotive materials. The use of UHSS in automotive manufacturing has the greatest potential to reduce the production costs even further. The development of Ultra High Strength Steels (UHSS) with even higher strengths and ductility makes it possible to manufacture single and lighter components where traditionally, components would be joined together. In addition to reduced welding costs, this has the added advantage of reducing regions of high stress concentrations brought about by hydrogen embrittlement introduced through welding. Crash performances are boosted by the additional strength while weight reduction is achieved through thickness reduction at the same time. The large orange area in Figure 2.5 shows the region where future steels (UHSS) are likely to fit in within the elongation-strength diagram. The aim is to improve the strength range without compromising formability while simultaneously reducing the overall production costs and improving weldability.

Despite the pitfalls encountered so far, the TWIP steels similar to those proposed by Dini et al.[34] also fall into this category. Grajcar et al.[50] proposed steels comprising complex multiphase structures combining microalloying, solid solution strengthening, precipitation strengthening, grain refinement as well as TRIP and TWIP effects. Some authors have suggested that nanoprecipitation strengthened steels can provide the solution [7, 10, 13].

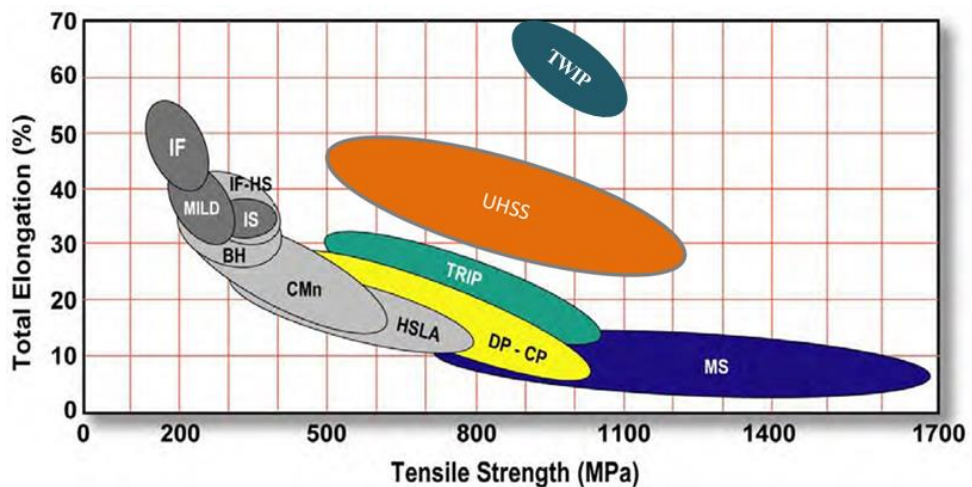


Figure 2.5 – Schematic diagram of total elongation vs strength for automotive steels. The region in orange represents future steels (UHSS), (adapted from WorldAutoSteel)[23].

2.1.13 Martensitic Steels

Martensite forms when austenite is rapidly quenched to temperatures below the martensite start (M_s) temperatures (uninterrupted cooling in commercial steels). The M_s and M_f temperatures are controlled by alloying additions. The high cooling rates involved leaves no time for the carbon dissolved in the austenite to diffuse resulting in the martensite formed having the same composition as the original austenite phase, resulting in a super saturation of the carbon. The result is a tetragonal (BCT) crystal symmetry. The hardness of the martensite formed is dependent on the degree of tetragonality, which is also dependant on the concentration of carbon. Martensite exists in the form of either lath or plate martensite, depending on the carbon content. Lath martensite is made up mainly of high dislocation density and fine twins.

Ultra high strength in DP and multiphase steels can be attained through a combination of finely dispersed precipitates in the ferrite and a fine lath martensitic matrix whose strength is mainly attributed to the high dislocation density[51, 52]. Lath martensite can be formed through an appropriate solution treatment followed by quenching to below the martensite start temperatures (M_s). Very high dislocation density constitutes the substructure of lath martensite. The high dislocation density is not only responsible for strengthening; it also forms potential sites for nucleation of precipitates in several steel commercial grades [53-55].

2.1.14 Quench and Partition Steels

The conventional way of producing carbon enriched retained austenite has always been through intercritical annealing heat treatments. However, it has been established that the same result can be attained through partially quenching to martensite and this is known as the Quench and Partition (Q & P) process [56-59]. The heat treatment cycles are illustrated in Figure 2.6. The process involves quenching from the austenising temperature (AT) to intermediate temperatures between the martensite start (M_s) and martensite finish (M_f) temperatures. This is then followed by partitioning at a partitioning temperature (PT) which takes place either at the initial quench temperature or above. The partitioning treatment ensures that the excess carbon from the supersaturated martensite partitions into the unstabilized austenite [56, 58, 59]. Complete stabilization of the retained austenite is then achieved through reducing the temperature to room temperature or below[59].

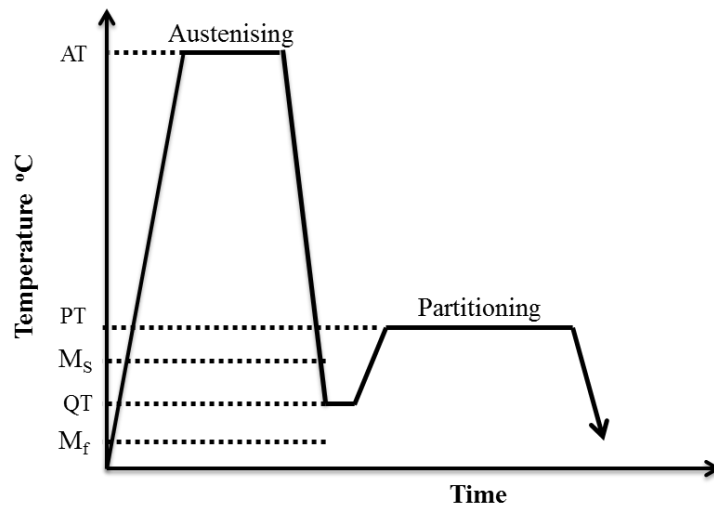


Figure 2.6 – Schematic of the Q and T heat treatments adapted from[59]

The final microstructure comprises various phases formed during the process and this includes ferrite, stabilized austenite, some bainite formed during the longer partitioning times, lower carbon martensite formed after the initial quench and high carbon martensite formed following the depression of the temperature to below room temperature. Working on steels of various chemical compositions, Edmonds et al.[59] demonstrated that through controlling thermodynamic and kinetic process parameters, the Q & P process has great potential over the evolution of the microstructure especially the extent to which the austenite could be enriched.

2.1.15 Bainite in Steels

The control of bainitic structures can play a major role in the strength-ductility balance in steels[60]. As an example, it is well established that the strength-ductility balance is quite sensitive to the distribution of the second phase. Bainite exists mainly in three major forms; granular, upper and lower bainite[60, 61]. Elongated carbides tends to form between bainitic ferrite in upper bainite whereas carbides are inclined at an angle to the longitudinal axis in lower bainite.

2.1.15.1 Granular Bainite

Granular bainite is most common in low carbon steels. Zajac et al.[60] defined it as having a microstructure consisting of irregular ferrite with second phases sandwiched between the ferrite. The ferrite is believed to form through diffusion controlled ledge mechanism. Retained austenite is sometimes present as a result of carbon partitioning from the bainitic ferrite. The granular or equiaxed shape of the retained austenite within granular bainite has been attributed to it being constrained by the granular, lath-less ferrite. The major characteristic of granular bainite is the absence of carbides in the microstructure. Different phases can form depending on the alloying elements. Zajac et al.[60] observed degenerate pearlite, martensite and mixtures of incomplete transformation products in steels of different chemical compositions. As an example, pearlite and/or cementite is likely to form in steels alloyed with Mo due to the lowering of C activity in austenite. In this case, cementite can form easily from the retained austenite. Figure 2.7 is a SEM image of a V microalloyed steel showing granular bainite.

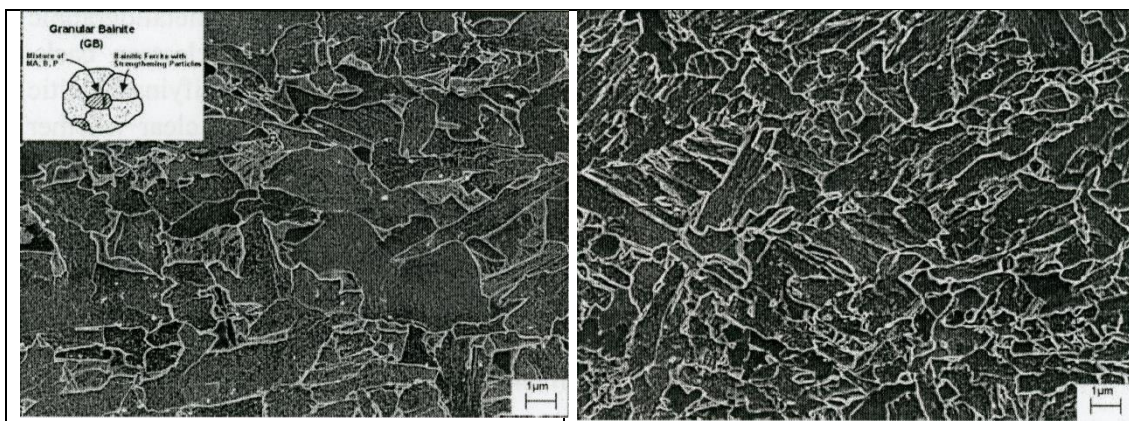


Figure 2.7 – Granular bainite in .06C-B-free Steels and 0.04C complex B-steel[60]

2.1.15.2 Upper Bainite

Upper bainite is formed at temperatures below that of pearlite formation (550 to 400°C)[11]. Nucleation of ferrite laths starts from the grain boundary having a Kudyumov-Sachs or Nishiyama-Wasserman orientation relationship between austenite and bainitic ferrite[62]. The transformed region changes shape resulting in large strains being exerted on the neighbouring austenite grains. These strains cause the dislocation density to increase, stopping plate growth, and creating a much smaller ferrite grain size as compared to the original austenite grain size. Neighbouring ferrite grains formed have a small misorientation, which normally does not exceed 18°[11]. The growth of ferrite laths results in the accumulation of carbon in the neighbouring austenite grains exceeding equilibrium. Excess carbon is then precipitated directly from the austenite to form cementite. The growth of bainite in thin plates is associated with the minimization of strain energy. High carbon content and lower transformation temperatures results in larger regions enriched with carbon. Carbide aggregates associated with upper bainite are a result of this carbon accumulation. Lower transformation temperatures reduce carbon diffusion ahead of the ferrite-austenite front, reducing the rate of ferrite laths growth and resulting in narrow ferrite being formed. The narrow ferrite tends to be saturated with carbon due to slower carbon diffusion. If the carbon concentration in the residual austenite is high enough, continuous layers of cementite can be found separating the ferrite plates as shown in the TEM image in Figure 2.8.

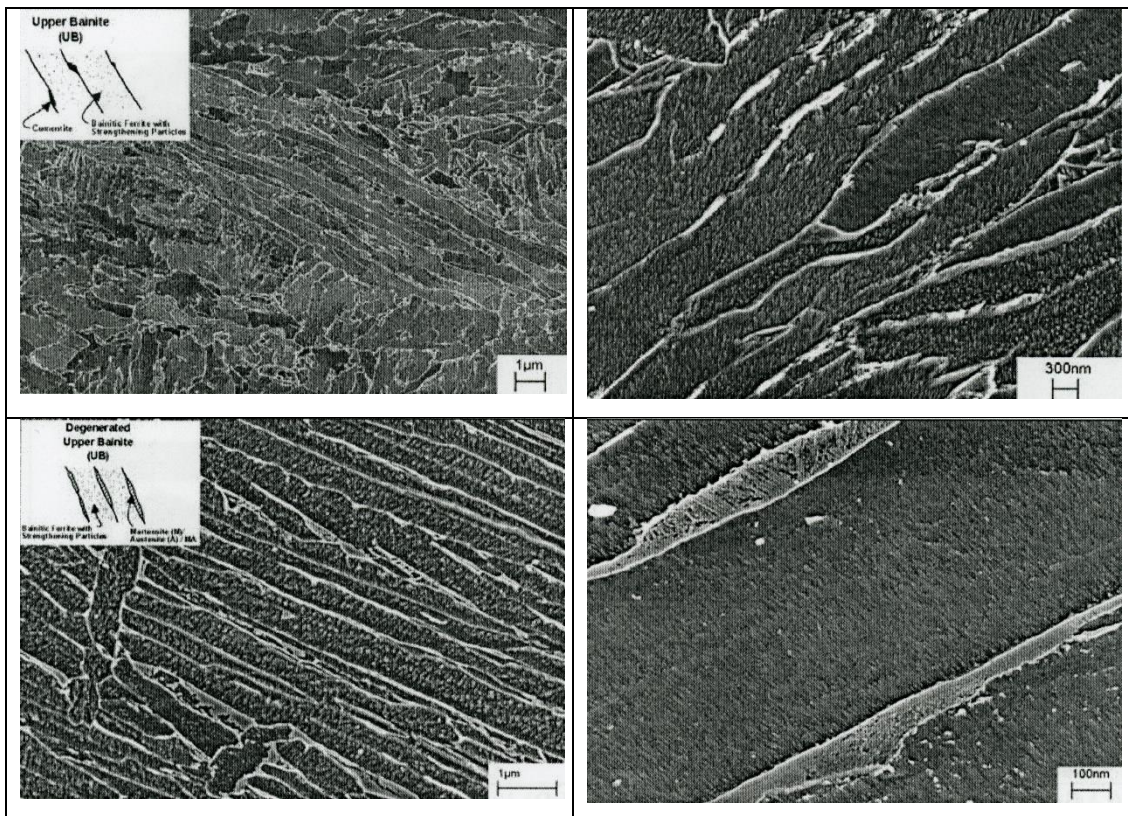


Figure 2.8 - TEM thin foil image showing upper bainite produced by carbon enrichment of austenite in a V microalloyed steel

2.1.15.3 Lower Bainite

Further cooling results in carbon diffusion ahead of the austenite-ferrite boundary becoming slow such that no diffusion can take place ahead of the boundary. The concentration of C in ferrite becomes too high and upper bainite cannot be formed any longer. At this stage, the transformation to lower bainite begins. Bainitic ferrite initially forms by shear, followed by precipitation of carbides with similar orientation relationships to that of ferrite and carbide in tempered twinned martensite. The lowering of the carbon content as a result of precipitation provides the driving force for the bainitic ferrite to grow. This new growth results in saturation, followed by precipitation, and then ferrite growth again. The process repeats itself until impingement into the adjacent plate occurs.

Lower bainite forms at temperatures closer to the martensite start (M_S) temperatures (400 – 250°C). Both lower and upper bainite have the same features in terms of microstructure and crystallographic features. The major difference is the existence of cementite precipitated within lower bainite; some from carbon enriched austenite

separating the platelets and the other from supersaturated ferrite[11]. In high carbon steels containing high silicon content (~1 wt %), epsilon carbides can be found in the bainite. Though the carbides formed are normally fine, this reduces the carbon available for partitioning into retained austenite. Lower bainite is also susceptible to crack and void nucleation due to coarse cementite particles. However, it is much tougher and stronger compared to upper bainite.

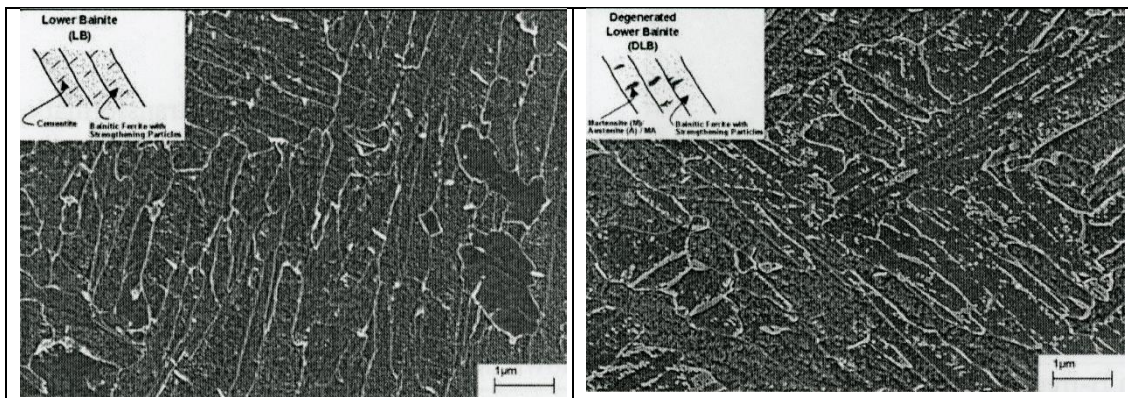


Figure 2.9 - SEM images showing lower bainite type carbides in a Ti microalloyed steel

2.1.15.4 Strengthening Mechanisms in Bainite

Some of the strengthening mechanisms in bainite includes:-

1. Bainitic ferrite grain sizes – In general, the bainite grain size becomes finer with decreasing transformation temperature. The yield strength can be linked through the Hall-Petch relationship[11]. Pickering[62] showed that there was an incremental linear relationship between the tensile strength and the reciprocal of the square root of the bainitic ferrite grain size.
2. Dispersion of carbides – At lower transformation temperatures, the bainitic carbides tend to become finer and increase in number density. Hence, dispersion strengthening increases with decreasing transformation temperature.
3. Dislocation density - Strains associated with shear transformation leads to high dislocation densities both in the bainitic ferrite as well as the adjacent austenite grains. The high strength can be attributed to additional forces being required to transport dislocations through the structure. Dislocation density tends to increase with decreasing transformation temperatures; with lower bainite having much higher dislocation density as compared to upper bainite.

Bainite in steels can be boosted by increasing the carbon content to about 0.15% as well as retarding the transformation from austenite to ferrite by adding alloying elements such as Mo and B[60]. Suppressing the transformation from austenite to ferrite or martensite is required while the transformation to bainite over a wide temperature regime is the ultimate goal. The strength derived from bainite has been found to be a function of the transformation temperature[62]. Better toughness can be promoted through lowering temperatures to form lower bainite as compared to upper bainite. 50% transformed and complete transformation to bainite can be related to the bainite start temperatures through the following equations[18]

$$B_{50(oc)} = B_s - 60 \quad \text{Eq. 2.1}$$

$$B_{f(oc)} = B_s - 120 \quad \text{Eq. 2.2}$$

Figure 2.10 shows the relationship between the tensile strength and 50% transformation temperature.

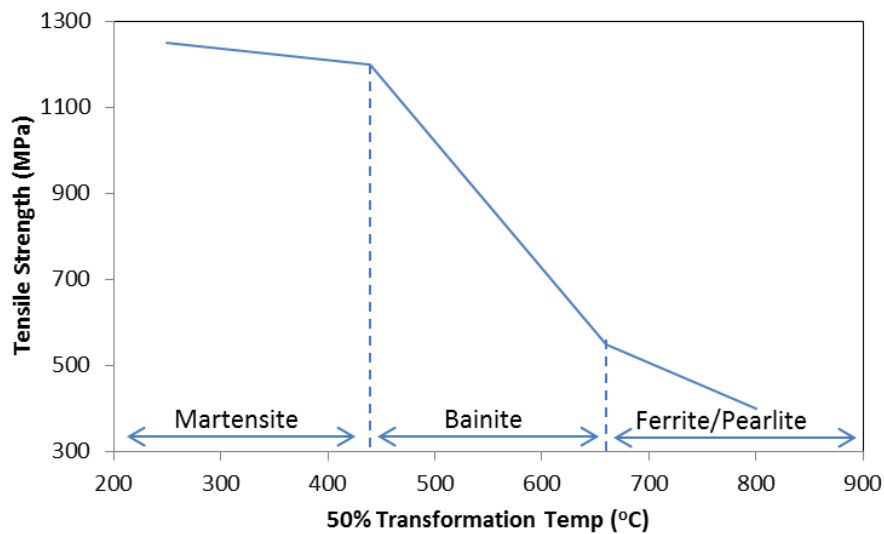


Figure 2.10 - Effects of 50% transformation temperature on tensile strength of bainite.
Adapted from F.B. Pickering[62]

2.1.16 Ferrite-Pearlite Steels

The carbide distribution in steels greatly influences the mechanical properties. Spheroidal cementite and lamellar pearlite as an example can withstand cracking at small strains. The strain needed to nucleate voids tends to decrease with increasing volume fraction of pearlite or cementite, hence, the higher the carbon content, the lower the strain needed to nucleate voids. The other contributing factor to reduced ductility is the fast propagation of the crack across the lamellae once the crack has been nucleated. For carbon steels with high pearlite content, Gladman et al.[63] showed the relationship between the yield strength and the pearlite content.

$$\sigma_y = 15.4 \left\{ f_\alpha^{\frac{1}{3}} \left[2.3 + 3.8Mn + 1.13d^{-\frac{1}{2}} \right] + \left[1 - f_\alpha^{\frac{1}{3}} \right] \left[11.6 + 0.25S_p^{-\frac{1}{2}} \right] + 4.1Si + 27.6N \right\} \quad \text{Eq. 2.3}$$

where f_α is the volume fraction of the ferrite, S_p is the interlamellar spacing of the pearlite in mm and d is the mean grain size in mm. The term $f_\alpha^{\frac{1}{3}}$ implies that the yield strength varies non-linearly with pearlite content.

Equation 2.1 demonstrates that the grain size becomes increasingly insignificant with increase in pearlite content. Decreasing the pearlite content ensures little or no contribution of pearlite to the yield strength. The interlamellar spacing also controls the yield strength especially in high carbon steels. Improved yield strengths can be attained through smaller pearlite interlamellar spacings. This can be done by fast cooling from the austenising temperatures to ensure pearlite formation starts at lower temperatures.

Further to Gladman's work, Heller[64] proposed a simpler equation based on the assumption that alloying elements had no effect on the yield strength in eutectoid carbon steels.

$$\sigma_y = -85.9 + 8.3S_p^{-\frac{1}{2}} \quad \text{Eq. 2.4}$$

Due to the effect of pearlite on work hardening, Heller[64] then proposed that the pearlite content had a greater effect on the UTS than the yield strength

$$UTS = 15.4 \left\{ f_\alpha^{\frac{1}{3}} \left[16.0 + 74.2\sqrt{N} + 1.13d^{-\frac{1}{2}} \right] + \left[1 - f_\alpha^{\frac{1}{3}} \right] \left[46.7 + 0.23S_p^{-\frac{1}{2}} \right] + 6.3Si \right\} \quad \text{Eq. 2.5}$$

2.1.16.1 Banding in Pearlitic Steels

Banding refers to the microstructure with alternate layers rich in either pearlite or ferrite. Segregation of Mn during solidification is the major cause of banding and it is most noticeable in steels with equal proportions of C and Mn, e.g. 0.25C and 1.5Mn wt. %[18]. Mn additions reduce the activity coefficient of C in austenite, resulting in the segregation of C with Mn. Regions with high carbon content becomes prone to pearlite formation. Crack propagation is much easier parallel to the bands as compared to normal to the bands. Hence, banded microstructures in carbon steels should be avoided where possible. Homogenisation can reduce banding in some cases.

2.1.17 The Role of Microalloying Elements

The four major roles of microalloying elements includes:-

- the control of grain coarsening by pinning the grain boundaries,
- solid solution strengthening,
- increasing the hardenability and
- precipitation strengthening.

2.1.17.1 Carbon

In multiphase steels, carbon plays a crucial role by enriching austenite to form retained austenite, which is stable at room temperature. Good mechanical properties in transformation induced plasticity (TRIP) steels are a result of the stabilized retained austenite. Carbon also plays an important role by combining with other microalloying elements such as Ti, Mo, V and Nb to form composite carbides or finely dispersed precipitates in ferrite, which are crucial in precipitation strengthening. However, quantities greater than 0.25 wt% does not only create weldability issues[40], they also promotes martensite formation, which is detrimental to uniform elongation. Preventing the precipitation of iron carbides during bainite transformation results in carbon being partitioned from the bainitic ferrite to the residual austenite[65]. Quantities less than 0.1 wt% are most effective for precipitation strengthening and care should be taken to prevent carbon from forming unwanted intermetallics and to ensure that all the available carbon is used for the intended purpose.

2.1.17.2 Nitrogen

Just like C, N forms composite nitrides when coupled with V, Ti, Nb or Mo. In the presence of C, it can also combine with the C to form carbonitrides. The nitrides and carbonitrides formed also play a crucial role in precipitation strengthening as well as grain refinement. Nitrides are far less soluble in austenite compared to carbides. As a result, they dominate at higher temperatures whereas the carbides starts to dominate at lower temperatures. However, excessive amounts of N can lead to coarse precipitates which are not suitable for either grain refinement or precipitation strengthening. Hence, the N content should always be kept as low as possible[13].

2.1.17.3 Silicon

Si significantly contributes to the overall solid solution strengthening while also improving the activity coefficient of C in both austenite and ferrite. However, Si reduces solubility of C in ferrite. It also reduces bainitic transformation kinetics, which means that longer overaging stages are required in industrial processes. Carbon partitioning from bainite to the remaining austenite is promoted while suppressing the formation of cementite. Some authors have suggested that since Si is insoluble in Fe₃C, nucleation and growth of cementite can only take place after Si has diffused away, a process which takes time to complete, thus retarding the rate of cementite formation[66]. Si additions less than 0.001wt% do not have any significant impact on the alloy. However, additions greater than 0.5wt% creates problems with surface quality and galvanising[13]. The formation of stable oxides e.g. Mn₂SiO₄ and SiO₂ in the presence of oxygen and other alloying elements creates conditions unsuitable for galvanising. However, Si has been found to be one of the most effective cementite inhibitor during austempering.

2.1.17.4 Niobium

It has been shown that small additions of Nb can yield both grain refinement and precipitation strengthening [67-69]. The lower solubility of niobium carbides or carbonitrides in austenite makes it more stability at high temperatures, which makes it more effective for grain refinement as compared to V which can completely dissolved in austenite at high temperatures[70, 71]. Nb is also known to suppress the formation of cementite and to lower the martensite start temperature. Carbide precipitation in the bainitic transformation region is also suppressed, thereby providing incremental carbon for partitioning into retained austenite[72]. Niobium additions are generally limited from 0.025 to 0.11wt%. However, in commercial processes, quantities beyond 0.08wt% are usually avoided in order to limit the rolling forces[13].

2.1.17.5 Vanadium

The fact that the solubility of V in austenite is much higher compared to Ti, Mo and Nb makes it more effective for precipitation strengthening rather than grain refinement. It has been shown that a fine dispersion of precipitates can be obtained in steels alloyed with V. It has been well established that V is the most effective element as far as the formation of interphase precipitates which are known to be most effective in precipitation strengthening is concerned [11, 70, 73]. However, it is also well known that it is the least effective in terms of grain refinement. This is attributed to the high solubility of VC in austenite, which means that it tends to completely dissolve in austenite at higher temperature. In microalloyed steels, V additions lower than 0.05wt% do not have any significant impact on the strength, however, amounts greater than 0.5wt% can lead to coarsening of precipitates formed, thereby reducing the overall strength of the alloy[13].

2.1.17.6 Titanium

Ti, just like V, Nb and Mo, forms composite carbides or carbonitrides in the presence of carbon and/or nitrogen. Solubility products show that TiCN, just like NbCN, are by far less soluble in austenite as compared to VCN. As a result, TiC tends to form at much higher temperatures compared to VC. This is the major reason why titanium carbides are more effective for grain refinement as compared to VC. Strain induced TiC plays an important role in grain refinement whereas if formed at lower temperatures, they are more effective in precipitation strengthening. At compositions below 0.02wt%, the numbers of precipitates formed are not sufficient enough to make significant contributions to precipitation strengthening. Compositions exceeding 0.4wt% tends to promote coarsening of the precipitates, rendering them ineffective for either grain refinement or precipitation strengthening[13].

2.1.17.7 Boron

Microalloying additions of boron (as low as approx. 0.002wt%) significantly reduces the formation of ferrite and pearlite, thereby promoting martensite formation during fast cooling[11]. Boron has the tendency to segregate to prior austenite boundaries thereby inhibiting the formation of ferrite. In the presence of Mo, bainite formation is accelerated while the formation of martensite is suppressed. Hence, fully bainitic microstructures can be obtained through microalloying with boron followed by normalising heat treatments. Boron additions also enhance bainitic hardenability. However, hardenability tends to decrease as the carbon content is increased.

2.1.18 Effects of Other Alloying Elements

2.1.18.1 Aluminium

Al has been found to compare very well with Si in retarding cementite formation and promoting C partitioning into retained austenite. Besides being a good deoxidising agent, it also reduces the C activity coefficient while promoting higher solubility of C in ferrite without affecting the plating properties of the alloy. Unlike Si, the formation of bainite is accelerated, thereby reducing the overaging time during industrial processing. However, Al does not make any contribution to solid solution strengthening unlike Si; it also increases the martensite start and finish (M_s and M_f) times to above room temperature[35]. Girault et al.[74] compared Al and Si alloyed TRIP steels and concluded that Al was equally good despite the substantial decrease in strength to ductility balance. It has been established that Al less than 0.50wt% does not make any significant contribution to the properties of the alloy, however, quantities greater than 3wt% increases surface defects and also reduces total elongation and stretch flangeability[13]. It has been suggested that the best results can be realised through partial substitution of ~1wt% Si with 1wt% Al [46, 74]. 0.5wt% to 3wt% have been found to be the optimum quantities since quantities above 3wt% have been found to cause surface defects during casting and also to decrease elongation and stretch flangeability of the final product.

2.1.18.2 Molybdenum

Mo has been known to play an important role in increasing the slope of A3 line, giving more flexibility during heat treatments. It also plays a part in solid solution strengthening. Mo has also been known to play a crucial part in the formation of fine precipitates when coupled with Ti and C[10, 13, 75]. It is also known to play a similar role when Ti is substituted with Nb[67, 76]. JFE steels[13] showed that strengths of up to 780MPa and high ductility can be attained on a steel microalloyed with Ti, Mo, Al and C. The strength was derived from the TiAl(Mo)C composite carbides finely dispersed throughout the ferrite. Park et al.[76] showed that the same result can be achieved when Ti is substituted with Nb. Quantities below 0.1wt% have been found to be insufficient to make any significant impact on the precipitation strengthening. However, the saturation point has been found to be 0.8wt%, beyond which additional Mo only contributes to the manufacturing costs without adding value to the steel[13].

2.1.18.3 Manganese

Manganese in TRIP steels is often used as an austenite stabilizer and also to reduce the cementite precipitation start temperature. It suppresses cementite formation while promoting carbon partitioning into retained austenite[40]. Mn in ferrite also lowers the activity coefficient of C, thereby increasing the solubility of carbon in ferrite. It also acts as a mild solid solution strengthener in ferrite. Mn in TRIP steels is generally limited to approximately 1.5%. Quantities above 2.5% can result in excessively stabilized retained austenite while segregation becomes an issue when quantities exceeds 3 wt.%[13].

2.2 Strengthening Mechanisms in Microalloyed Steels

2.2.1 Contributions to Yield Strength

The process of calculating the contributions to the yield strength by various strengthening mechanisms are quite complex. The strength in microalloyed steels is derived from several mechanisms including grain refinement (σ_d), solid solution strengthening (σ_{ss}), precipitation strengthening (σ_{ppt}), dislocation hardening (σ_{dis}) and transformation hardening such as bainite, martensite etc (σ_{trans}). The relationship between the microstructure and the yield strength can be summarised by the following equation where the base strength σ_b takes into consideration solid solution strengthening and grain refinement.

$$\sigma_y = \sigma_b + \sigma_d + \sigma_{ppt} + \sigma_{trn} \quad \text{Eq. 2.6}$$

Empirical equations which take into consideration the chemical compositions as well as the grain diameter have been used to calculate the yield strength of low carbon steels [67, 77, 78].

$$\sigma_b = \sigma_o + \left[15.4 - 30C + \frac{6.09}{0.8 + Mn} \right] d^{-\frac{1}{2}} \quad \text{Eq. 2.7}$$

$$\text{where } \sigma_o = 63 + 23Mn + 53Si + 700P \quad \text{Eq. 2.8}$$

The contribution to the yield strength due to dislocation density can be estimated using the following equation.

$$\sigma_d = \alpha M G b \rho^{\frac{1}{2}} \quad \text{Eq. 2.9}$$

Where α is a constant (0.3), M is the average Taylor factor (~ 3), b is the magnitude of the burger's vector (0.25nm), G is the Shear modulus (64GPa) and ρ is the dislocation density ($\sim 10^{14}/m^2$).

The contribution to yield strength by the precipitates can be calculated using the Ashby-Orowan equation and this will be discussed in the next chapter.

2.2.2 Grain Refinement in Microalloyed Steels

The grain size of any polycrystalline metal plays a very important role in influencing the mechanical properties of the metal. Regrettably, the improved yield strength is often at the expense of ductility and uniform elongation. This is attributed to different crystallographic orientation between adjacent grains which forces dislocations to change direction as they try to pass into the neighbouring grain[79]. The atomic disorder within the grain boundary also causes discontinuity of slip planes which further impedes dislocation motion as they try to pass from one grain to the next[80]. Fine grained materials have higher yield strength than coarse grained materials due to the reduced grain size which effectively increases grain boundary area, creating an obstacle to slip or dislocation motion, thus increasing the strength of the material. According to the Hall-Petch relationship, reduction in grain size can greatly increase the yield strength[11]. The yield strength and the grain diameter can be related through the Hall-Petch relationship [11]:-

$$\sigma_y = \sigma_0 + k_y d^{-\frac{1}{2}} \quad \text{Eq. 2.10}$$

where σ_y is the yield strength, σ_0 is the friction stress which is sensitive to temperature and composition and represents the stresses required to move free dislocations along the slip planes in BCC crystals. k_y is a constant sensitive to temperature, composition and strain rate.

To circumvent low uniform elongations brought about by fine grains, some reports have suggested that bimodal size distribution of ferrite grains can enhance both the strength and ductility in ultrafine grained low carbon steels[12]. Azizi-Alizamini et al.[81], working on a low carbon steel produced a microstructure composed of approximately 40% coarse grains between 3 μ m and 15 μ m and 60% fine grains. However, they only managed to achieve 14% uniform elongation and comparatively low yield strength of 550MPa. Okitsu et al.[82], working on a fully annealed ultrafine-grained low carbon steel with dispersed cementite, managed to achieve a high yield strength of 658MPa and a significantly low uniform elongation of 4%. Wang et al.[12] made a breakthrough by combining nanoprecipitates (approximately 6nm in diameter) with approximately 60% fine grains of mean size 0.7 μ m and

40%coarser grains with a mean size of 5 μ m. High yield strength of 663MPa and a high total elongation of 21.6% were achieved at this stage.

Two approaches have been widely used to produce ultrafine grained steels[83]. The first approach involves severe plastic deformation. This technique is dependent on the accumulation of large plastic strains either at room or at elevated temperatures [84-86]. The so called “advanced thermomechanical processing” is the second technique[83]. The advanced thermomechanical processing technique is fundamentally adapted to industrial controlled rolling processes since they can be easily optimised to operate at different temperature regimes to exploit phase transformations and controlled cooling.

2.2.2.1 Effects of Particle Pinning and Solute Drag on Grain Growth

The homogenisation stage before rolling is supposed to dissolve carbides and nitrides into solution. Hence, strain induced precipitates start to form during rolling as the temperature drops and the particles formed retards the rate of recrystallization of the deformed austenite grains. Meyer et al.[87] showed the effectiveness of the carbide formers on grain refinement and it is clear from Figure 2.11 that they are in the same order as their carbide solubilities. The carbide solubilities in austenite are shown in Figure 2.12. Hence, the high solubility of V makes it the least effective while Nb, being the least soluble in austenite, forms the most effective carbides and carbonitrides for grain refinement.

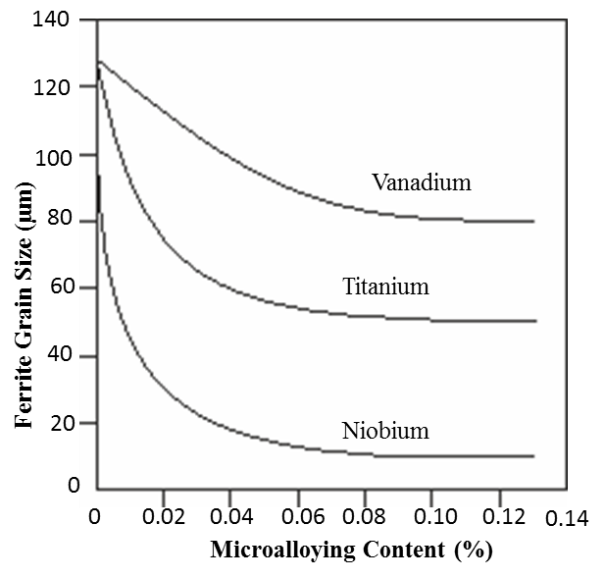


Figure 2.11 – Effect of alloying elements on grain refinement in microalloyed steels adapted from [87]

Gladman[88, 89] suggested that grain coarsening is complemented by the inward movement of the shrinking grains and the outward movement of the growing grains. The driving force of the inward motion (G_s) decreases the energy by[90]

$$G_s = \frac{3\sigma}{2R_o} \quad \text{Eq. 2.11}$$

while that for the outward motion which is the retarding force (G_o) result in an energy increase which is given by

$$G_o = \frac{2\sigma}{R} \quad \text{Eq. 2.12}$$

The net driving force (G) is given by

$$G = \frac{3\sigma}{2R_o} - \frac{2\sigma}{R} \quad \text{Eq. 2.13}$$

where σ is the grain boundary energy, R_o is the average radius of the grain and R is the radius of the growing grain. It has been shown that grains that have the potential to grow are always larger than 4/3 of the average[90]. The tendency for commercial steels to coarsen can always be retarded by introducing forces that deters boundary motion. It has been suggested that particle pinning and solute drag are the two most important mechanisms [91-94].

Zener showed that grain growth ceases and a limiting grain is reached when the particle pinning pressure on the boundary and the grain growth driving pressure became equal[93]. Assuming that the boundary to be macroscopically planar, the pinning pressure per unit area of boundary or Zener pinning pressure (P_Z) is given by:-

$$P_Z = N_S f_s = \frac{3F_v \gamma}{2r} \quad \text{Eq. 2.14}$$

where N_S is the number of particles intersecting a unit area of the grain boundary, F_s is the force on the boundary, γ is the specific energy of the boundary and r is the particle radius.

The driving pressure for growth (P) is given by

$$P = \frac{3\gamma}{D} \quad \text{Eq. 2.15}$$

where D is the mean grain diameter.

Assuming the mean grain radius to be equal to the mean radius of curvature (R)

$$P = P_Z \quad \text{Eq. 2.16}$$

Therefore

$$\frac{3F_v \gamma}{2r} = \frac{3\gamma}{R} \quad \text{Eq. 2.17}$$

The Zener limiting grain size is therefore given by

$$D_Z = \frac{4r}{F_v} \quad \text{Eq. 2.18}$$

As previously stated, a solute atom located or attached to the grain boundary tends to slow down the rate of migration of the boundary[94, 95]. Further to Zener's work, Gladman et al.[96] showed that grain growth can only be suppressed provided that the pinning particle radius is below the critical radius (r_c).

$$r_c = \frac{6R_o f}{\pi} \left(\frac{3}{2} - \frac{2}{z} \right)^{-1} \quad \text{Eq. 2.19}$$

f is the volume fraction of the precipitates, R_o is the grain size; z is the ratio of radii of growing grains to original grains $\left(\frac{R}{R_o}\right)$. Hence, as the volume fraction of particles

increases, so does the critical particle size. Increasing the original particle size has a similar effect. Thus, maintenance of austenite grain boundary stability at high temperatures requires not only sufficient volume fractions of particles; the particle sizes and spacing should also be below the critical values (r_c) and the coarsening rate should be sufficiently low. Sufficient microalloying elements should be added to get the right stoichiometric balance for optimum solubility at the highest possible controlled rolling temperature. NbCN, followed by TiCN, have the best pinning effect[70]. The pinning of both the grain boundaries and the dislocations by these fine precipitates formed at high temperature causes delayed recrystallization. The result is the formation of finer recrystallized grains after heavy deformation. VCN are not as effective as NbCN and TiCN, however, they have the advantage of forming finer precipitate dispersion in ferrite during the transformation from γ to α , which makes significant contribution to precipitation strengthening. The driving pressure for coarsening to occur when solute is the limiting factor can be given by the combined Cahn-Lucke-Stuwe theories[97, 98]:

$$P = \frac{V}{M} + \frac{\alpha C_o V}{1 + \alpha \alpha' V^2} \quad \text{Eq. 2.20}$$

where V is the boundary velocity, M is the mobility, C_o is the equilibrium solute level, α and α' are constants. The first term $\left(\frac{V}{M}\right)$ represents the regime where the driving force is quite high to be slowed by solute atoms while the second term represents the regime where the driving force is considered weak and can be considerably slowed by solute.

2.2.2.2 Effects of Particle Pinning and Solute Drag on Recrystallization

DeArdo[90] described the driving force for recrystallization as being “the difference in dislocation density between the deformed and the recrystallized matrix.” For effective retardation of recrystallization, the driving force for recrystallization (F_R) must always be lower than the pinning force (F_{pin}). F_R is usually estimated from[69]

$$F_R = \frac{\mu b^2 \Delta\rho}{2} \quad \text{Eq. 2.21}$$

where μ is the shear modulus, b is the Burgers vector, $\Delta\rho$ is the change in dislocation density. The pinning force is usually estimated from

$$F_{pin} = 2\gamma N_v r l \quad \text{Eq. 2.22}$$

where γ is the boundary energy, N_v is the particle number density, r is the radius of the particles and l is the average subgrain diameter. In order to constrain recrystallization,

$$N_v r \geq \frac{\mu b^2}{4\gamma l} \Delta\rho \quad \text{Eq. 2.23}$$

Cuddy et al.[94] showed that the recrystallization stop temperature increases with increasing solute concentration. They also showed that inhibition of recrystallization can only be effective when the grains are pinned by particles of sizes ranging from 0.5 to 10nm.

2.2.2.3 Effect of Coiling Temperature On Grain Size

It has been established that microstructural features such as grain size can also be attained through controlling the coiling temperature after hot rolling[99-101]. Recently, Park et al.[76] showed that the yield strength (YS) of microalloyed steels tends to increase with reduction in coiling temperature. This is partly due to the grain size contribution to YS. A lower coiling temperature effectively reduces the grain size of the steel, leading to improved strength.

2.2.3 Solid Solution Strengthening

Introduction of solute atoms into the solvent atom lattice generally produces a stronger alloy than the pure metal. Substitutional solid solution occurs when solid and solute are approximately the same size such that solute atoms occupy lattice positions within the solvent lattice. Interstitial solid solution is when the solute atoms are smaller than the solvent atoms and they occupy interstitial positions within the lattice. Impurity atoms that go into solid solution impose lattice strains on the surrounding host atoms that restrict dislocation motion. An impurity atom that is smaller than the host atom that it substitutes exerts a tensile strain on the surrounding crystal lattice. Larger impurities exerts compressive strains. Solute atoms also have the tendency to segregate to dislocation cores, reducing the overall strain energy. Smaller interstitial atoms tend to position themselves where they can nullify some compressive strain from the dislocation. The resistance to slip is greater when impurity atoms are present; hence, greater applied stresses are required for plastic deformation to occur in metals with impurities as compared to those without [4].

2.2.4 Strengthening at High Interstitial Concentrations

High strength can be achieved through increased interstitial solid solution strengthening as well as high dislocation density associated with martensite. It has been well established that austenite can take up to 10% C in solid solution[11]. Rapid quenching can result in diffusionless transformation resulting in a supersaturated solid solution with a tetragonal iron matrix in excess of the equilibrium carbon concentration.

2.2.5 Strain Hardening or Work Hardening

Strain hardening or work hardening occurs when a ductile metal hardens during plastic deformation at much lower temperatures than the melting temperature of the metal. New dislocations are formed during work hardening, increasing the net dislocation density of the alloy. Repulsive dislocation-dislocation strain interactions hinder dislocation motion thereby increasing the stress needed to deform the metal [4]. The full details of strain hardening are beyond the scope of this literature review, but there are numerous review papers and books on the subject.

2.2.6 Dispersion Strengthening

Dispersion strengthening is a phenomenon associated with strength brought about by the existence of other phases within the matrix. This includes carbides formed due to the low solubility of carbon in ferrite such as cementite, nitrides, intermetallic compounds and graphite (in cast iron). Controlling the other phases within the matrix can bring about several benefits in terms of strength; though it can also have adverse effects on ductility and toughness[11]. In fine dispersion, the Ashby-Orowan equation relates the yield stress or initial flow stress τ_s to the parameters of the dispersion alloy τ_0 and to the interparticle spacing Λ [102]

$$\tau_0 = \tau_s + \frac{T}{b\Lambda/2} \quad \text{Eq. 2.24}$$

2.3 Precipitation Strengthening

2.3.1 Precipitate Types

Carbonitride precipitation in microalloyed steels has been known to occur at various stages during casting and processing of steels. Where in the thermal cycle the precipitates are formed distinguishes between the different types of precipitates.

2.3.2 Nucleation in the Liquid Phase, During and after Solidification

The first type of precipitates is known to form either in the liquid phase, during and after solidification, at the liquid-solid interface or in the delta phase [103-105]. These precipitates are known to be highly stable and most of them are too large to make an impact on the recrystallization of austenite. However, smaller precipitates potentially slow down grain coarsening during heat treatment.

2.3.3 Strain Induced Precipitates

Strain induced precipitates have been extensively studied over the past decades and it has been well established that they are heterogeneously precipitated on dislocations e.g. during controlled rolling following solution treatment. They are known to reduce the rate of, or stop, austenite recrystallization; hence, they play a critical role in grain refinement [106, 107].

Akben et al.[108] studied strain induced precipitation kinetics in deformed austenite and their observation was that addition of 0.1 wt % Ti retarded dynamic recrystallization kinetics and increased the high temperature yield strength. While studying the precipitation behaviour of Ti(CN) in deformed austenite, Liu et al.[109, 110] developed a model for predicting dislocation motion in metals. By studying a series of stress relaxation curves, the precipitation start (P_s) and finish (P_f) times were obtained and these were then used to draw Precipitation/Time/Temperature (PTT) diagrams. However, the validity of the results is hampered by the difficulty in extracting detailed information on the softening and recrystallization behaviour of the deformed austenite from stress relaxation curves especially when there is simultaneous precipitation and recrystallization during softening. The applied strain

rate of 0.1/s and 5% strain used during the experiments can also be considered to be too low compared to those applied in commercial strip steel production [111, 112].

Recently, the two stage deformation technique has since been used to study strain induced precipitation behaviour as well as the interaction between strain induced precipitates with recovery and recrystallization in hot deformed austenite [69, 113-115]. Kang et al.[114] studied the strain induced precipitation behaviour of Nb microalloyed steels and their conclusion was that strain induced precipitation was a very rapid process with the shortest nucleation time of approximately 3s. Rainforth et al.[69] studied the precipitation behaviour of a model Fe-30% Ni with Nb microalloying additions which did not transform from austenite on cooling. A two stage deformation process with an inter-pass delay was used to describe the precipitation behaviour of NbC, linking the nucleation of the precipitates to the thermomechanical processing as well as the dislocation assemblies. They observed that strain induced NbC formed entirely on dislocations. Their conclusion was that the preferred nucleation sites for strain induced precipitates in hot worked austenite could be on dislocations and dislocation sub structures. Recently, Wang et al.[116] investigated the strain induced precipitation behaviour of Ti microalloyed steel using the same technique as that used by Rainforth et al.[69] and their results revealed that strain induced precipitates were not randomly distributed; however, they were heterogeneously distributed in a chain like manner, confirming the findings by Rainforth et al.[69] that the preferred nucleation sites for strain induced precipitates in hot worked austenite are mainly dislocations and dislocation sub structures.

2.3.4 Precipitates Contributing to Yield Strength

The precipitates that are formed during and after transformation from austenite to ferrite have been extensively studied and they are known for their role in significantly contributing to the overall yield strength of the alloy [11, 70]. Precipitates nucleated in the ferrite are believed to play an important role in direct strengthening as compared to those formed in the austenite. They normally exist in form of carbides, carbonitrides or nitrides depending on which alloying element are present. The thermal history and the composition of the alloy determines which type of precipitate is favoured. Generally, they are nucleated either in the austenite, at the interphase boundary during transformation from γ to α or in supersaturated ferrite during the final cooling in thermomechanical processing [70, 117]. Precipitation in austenite, though important for grain refinement, reduces the microalloying elements in solution, thereby reducing the volume fraction of precipitates formed in the ferrite[96]. When they are formed, they tend to be coherent or at least semi coherent, however, they tend to loose coherence during transformation from austenite to ferrite making them unsuitable for precipitation strengthening.

Precipitates formed in the ferrite tend to be coherent or at least semi coherent, which makes them most suitable for precipitation strengthening. Interphase precipitates are believed to form at the interphase transformation front in bands parallel to and following the direction of the interphase boundary during the transformation from austenite to ferrite at high temperatures. Other precipitates are known to form on dislocations and grain boundaries (niobium and vanadium carbides formed in the ferrite). The driving force for precipitation can be defined as the free energy change for the formation of the nucleus from the parent matrix and this is normally provided by the difference in energy between the parent phase and the product. Gibbs[118] describe the free energy (ΔG^*) or work required to produce a nucleus in a system of unstable equilibrium with the matrix as a measure of the stability of the system. The overall precipitate size and density produced by a phase transformation is normally a function of the process of nucleation, growth and coarsening[119].

2.3.5 Nucleation on Dislocations

Precipitates are not always formed during transformation from γ to α , they are also known to nucleate in ferrite mainly on grain boundaries and on dislocations after the γ to α transformation[11, 73]. Smith et al.[120], working on a microalloyed steel of composition Fe-0.2Ti-0.08C, showed that the number of fine TiC increased with increasing dislocation density. This normally occurs when the temperatures are held at longer times or at lower temperatures, e.g. during cooling.

Russel[121] defined dislocations as line discontinuities within a crystal. Edge dislocations are formed when an extra half plane of atoms is inserted into the crystal lattice. Four different ways have been suggested for the nucleation of precipitates on dislocations[121]

- a) Incoherent precipitates can form on dislocations, thereby lowering the strain energy of the dislocation.
- b) Coherent precipitates can form close to dislocations in order get the transformation strain from the dislocation.
- c) Semi-coherent particles can nucleate on dislocations, thereby utilising the dislocation core energy to create the incoherent interface.
- d) Precipitates can also nucleate between two partial dislocations where high strain energy exists.

A significant aggregate of strain energy exists at the core of the dislocation as a result of the disorder associated with this point. Cahn[122] considered the nucleation of precipitates on dislocations as strain energy relief from the high energy dislocation core. He suggested that a “tube of precipitates of radius r_0 ”, nucleates all over the dislocation as a way of strain energy relief. Gomez-Ramirez and Pound[123] agreed with Cahn[122] that preferential nucleation of precipitates on dislocation was a way to release strain energy from the dislocations; however, they suggested that the nuclei were in closed form shape. A number of particle morphologies such as ellipsoids were investigated, but they failed to identify the equilibrium form of the particle on dislocation, eventually coming to the conclusion that ΔG^* was not a function of the particle shape. They also concluded that dislocations were tremendous nucleation catalysts such that meta-stable embryos always existed on

dislocations even under unsaturated conditions. At steady state, Russel[121] developed the equation to calculate the nucleation rate of carbonitrides due to controlled diffusion of microalloying elements

$$J \cong \frac{\rho}{a_Y^3} D_{MA} X_{MA} \exp\left(-\frac{\Delta G^*}{kT}\right) \quad \text{Eq. 2.25}$$

where $J\left(\frac{1}{m^3s}\right)$ is the nucleation rate at steady state, ρ is the dislocation density, a is the lattice parameter of the matrix, D_{MA} is the diffusivity of MA and X_{MA} is the concentration of the MA. From this equation it is clear that lowering the temperature increases the rate of nucleation.

2.3.6 Nucleation at the Interphase Boundary

It has been shown that incoherent boundaries between grains provides excellent conditions for nucleation of precipitates[124]. It has also been suggested that the interphase boundary between coherent particles and the matrix provides excellent conditions for nucleation of further precipitates[125]. Russel[121] suggested two possible mechanisms for incoherent nucleation at the interphase boundary. He suggested that solute may either

- a) Diffuse radially into the matrix from the interphase or
- b) Diffuse outwards along the grain boundary and gradually seep into the matrix.

Johnson et al.[126] studied nucleation through volume and boundary diffusion and they concluded that boundary diffusion was always faster than volume diffusion.

2.3.7 Solubility Products of the Carbide Formers

Solubility products as a function of temperature have already been studied and these are illustrated in Figure 2.12[71, 127]. A comparison of the solubilities clearly shows that NbC and TiC are less soluble in austenite compared to VC. Nitrides are far less soluble as compared to their carbide counterparts and this implies that nitrides dominate at higher temperatures, while the carbide precipitation starts to dominate as the temperature is lowered. At high temperatures, Ti and Nb, with low solubility will precipitate carbides or nitrides while V with higher solubility will form carbides and nitrides at lower temperatures. Nb, Ti and V are known to retard the recovery rate thereby retarding the recrystallization rate. The solubility products in Figure 2.12 shows that Nb has the greatest effect, followed by Ti and lastly V. The fine carbides and carbonitrides produced during controlled rolling have the effect of pinning the grain and sub-grain boundaries and dislocations, thereby limiting grain growth[106].

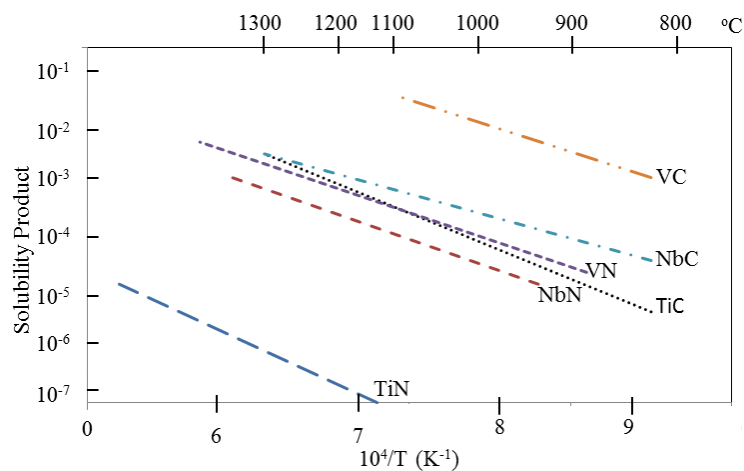


Figure 2.12 - Solubility products of carbides and nitrides as a function of temperature adapted from K. Narita[71]

In alloys containing more than one microalloying element, a wide range of precipitates can be formed. Houghton et al.[105], studied a Ti/Nb microalloyed steel containing nitrogen and carbon. Their observation was that the precipitates formed had a wide range of chemical compositions such as TiC, TiCN, Ti(Nb)C, Ti(Nb)CN, NbC, NbCN etc. They concluded that the precipitates formed were dependent on the alloying elements.

2.3.8 Coarsening of precipitates

Precipitate coarsening can be modelled based on the relationship derived from the Lifshitz-Wagner theory[128]:-

$$\bar{r}_t^3 - \bar{r}_o^3 = \left(\frac{K}{RT} \right) V^2 C D \gamma t \quad \text{Eq. 2.26}$$

Where \bar{r}_t is the mean particle radius at time t, \bar{r}_o is the mean particle radius at zero time, C is the concentration of the solute in equilibrium with a particle of infinite radius, γ is the interfacial energy of the particle/matrix, V is the precipitate molar volume, D is the solute diffusion coefficient and k is a constant.

Equation 4.2 demonstrates that a high volume fraction of particles can result in higher particle coarsening rate as compared to lower particle volume fraction. It is also clear that particles with lower solubility will coarsen less compared to particles with higher solubility. Balliger and Honeycombe[129] showed that VC coarsens more compared to VN. They also revealed that substituting carbon with nitrogen can greatly reduce the precipitate size. The lower coarsening rate of nitrides as compared to carbides can be attributed to the lower solubility of N as compared to C. Similar work carried out by Dunlop and Honeycombe[130] revealed that VC or VCN tends to coarsen much more than TiCN. Hence, substituting V with Ti can slow down the rate of coarsening, resulting in the formation of finer precipitates. Similarly, the lower coarsening rate of TiCN as compared to VCN can be attributed to the lower solubility of Ti as compared to V.

2.3.9 Precipitation Strengthening Mechanisms

Improved strength, not only in steel, but also in other metal alloys, can be enhanced through the introduction of uniformly dispersed precipitates. However, the precipitation strengthening process, which is dependent not only on thermodynamics, but also on kinetic factors, is quite complex[131]. The precipitation of Nb and Ti carbides and their interaction with recrystallization and grain growth has since been studied [11, 69, 132]. A lot of attention has since been given to the decomposition of austenite as well as carbide precipitation in the ferrite [78, 133].

Precipitates are known to impede dislocation motion within a crystalline lattice and it has been established that introducing nanoprecipitates can bring about enhanced strength without compromising the ductility of the steel [7, 11, 12]. This is credited to supplementary stresses required to enable the dislocations to either shear the precipitates or loop between them. The preferred mechanism is mainly dependent on the size, spacial distribution, density and coherence of the precipitates[131]. The most desirable combination can only be achieved through controlling the precipitation kinetics, which is a function of alloy composition and heat treatment. The latter requires minimising the alloy addition. The optimum is a large number density of precipitates just a few nm in size, and therefore the control of the nucleation (e.g. by interphase precipitation rather than strain induced precipitation) is important[102]. The process is not only dependent on the potential nucleation sites and driving force for precipitation but also the chemical composition of the steel. The challenge is to promote the precipitation of a high number density of fine precipitates, rather than a small number density of coarser precipitates.

The Ashby-Orowan model for precipitation strengthening has been widely adopted for HSLA steels in commercial manufacturing processes[78]. Assuming that all the carbon in the steel is used for precipitation strengthening, the Ashby-Orowan equation can be used to estimate precipitation strengthening[7, 134].

$$\Delta\delta = \frac{K}{d} f^{\frac{1}{2}} \ln \frac{d}{b} \quad \text{Eq. 2.27}$$

where K is a constant (5.9N/m), b is the Burger's vector (0.246nm) and d is the average diameter of the precipitate and $f(\%)$ is the volume fraction of the nano-sized carbides.

However, the use of the Ashby-Orowan equation is complicated by the existence of critical sizes where it can be applied. It has been suggested that it is only valid when precipitates are large enough to avoid shearing by dislocations[78, 135]. In 1999, Gladman[135] suggested that the transition between sheared and non-sheared particles was approximately 5nm. Two years later, Charleux suggested a size range of 4 to 5nm. Imaging particles less than 5nm presents its own challenges since it can be difficult to distinguish between the actual precipitates and dark contrast especially when analysing TEM carbon extraction replicas. Most of the studies on nanoprecipitates have focused on particles >5nm partly because these particles falls within the limits of non-shearable precipitates [7, 136]. For effective precipitation strengthening, particles ranging in size from 5 to 20nm have been suggested as being most effective [67, 136, 137].

Recent studies have shown that the nucleation of precipitates requires nucleation sites such as grain boundaries, dislocations, second phase particles etc. Interphase precipitation has also been found to be one of the most important mechanisms as far as precipitation strengthening is concerned. Interphase precipitates as well as any other precipitates formed in the ferrite have always been found to obey the Baker-Nutting relationship with the ferrite matrix and this has been used as a way to distinguish between precipitates formed in the ferrite and in other phases, e.g. in austenite. Kestenbach[138] studied NbC precipitation in microalloyed steel containing 0.34 wt.% Nb and they found that 90MPa was the contribution to yield strength from precipitation on dislocations while more than 200MPa were attributed to interphase precipitates. Itman et al.[139] later suggested a contribution of 60 to 80MPa from strain induced precipitates in the austenite for commercial hot strip rolled steels. They suggested that the precipitates were likely to remain fine as a result of the short processing time in the finishing mill.

Some authors have suggested that alloying additions of Mo to Ti microalloyed steels and reducing the coiling temperature to approximately 650°C can result in the

formation of fine precipitates of high number densities[7, 13, 75]. The low coiling temperature is supposed to provide precipitation refinement. Conflicting results regarding the lattice structure, lattice parameter and the chemical composition of the (Ti,Mo)C formed have been reported in literature[7, 13, 75]. Yokota et al.[13] reported the precipitates formed to be (Ti, Mo)C, aligned in rows and having a cubic lattice with a lattice parameter of 0.433nm. Funakawa et al.[7] investigated a Ti microalloyed steel with alloying additions of 1.5wt.%Mn, 0.2wt.%Mo and 0.04wt.%C. Rows of fine precipitates averaging 3nm and average row spacings of approximately 15nm were observed. The contribution to the overall yield strength as a result of these fine carbides was estimated to be approximately 300MPa. However, since precipitation strengthening is a function of the volume fraction of the precipitates, this figure could be an underestimation due to the continuous improvement in alloy design, which can result in higher precipitate number densities. As previously described by Yokota et al.[13], Funakawa et. al.[7] confirmed that that the nanosized carbides had a NaCl structure with a lattice parameter of 0.433nm. However, similar work conducted by Timokhina et al.[75] on steels of almost similar chemical composition were not consistent with the initial results by Funakawa et al.[7]. They suggested that the fine precipitates were $Ti_{0.98}Mo_{0.02}C_{0.6}$, having a hexagonal lattice and lattice parameter of 0.423nm. However, one point worth noting from both reports was that the nanosized carbides possessed excellent thermal stability.

Lee et al.[137] also observed increased precipitate number densities with increasing Mo additions to a Nb microalloyed steel. They concluded that Mo suppressed the annihilation of dislocations at high temperature, resulting in increased nucleation sites for precipitates. The lower coiling temperatures suppresses precipitate coarsening, resulting in fine precipitates of high number densities.

2.3.10 Heat Treatments for Precipitation Hardening

In order for precipitation strengthening to occur, two conditions have to be satisfied. Firstly, there must be an appreciable maximum solubility of one of the components into the other and secondly, there should be a decrease in solubility with decreasing temperature[80]. For effective precipitation strengthening, the alloy composition should be lower than the maximum solubility. The traditional heat treatment cycle for precipitation hardening is shown in Figure 2.13.

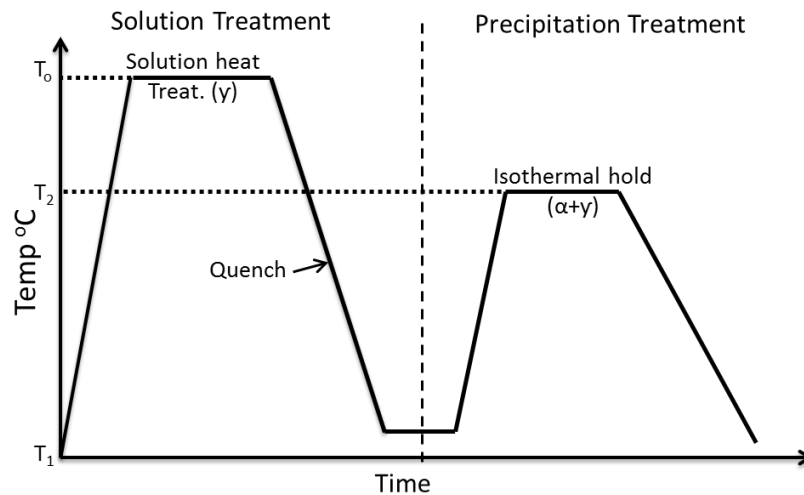


Figure 2.13 – Traditional heat treatment cycles for precipitation strengthening

Solution treatment - The alloy is heated from the initial room temperature (T_1) to a temperature (T_0) in the austenitic region. It is then held at this temperature for sufficient time to allow the alloying elements to completely dissolve, resulting in the formation of a single γ phase of composition C_0 . The solution is then quenched to room temperature T_1 to prevent diffusion of alloying elements such as carbon. This results in a non-equilibrium situation whereby the ferrite phase is supersaturated with carbon.

Precipitation treatment - The second stage involves reheating the alloy to the precipitation heat treatment temperature T_2 , which is in the intercritical ($\alpha + \gamma$) region where the precipitation strengthening is dependent on both T_2 and the aging time. This process is also known as the intercritical annealing process.

Modern practices tend to incorporate both solution treatment and precipitation treatment into one process. Commercially, this process is more viable due to the removal of the reheating for precipitation treatment shown in Figure 2.13; cutting the overall costs to the production process. The modified process is shown in Figure 2.14.

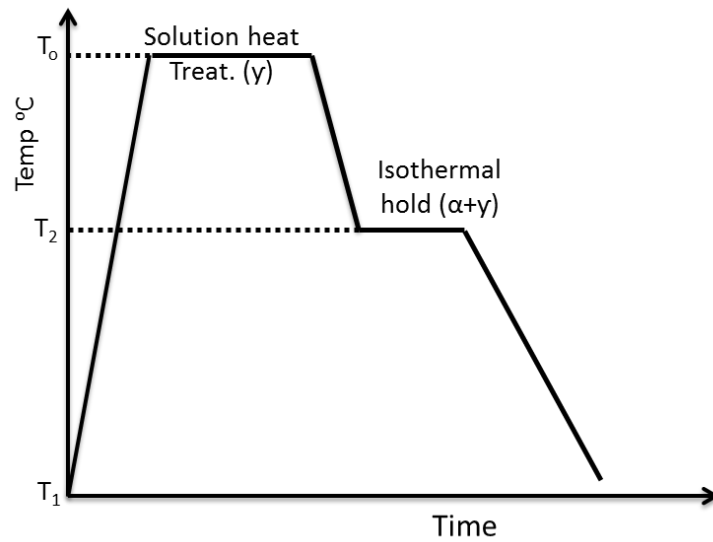


Figure 2.14 – Modern heat treatment cycles for precipitation strengthening

2.3.11 Interphase Precipitates (IP)

The existence of interphase precipitates in steels were first observed by Gray and Yeo[140] in 1968. Periodic rows of niobium carbonitrides precipitates were observed and their conclusion was that these precipitates were neither formed on coherent twin interfaces nor on slip planes formed by the rolling process; instead, they were believed to have been formed on the interphase boundary during the transformation from austenite to ferrite. Many studies have since been carried out and IP is now known to occur in similar carbides or carbonitrides such as VC, VCN, TiC, etc.

Solubilities of carbides are slightly higher in austenite than in ferrite. As the temperature is lowered, as long as adequate diffusion time is provided, substantial precipitation should occur during and after transformation from austenite to ferrite. This is dependent on diffusivity of the alloying elements in addition to that of carbon. The migrating interphase boundary forms the nucleation site for interphase precipitation (IP). Iron carbides have the tendency to form if the cooling rate is slow enough and the carbon content is high enough [11, 70]. However, cementite and pearlite formation consumes the useful carbon that is required to form the precipitates at the $\gamma + \alpha$ interphase. As a result, fast cooling is often employed in commercial processes to avoid their nucleation.

Davenport and Honeycombe[141] developed a model for the formation of interphase precipitates and the schematic diagram is shown in Figure 2.15.

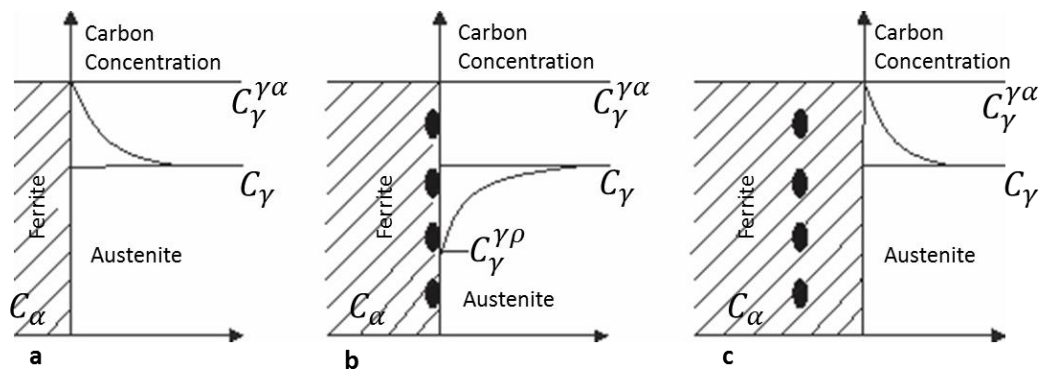


Figure 2.15 - Schematic model of the interphase precipitation process adapted from Davenport and Honeycombe[141]

At stage (a) shown in Figure 2.15, since carbon is less soluble in ferrite, the concentration of carbon in austenite at the γ/α boundary increases as γ to α transformation progresses. At stage (b), precipitates nucleate on the ferrite side of the boundary as a result of the high carbon concentration. Pinning of the boundary by the precipitates follows and this results in the depletion of carbon on the austenite side of the boundary. The carbon depletion on the austenite side provides the Gibbs free energy required for the further transformation from austenite to ferrite. At stage (c), the boundary breaks free from the precipitates and migrates forward, away from the precipitates and the process repeats itself at this stage.

The interparticle as well as row spacing is closely related to the transformation temperature. Balliger and Honeycombe[129] correlated the row spacing to the transformation temperature for a V alloyed steel. Figure 2.16 was adapted from Ballinger and Honeycombe[129] and it shows the relationship between the row spacing and the transformation temperature.

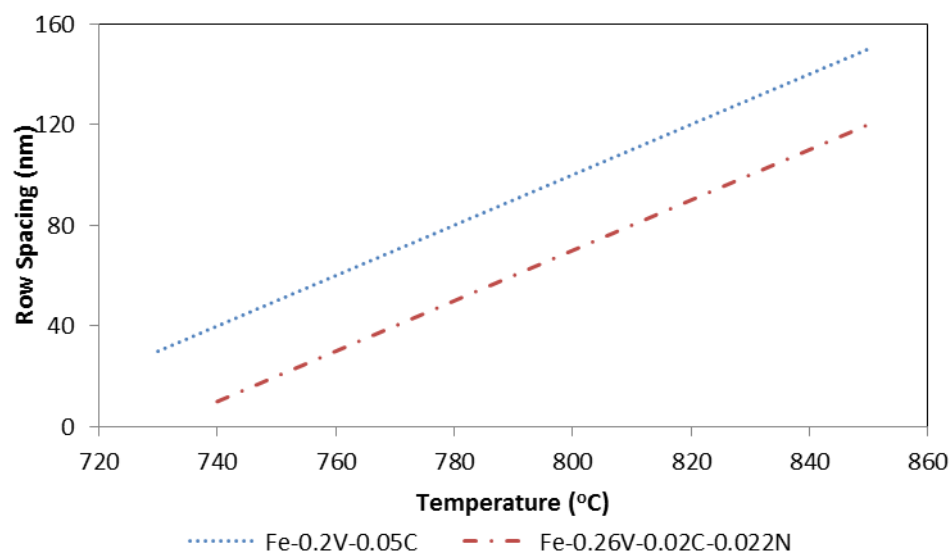


Figure 2.16 – Precipitate row spacing as a function of temperature [129]

Essentially, the row spacing decreases with decreasing transformation temperature and this characteristic has been recently exploited in fixing the coiling temperature after controlled rolling in commercial processes. At high energy interphase boundaries, the migrating step can move rapidly to accommodate the transformation, however, this might be at the expense of nucleation of the carbide particles[142]. This can result in nucleation occurring behind the step resulting in the row spacing

being almost equal to the step height. Honeycombe[70] reported that the row spacing can vary between 5nm and 500nm and this variation in row spacing was credited to wide variations in transformation temperatures during processing. The interparticle spacing was reported to be relatively small compared to the row spacing. Unlike row spacing, two major factors play an important role in determining the interparticle distance. Firstly, the concentration of carbon and other alloying elements at a particular transformation temperature influences the interparticle spacing[70]. The effect of the transformation temperature on the interparticle spacing has been found to be similar to row spacing. Lowering the transformation temperature also results in the reduction of the interparticle spacing. Hence, for hot rolled strip steels, the optimum microstructure comprising fine grains and fine precipitates can be attained by controlling the coiling temperature after hot rolling [99-101]. Park et al.[76] studied the effect of coiling temperature on Ti-Mo-C, Nb-Mo-C, Ti-W-C and Nb-W-C alloyed steels and they observed that precipitate sizes tends to decrease with decreasing coiling temperature. This was attributed to supercooling that promoted a higher the number of nucleation sites and lower precipitate growth rate [76]. Lower coiling temperatures also results in increase in dislocation density, which acts as nucleation sites for precipitates. Optimisation of row and interparticle spacing can be achieved through microalloying addition of austenite stabilizers which depresses the transformation temperatures (e.g. Mn and Ni). Hence, optimising the maximum strength can be attained at the point when the both row and interparticle spacing are at their minimum. Commercially, alloying additions that depresses the transformation temperature are sometimes used commercially to depress the coiling temperatures. Lee et al.[99, 137] revealed that small additions of Mo can suppress the annihilation of dislocation density at higher coiling temperatures resulting in increased precipitate nucleation sites. Mo is also known to retard precipitate growth in Nb and Ti microalloyed steels [10, 75, 99, 137].

The morphology of interphase precipitates formed is directly related to the category of γ to α interphase involved. Three main types have been identified so far:

- a) Planar interphase precipitates which exists in form of discrete particles on parallel bands[141, 143].

-
- b) Random precipitate arrays also classified as non-planar interphase precipitates[144].
 - c) Curved/irregular bands of precipitates also classified as non-planar interphase precipitates[142, 145]

2.3.11.1 Planar Interphase Precipitates

High volume fractions of precipitates formed mainly at the interphase boundary during the transformation from γ to α forms parallel bands of discrete particles as shown in Figure 2.17.

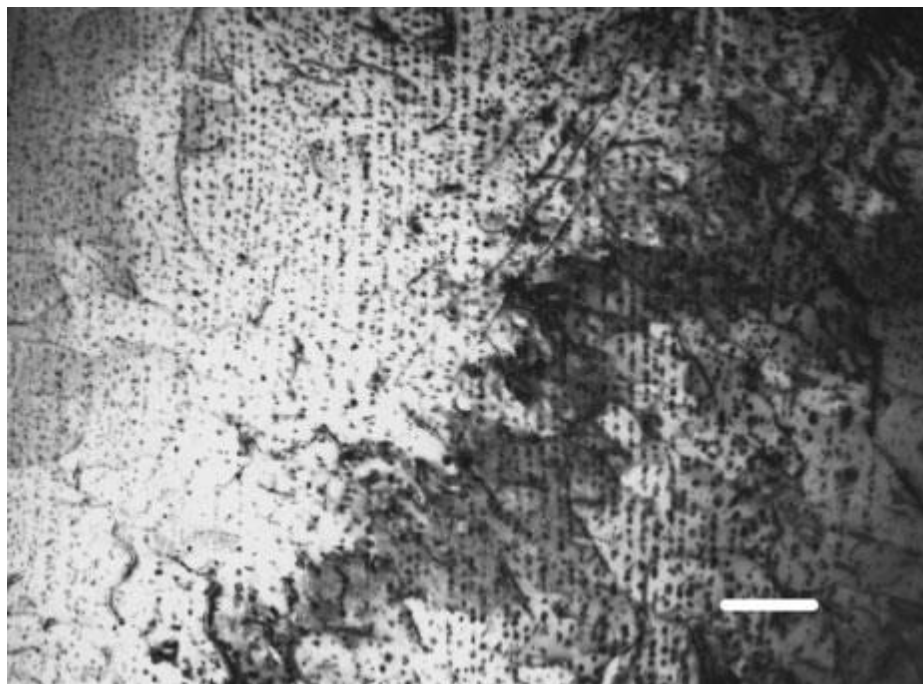


Figure 2.17 – Bands of discrete particles (interphase precipitates) formed at the interphase boundary during transformation from γ to α [73]

In 1974, while studying chromium steels, Campbell and Honeycombe[142] observed that the rows of precipitates were always nucleated on the lowest energy immobile $[110]\alpha//[111]\gamma$ interphase boundaries. Their conclusion was that high mobility boundaries, though accommodating the transformation from γ to α , do not always result in the formation of precipitates. The step height and inter particle spacing tends to increase with increasing transformation temperature. The inter particle distance is generally smaller than the band spacing and is generally a function of the concentration of microalloying elements and carbon content[11]. Honeycombe[70] later suggested that the planar interphase precipitates were formed through a ledge

mechanism on newly created low mobility migrating low energy planar interphase boundaries just behind the step; with equivalent band spacing and step height as illustrated in Figure 2.18.

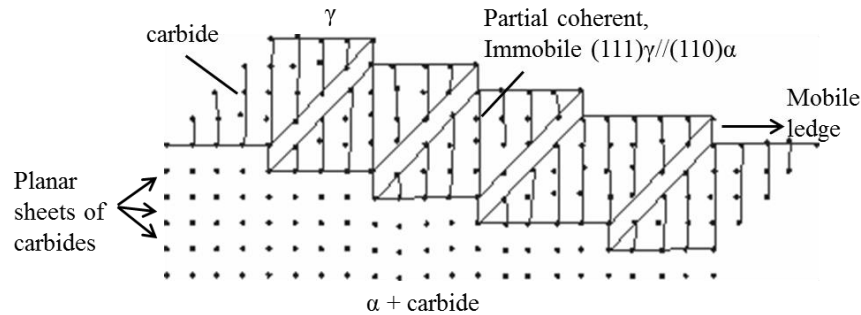


Figure 2.18 – Mechanism for nucleation and growth of precipitates on the γ/α interphase (adapted from Ricks and Howell)[70]

This phenomena was most noticeable in V steels due to the higher solubility of VC as compared to others (NbCN and TiCN)[143]. Depressing the γ to α transformation temperature by microalloying with elements such as as Mn and Ni promotes high precipitate number densities through the reduction of both the band and interparticle spacing as previously explained.

2.3.11.2 Random Interphase Precipitates

Ricks and Howell[144] observed that irregular arrays are sometimes observed, sometimes within the same grains as planar arrays [142]. Figure 2.19 is a typical example of random interphase precipitates.

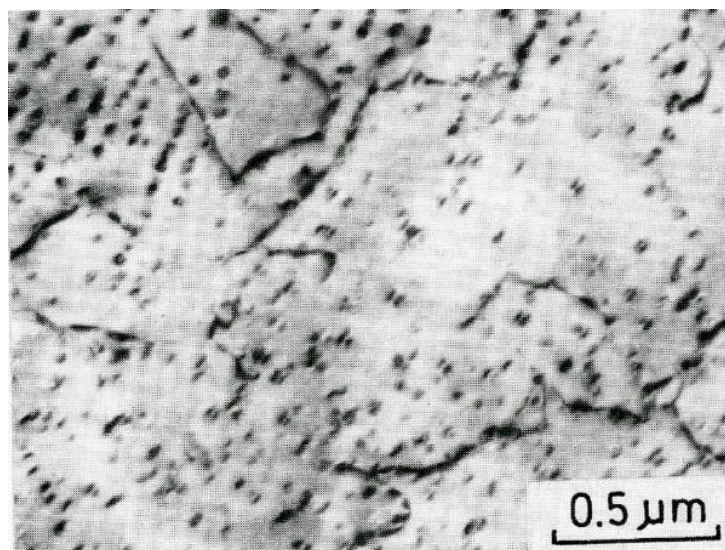


Figure 2.19 – Random interphase precipitates formed through the interphase boundary bowing around particles[70]

These precipitates are believed to nucleate at higher energy γ to α interphase that migrates without the step propagation. The interphase boundary is believed to bow around particles using a mechanism similar to Orowan looping mechanism of dislocations and precipitates. Using free energy balances, Ricks and Howell[145] developed a model assuming an increase in interface energy due to the increase in γ to α interphase as the bulge develops:

$$a_{\text{crit}} = \frac{2\sigma V}{\Delta G} \quad \text{Eq. 2.28}$$

where a is half the interspacing distance between the precipitates, σ is the interfacial energy per unit area and ΔG is the free energy change per mole of γ . Using the above relationship, the minimum interspacing distance between precipitates for which bowing occurs can be calculated. Even though the same mechanism can produce curved banded arrays of precipitates, it has been shown that the irregular dispersion of precipitates with no clear interphase origin has the highest probability of forming[145].

2.3.11.3 Irregular Banded Arrays

While studying chromium steels, Ricks and Howell[145] observed periodic non planar or curved arrays of precipitates. They suggested that quasi ledges might have been formed in regions where the spacing is larger than average; the bulge formed being pinned by further precipitates resulting in the propagation of the ledges in two directions. They also suggested that the mechanism was triggered by high energy γ to α interphase boundaries obstructed by fine particles whose interparticle distance are too small to allow the bowing mechanism to occur. The mechanism is illustrated in Figure 2.20 and Figure 2.21.

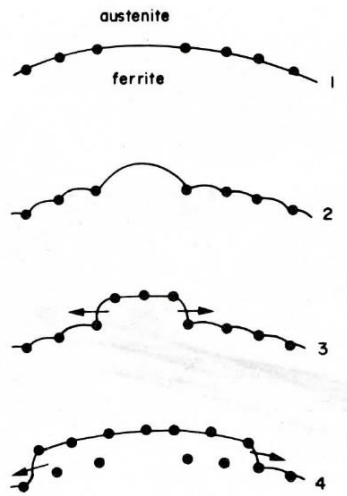


Figure 2.20 - Ledge formation through localised bulges[145]

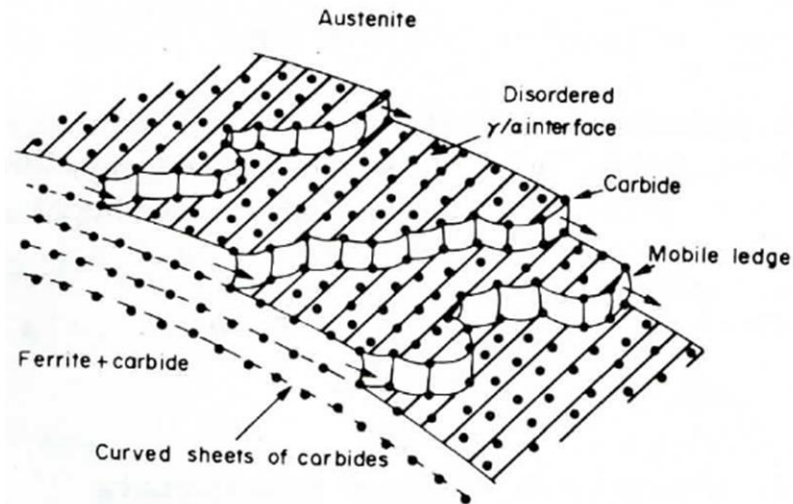


Figure 2.21 – Curved sheets formation as result of localised bulges (Adapted from Ricks and Howell[145])

However, the mechanisms involved are too complex and not yet fully understood. Hence, further studies needs to be carried out to understand the mechanisms involved as well as verifying why this happens.

CHAPTER 3:

EXPERIMENTAL PROCEDURE

3.1 Introduction

As previously stated, the major objective of this project was to produce an ultra-high strength steel with the ferrite matrix strengthened by nanoprecipitates. Mechanical properties are largely influenced by the microstructure, as a result, thermal cycles for heat treatment to optimise the mechanical properties were developed and the microstructures were fully analysed at each stage. Mechanical tests were then carried out on the samples to correlate the microstructure with the mechanical properties. In order to achieve this goal, three different strategies were stipulated at the beginning of the project and these formed the three major parts of this project.

Stage 1 - This part involved comparing multiphase steel alloys of different chemistries in order to verify which one was most likely to produce the desired mechanical properties. Low alloyed hot rolled steel samples with different chemical compositions were produced by Tata Steel (IJmuiden). Mechanical testing was then carried out at Tata Steel while comprehensive characterisation of the samples was done at Sheffield University.

Stage 2 - The second part involved finding the dependence of microstructure and precipitates on thermal history for one of the chemistries from stage 1. This involved simulation of the industrial thermal cycles of commercially steels produced by Tata Steel in the laboratory in order to optimise the mechanical properties. Some of the samples were received after having been heat treated while others were heat treated in the laboratory at Sheffield University. Comprehensive characterisation was then carried out and the results correlated to mechanical properties following mechanical testing in the laboratory.

Stage 3 - The last stage involved optimisation of mechanical properties of commercially produced ferritic steels strengthened by nanoprecipitates. New alloy compositions were developed and comprehensively characterised and tested to verify

whether these new alloys could produce better properties which could enable them to be adopted in the production line at Tata Steel.

3.2 Stage 1 Materials - Multiphase Steels with Different Chemical Compositions

Six samples of three different chemical compositions were initially supplied by Tata Steel to kick start the project. The as-received samples were in form of tensile test bars cut along the longitudinal direction from the grip section after the tensile tests. The dimensions were approximately 35mm x 30mm x 2.5mm. Typical specimens are shown in Figure 3.1.



Figure 3.1 – Images of tensile test bar grip heads received from Tata Steel for characterisation

For each chemical composition, two samples were supplied; the difference being that one had been subjected to continuous cooling, while the other had been subjected to a four seconds temperature hold in the intercritical temperature region during heat treatment. The differences between the two processes will be explained later in this chapter. The chemical compositions of the samples supplied are tabulated in Table 3.1.

Table 3.1 – Table of Chemical compositions [wt%]

Sample	Chemical Compositions [wt %]								
	C	Mn	Cr	Si	Ti	Mo	Al	V	N
TiAlMo	0.155	1.60	0.00	0.31	0.141	0.26	1.25		
Ti	0.098	1.72	0.30	0.10	0.095				
V	0.09	1.66	0.30	0.09	0.0025			0.099	0.013

The chemical compositions in Table 3.1 were chosen for the following specific reasons:-

1. The TiAlMo strip steel was chosen as the most likely to produce nanoprecipitation as claimed by other authors such as Raabe et al.[10] and JFE steel[13]. Mo is believed to retard precipitate coarsening, while Al promotes the production of retained austenite and therefore, the TRIP effect. This was also a chance to verify the claims by these authors. If the claims were proved to be true, then this steel would form the benchmark for making a suitable comparison with the other steels.
2. The Ti strip steel was devised in order to make a comparison with TiAlMo. This was taken as an opportunity to verify whether nanoprecipitation and the TRIP effect could be observed in the absence of Mo and Al.
3. Finally, the V strip steel was chosen since it is known to give fine precipitation. This would also provide a useful comparison to Ti and TiAlMo steel. Interphase precipitation (IP) has been reported in V steels in the past; however, due to the complexity of the steels being currently produced, it would be of interest to verify whether IP can be observed in such steels. Hence, the V microalloyed steel was chosen so that IP in complex multiphase V alloyed steels could be verified.

3.2.1 Thermomechanical Treatment of Multiphase Steel Samples

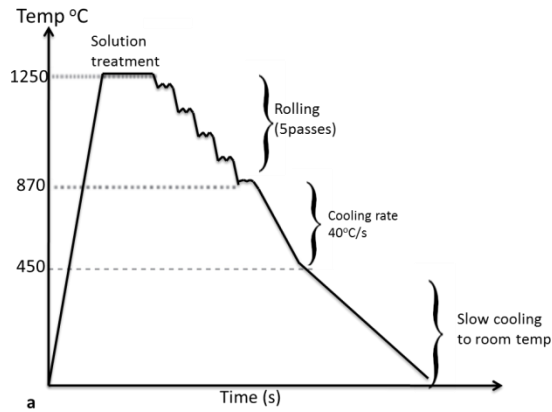
For each of the chemistries in Table 3.1, two samples of each were supplied by Tata Steel; the difference between the two being the thermal cycles adopted during thermomechanical treatment. One of each of the samples was subjected to continuous cooling while the other was subjected to the two step cooling process as shown in Figure 3.2.

The continuous cooling process is shown in Figure 3.2a. The 25mm slab was initially heated to the austenising temperature of 1250°C at a heating rate of approximately 10°C/s. The temperature was then maintained at 1250°C for 30 minutes in order to dissolve most of the carbides into solid solution. Vanadium carbides and carbonitrides would have dissolved completely at this temperature. However, Nb and Ti carbides and carbonitrides, due to their lower solubilities, will have only partially dissolved. Hence, they play an important role in pinning the grain boundaries, thereby reducing the recrystallization rate. The slab was then hot rolled to a thickness of 2.5mm in five passes to a finish hot rolling temperature of approximately 870°C. They were then fast cooled to the bainitic transformation temperature of 450°C at a cooling rate of 40°C/s. The fast cooling at the stage was performed in order to minimize the formation of cementite and/or pearlite. Slow cooling was then applied to room temperature after which the samples were ready for further characterisation and mechanical testing.

The two-step cooling process in Figure 3.2b involved pre-heating the 25mm slab to the solution temperature of 1250°C at a heating rate of 10°C/s. The samples were then maintained at that temperature for further 30minutes in order to dissolve most of the carbides. The slabs were then hot rolled to the finish thickness of 2.5mm under five rolling passes to a final hot rolling temperature of approximately 870°C. They were then fast cooled to 670°C at 40°C/s after which the temperature was held at 670°C for four seconds. The four seconds hold was applied to allow sufficient time for the austenite to transform to ferrite, thereby creating suitable conditions for interphase precipitates to form. After the four seconds temperature hold, further fast cooling was then applied at 40°C/s to a final temperature of 450°C in the bainitic

transformation region. The samples were then left to slowly cool to room temperature.

Continuous Cooling Process



Two-step Cooling Process

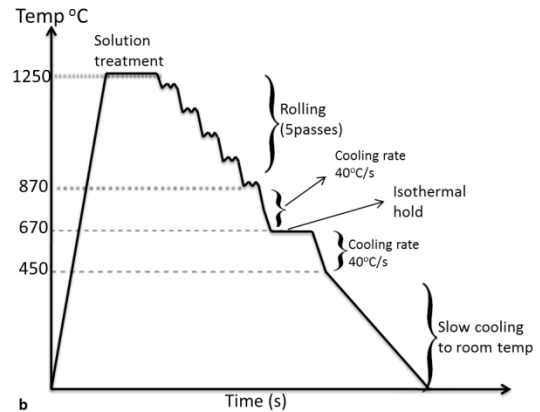


Figure 3.2 – a) Thermomechanical processing conditions for a) 2 steps cooled samples and b) continuously cooled samples

Following thermomechanical processing, tensile specimens were then cut from the samples and the tensile tests were performed by Tata Steel (IJmuiden). The remnants of the tensile bars were then received for further characterisation which included X-ray Diffraction (XRD), Scanning Electron Microscopy (SEM) and Transmission Electron Microscopy (TEM).

Having analysed all the results from stage 1, a decision was then made that stage 2 would encompass optimisation of the vanadium (V) alloyed steel from stage 1. This steel was chosen mainly because V has been known to produce interphase precipitates [11, 70, 146]. This composition was also chosen as it would be most commercially appealing to Tata Steel.

3.3 Stage 2 Materials – V Microalloyed Samples

As previously stated, the V alloyed samples from stage 1 were used for this part of the project. The chemical composition of the steel was 0.09C-1.66Mn-0.3Cr-0.09Si-0.025Ti-0.099V-0.0005B-0.013N. Heat treated samples of dimensions 20mm x 5mm x 2mm were received from Tata Steel (IJmuiden). Figure 3.3 is a schematic diagram representing the rolling as well as the heat treatment schedule applied to the samples. Note that the thermomechanical processing stage shown is similar to the continuous cooling process discussed for stage 1 processes and shown in Figure 3.2a. Table 3.2 gives the sample codes and heat treatment conditions.

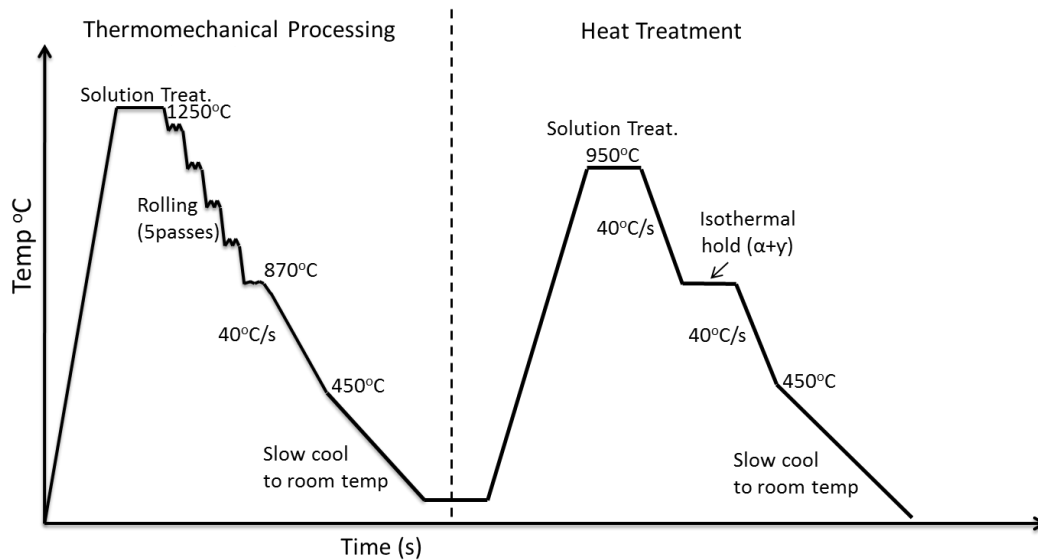


Figure 3.3 – Schematic diagram of the manufacturing process adopted by Tata Steel

Further to thermomechanical treatments, 950Q, 950-60Q and 950-120Q were produced by soaking the vanadium alloyed sample at 950°C over a range of soaking times (0, 60 and 120 seconds respectively) in order to dissolve all the VN and VC into solution. They were then quenched to 450°C after which they were slowly cooled to room temperature. The rest of the samples were produced by pre-heating them to the solution temperature of 950°C at a heating rate of 10°C/s. The temperature was then maintained at 950°C for 120s to dissolve the carbides and nitrides into solid solution. The samples were then fast cooled to a temperature in the intercritical temperature region (between 625°C and 750°C). An isothermal hold was then introduced at this stage to allow the transformation from γ to α to take place. This hold was also meant to influence the formation of interphase precipitates, which

are known to be very effective in precipitation strengthening. The different transformation times and temperatures were used to create and to verify the optimum conditions for interphase precipitation. The samples were then fast cooled at 40°C/s to the bainitic transformation temperature of 450°C and then left to cool slowly to room temperature.

In addition to the heat treated samples (described above), a further strip steel of dimensions 120mm x 50mm x 3mm (l x w x t) was also received in the as-rolled condition. From this sample, tensile bars were cut into four specimens which were later heat treated according to the thermal cycles for samples 725-1800s, 700-30s, 700-1200s, 650-60s and 650-600s shown in Table 3.2. The reasons for selecting these thermal cycles were based on the microstructural observations; they were believed to have the highest potential to produce the required mechanical properties. The heat treatments were also carried out on fresh hot rolled samples. This was done in order to regenerate another full set of samples for comparison with the original set of samples received in the heat treated condition from Tata Steel.

Table 3.2 – Thermal cycle schedule for V alloyed steel

Sample	Soaking		Isothermal holding	
	Temp. °C	Time (s)	Temp. °C	Time (s)
950Q	950	0	0	0
950-60Q	950	60	0	0
950-120Q	950	120	0	0
750-60S	950	120	750	60
750-1800S	950	120	750	1800
725-1800S	950	120	725	1800
700-30S	950	120	700	30
700-1200S	950	120	700	1200
650-60S	950	120	650	60
650-600S	950	120	650	600
625-300S	950	120	625	300

3.3.1 Heat Treatments on the Thermomechanical Compression Machine (TMC)

The heat treatment cycles were carried out in the thermal treatment unit of the TMC machine at the university of Sheffield. The heating induction coil in the furnace of the TMC machine was designed to give accurate temperature control through active feedback. A special holder was made in a way that the sample could be placed inside, with a lid bolted at the top to tightly enclose the sample inside as shown in Figure 3.4. Both ends of the sample were left exposed on the outside so that thermocouples could be positioned into the holes drilled on both ends of the sample. Grooves were chiselled on both ends of the holder to enable the robot arms of the TMC to hold the sample holder tightly and in place during heat treatment. The design as well as the full operating details of the TMC machine were as describe by Lacey et al. [147].

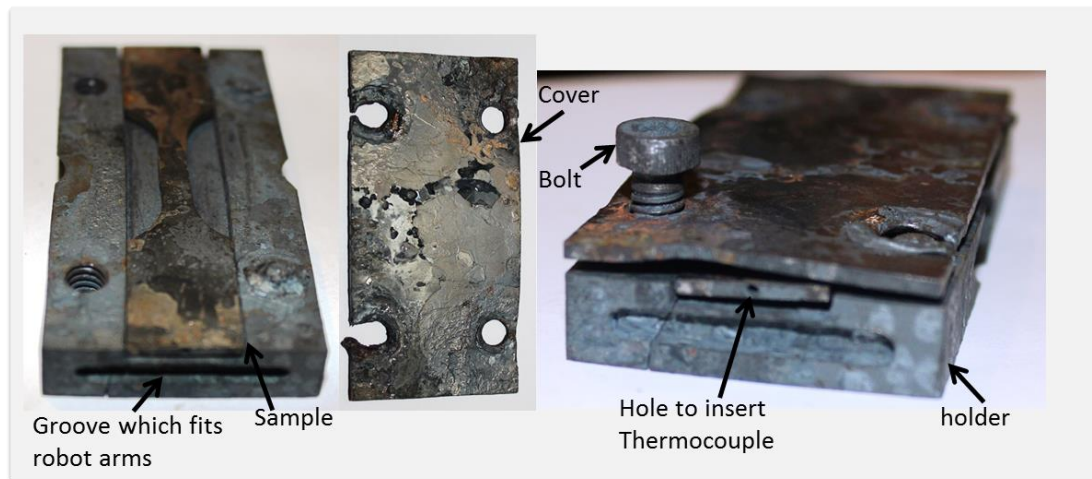


Figure 3.4 – Purpose made holder used during heat treatment of samples in the TMC machine

Thermocouples attached to the sample were used to control and monitor the temperature in the heating chamber. Initially, the samples were heated from room temperature to the austenising temperature of 950°C in 95seconds, representing a heating rate of approximately 10°C/s. They were then held at the austenising temperature for 120s, allowing enough time for the vanadium carbides to dissolve into solution. Compressed air was then used to cool the samples at a cooling rate of 40°C/s to a range of temperature ranging from 625 to 750°C as per thermal cycle schedule in table 3.2. The high cooling rate of 40°C/s was used to prevent cementite and/or pearlite from forming. Isothermal holds were then applied varying from 30

seconds to 1800s. Holding the temperature allows more time for the transformation from austenite to ferrite, creating conditions suitable for interphase precipitation to occur. Following the isothermal hold, the samples were air cooled again at a cooling rate of 40°C/s to 450°C/s, which was within the bainite transformation temperature region. At the bainite transformation temperature, the remaining austenite was further enriched with carbon, and reduced in size. Figure 3.5 is the diagrammatic representation of the simulated heat treatment process on the TMC machine.

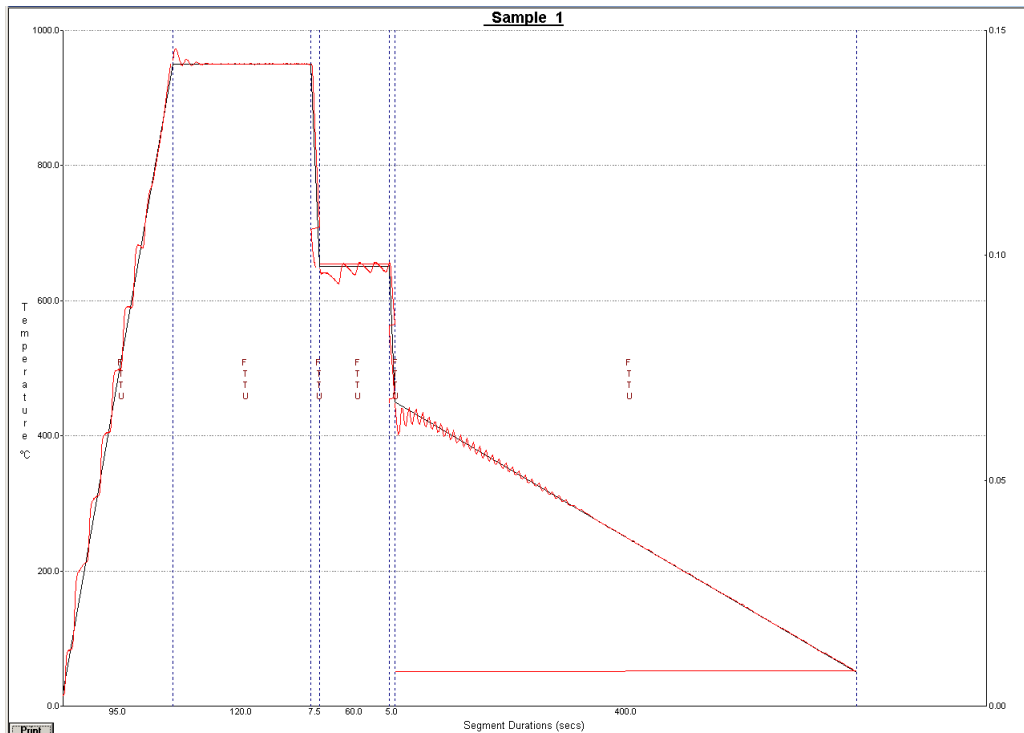


Figure 3.5 – Actual heat treatment Cycle adopted from the TMC machine for sample 650-60s

Tensile testing was then carried out on selected samples while characterisation was performed on the additional samples generated.

3.4 Stage 3 Materials - New Alloy Compositions Strengthened by Nanoprecipitates

Twenty six samples of variable chemical compositions and approximately 100mm x 15mm x 2.5mm (L x W x T) were received from Tata Steel (IJmuiden). Of the twenty six samples, fourteen were selected for characterisation based on the assumption that they were likely to allow the determination of the key microstructural variables. This decision was based on similarities in chemical compositions as well as the coiling temperatures. The nomenclature and chemical compositions of the steels examined are shown in Table 3.3. The first two digits on the sample name represent the sample code which will be referred to in cases where space is limited, (e.g. in graphical representation of data). The next three digits represent the coiling temperature. The letters at the end represents the alloying elements. For example, in sample 01-630Nb⁺VMo, 01 is the sample code while the coiling temperature was 630°C. The alloying elements of interest are Nb, V and Mo. The +sign (e.g. Nb⁺) implies the addition of that element in that particular sample is higher as compared to the other samples.

Table 3.3- Table of Chemical Composition

Sample	Chemical Composition (wt %)								
	C	Si	Mn	Mo	Nb	V	Ti	Al	N
01-630Nb ⁺ VMo	0.061	0.10	1.570	0.200	0.057	0.10	-	0.044	0.0050
02-630Nb ⁺ VMo	0.091	0.19	1.560	0.500	0.054	0.24	-	0.048	0.0038
06-600Nb ⁺ VMo	0.096	0.026	1.560	0.510	0.056	0.25	-	0.050	0.0038
07-630NbVMo	0.037	0.031	1.560	0.240	0.027	0.16	-	0.044	0.0034
10-630Nb ⁺ VMo	0.096	0.026	1.560	0.510	0.056	0.25	-	0.050	0.0038
14-650Nb ⁺ VMo	0.096	0.026	1.560	0.510	0.056	0.25	-	0.050	0.0038
15-650TiMo	0.044	0.180	1.580	0.200	0.009	-	0.070	0.039	0.0046
16-650Ti	0.051	0.190	1.630	-	0.009	-	0.079	0.036	0.0070
17-650VMo	0.045	0.190	1.620	0.200	-	0.19	-	0.046	0.0060
18-650V	0.047	0.180	1.600	-	-	0.20	-	0.043	0.0049
19-650NbMo	0.047	0.180	1.590	0.190	0.056	-	-	0.037	0.0047
20-650Nb	0.039	0.180	1.600	-	0.055	-	-	0.039	0.0042
21-650TiMo	0.092	0.180	1.570	0.500	0.008	-	0.170	0.044	0.0050
22-630 N ⁺	0.044	0.096	1.587	0.244	0.030	0.164	-	0.010	0.0170

The following is a brief description of the process adopted by Tata Steel to manufacture these samples. 25 to 30 kg ingots were re-heated to 1250°C prior to hot rolling. They were then forged to a thickness of approximately 35mm followed by air cooling to room temperature. The forged section was then cut into sections of dimensions 75mm x 100mm x 35mm followed by re-heating to approximately 1220°C to 1240°C. The samples were then maintained at this temperature for further 40 to 45minutes in order to dissolve the carbides and nitrides. The samples were then hot rolled in five passes with the thickness evolving from 35mm to 19mm during the first pass, 19mm to 11mm during the second pass, 11mm to 7mm in the third pass, 7mm to 4.5mm in the fourth pass and finally 4.5mm to 3.5mm in the last pass. The finish rolling temperature was aimed at 890°C. The samples were then water cooled at approximately 50°C/s to the coiling temperature and then immediately placed into a furnace pre-heated to the coiling temperature. At the coiling temperature, the furnace was then turned off and the samples left to slowly cool over a period of up to, or over, 12 hours to simulate coiling. The diagrammatic representation of the process is shown in Figure 3.6.

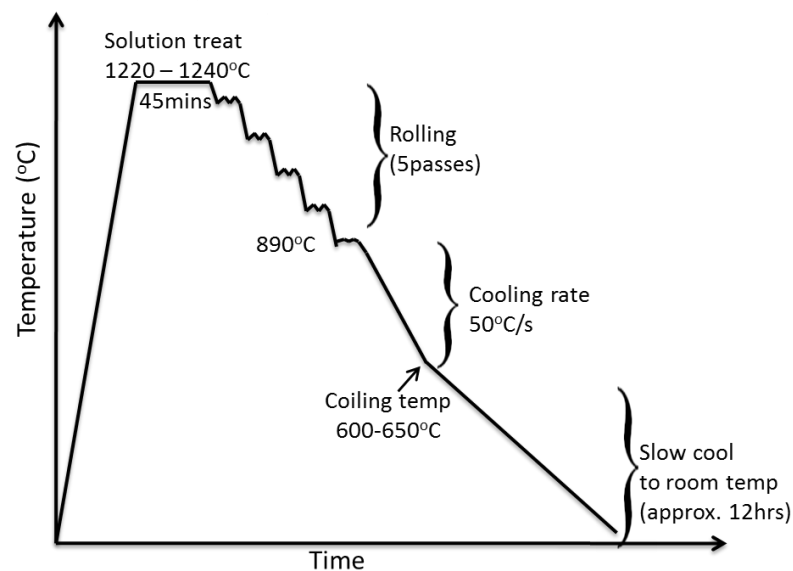


Figure 3.6 – Schematic diagram of the process used to produce the samples by Tata Steels

3.5 Tensile Specimens

In order to determine the tensile properties of the samples, tensile specimens conforming to ASTM standard E8/E8M – 09[148] with a gage length (L) of 25mm, gage width (W) of 6mm and thickness (t) of 1.5mm were machined along the rolling direction from the as rolled strip steel.



Figure 3.7 – Tensile specimen prepared according to ASTM standard E8/E8M – 09[148]

The tensile specimens were then heat treated in the thermal treatment unit of the TMC machine as previously described. They were then ground and polished to remove the oxide scales developed during thermal treatment. Tensile tests were then carried out at room temperature at a constant cross-head speed of 1mm/minute on the Hounsfield-H100KS tensile testing machine.

3.6 X-ray Diffraction (XRD)

X-ray diffraction, to determine the volume fraction of the retained austenite in the samples, was performed using the Siemens D5000 refraction diffractometer. The major problem with this technique is always associated with crystallographic texture in the material [149]. This problem was minimised by mounting the specimens onto a rotating sample holder, which helped eliminate the effect of preferential crystallographic orientations on diffracted peak intensity.

Sample preparation included grinding using the 240, 400, 600 and 800 grade silicon carbide papers under running water to remove the oxide layer and excessive roughness on the surface. The final thicknesses of the samples were approximately 1mm. The Siemens D5000 diffractometer used, had variable divergence and anti-scatter slits that made it easier to illuminate X-rays over larger surface areas; hence larger samples were used which meant illumination of X-rays over wider surface areas. Specimens were then cut to approximately 25mm (l) x 25mm (w) which is almost the maximum sample size that could fit into the diffractometer's specimen holder. The diffractometer was operated using Bragg-Brentano conditions with an X-

ray generator equipped with monochromatic Co K α radiation with a wavelength of 1.78896 Å, and tube operating conditions of 40kV and 30mA. A step size of 0.05 and a time step of 3s were used.

The phases within the samples were quantified by X-ray diffraction through determination of the intensities diffracted by the different phases within the material. The retained austenite content was measured on the assumption that the diffraction obeyed Bragg's law.

$$n\lambda = 2d\sin\theta \quad \text{Eq. 3.1}$$

where n is the order of reflection, which always takes a value of one of the monochromatic radiation, d is the interatomic spacing, λ is the wavelength of the radiation source and θ is the Bragg angle (angle between the incident beam and crystal planes of interest)[150]. To ensure consistent results were obtained, both sides of the sample were subjected to XRD analysis.

3.7 Retained Austenite Content Estimation

The X-ray diffraction method for the analysis of volume fraction of phases within the sample has been found to be one of the most efficient and accurate method for determining the volume fraction of retained austenite in steel [149, 151]. The volume fraction of the retained austenite randomly oriented sample can be calculated on the assumption that the integrated intensity from any diffraction peak is directly proportional to the volume fraction of that phase[151]. For steel containing either martensite or ferrite and austenite, the integrated intensities from the (h k l) planes of the ferrite and austenite can be calculated from the following equations (for α , substitute γ with α):-

$$I_{\gamma} = \frac{KR_{\gamma}V_{\gamma}}{2\mu} \quad \text{Eq. 3.2}$$

The above equation only applies in cases where either ferrite or martensite and austenite are the only phases present and are randomly oriented in the sample [152]. Taking into consideration the fact that the sum of the volume fractions of the various phases in the sample is always equal to unit,

$$V_{\alpha} + V_{\gamma} = 1 \quad \text{Eq. 3.3}$$

where I is the integrated intensity of each phase, μ is the linear absorption coefficient for each steel, V is the volume fraction of the respective phase, K is a constant which is independent of the sample, but dependant on the instrument geometry and radiation and R is a term which is characteristic to each steel alloy and is dependent on the interplanar spacing (hkl), Bragg angle (θ), crystal structure and composition of the phase being measured[152, 153].

Combine equations 1, 2 and 3 to get the following equations which can be used to calculate the volume fraction of the retained austenite.

$$V_{\gamma} = \left[\frac{R_{\gamma}I_{\alpha}}{R_{\alpha}I_{\gamma}} + 1 \right]^{-1} \quad \text{Eq. 3.4}$$

$$V_{\gamma} = \frac{I_{\gamma}/R_{\gamma}}{I_{\alpha}/R_{\alpha} + I_{\gamma}/R_{\gamma}} \quad \text{Eq. 3.5}$$

Hence, the austenite volume fraction can be calculated using the ratio of austenite and ferrite diffraction peak intensities and the R value for each phase. In cases where there are numerous ferrite and austenite peaks, the ratios of measured integrated intensity for a number of planes of (h k l) produced from the same orientation of a single specimen surface to R value of that plane can be summed up [152, 153].

For α -Fe (BCC structure), the planes that diffract are of the order of $n = 2, 4, 6, 8, \dots$, where $n = (h^2 + k^2 + l^2)$, hence, the corresponding d spacing (h k l) values for the above are (110), (200), (211) (220) etc. For the γ - Fe, (FCC structure), the planes that diffract are of the order of 3, 4, 8, etc., therefore the d spacing (h k l) for the above are (111), (200), (220), (311), etc.

3.8 Optical and Scanning Electron Microscopy (SEM)

Optical metallographic specimens were cut and mounted in bakelite with the transverse section facing the outside as shown in Figure 3.8.



Figure 3.8 – Sample mounted in bakelite for optical microscopy, SEM and TEM carbon extraction replicas

The samples were then mechanically ground starting with 240 and ending with the 1200 grade silicon carbide papers under running water. They were then polished using 6 μ m and finishing with 1 μ m diamond cloths under respective water based diamond suspension lubricants. The specimens were finally polished using colloidal silica (Silco) for 10 minutes to give a final polish of 0.04 μ m. The polished specimens were then thoroughly cleaned using teepol, a water based lubricant, followed by isopropanol. They were then etched in 5% nital solution for up to 15 seconds, depending on the sample. They were then thoroughly cleaned to ensure that the etchant was completely removed from the surface. To ensure that any particles of dirt that might have adhered to the sample surface were completely removed, the samples were fully immersed in isopropanol and placed in an ultrasonic bath for 10 minutes. They were then thoroughly dried and stored in a desiccator, ready for optical microscopy and/or SEM analysis.

Optical microscopy to gain an insight into the microstructure was carried out on a Leica Polyvar optical microscope while scanning electron microscopy was performed on the JEOL JSM 6400 scanning electron microscope operating between 10kV and 20kV and at a magnification of 1000x to 3500x. In order to get a better resolution of some of the features, further SEM was carried out on the FEI Inspect F scanning electron microscope which is equipped with a field emission gun (FEG) for better resolution. Images from the specimens were taken on the FEI Inspect F SEM

operating between 10 and 20kV and at magnifications ranging from 1000x to 15000x.

3.9 TEM Carbon Extraction Replicas

In order to analyse the precipitates alone without interference from the surrounding matrix, carbon extraction replicas specimens were prepared. The samples were mounted in bakelite as shown in Figure 3.8. They were then mechanically ground using silicon carbide paper starting with 240 and ending with the 1200 grade under running water as previously described for optical and SEM samples. Polishing was also done for 10 minutes using 6 μ m diamond cloth and water based diamond suspension lubricant, followed by another 10 minutes using 1 μ m diamond cloths under a water based 1 μ m diamond suspension lubricant. The final polish was then done using colloidal silica (Silco) for another 10 minutes to give a final polish of 0.04 μ m. They were then cleaned using teepol before a final clean with isopropanol. Lightly etching was the done using 5% nital solution followed by thorough cleaning with teepol to ensure that the etchant was completely removed from the surface. The samples were then immersed in isopropanol and then placed in an ultrasonic bath for 10 minutes to ensure that any particles of dirt adhering to the sample surface were completely removed. They were then thoroughly dried and stored in a desiccator before carbon coating.

A thin amorphous carbon film was then applied to the samples using the Speedivac carbon coating unit. Approximately 2mm square grids were then scratched on the surface of the specimens. The rest of the matrix was then etched away by carefully submerging the specimen into 10% nital solution until bubbles started to form on the surface. The carbon extraction replicas process is shown in Figure 3.9

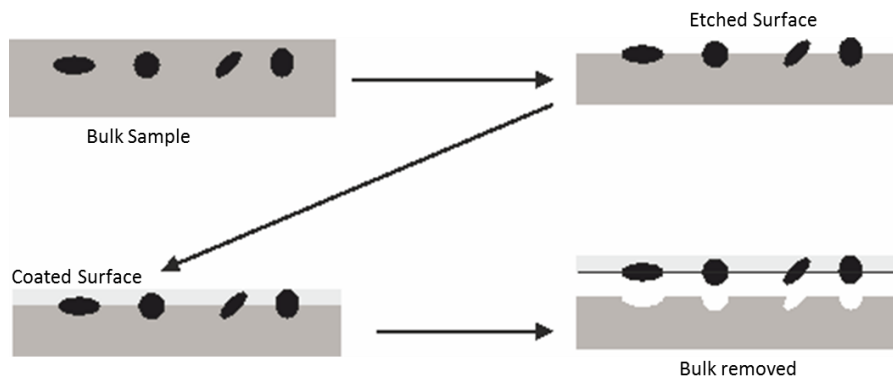


Figure 3.9 - Schematic diagram of the carbon extraction replica process[154]

The samples were then removed from the nital solution and placed in methanol at an angle in order to allow the carbon replicas to lift off the surface through surface tension. The replicas were then fished out of the methanol using 400 mesh copper grids and stored. TEM images for further precipitate analysis were taken using the FEI Tecnai T20 transmission electron microscope operating at 200kV. Further chemical analysis of the precipitates was undertaken using energy loss spectroscopy (EELS) and Energy Dispersive X-ray Spectroscopy (EDX) on the Jeol 2010F transmission electron microscope. The Jeol 2010F TEM was equipped with a CCD slow scan camera integrated into a Gatan image filter (GIF) for recording the spectrum and images.

3.10 TEM Thin Foils

Samples for TEM thin foil specimens were first cut from the original sample and then manually ground starting with 240 and ending with 1200 grade silicon carbide paper under running water. The grinding was done in order to reduce the thickness from the initial thickness of approximately 2mm to a final thickness of 120 - 150 μ m. 3mm diameter disks were then punched from the slice and these were then further ground to a thickness of approximately 60 to 90 μ m.

The discs were then electropolished using the Metalthin twin jet electropolisher operating at 30mA and a jet speed of 3. 220ml of freshly prepared electrolyte containing 5% perchloric acid, 35% butoxyethanol and 60% methanol was used in the electropolisher for thinning the samples. The solution was cooled and maintained at -50°C using liquid nitrogen. Immediately after perforation, the foils were rapidly removed from the electrolyte, cleaned using methanol and stored in methanol to prevent oxidation. The electropolished samples were then analysed in a Philips EM430 transmission electron microscope operating at 300kV while others were analysed using the FEI Tecnai T20 transmission electron microscope operating at 200kV.

3.11 Grain Size Measurements

In order to measure the average grain sizes of each of the samples, the linear intercept method was used. A series of equally spaced lines were drawn such that the minimum distance between the lines were greater than the largest grain within that image to ensure that each grain was not counted more than once. The number of times each line crossed the grain boundaries were then counted and the data collected was then used to estimate the average grain size. KS run software was also used to measure grain sizes in the second batch of vanadium microalloyed steels as well as the last batch of ferritic steels on SEM images. The same data was then used to calculate the standard deviation which enabled the 95% confidence limit to be calculated.

3.12 Quantification of Phases

The volume fraction of the second phases within the samples was calculated using the point counting technique. Equally spaced square grids were drawn on each of the micrographs analysed such that the points where they cross fall on a random array of points. The spacing was such that the square grid was larger than the largest grain to ensure that no grain was counted more than once. In cases where the grid points crossed within the second phase, this was counted as 1, whereas when the points crossed at the interphase boundary, it was counted as 0.5. The counting was repeated on all the lines and the results from each line were used to perform the statistical analysis. From this data, the volume fraction of the phases was calculated. The standard error was also calculated from the standard deviation.

3.13 Precipitate Sizes and Distribution

TEM images taken from carbon extraction replicas were used for precipitate size distribution analysis. The images were taken from random areas within the samples in order to get a reasonable representation of the precipitate distribution. ImageJ analysis software was used to analyse the precipitates. However, in some cases, the software could not distinguish between dark contrast and the actual precipitates. As a result, manual count was also used to reinforce the software and this was made simple by the observation that most of the particles were circular. Where ImageJ software was used, the software provided values in square nanometres and these were subsequently converted to particle diameters in nanometres on the assumption that most of the precipitates were circular. A samples size ranging from 800 to 4000 precipitates were counted for each of the samples. Energy Dispersive X-ray Spectroscopy (EDX) and Energy Loss Spectroscopy (EELS) were used to identify the precipitates. The size distributions were then plotted as a histogram and mean values, standard errors etc. were then calculated from the precipitate counts.

CHAPTER 4: MULTIPHASE STEELS OF DIFFERENT CHEMICAL COMPOSITIONS

4.1 Introduction

This chapter presents the results from the initial three multiphase steels that were provided by Tata Steel to start the project. The Ti, Al and Mo (TiAlMo) alloyed strip steel was chosen as the most likely to produce nano-precipitation as claimed by Raabe et al.[10] and JFE steel[13] as well as to verify these claims. The titanium (Ti) microalloyed strip steel was chosen as a suitable comparison to the TiAlMo steel to see whether nanoprecipitation and the TRIP effects could be observed in the absence of Mo and Al. Finally, the vanadium (V) alloyed strip steel has always been known to give fine precipitation and therefore provided a useful comparison to the TiAlMo steel. It was also investigated to see whether interphase precipitation could be observed. Two samples were provided for each of these steels, one of them having undergone continuous cooling (CC), with the other one having been subject to a 4 seconds temperature hold (2 step cooling abbreviated 2S) during the thermal cycle. The purpose of the study was to characterise the microstructure with the aim of quantifying the various phases and correlating the microstructure obtained to the mechanical properties.

4.2 Tensile Properties

In order to relate the microstructure to the mechanical properties, tensile tests on the six multiphase steel samples were carried out by Tata Steel and the summarised results are shown in Table 4.1.

Table 4.1 – Table of tensile properties

Sample	UTS (MPa)	Total Elongation (% ϵ)
TiAlMo-2S	780	19
TiAlMo-CC	773	22
Ti-2S	755	12
Ti-CC	810	8
V-2S	623	21
V-CC	794	9

A comparison of the tensile properties is shown in Figure 4.1. The results show that the best combination of strength and total elongation was attained in the TiAlMo samples. The two step cooled sample TiAlMo-2S produced the best result with a UTS of 780MPa and a total elongation of 18.9%, followed by the continuously cooled sample TiAlMo-CC, which had a UTS of 773MPa and a total elongation of 21.8%. The Ti alloyed samples did not yield very good results. The two step cooled sample Ti-2S had a tensile strength of 755MPa and a total elongation of 12.1% while the continuously cooled sample Ti-CC had a tensile strength of 810MPa, which was the highest in comparison to the other samples. However, its total elongation was 8.1%, which was the lowest as compared to the others. This is another good example of cases where higher strength is achieved at the expense of ductility. However, the two step cooled V-2S was completely different to the continuously cooled V-CC. V-2S had the lowest tensile strength of 623MPa and a high total elongation of 21% which shows that ductility seems to have taken precedence over tensile strength. The continuously cooled vanadium alloyed sample V-CC followed the same trend as that of the Ti-CC. A high strength of 794MPa was attained at the expense of the uniform elongation which was found to be 9%.

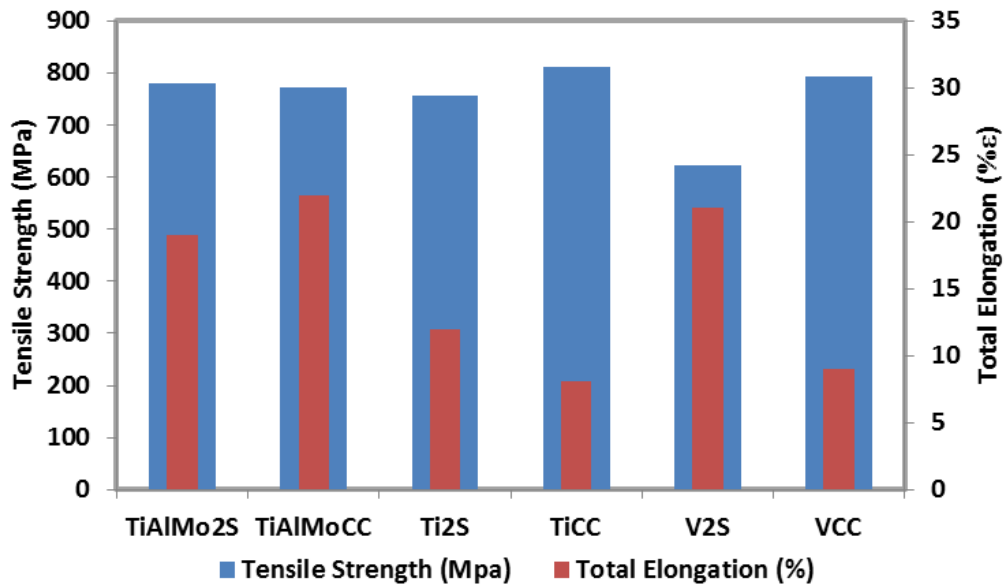


Figure 4.1 – Summarised tensile test results

4.3 Retained Austenite Content

Retained austenite plays a major role in creating a good balance between strength and ductility in multiphase steels. Following the tensile tests, samples were then prepared for XRD in order to measure the volume fraction of the retained austenite within the samples. The XRD patterns for the six samples analysed are shown in Figure 4.2.

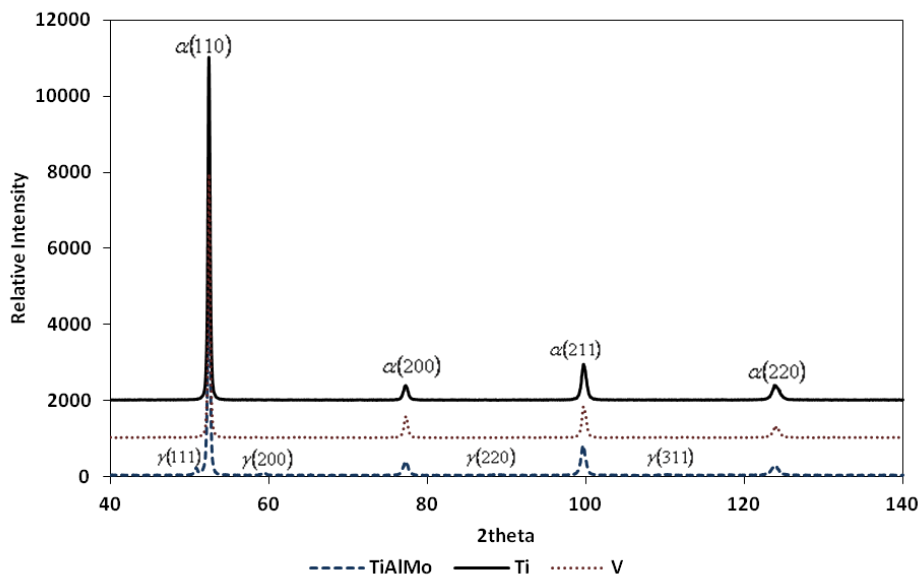


Figure 4.2 – XRD results for TiAlMo, Ti and V alloyed multiphase steels.

TiAlMo samples (both TiAlMo-2S and TiAlMo-CC) exhibited peaks corresponding to bcc-ferrite (α -ferrite) and fcc-austenite (γ -austenite). The α -ferrite peaks were found to be $\alpha(110)$, $\alpha(220)$, $\alpha(211)$ and $\alpha(220)$ while the γ peaks were found to be $\gamma(111)$, $\gamma(200)$, $\gamma(220)$ and $\gamma(311)$. However, the γ peaks were quite weak as compared to α peaks. Using the integrated intensities of the peaks obtained, the volume fractions of the retained austenite in the samples were calculated. The retained austenite content in both TiAlMo-2S and TiAlMo-CC were found to be 7%. However, Ti samples (Ti-2S and Ti-CC) and V samples (V-2S and V-CC) only exhibited diffraction peaks corresponding to $\alpha(110)$, $\alpha(220)$, $\alpha(211)$ and $\alpha(220)$; hence, retained austenite (γ) was not detected at all. The results are summarised in Table 4.2

Table 4.2 – Table of Retained Austenite Content

Sample	Retained Austenite (%)
TiAlMo-2S	7
TiAlMo-CC	7
Ti-2S	0
Ti-CC	0
V-2S	0
V-CC	0

4.4 Characterization of the Microstructure

In order to identify the various phases within the six samples, Optical Microscopy, Scanning Electron Microscopy (SEM) and Transmission Electron Microscopy (TEM) were used.

4.4.1 Optical Microscopy

Initially, optical microscopy was used to identify the various phases within the multiphase steels. The problem at this stage was that even though phases could be clearly seen within the microstructures, it was difficult to identify them. For the TiAlMo multiphase steels shown in Figure 4.3, both samples were found to contain two distinct phases, the only difference being that the second phase in TiAlMo-2S in Figure 4.3b was coarser than TiAlMo-CC in Figure 4.3b. It was also noted that in both cases, the 2nd phases could not be resolved.

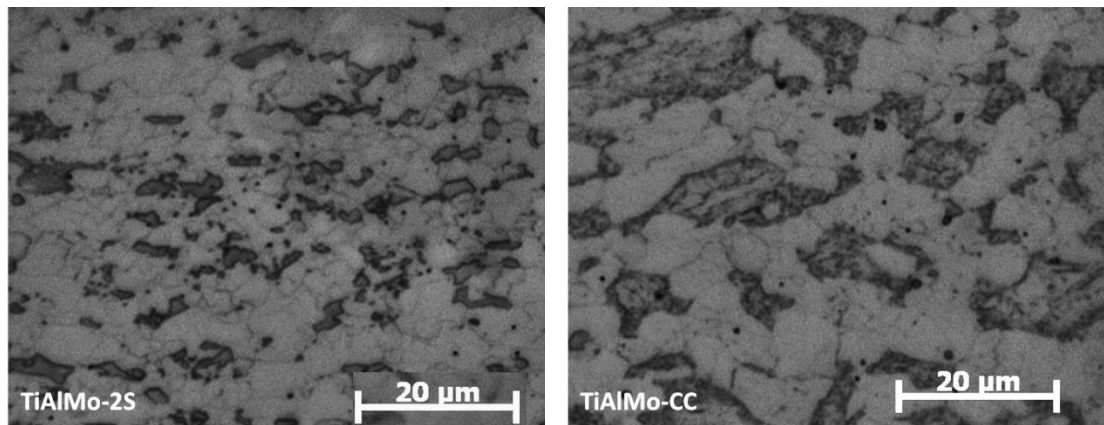


Figure 4.3 – Optical micrographs showing distinct ferrite grains and an unresolved second phase in TiAlMo-2S and TiAlMo-CC.

Just like TiAlMo which showed very little difference in microstructure between the two steps and the continuously cooled samples, the Ti alloyed steels were also quite similar. Both Ti-2S and Ti-CC had a very fine microstructure and the phases could not be resolved through optical microscopy.

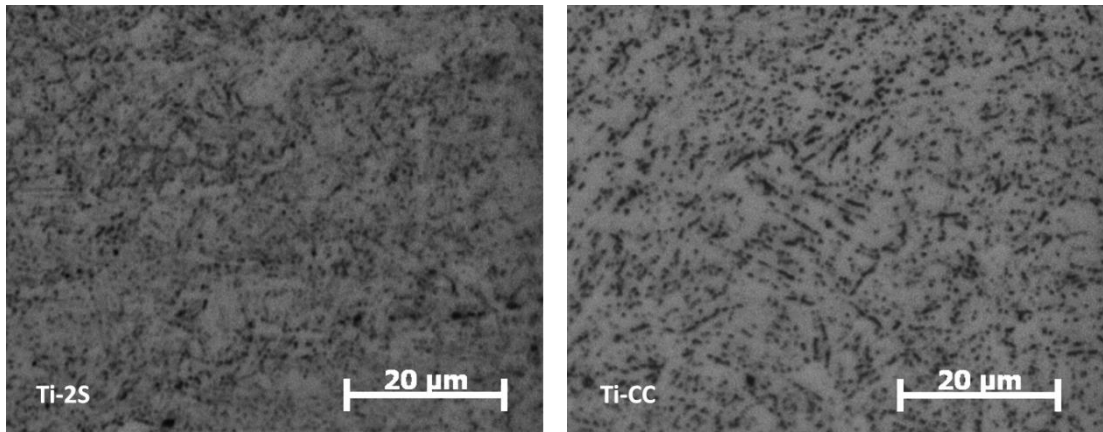


Figure 4.4 - Optical micrographs showing a fine unresolved microstructure in Ti-2S and Ti-CC

Further analysis needed to be carried out in order to get a clearer identification of the 2nd phases.

Figure 4.5a and b shows the microstructures of the two-step cooled vanadium microalloyed sample V-2S and the continuously cooled vanadium microalloyed sample V-CC respectively. V-2S had distinct ferrite grains with an unresolved 2nd phase as compared to V-CC, which had a very fine microstructure similar to that of the Ti alloyed samples. Once again, optical microscopy failed to resolve the phases at this stage meaning that further investigations needed to be carried out.

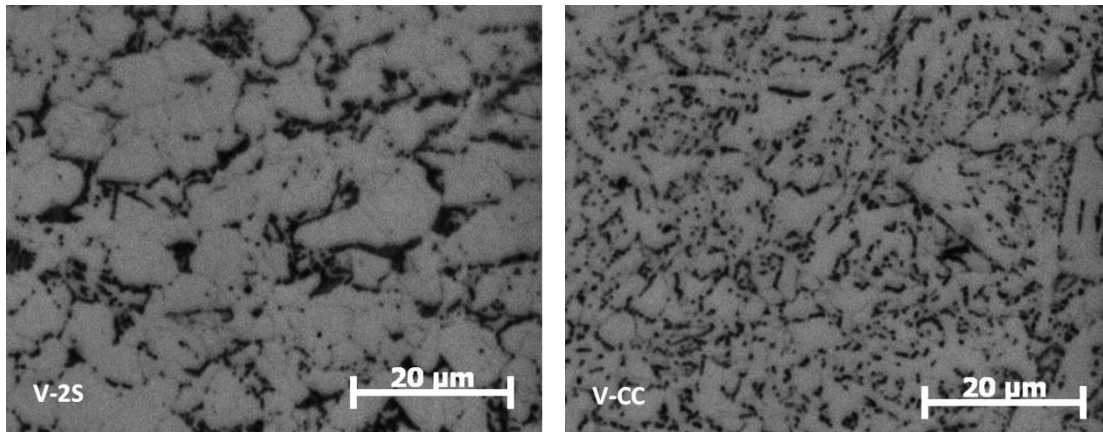


Figure 4.5 - Optical micrographs showing an unresolved 2nd phase within the ferrite matrix in V-2S and a fine unresolved microstructure for V-CC.

Optical microscopy, having failed to yield conclusive results in terms of identifying the phases in all the cases, SEM was then used to characterise the samples.

4.4.2 Scanning Electron Microscopy (SEM)

SEM of nital etched samples was used to resolve the phases. SEM imaging enabled the microstructures to be analysed in terms of the size, morphology and substructure. The main similarities between the optical and SEM micrographs were the variations in the microstructure mainly between the different chemistries.

Figure 4.6a and b are the SEM images of the two step cooled and the continuously cooled TiAlMo alloyed sample respectively. The samples had similarities, both being dominated by a ferrite matrix with bainite located inter-granularly within the ferrite. Islands of martensite were also found scattered throughout the sample. Retained austenite, though few and far between and difficult to distinguish from martensite, was also found.

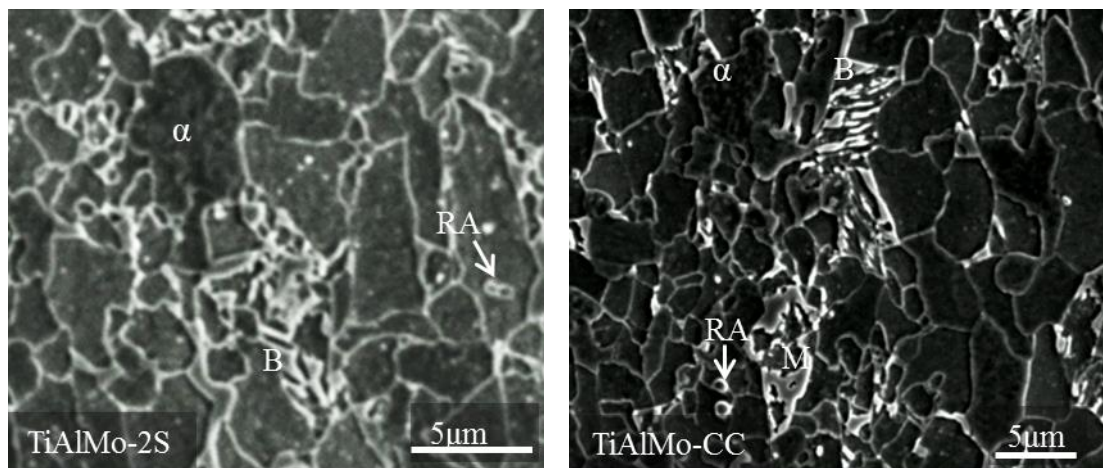


Figure 4.6 – Secondary electron SEM images showing similar features in TiAlMo-2S and TiAlMo-CC.

Figure 4.7 shows SEM images for Ti-2S and Ti-CC respectively. The fine microstructure previously revealed through optical microscopy was confirmed to be bainite in both samples.

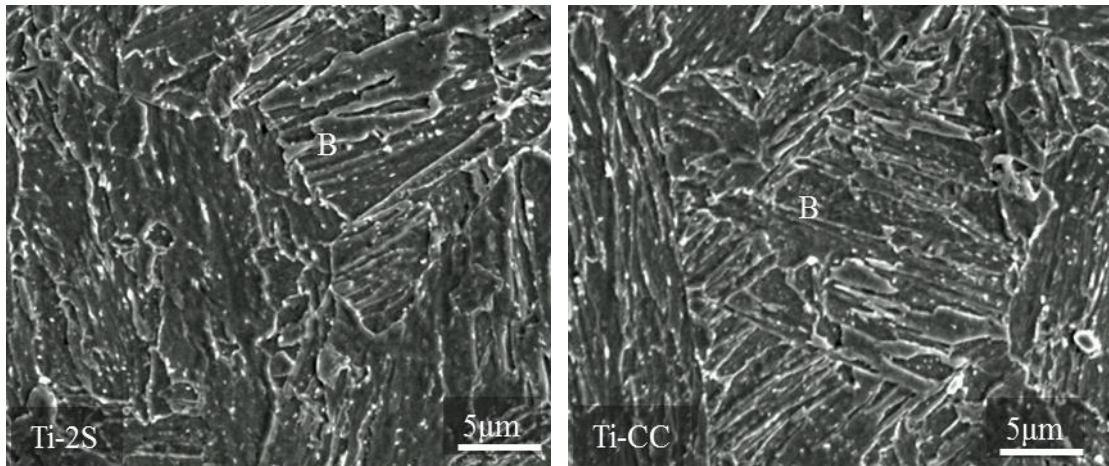


Figure 4.7 - SEM images showing the bainitic microstructure in samples Ti-2S and Ti-CC

Unlike the Ti samples which showed little or no microstructural differences, the V microalloyed samples were completely opposite. Large ferrite grains with occasional islands of martensite dominated V-2S while V-CC was mainly dominated by bainite located both at the grain boundaries and inter-granularly within the ferrite grains as shown in Figure 4.8. On the other hand, large precipitates seemed to decorate the ferrite grains in V-2S and these were later confirmed through TEM analysis.

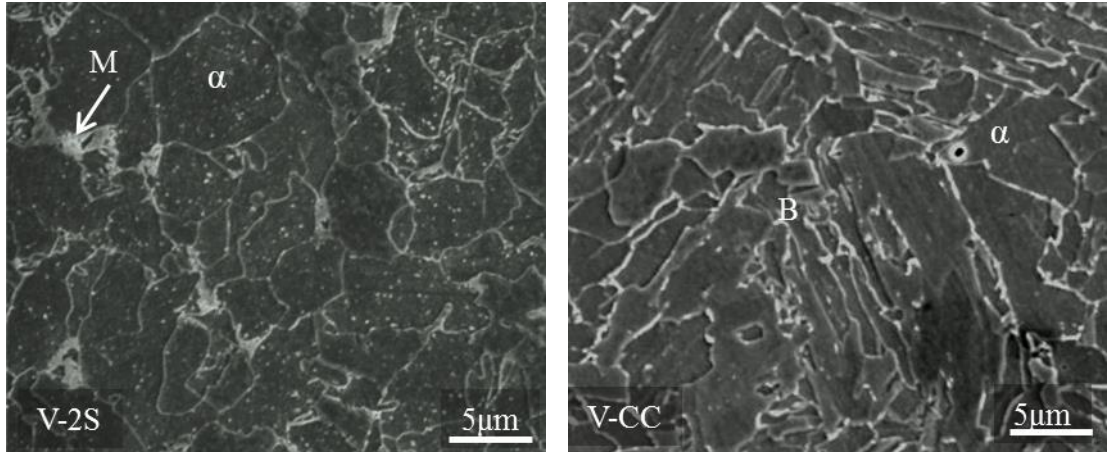


Figure 4.8 – SEM images showing the distribution of phases in V-2S and V-CC.

4.5 Grain Size Measurements

Using the linear intercept method, grain size measurements were also carried out on the two TiAlMo samples and V-2S. The measurements were taken from optical microscopy images and the summarised results are shown in Table 4.3.

Table 4.3 – Table of grain size measurements and phase summaries (B= bainite, M=martensite)

Sample	Grain Size (μm)	Phases
TiAlMo-2S	1.39 \pm 0.04	$\gamma + \alpha + M + B$
TiAlMo-CC	1.56 \pm 0.04	$\gamma + \alpha + M + B$
Ti-2S	-	B
Ti-CC	-	B
V-2S	3.67 \pm 0.25	$\alpha + M$
V-CC	-	$\alpha + B$

TiAlMo-2S had an average grain size of $1.39 \pm 0.04\mu\text{m}$ while TiAlMo-CC had $1.56 \pm 0.04\mu\text{m}$. V-2S was found to have an average grain size of $3.67 \pm 0.25\mu\text{m}$. Unfortunately, measurements could not be carried on any of the other samples due to their fine bainitic microstructures.

4.6 TEM Thin Foils and Carbon Extraction Replicas

4.6.1 Ti-Al-Mo Microalloyed Samples

The size and distribution of the phases within the two step (TiAlMo-2S) and continuously cooled (TiAlMo-CC) samples were quite similar. Some of the features common to both samples was the random precipitates and extensive dislocation density distributed throughout the sample as shown in Figure 4.9a. The high dislocation density was quite common to both bainitic and ferritic regions. However, some areas had very little and sometimes no precipitates at all. Nanoprecipitates were found randomly distributed in most of the ferrite grains and occasionally in the retained austenite. Some regions within the ferrite contained very fine and well-aligned precipitates which could have been interphase precipitates, but this was uncommon. A typical example is shown in Figure 4.9b. Another sign of interphase precipitation were within strings of fine ferrite grains shown in Figure 4.10a. These were not only found within the grains, but also in the adjacent lower grains.

Figure 4.10b shows relatively small and rounded austenite grains. These were also found randomly distributed throughout the sample. Their location was mainly intragranular within the ferrite grains and they showed little or no evidence of interphase precipitation. Bainitic regions, both granular bainite and bainitic laths shown in Figure 4.11a and b respectively, were also a common feature. However, some of the regions were predominantly bainitic while others were ferritic. Islands of martensite shown in Figure 4.11b, though rare, were also found within both samples.

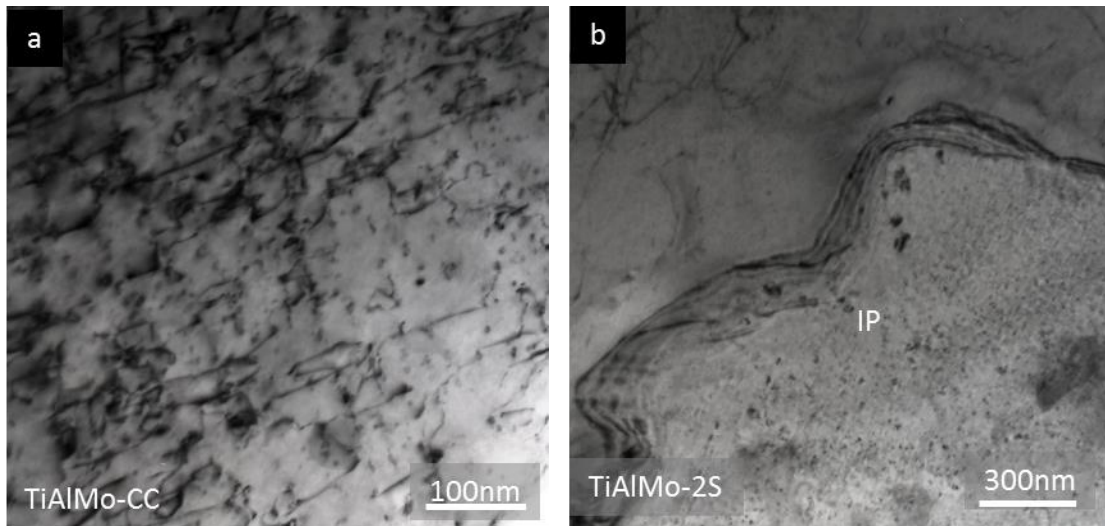


Figure 4.9 – TEM images for TiAlMo showing a) Random precipitates and high dislocation density within the ferrite in TiAlMo-CC and b) possible interphase precipitates in the ferrite in TiAlMo-2S.

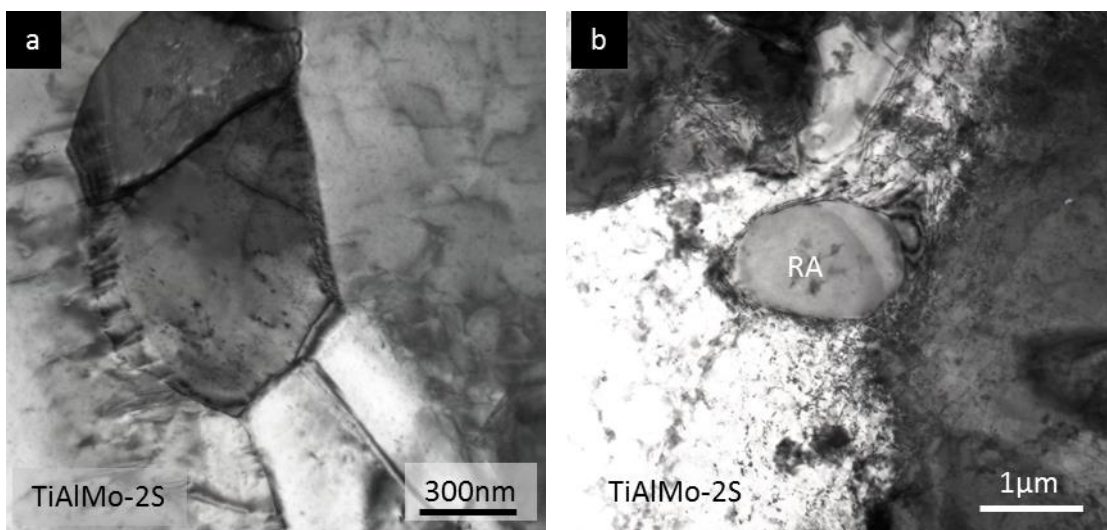


Figure 4.10 – TEM thin foil images showing a) region of fine ferrite within and in adjacent lower grain in TiAlMo-2S and b) Retained austenite located intragranularly within ferrite.

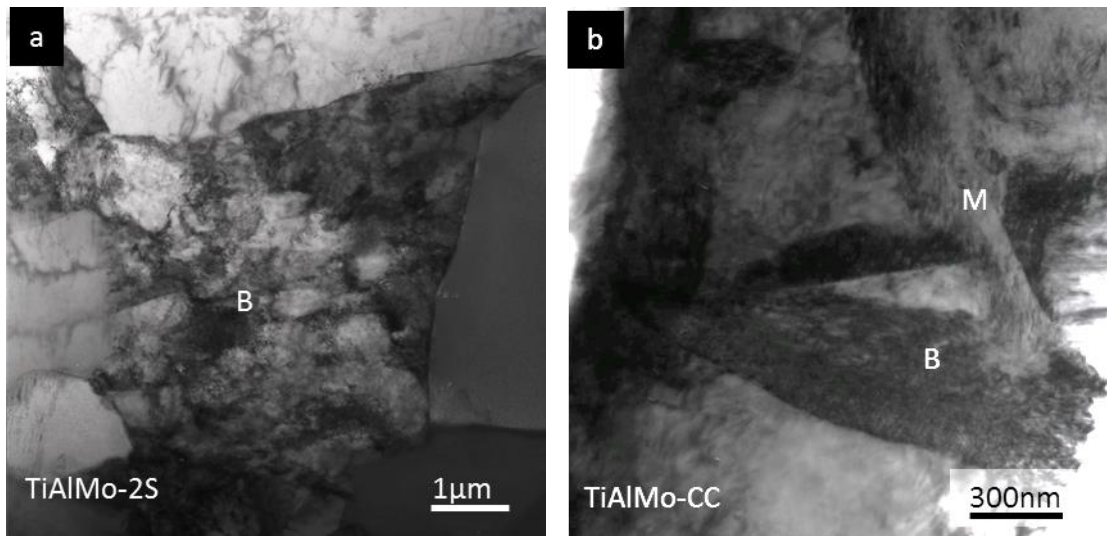


Figure 4.11 – TEM thin foil images showing a) Local region of bainite in TiAlMo-2S and b) region of bainite and fine lath martensite in TiAlMo-CC.

Figure 4.12 are TEM carbon extraction replica images for samples TiAlMo-2S and TiAlMo-CC respectively. Common to both samples was the existence of fine randomly distributed precipitates. The precipitate type and distribution were similar for both specimens. The 4 seconds hold which was introduced in the two-step cooled sample (TiAlMo-2S) might have been insufficient to produce any major difference between the two samples. This observation was also in-line with the TEM thin foil results which did not show any significant differences between the two samples.

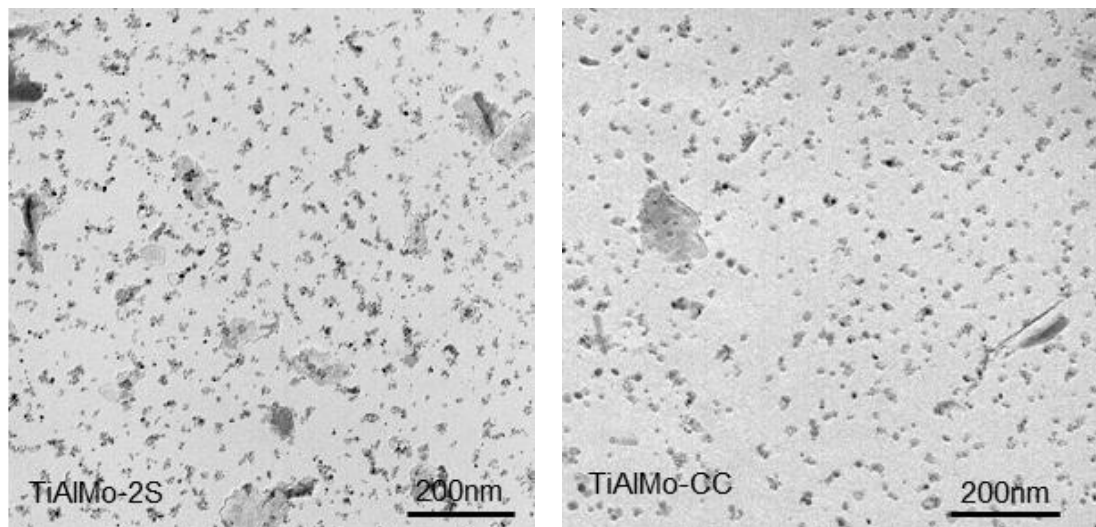


Figure 4.12 – Carbon extraction replica images showing region with random and high precipitate number densities in TiAlMo-2S and TiAlMo-CC

4.6.2 Ti Microalloyed Samples

TEM thin foil micrographs in Figure 4.13 to Figure 4.16 summarises the features found in both the two step cooled Ti-2S and the continuously cooled Ti-CC samples. Even though Ti-2S was dominated by bainite, TEM thin foil analysis showed that there was a significant amount of ferrite as shown in Figure 4.13a. Some odd features like those in the same image (Figure 4.13a) were also observed, believed to be MnS. Most of the ferrite grains in this sample contained little or no precipitates at all and there was certainly no evidence of interphase precipitation. Bainite with bainitic carbides dominated the microstructure as shown in Figure 4.13b and Figure 4.14. The morphology indicated an upper bainite structure typical to those shown in Figure 4.14b in some of the regions. As previously confirmed by SEM, fine lath martensite, though few and far between, was also randomly found (see Figure 4.15a). However, retained austenite was not found within this sample.

TEM thin foil analysis also confirmed all the phases previously identified through SEM in the Ti-CC sample. The microstructure was predominantly bainitic and the morphology was typical to those previously discussed for Ti-2S (Figure 4.13 and Figure 4.14). Random bainitic carbides were quite common within the bainite. Occasional ferrite grains with high dislocation density and fine precipitates were also randomly distributed throughout specimens. Narrow ferrite grains with few or no precipitates like those shown in Figure 4.15b were a common feature and these occupied positions within the bainite. Ferrite grain boundary carbides shown in Figure 4.16a were also quite common. Regions of high dislocation density were quite common in both ferrite and bainite. Interestingly, many of the boundaries had an irregular appearance as in Figure 4.16b, which is consistent with pinning of the boundary by second phase particles. Surprisingly, as stated before, most grains contained little or no precipitates at all and certainly there was no evidence of interphase precipitation. There was also no evidence of retained austenite.

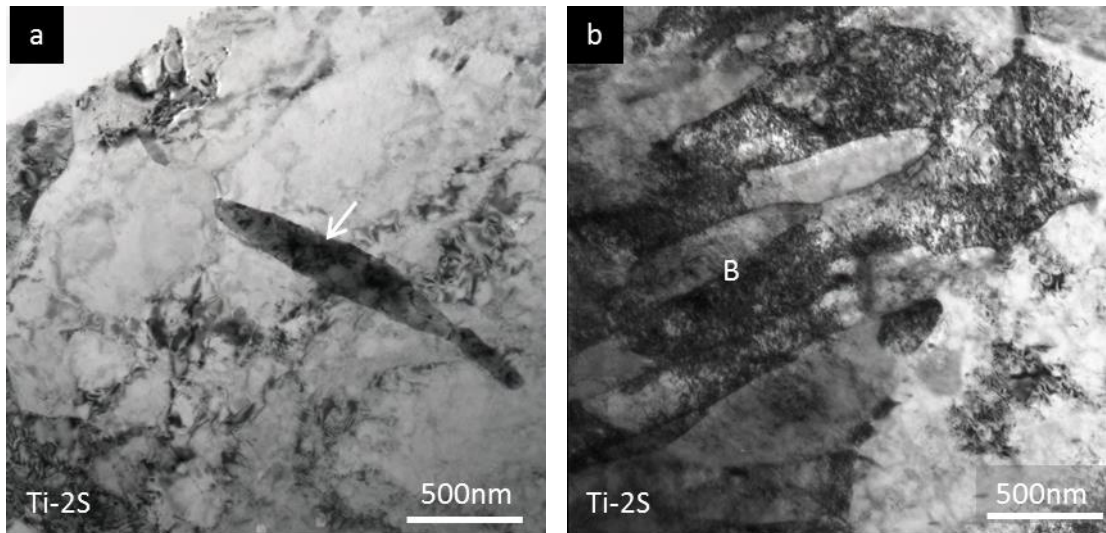


Figure 4.13 – TEM thin foil images for Ti-2S showing a) Ferritic region with few precipitates and an unidentified feature (probably MnS) in Ti-2S and b) Bainitic region with high dislocation density

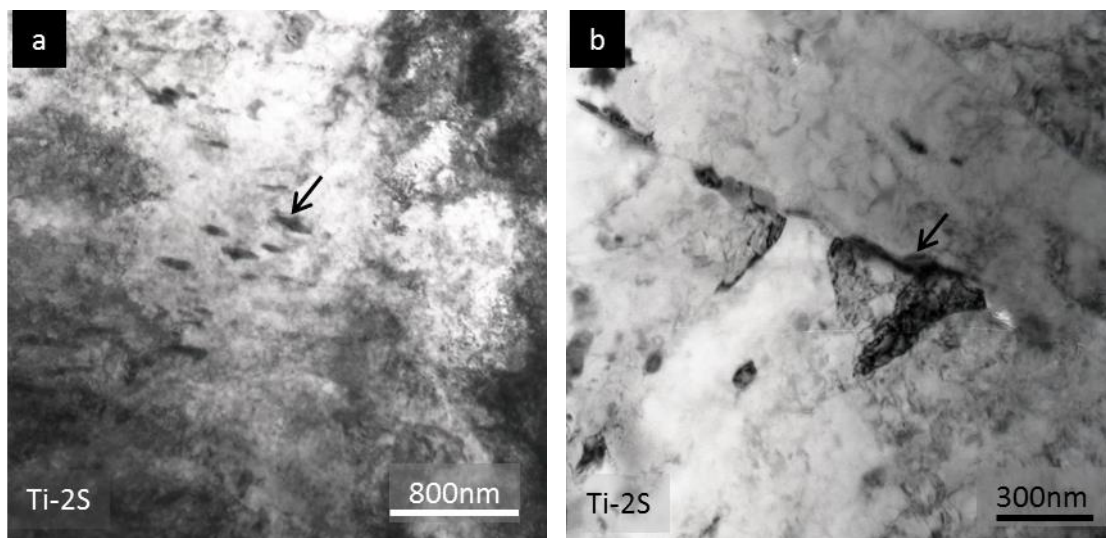


Figure 4.14 – TEM thin foil images for Ti-2S showing a) carbides within a bainite sheaf and b) upper bainite type carbides

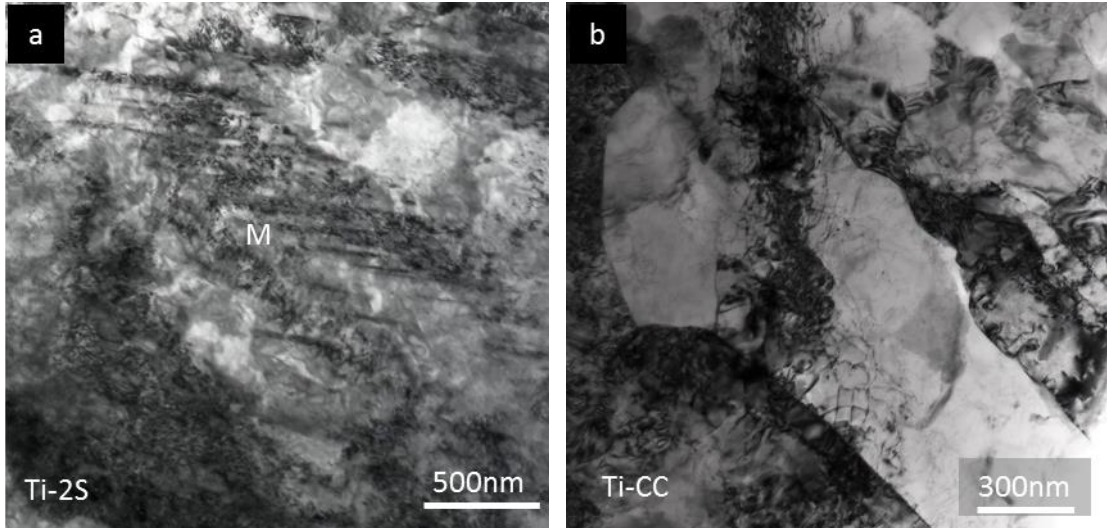


Figure 4.15 – TEM thin foil images showing; a) region of fine martensite in Ti-2S and b) narrow ferrite with occasional precipitates in a bainitic region in Ti-CC

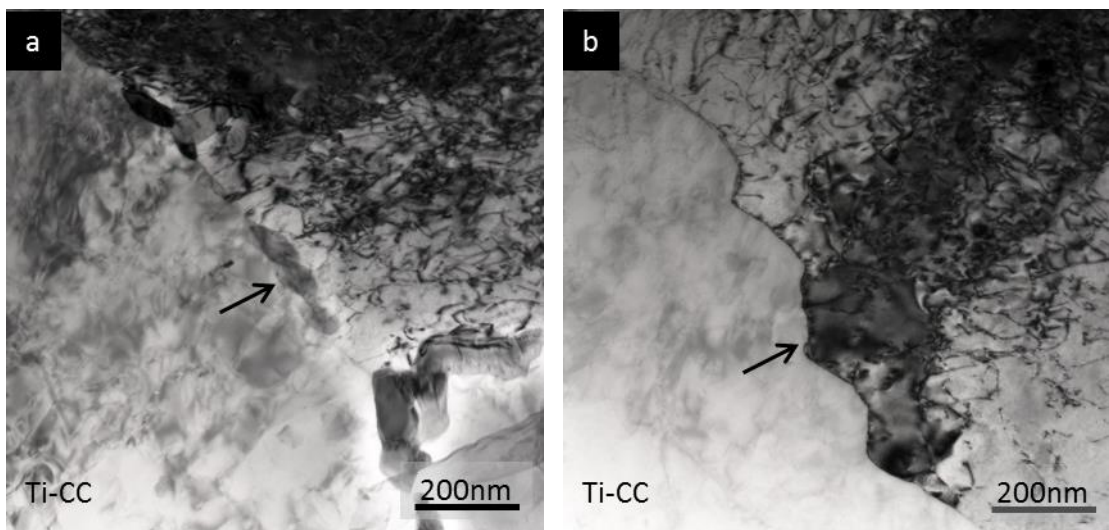


Figure 4.16 – TEM thin foil images for Ti-CC showing a) carbides within the grain boundary and b) irregular grain boundaries

The morphology as well as the size and distribution of the precipitates in Ti-2S and Ti-CC are shown on the TEM carbon extraction replica images in Figure 4.17. Both samples were dominated by regions with very little or no precipitates at all as previously shown through TEM thin foil analysis. However, where precipitates could be found, they were mostly spherical. Ti-2S had coarser precipitates as compared to Ti-CC.

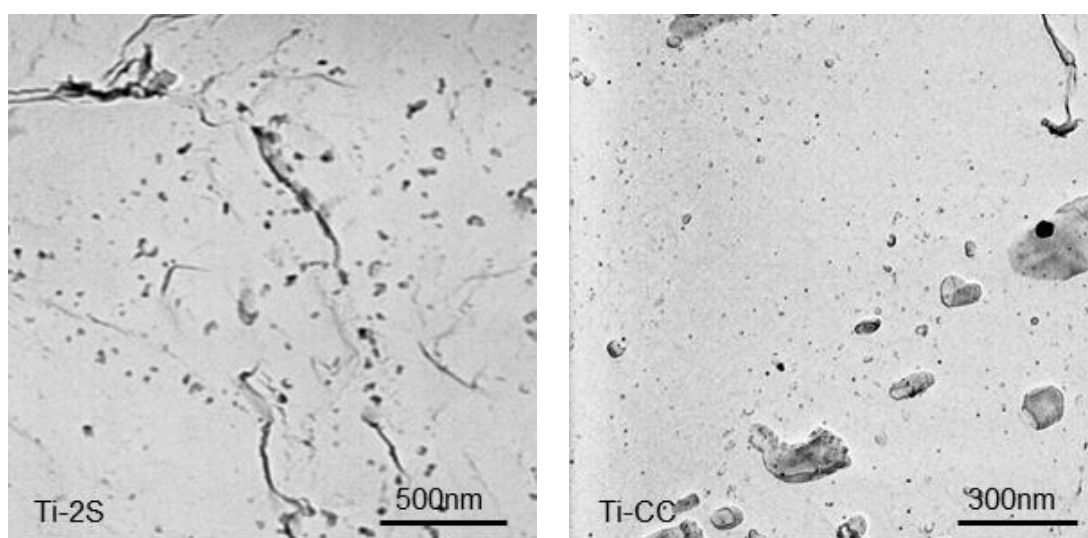


Figure 4.17 – TEM carbon extraction replica images showing random and coarse precipitates in Ti-2S and finer precipitates in Ti-CC

4.6.3 V Microalloyed Samples

Following optical microscopy and SEM examination, the morphology of the different phases within the microstructures for the V alloyed samples were further studied through TEM thin foil analysis. Surprisingly, the features in both V-2S and V-CC were quite similar despite their differences in tensile properties. Some regions were dominated by ferrite while others were dominated by bainite. In some regions, there was a co-existence of both bainite and ferrite. A unique feature found in V-CC and not in V-2S was some odd ferrite morphologies shown in Figure 4.18a. Zuno-Da Silva[155] identified features similar to these as being elongated retained austenite. Though few and far between, pearlitic features were also found within the samples and typical examples are shown in Figure 4.18b and Figure 4.19. Another unexpected feature was the existence of retained austenite shown in Figure 4.20a. The reason why XRD failed to detect it could be due to its low volume fraction.

High dislocation densities were quite common in both bainite and ferrite, as observed in both TiAlMo and Ti samples. Low number densities of precipitates were found scattered throughout the sample, mainly in the ferrite, and these precipitates were quite difficult to image in comparison to TiAlMo. However, a few regions were also found with high precipitate number densities. Irregular grain boundaries shown in Figure 4.20b were quite common in both V-2S and V-CC. However, these were not as distinct as those found in Ti-CC. The existence of such boundaries is clear evidence of the presence of precipitates pinning the grain boundaries, hence, inhibiting grain growth during hot deformation.

Figure 4.21a show an example of a grain boundary that exhibited strong contrast in both V-2S and V-CC. The high contrast suggests that this was not a low angle boundary, but rather a high angle boundary. Grain boundary precipitates and carbides shown in Figure 4.21b and Figure 4.22a respectively were also another common feature within both samples. Unlike TiAlMo, evidence of interphase precipitation could not be established. Figure 4.22b is a typical example of bainite with carbides which was also common in both samples.

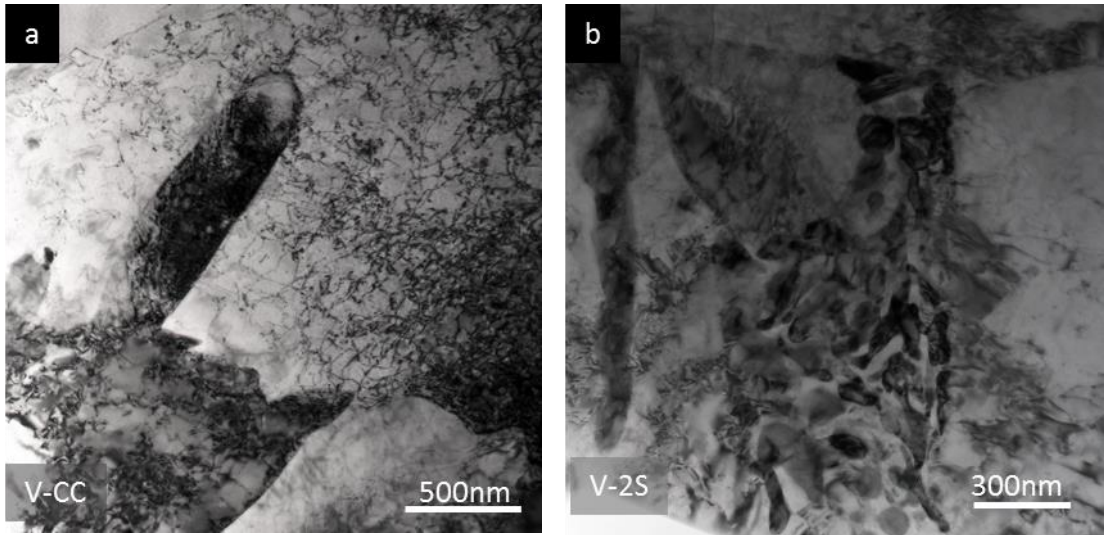


Figure 4.18- TEM thin foil images a) odd morphologies in ferrite for V-CC and b) pearlitic features in V-2S

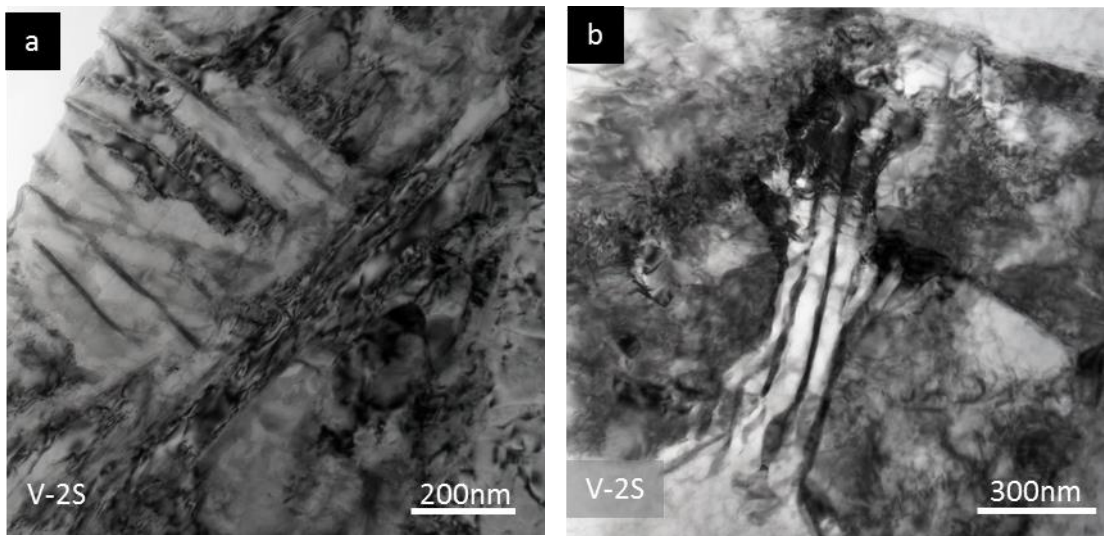


Figure 4.19 - TEM thin foil images showing the presence of pearlite V-2S

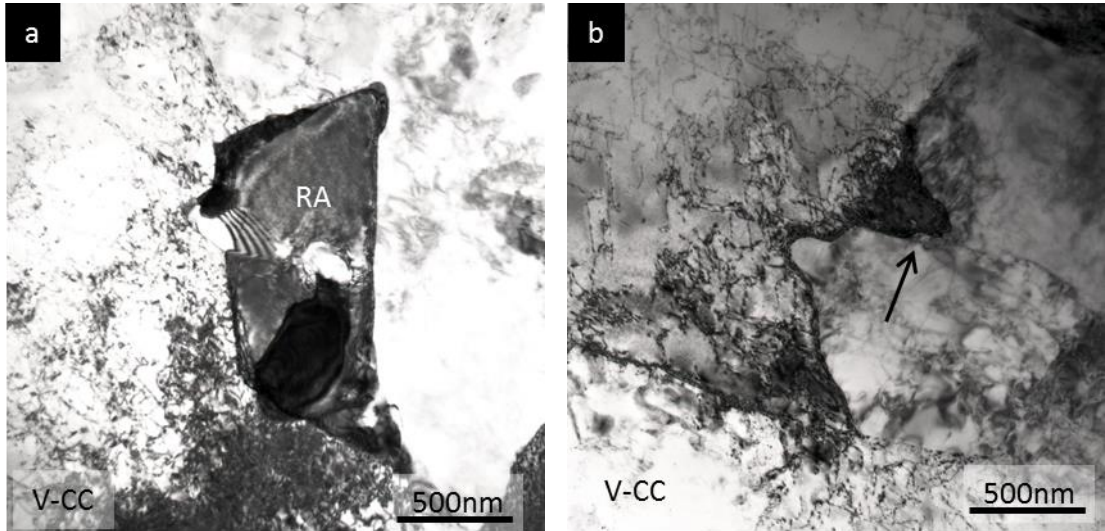


Figure 4.20 – TEM thin foil images for V-CC showing: a) retained austenite and b) curved grain boundaries

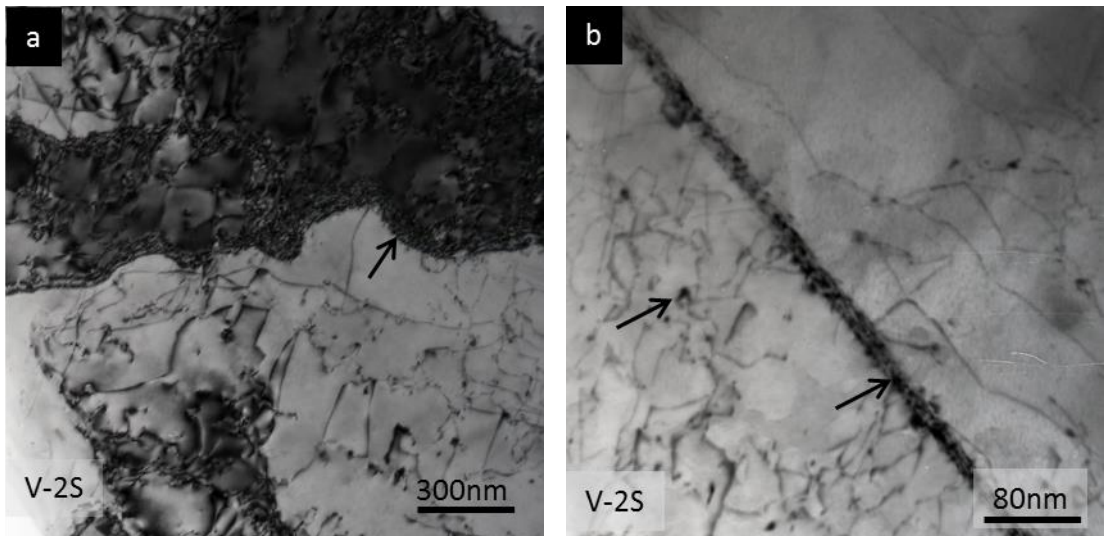


Figure 4.21- TEM thin foil images for V-2S showing: a) high angle grain boundary and b) precipitates in the grain boundary and in ferrite

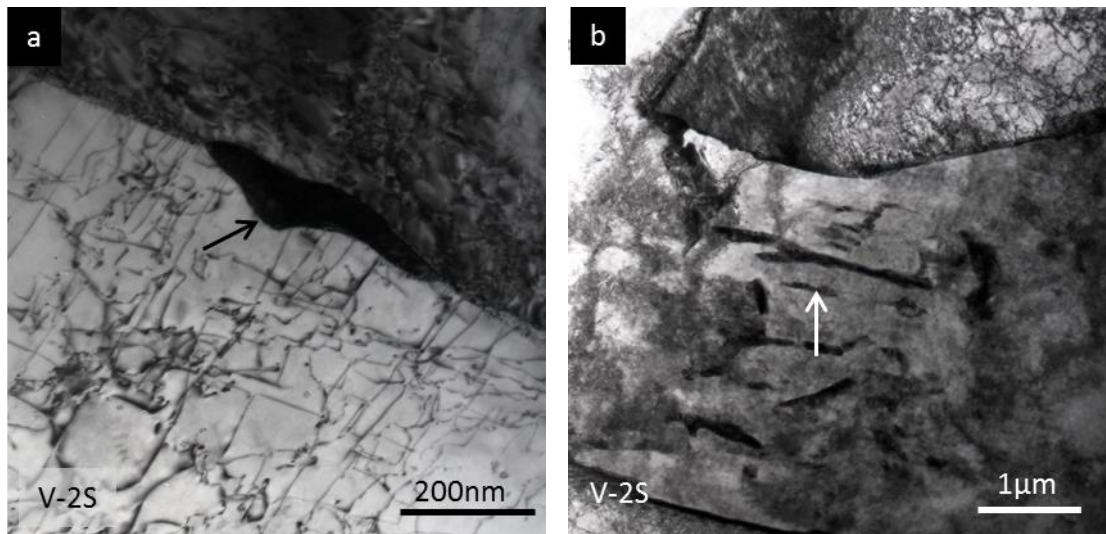


Figure 4.22 TEM thin foil images for V-2S showing: a) carbides in grain boundary and b) bainite with carbides

The TEM carbon extraction replica images for the V alloyed samples are shown in Figure 4.23. Just like the Ti alloyed samples in Figure 4.17, the V alloyed samples had regions with coarse precipitates while other regions had little or no precipitates. Of interest was the observation that most of the precipitates seemed to be clusters of two or three precipitates joined together, the reason of which could not be established. The precipitates in the two step cooled sample V-2S were much coarser as compared to V-CC.

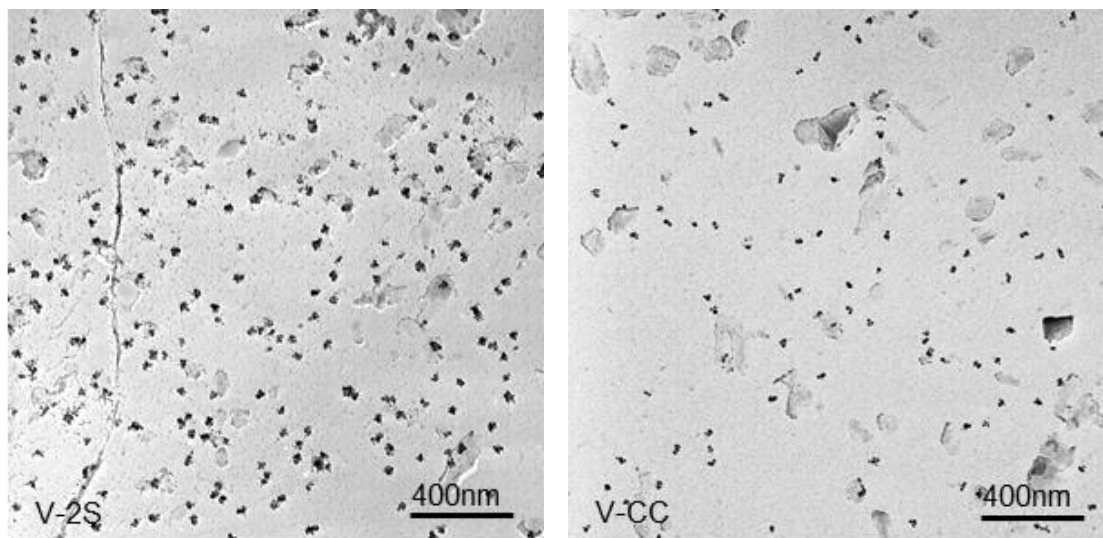


Figure 4.23 – TEM carbon extraction replica images showing regions with random precipitates in V-2S and V-CC

4.7 Summary

Tensile tests carried out on the samples revealed that the best combination of both strength and ductility were found in TiAlMo-2S with UTS of 780MPa and total elongation of 19%. TEM thin foils and SEM analysis showed the microstructure for both the continuously cooled and the two steps cooled TiAlMo samples to consist of a ferrite matrix, some bainite, martensite and retained austenite which is consistent with the good strength and ductility. XRD analysis on the samples revealed 7% retained austenite content in TiAlMo samples as compared to the other samples with none at all. Though not very distinct, there was also some evidence of interphase precipitates in TiAlMo and this was not found in any of the other samples.

The microstructure for the Ti microalloyed samples were predominantly bainite with bainitic carbides. The occasional ferrite grains in both samples had few or no precipitates at all and there was no evidence of interphase precipitation. The highest UTS of 810MPa were obtained in Ti-CC; however, the total elongation was found to be the lowest at 8%.

SEM analysis revealed contrasting microstructures between V-2S and V-CC. The microstructure for V-2S consisted of fully recrystallized ferrite grains with a few islands of martensite located mainly along the grain boundaries. TEM thin foils confirmed the presence of martensite. Occasional retained austenite, though not detected by XRD, was also detected through TEM thin foils. Pearlite was also found in this sample. The large ferrite grains coupled with the presence of pearlite and a few occurrences of retained austenite in this sample could be the reason why a high total elongation was obtained at the expense of the strength. Unlike V-2S, V-CC was predominantly bainitic with few ferrite grains within the microstructure. Coarse precipitates, though few and far between were also found in both samples and there was no evidence of interphase precipitates in either of the samples.

CHAPTER 5 :

TIME/TEMPERATURE/TRANSFORMATION BEHAVIOUR OF A VANADIUM MICROALLOYED STEEL

5.1 Introduction

This chapter presents the results from the V microalloyed strip steels provided by Tata Steel (Ijmuiden). Of the three different chemistries initially investigated and discussed in the previous chapter, the vanadium alloy composition was specifically chosen since it has been well known that interphase precipitation (IP) can be produced in V alloyed steels. Another reason was that V presents itself as a commercially viable and cheaper option as compared to other alloying elements such as Nb and Mo. Even though the TiAlMo composition showed more potential than any of the other compositions, this would not have been a suitable option for Tata Steel since it was also subject to a patent by JFE Steels[13]. The focus was mainly to study the time/temperature/transformation behaviour of the vanadium microalloyed steel paying particular attention to the effects of heat treatment on the microstructure as well as the morphology and composition of the precipitates formed during the different thermal cycles. The chemical composition was 0.09C-1.66Mn-0.3Cr-0.09Si-0.025Ti-0.099V-0.0005B-0.013N and the thermal cycle schedule was shown in the experimental procedure section in table 3.2.

5.2 Tensile Properties

Tensile tests were carried out on the selected samples and Figure 5.1a shows the stress-strain curves for four specimens, selected on the basis of the precipitate counts, presented later in this chapter. Figure 5.1b compares the tensile properties while the results for the selected samples are summarised in Table 5.1.

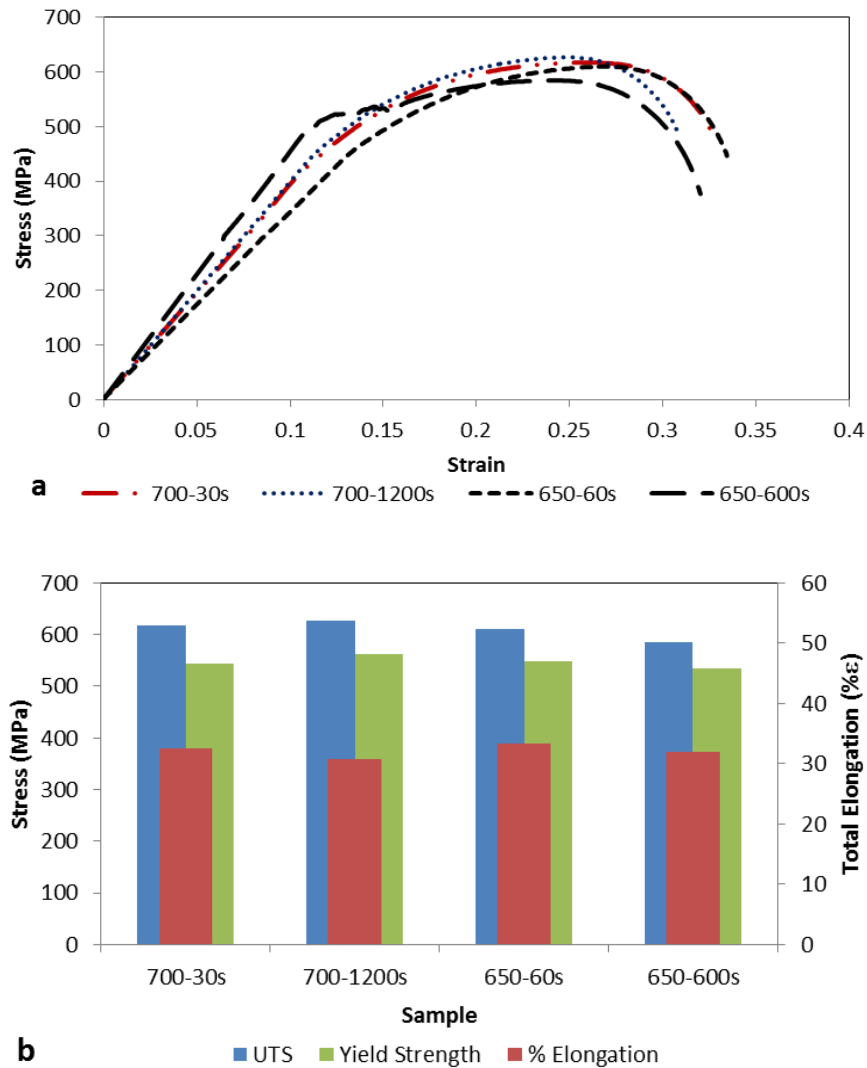


Figure 5.1 – a) Stress-strain curves and b) comparison of mechanical properties

The highest UTS and yield strength were obtained in sample 700-1200s which was transformed at 700°C for 1200s (UTS of 627MPa and YS of 562MPa). The sample transformed at the same temperature of 700°C but for less time of 30s (sample 700-30s) had lower UTS of 618MPa and YS of 534MPa as compared to 700-1200s. However, the total elongation for 700-30s was higher at 32.5% as compared to 700-

1200s with 30.8%. For those transformed at 650°C, the sample transformed for 60s had a higher UTS and YS of 610MPa and 548MPa respectively as compared 650-600s with 585MPa and 533MPa respectively. The total uniform elongation was also higher for 650-60s with 33.4% as compared to 32.0% for 650-600s. The reason why there were so many discrepancies can be explained in terms of microstructural evolution and strengthening mechanisms during thermal cycles. This will be explained later in the chapter after discussing the microstructure and precipitation behaviour during the heat treatments.

5.3 Vickers Hardness

Vickers hardness tests were also carried out along the width of each of the eleven samples at an interval of 0.5mm between the points. Table 5.1 summarises the Vickers hardness as well as tensile tests carried on the samples.

Table 5.1 – Summarised Hardness and Tensile Test Results

Transformation Temp (°C) / Time (s)	Vickers' Hardness (HV10)	Yield Stress (MPa)	Ultimate Tensile Strength (MPa)	% Total Elongation (%ε)
950-Q	280.1 ± 3.3			
950-60Q	280.0 ± 3.8			
950-120Q	279.2 ± 2.5			
750-60s	277.6 ± 2.8			
750-1800s	264.1 ± 3.5			
725-1800s	246.1 ± 9.0			
700-30s	234.0 ± 3.5	543	618	32.5
700-1200s	226.9 ± 3.7	562	627	30.8
650-60s	225.1 ± 1.8	548	610	33.4
650-600s	223.4 ± 4.7	533	585	32.0
625-300s	193.4 ± 1.3			

The Vickers hardness profiles in Figure 5.2 show that the hardness decreased with decreasing transformation temperature (from 950Q to 625-300s). The Vickers hardness was highest in samples that were quenched from the austenising temperature of 950°C. The lowest Vickers hardness was the sample transformed at 625°C for 300s.

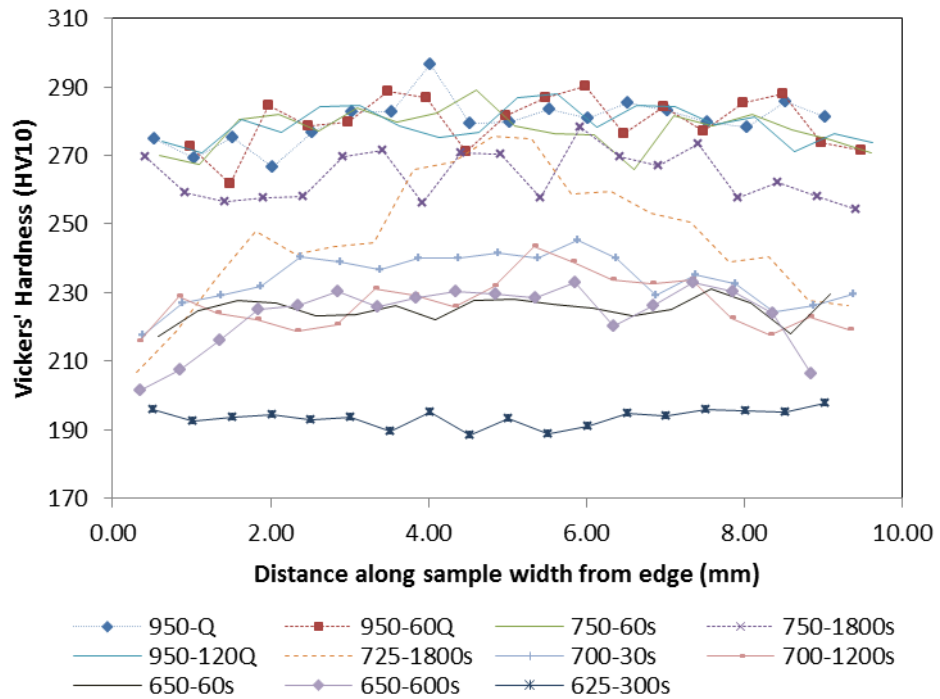


Figure 5.2 – Vickers hardness test profiles for all the samples

5.4 Retained Austenite Content

XRD analysis was performed to check the retained austenite content in all the samples and it was observed that all samples exhibited diffraction peaks corresponding to $\alpha(110)$, $\alpha(220)$, $\alpha(211)$ and $\alpha(220)$; hence, retained austenite (γ) was not detected in any of them.

5.5 The Microstructure - Optical Microscopy and SEM

Optical microscopy was carried out in order to analyse the various phases within the microstructure. However, due to the complexity of the multiphase microstructure, comprehensive SEM was also performed following optical microscopy since optical microscopy could not capture some of the features. The microstructures varied from one sample to the other; however, there was considerable uniformity within regions of the same sample.

Figure 5.3 are optical micrographs while Figure 5.4 are SEM micrographs for 950Q and 950-60Q. Optical microscopy showed a fine microstructure only partially resolved in some areas. The SEM images showed that the microstructures for the two samples were mainly bainite and martensite with few patches of ferrite.

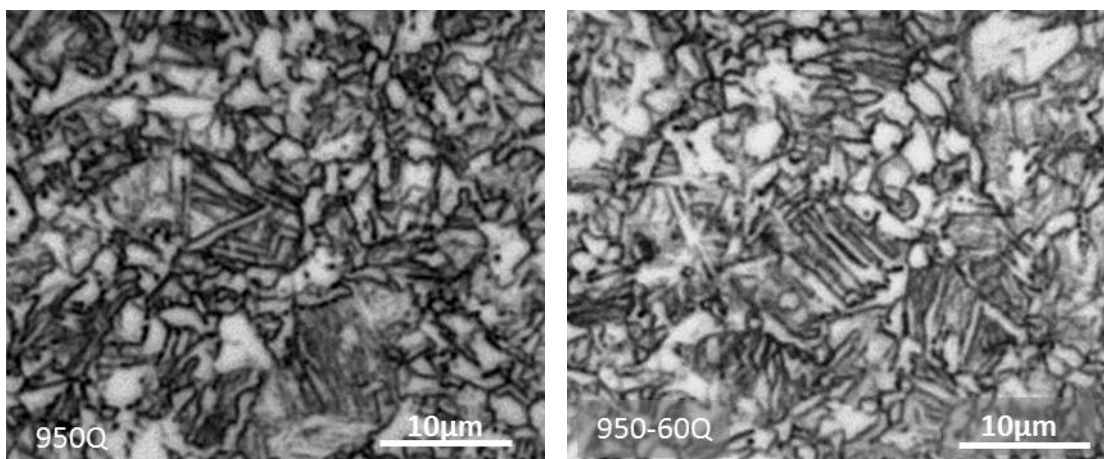


Figure 5.3– Optical microscopy images showing unresolved fine microstructures for 950Q and 950-60Q

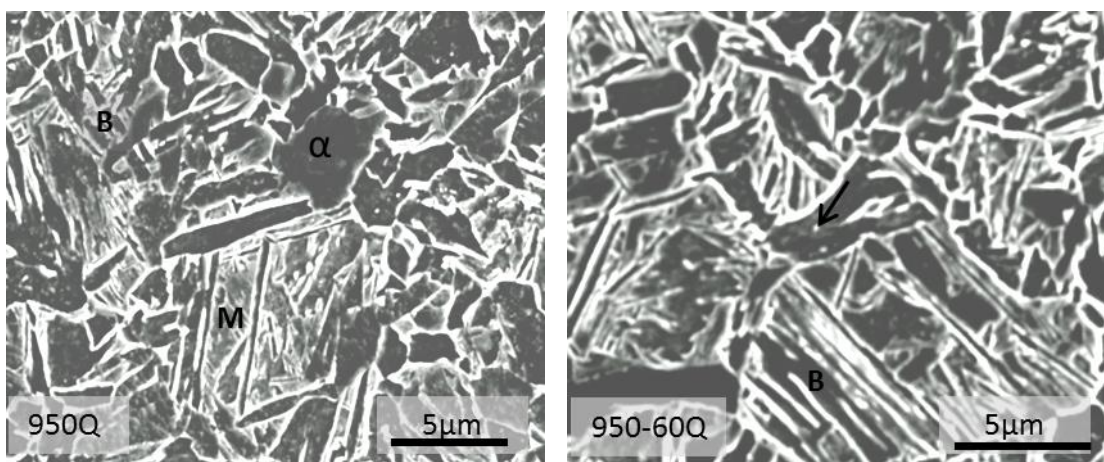


Figure 5.4– SEM images showing predominantly bainitic microstructures for samples 950Q and 950-60Q

Similar microstructures were also observed in 950-120Q and 750-60s as shown on optical micrographs in Figure 5.5 and SEM images in Figure 5.6. In 750-60s (Figure 5.6b), a few ferrite grains can be seen within the microstructure which was composed mainly of upper and lower bainite as well as martensite. These ferrite grains were likely to have developed at the intercritical temperature of 750°C. However, the grains were not fully developed and this might have been due to the shorter transformation time of 60s which might have been inadequate time for more transformation to ferrite to occur.

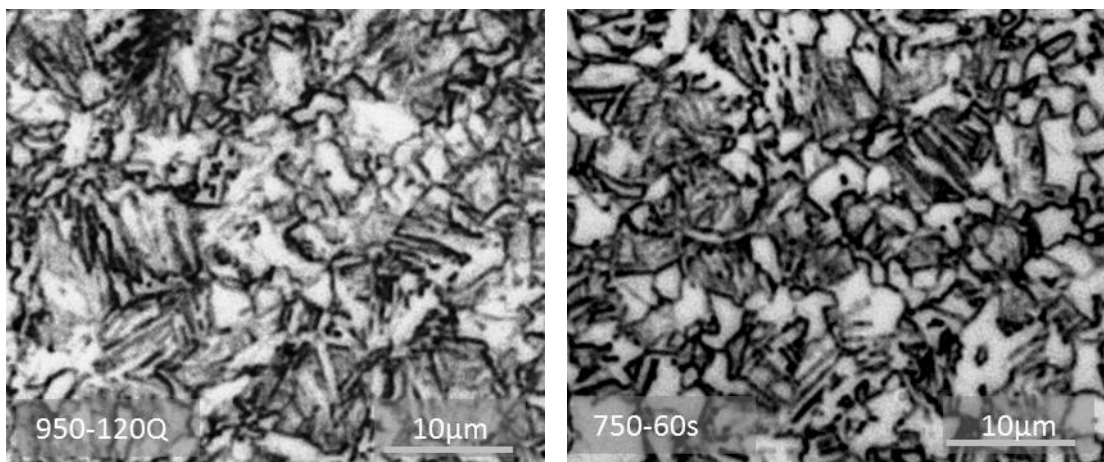


Figure 5.5 – Optical microscopy images for 950-120Q and 750-60s

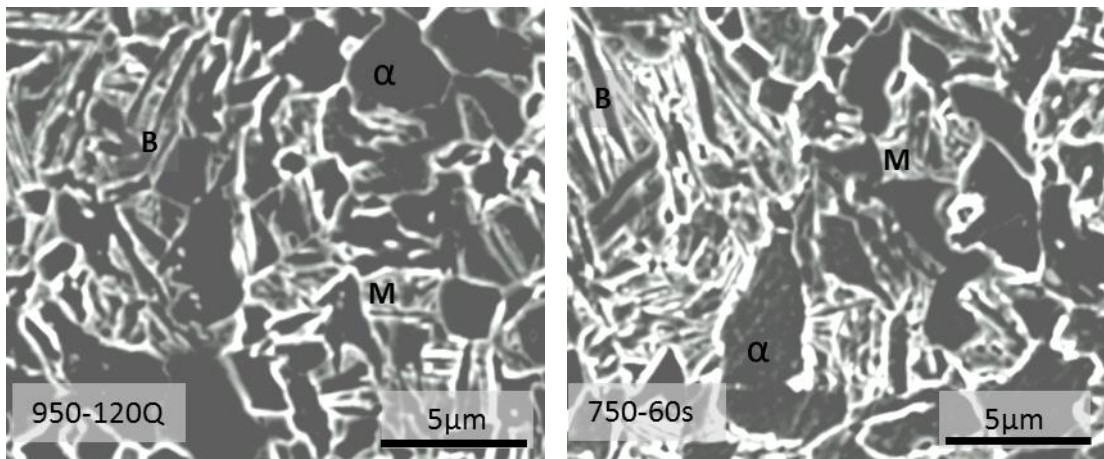


Figure 5.6 – SEM images for 950-120Q and 750-60s showing bainitic microstructures with few martensitic and ferritic regions

Figure 5.7 are optical images while Figure 5.8 are SEM images for 750-1800s and 725-1800s. Even though samples 750-60s and 750-1800s were both transformed at the same temperature, by inspection the volume fraction of ferrite in 750-1800s shown in Figure 5.8 seems higher than in 750-60s. The ferrite grains in 750-1800s

appeared coarser as well. The longer holding time of 1800s in 750-1800s might have provided adequate time for grains to coarsen as compared to 60s holding time in 750-60s.

In contrast, the microstructures for 750-1800s and 725-1800s were quite similar. Both samples consisted of ferrite, bainite and martensite. A few precipitates could be imaged on the SEM images and these were later confirmed through TEM.

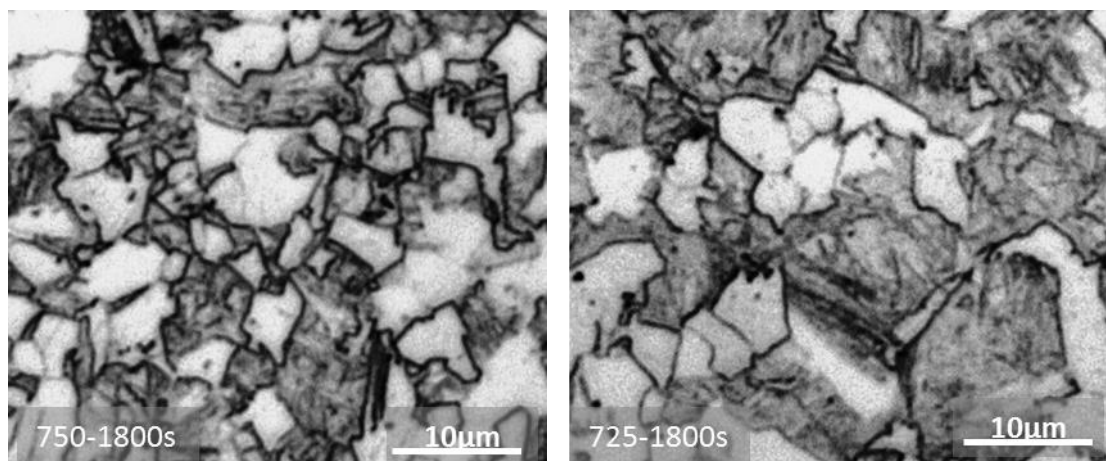


Figure 5.7 – Optical microscopy images for 750-1800s and 725-1800s showing a ferrite matrix with an unresolved second phase

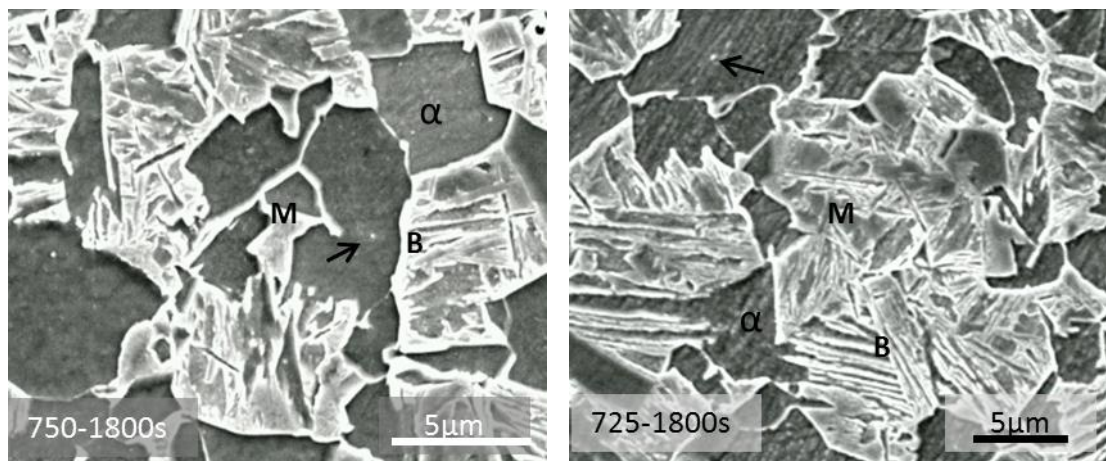


Figure 5.8 – SEM images for V3 750-1800s and 725-1800s showing a mixed ferrite, bainite and martensite microstructure. The arrows in both show possible precipitates

The optical micrographs for 700-30s and 700-1200s are shown in Figure 5.9 while the SEM micrographs are shown in Figure 5.10. 700-30s consisted of a ferrite matrix with bainite and pockets of martensite randomly scattered throughout the sample. The volume fraction of bainite and martensite in 700-30s were much less than in 750-1800s and 725-1800s. However, the 700-1200s sample exhibited a combination

of ferrite and martensite. A few coarse precipitates were also visualised in both samples and these were later confirmed through TEM.

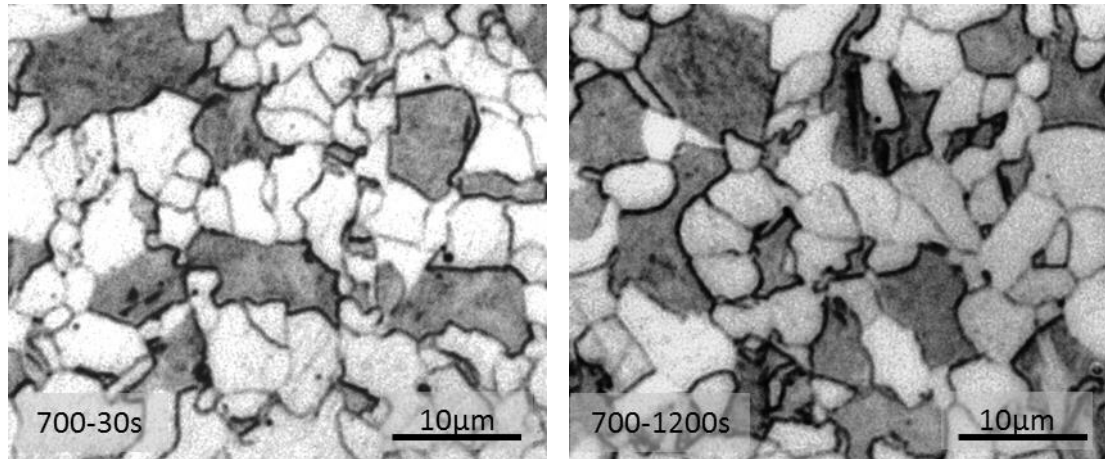


Figure 5.9 – Optical microscopy images for 700-30s and 700-1200s showing a ferrite matrix with an unresolved 2nd phase

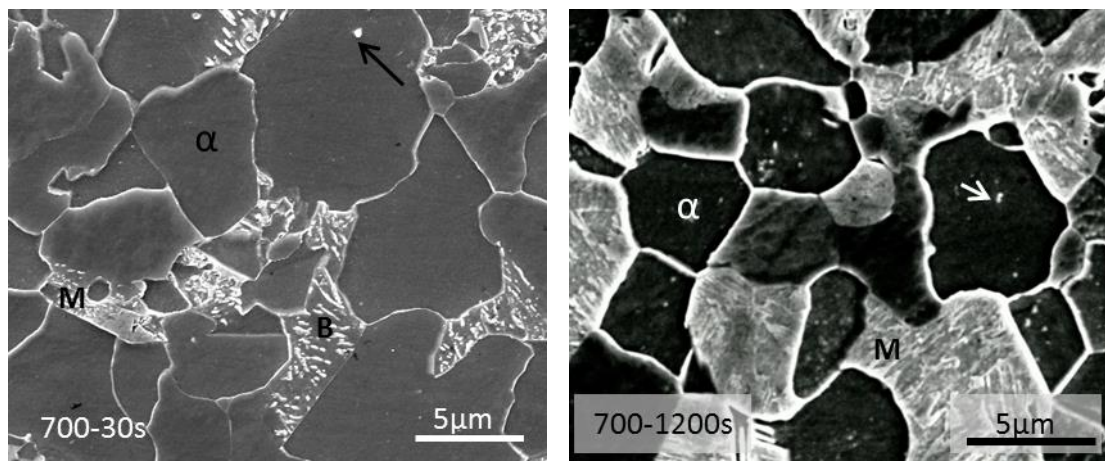


Figure 5.10 – SEM images for 700-30s showing a ferrite matrix with bainite and martensite and 700-1200s showing the ferritic and martensitic microstructure. The arrows in both show possible precipitates

Figure 5.11 are optical micrographs for 650-60s and 650-600s while Figure 5.12 gives the corresponding SEM images. The bimodality of the grains can be seen in both samples. 650-60s was predominantly ferrite, with a few islands of martensite scattered throughout the sample as shown on the optical microscopy image in Figure 5.11a. A better resolution of the phases is shown on the SEM images in Figure 5.12a.

Even though both samples were transformed at the same temperature of 650°C, 650-60s, was composed of a ferrite matrix with a few islands of martensite and while 650-600s was a combination of ferrite, martensite and bainite.

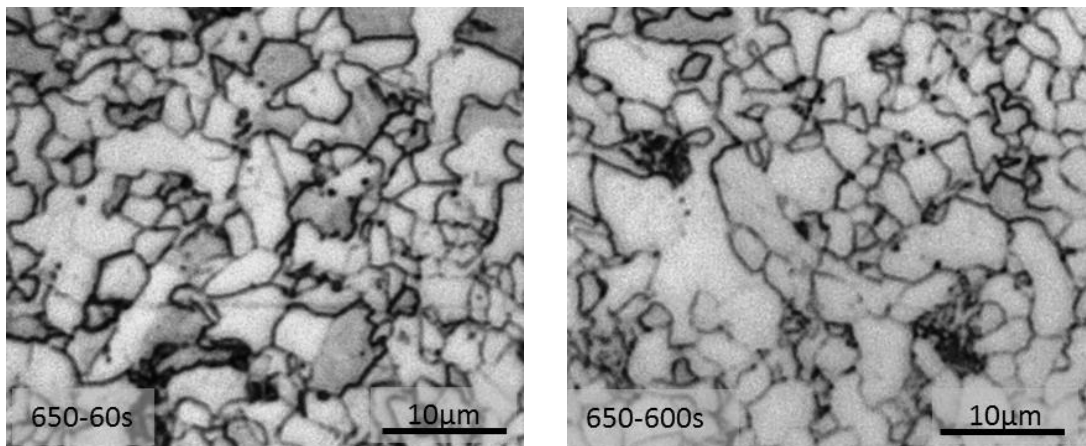


Figure 5.11 – Optical microscopy images for 650 – 60s and 650-600s showing ferrite with an unresolved 2nd phase

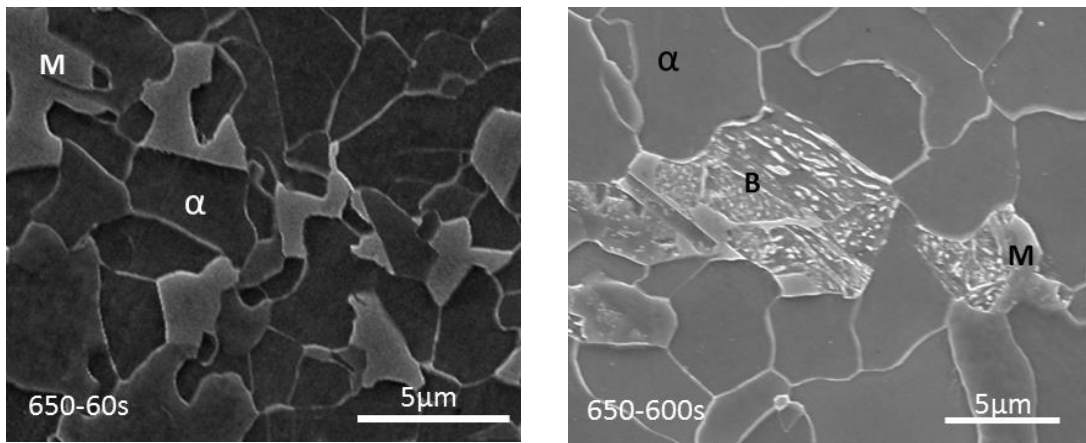


Figure 5.12– SEM images showing ferrite and martensite in 650 – 60s and ferrite, martensite and bainite in 650-600s

Figure 5.13 are optical and SEM images for 625-300s. Unlike all the other samples, occasional pearlite was one feature which was unique about this sample.

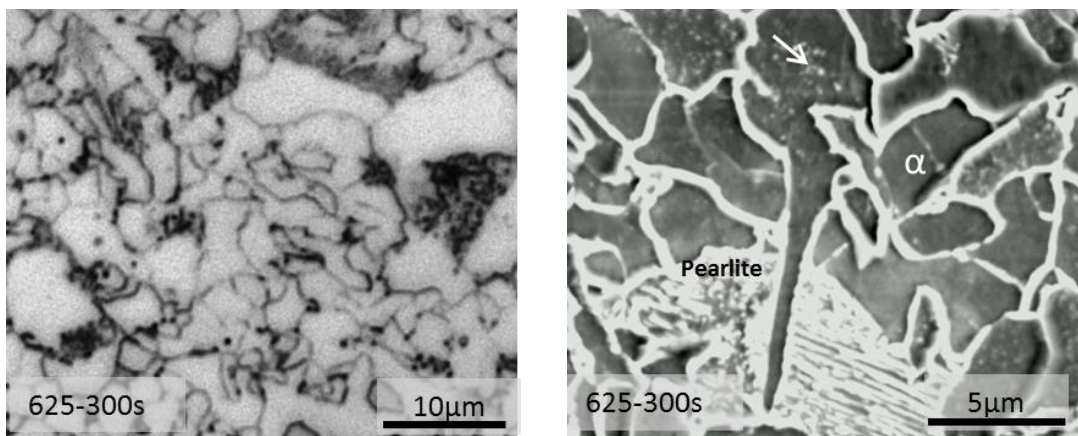


Figure 5.13 – a) Optical microscopy image and b) SEM image for 625-300s pearlite within a ferrite matrix. The arrow shows possible precipitates

5.6 Grain Sizes Measurements

Table 5.2 summarises the main features that were observed from the optical and SEM images. Grain size as well as volume fractions of ferrite in samples that had shown significant grain growth were measured using the linear intercept method and the calculated results were also summarised in the same table.

Table 5.2 – Summary of grain sizes, volume fractions and phases

Thermal Cycle	Phases	Average Grain Size (μm)	Volume Fraction of 2 nd Phase
950-Q	B+M		
950-60Q	B+M		
950-120Q	B+M		
750-60S	B+M		
750-1800S	F+B+M	5.78 ± 0.24	0.50 ± 0.05 (B+M)
725-1800S	F+B+M	4.75 ± 0.19	0.44 ± 0.05 (B+M)
700-30S	F+M+B	3.80 ± 0.16	0.29 ± 0.04 (B+M)
700-1200S	F+M	3.49 ± 0.14	0.36 ± 0.04 (B+M)
650-60S	F+M	2.58 ± 0.08	0.17 ± 0.02 (B+M)
650-600S	F+M+B	2.85 ± 0.13	0.022 ± 0.009 (B+M)
625-300S	F+P	2.69 ± 0.11	0.040 ± 0.009 (P)

It was noted that the volume fraction of ferrite increased with decreasing transformation temperature. At the transformation temperature of 750°C , the proportion of austenite transformed to ferrite in 1800s was 50% which increased to 66% when the temperature was further lowered to 725°C (1800s). At transformation temperatures of 650°C for 600s, the volume fraction of ferrite peaked to 98% as compared to 83% when the temperature was held for 60s.

The grain size decreased with decreasing transformation temperature. When the temperature was maintained at 750°C for 1800s, the average grain size was $5.8\mu\text{m}$ and this decreased to $2.69\mu\text{m}$ when the temperature was lowered to 625°C for 300s. However, the holding time at constant transformation temperature did not seem to have any significant influence on the grain size. For example, at 700°C , almost similar volume fractions of ferrite were observed for the sample with a 30s hold which had 70% α as compared to the sample with 1200s, which had a volume fraction of 64% α . Their average grain sizes were $3.80\mu\text{m}$ and $3.49\mu\text{m}$ respectively.

However, the grain sizes at a lower transformation temperature of 650°C for 60s and 600s led to finer grain size of 2.58 μ m and 2.85 μ m respectively. Apart from the difference in the grain size and the volume fraction of ferrite, the microstructures had a lot of similarities for samples transformed at the same temperature.

5.7 TEM Carbon Extraction Replicas

In order to gain an insight into the size and spatial distribution of the precipitates, TEM extraction replicas were prepared. Bright field TEM images were taken from random areas within the samples. Figure 5.14 to Figure 5.19 are carbon extraction replica images showing the morphology of precipitates common to all the samples. One important observation was that the precipitates were mostly spherical, with much fewer rods and cubes.

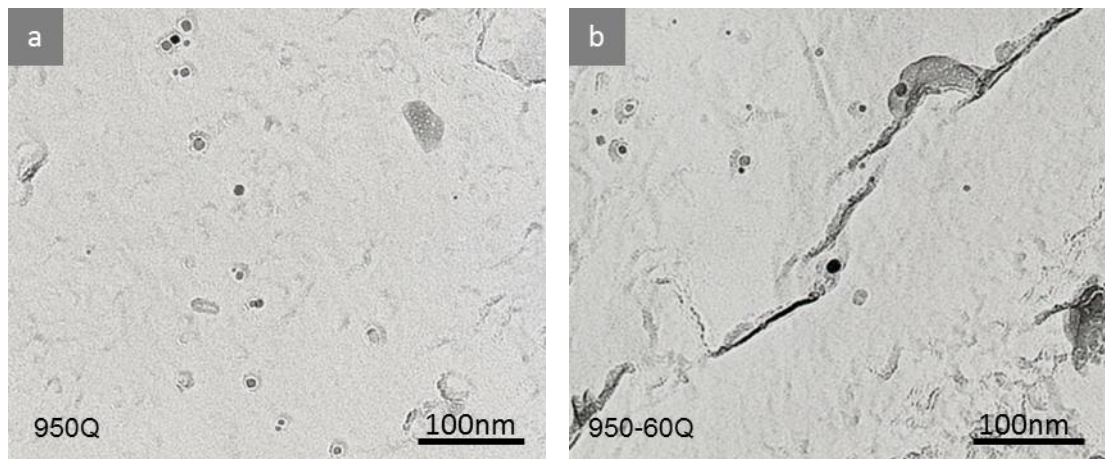


Figure 5.14 – TEM carbon extraction replica images showing lowing precipitate counts in 950Q and 950-60Q

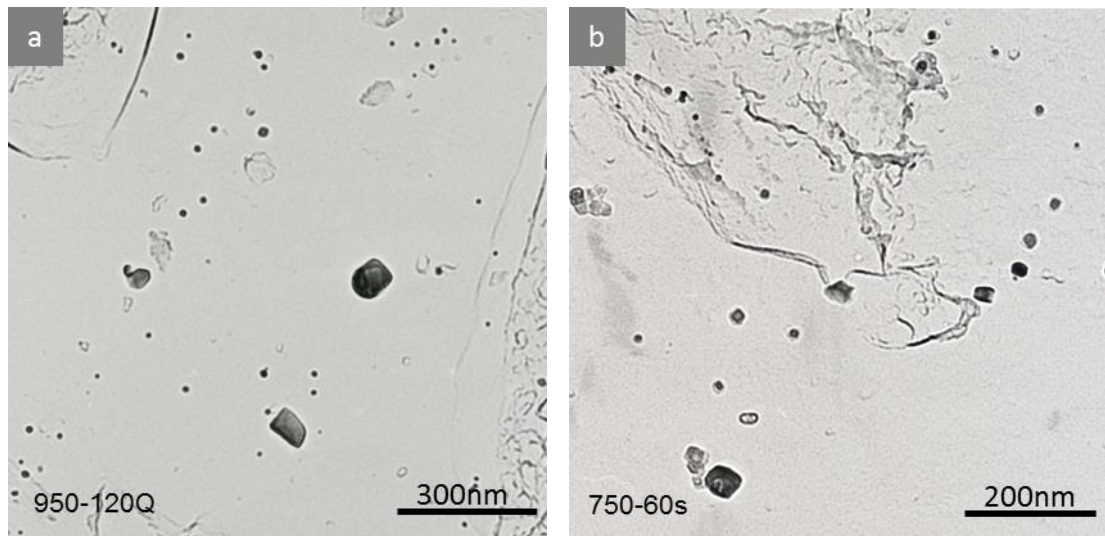


Figure 5.15 - TEM carbon extraction replica images showing some of the precipitates in 950-120Q and 750-60s

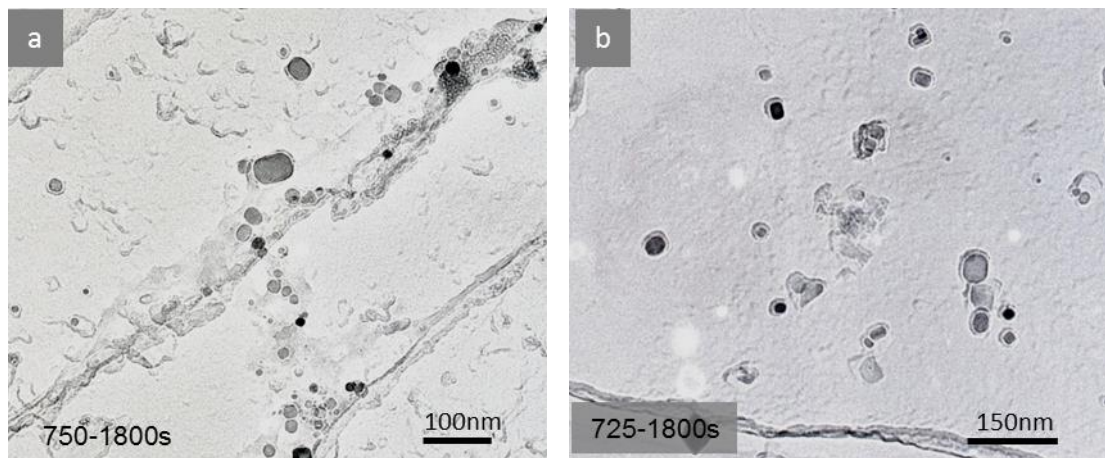


Figure 5.16 - TEM carbon extraction replica images showing some of the precipitates in 750-1800s and 725-1800s

Figure 5.17a shows an ordered array of precipitates, which may be taken as evidence of interphase precipitation. This feature was only found in the sample transformed at 700°C for 30s. The solid arrow in Figure 5.18b shows coarse precipitates that might have been formed in the austenite before transformation to ferrite. The solid arrow shows cube type precipitates while the dotted arrow shows spherical precipitates. Clusters of precipitates as circled in Figure 5.18b were also common in the majority of samples. The solid arrow in Figure 5.19a shows rod type precipitates which, though few and far between, were also a common feature among all the samples examined.

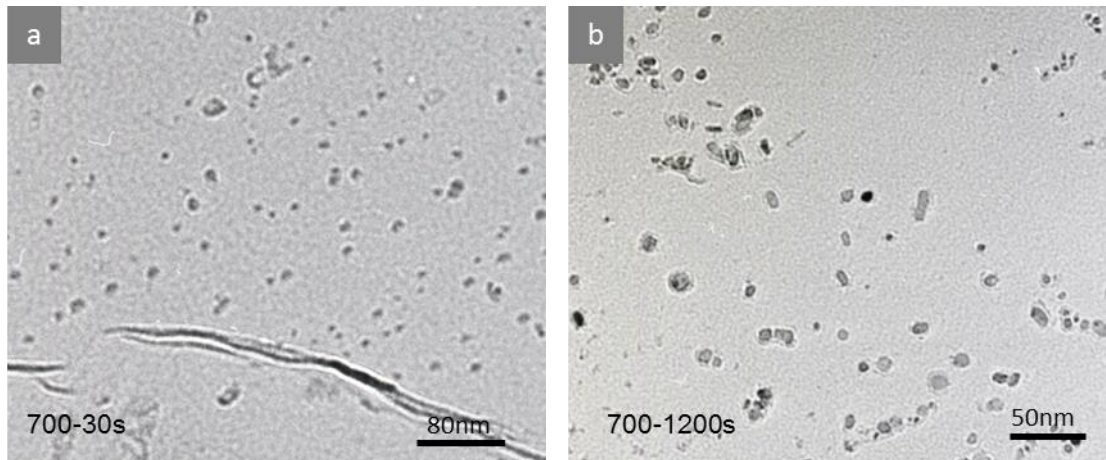


Figure 5.17 – TEM carbon extraction replica images showing a) region with high precipitate density and ordered array of precipitates in 700-30s and b) Region with high precipitate density and random distribution in 700-1200s

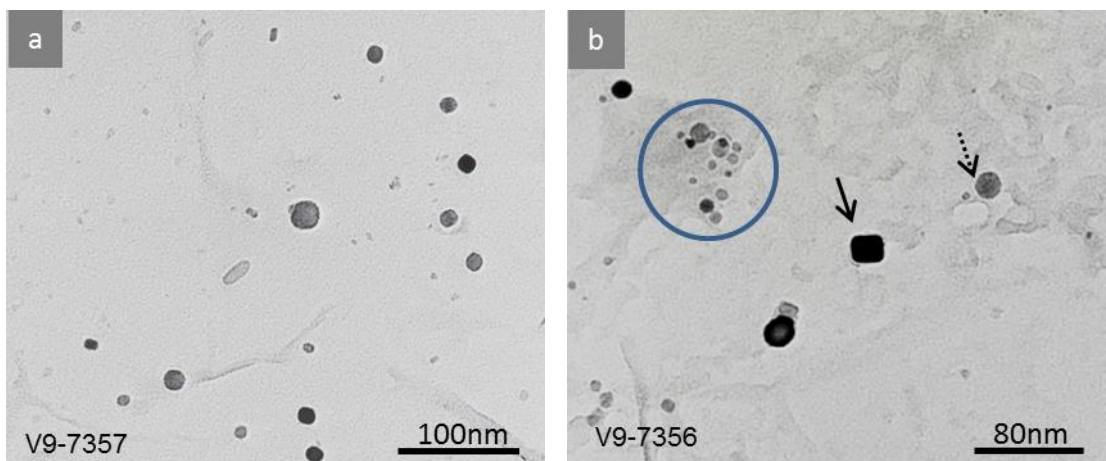


Figure 5.18 – TEM extraction replica images for 650-60s showing a) Random distribution of precipitates and b) circled region with precipitate cluster, dotted arrow pointing at a spherical precipitate and a solid arrow pointing at a cube type precipitate

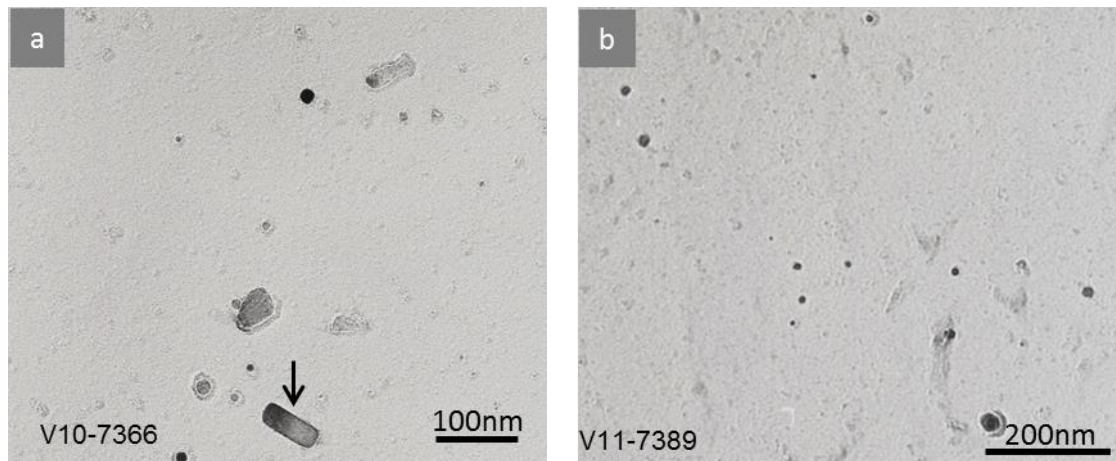


Figure 5.19 – TEM extraction replica images showing regions with low precipitation number densities a) arrow pointing at a rod type precipitate in 650-600s and b) randomly distributed precipitates in 625-300s

5.8 Precipitate Morphology and Chemistry

A detailed analysis of over fifty spherical precipitates per sample using electron energy loss spectroscopy analysis (EELS) revealed that none of them were pure vanadium carbides. Instead, the spherical precipitates which formed the majority were found to be VN and (TiV)N as shown on the energy loss spectra in Figure 5.20a and b. The cube type precipitates though fewer and far between, were also a regular occurrence. Energy loss spectroscopy revealed that they were V(CN), Ti(CN) and TiV(CN) as shown in Figure 5.20 c, d and e. Rod shaped precipitates were also much fewer and their chemical compositions were similar to spherical precipitates. This may be because they might have been the same rod like precipitate, but viewed along the long axis and end-on. However, a minority of them were identified TiV(CN), BC and B(CN) as shown in Figure 5.20e and f. The boron in these precipitates could have been due to possible boron contamination during casting.

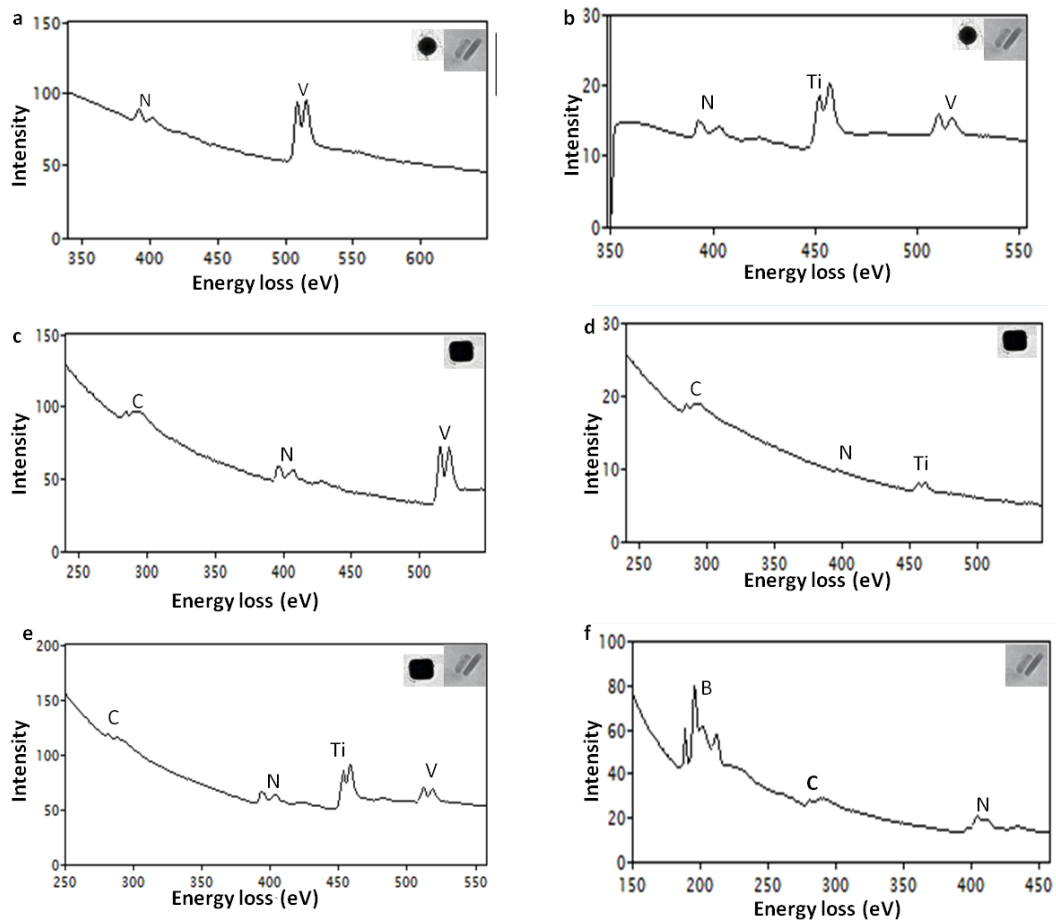


Figure 5.20 – Energy loss spectra (EELS) for the various precipitates analysed

5.9 Precipitate Sizes and Distribution

In order to get an insight into the precipitate sizes and spacial distribution for the various samples, precipitate counts were carried out on extraction replicas images. In most of the cases, ImageJ analysis software was used to count the precipitates; however, in some cases, the software could not distinguish between a local region of dark contrast not arising from a precipitate and the actual precipitates. In such instances, a manual count was also carried out, made easier by the fact that most of the particles were circular. A total of between 800 to 1000 precipitates were counted for each of the samples. The precipitate sizes and distribution curves for the various samples are shown in Figure 5.21 and Figure 5.22. The statistical size distribution analysis revealed that the sizes ranged mainly between 4 and 60nm with occasional particles of sizes above this range (some >100nm).

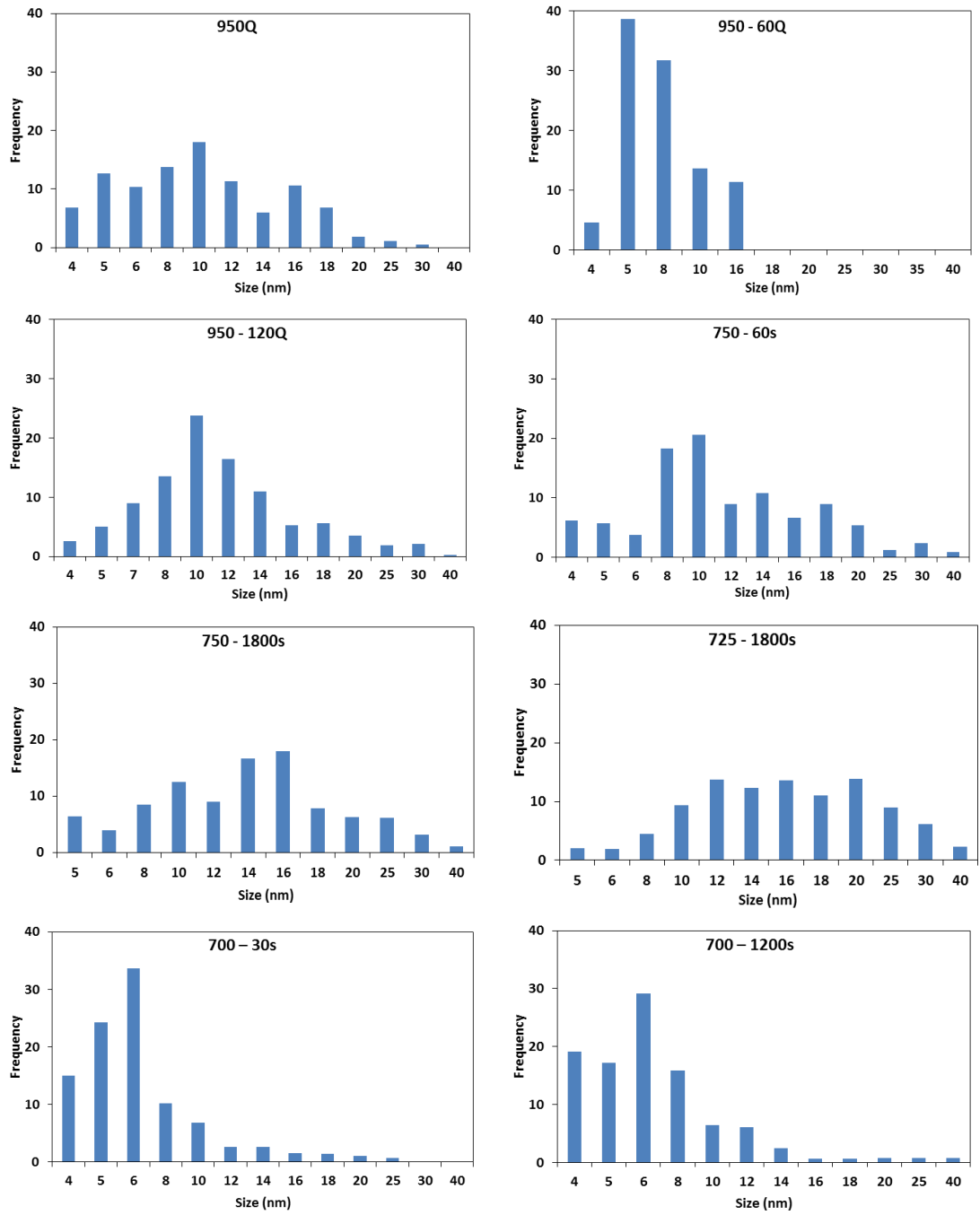


Figure 5.21 – Precipitate sizes and distribution curves for the various samples

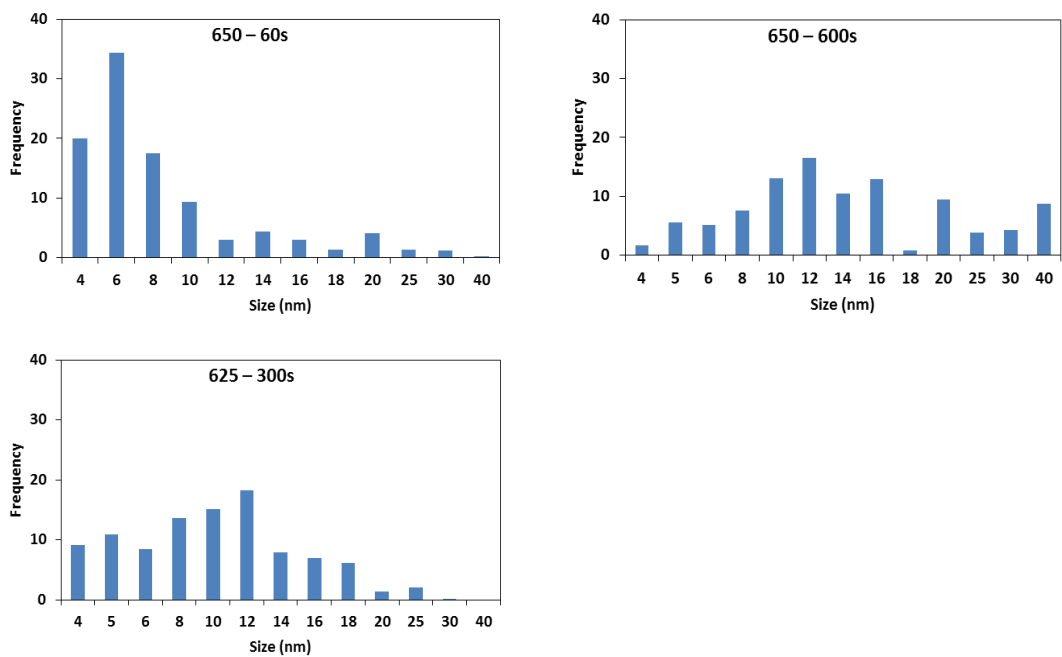


Figure 5.22 – Precipitate Sizes distribution curves (contd) for the various samples

The average precipitate size as well as the precipitate counts were summarised in Table 5.3. The average precipitate sizes are shown in Figure 5.23. It is clear from Table 5.3 that 700-1200s had the highest precipitate number density of 394 particles/ μm^2 . 650-60s and 700-30s were the second best with 174 and 194 particles/ μm^2 respectively. However, the rest of the samples had much lower counts. A good example is 750-1800s, 725-1800s and 625-300s which had the lowest counts of 23, 24 and 33 particles/ μm^2 respectively. For the three samples with the highest precipitate number densities (650-60s, 700-1200s and 700-30s), over 80% of the precipitates had sizes ranging from 4nm to 8nm with 6nm making the highest contribution.

Table 5.3 – Precipitate Summary

Sample	Precipitate Count (per μm^2)	Precipitate Size (nm)
625-300s	33	10.4 ± 1.9
650-600s	56	15.3 ± 1.6
650-60s	174	8.7 ± 0.4
700-1200s	394	14.1 ± 0.5
700-30s	194	6.9 ± 0.3
725-1800s	24	19.5 ± 1.6
750-1800s	23	13.5 ± 1.0
750-60s	50	12.0 ± 0.8
950-120Q	24	12.6 ± 0.4
950-60Q	20	6.0 ± 0.6
950Q	58	8.9 ± 1.0

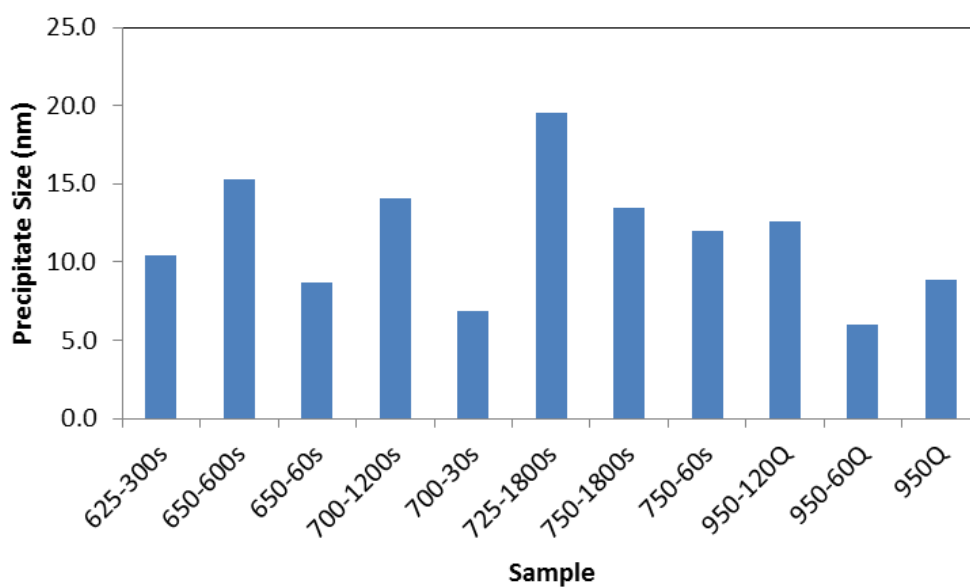


Figure 5.23 – Average precipitate sizes for the various samples

5.10 TEM Thin Foil Analysis

Following precipitate counts on TEM extraction replicas, five samples with the highest precipitation number densities were selected for further TEM thin foil analysis. The samples selected were 650-600s, 650-60s, 700-1200s, 700-30s and 725-1800s. Figure 5.24 to Figure 5.29 shows some of the precipitate morphologies dominating the ferrite in samples selected for TEM thin foil analysis.

Figure 5.24a show a region of high precipitate and dislocation density in 725-1800s while Figure 5.24b shows the random precipitate distribution in the same sample. The high dislocation density and random distribution of precipitates was common to all the samples examined. While 700-30s shown in Figure 5.25a had the same randomness of precipitates as 725-1800s in Figure 5.24b, Figure 5.25b shows a completely different picture; a ferritic region with very few fine precipitates. The arrows in the same image shows very coarse precipitates which were sometimes found in some of the samples.

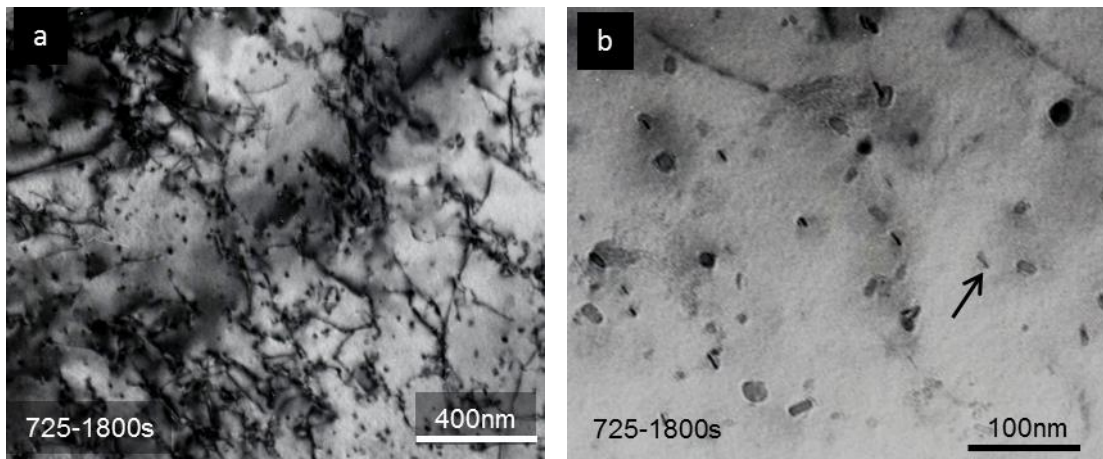


Figure 5.24 – TEM thin foil images for V6 showing a) region with high precipitate number densities and high dislocation density b) region of high precipitate density

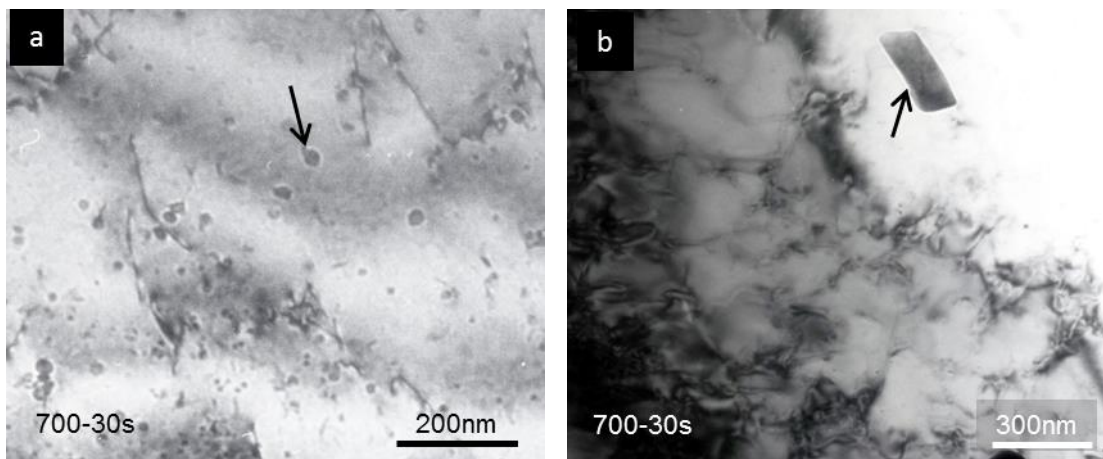


Figure 5.25 – TEM thin foil images for V7 showing a) region of high precipitate density and b) coarse precipitates in ferrite

Figure 5.26a shows an ordered array of precipitates that is likely to have been formed along a twin boundary in the austenite just before transformation to ferrite in 700-1200s. A higher resolution image in Figure 5.26b suggests coherency in some of these precipitates in the same sample. High precipitate density was also quite common in most of the regions in this area as shown on both images. However, there was no evidence of interphase precipitates in this sample. Figure 5.27 are images taken from different regions of the same sample. Figure 5.27a confirms the existence of other precipitate types which were found in all the samples analysed. The arrow shows rod type precipitates within a region dominated by spherical precipitates. Figure 5.27b confirms the existence of regions with high precipitate and dislocation densities in the same sample as previously mentioned.

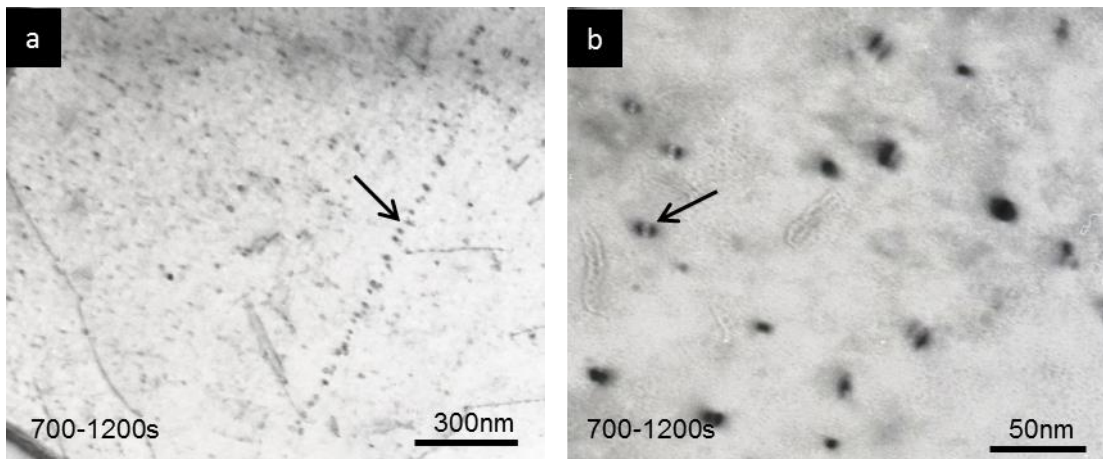


Figure 5.26 – TEM thin foil images for V8 showing a) region with high precipitate number density and arrow showing an ordered array of precipitates b) region with coherent precipitates in ferrite

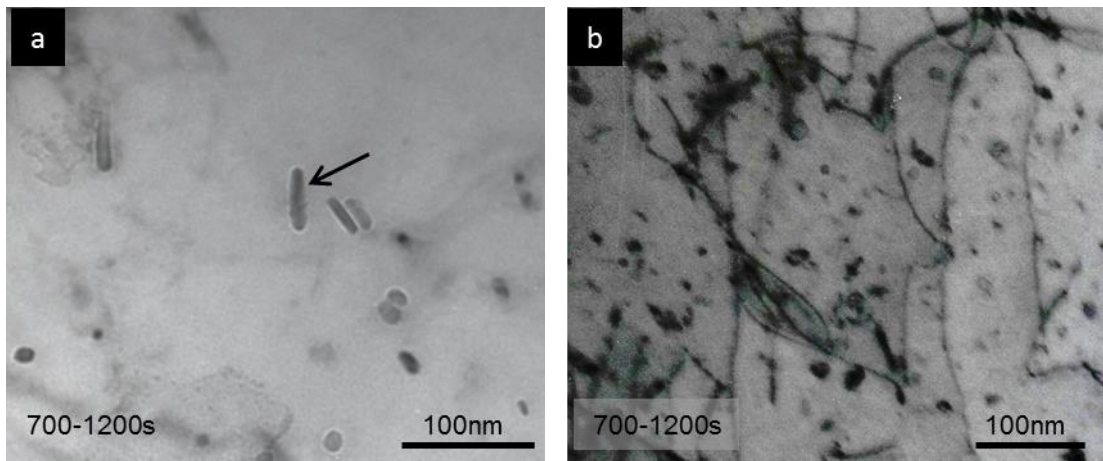


Figure 5.27 - TEM thin foil images for V8 showing a) rod type precipitates b) region with high precipitate and dislocation densities

The images in Figure 5.28 are TEM thin foil images for 650-60s. Just like the other samples, 650-60s had random precipitates scattered throughout the specimens and there was no evidence of interphase precipitates. The arrow in Figure 5.28a points at a typical example of cube type precipitate which were found in all the samples examined. The existence of high dislocation density in this sample is also confirmed on the micrograph in Figure 5.28b.

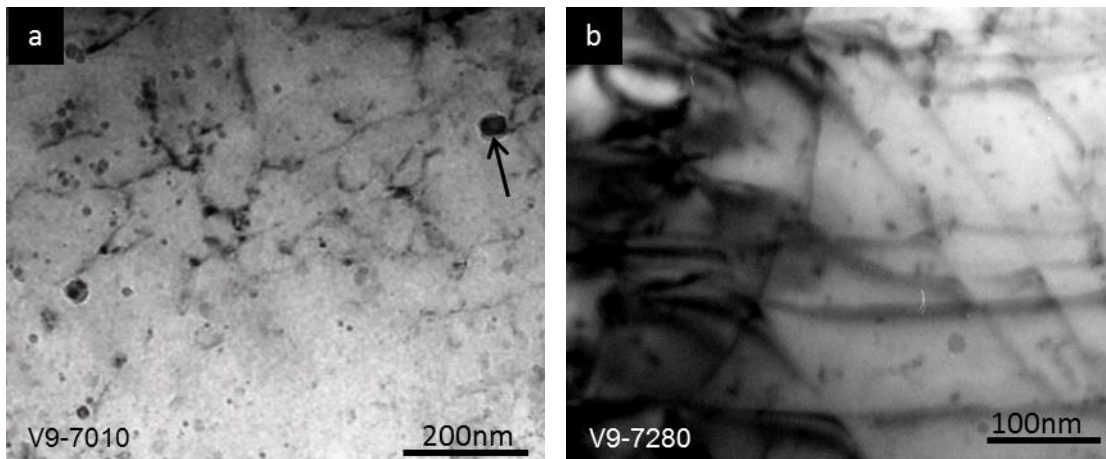


Figure 5.28 - TEM thin foil images for V9 showing a) randomly distributed precipitates and b) region with high precipitate and dislocation densities

Despite the observation that most of the regions in 650-600s had precipitates few and far between, it was interesting to find a region which showed all the positive signs of interphase precipitates. Figure 5.29a shows a region with interphase precipitates in 650-600s while Figure 5.29b shows a region with stringers that seemed to form rows typical of interphase precipitation as well. As previously stated, this was not a common occurrence; in general, the precipitate density was quite low.

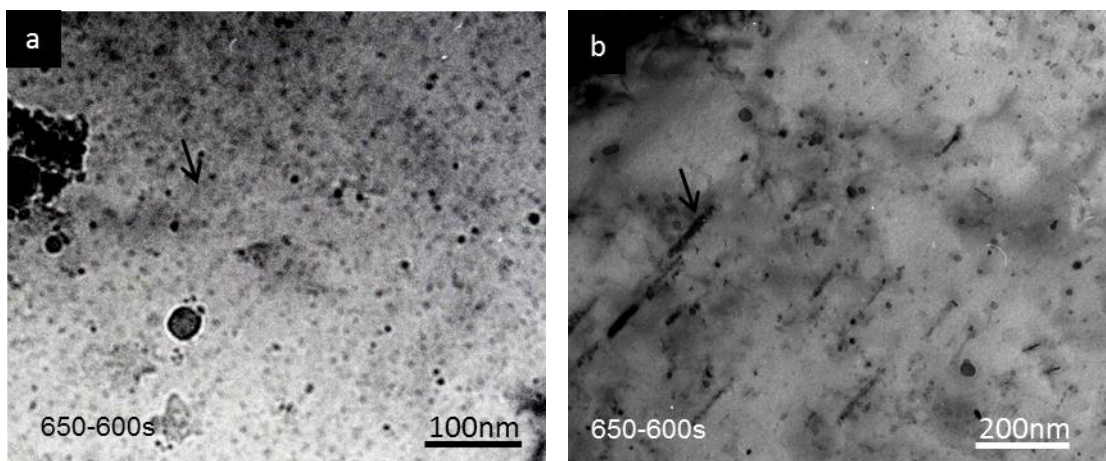


Figure 5.29 - TEM thin foil images for V10 showing a) region with ordered array of precipitates and b) region with high precipitate density

5.11 Summary

Thermal cycles developed during heat treatments plays a major role in the evolution of the final microstructure which in turn affects the mechanical properties of the steel. The microstructures for 950Q, 950-60Q and 950-120Q were mainly bainitic. This was due to the fact that the steels were quenched from the austenising temperature of 950°C to the bainite transformation temperature of 450°C before slow cooling to room temperature. This could be the main reason why all the austenite transformed to bainite and the remainder to martensite.

Ferrite grains started to appear as the temperature holds within the intercritical region were introduced. SEM image analysis showed that the microstructures for all such samples were mainly a ferrite matrix in combination with either martensite, bainite or both. 625-300s was the odd one since it also contained pearlite.

Further TEM analysis showed the existence of high dislocation density within all the samples analysed. The precipitate location and morphology were also revealed through TEM and it was found that they were mostly spherical in combination with a few rod and cube shaped ones. As expected, higher precipitate counts were also in some of the samples with thermal cycles that included the temperature hold. It was noted that 700-1200s had the highest precipitate count with an average of 394 particles / μm^2 . 700-30s and 650-60s had 174 and 194 particles / μm^2 respectively. More than 80% of the precipitates were below 8nm in all the samples that had high precipitate number densities. EDX and EELS analysis revealed that the precipitates were mainly VC and VCN with a few others being TiV(CN). One important observation was the non-existence of IP in any of the samples apart from one isolated incident in 650-600s.

700-1200s was also found to have the highest YS and UTS of 562MPa and 627MPa respectively. Its total elongation was 30.8% which was within the range obtained from the other samples. The highest total elongation was 33.4% in 650-60s. Hardness profiles carried out on the samples also showed that the hardness decreased with decreasing transformation. The sample with the lowest hardness was found to be 625-300 and this might have been due to the presence of pearlite scattered

throughout the sample. Since all the samples had the same chemical composition, the thermal cycles definitely had effects on the mechanical properties.

CHAPTER 6:

FERRITIC V-Nb-Mo MICROALLOYED STEELS STRENGTHENED BY NANOPRECIPITATES

6.1 Introduction

This chapter presents the results from steels microalloyed with vanadium, niobium and molybdenum. The samples were produced by Tata Steel (IJmuiden) and the chemical compositions were presented in table 2.3.

The aim was to produce a steel alloy with the microstructure composed mainly of ferrite and strengthened by nano-precipitates. This would take advantage of the ductility brought about by the ferrite while also taking advantage of the strength brought about by the nanoprecipitates and fine ferrite grain size. The major strengthening mechanisms contributing to the overall strength of the steel in this instance would be grain refinement, solid solution and precipitation strengthening.

6.2 Tensile Properties

Mechanical testing of all the samples was carried out by Tata Steel (IJmuiden). The tensile properties were tabulated in Table 6.1.

Table 6.1 – Mechanical test results courtesy of Tata Steel (IJmuiden)

Sample	Measured Results		
	Yield Strength [MPa]	UTS [MPa]	Total Elongation [% ϵ]
01-630 Nb ⁺ VMo	685	748	21.3
02-630 Nb ⁺ VMo	890	971	18.9
06-600 Nb ⁺ VMo	925	1023	16.8
07-630NbVMo	651	719	19.4
10-630Nb ⁺ VMo	902	964	18.2
14-650Nb ⁺ VMo	804	884	18.8
15-650TiMo	680	745	21.1
16-650Ti	555	634	22.2
17-650VMo	630	712	18.2
18-650V	537	624	20.4
19-650NbMo	572	625	25.4
20-650Nb	510	560	25.2
21-650TiMo	932	996	17.0
22-630 N ⁺	782	824	19.4

Figure 6.1 compares tensile properties from Table 6.1. Sample 02-630Nb⁺VMo had a high total elongation of 18.9% and high YS and UTS of 890 and 971MPa respectively while sample 10-630Nb⁺VMo had equally impressive properties with total elongations of 18.2% and YS and UTS of 902 and 964MPa respectively. The same could be said for samples 06-600Nb⁺VMo, 14-650Nb⁺VMo and 21-650TiMo even though their total elongations were slightly lower than 02-630Nb⁺VMo and 10-630Nb⁺VMo. Samples 06-600Nb⁺VMo had a uniform elongation of 16.8 with high YS of 925MPa and the highest UTS 1023MPa as compared to all the others. The highest total elongation of 25.4% and 25.2% were obtained in 19-650NbMo and 20-650Nb respectively. However, these two samples also exhibited the lowest YS and UTS.

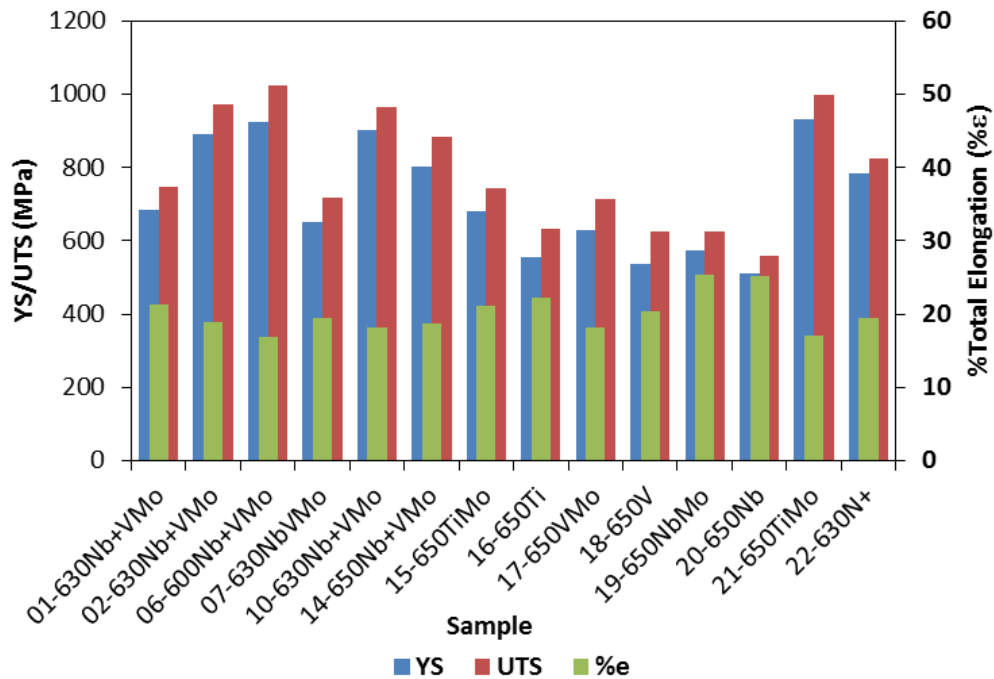


Figure 6.1 – Summarised Tensile test results for the ferritic steels supplied by Tata Steels

6.3 The Microstructure

In order to understand the microstructure of the microalloyed steels, SEM was carried out on all the samples. 5% Nital solution was used to etch the samples prior to SEM analysis. Optical microscopy was not carried out at this stage since it had failed to resolve some of the phases in samples in the previous chapters.

Recently, electron backscatter diffraction (EBSD) has become one of the most powerful scanning electron microscopy (SEM) techniques which utilizes diffraction patterns from the bulk sample to generate valuable data such as crystallographic texture analysis, microstructure analysis, grain boundary and phase quantification etc[156-158]. As a result, EBSD was performed at Tata Steel and the results were also reported in this chapter. Microstructural examinations were also performed through EBSD and the results compared to those obtained through SEM.

SEM images in this chapter were taken using the FEI Inspect F SEM operating between 10 and 20kV and using spot sizes ranging from 2 to 3. SEM analysis clearly revealed the microstructure of the various steels and was also helpful in the estimation of the grain size distributions. EBSD orientation maps provided a clear picture of the grain orientation for the various samples. Grain boundary

characterisation was carried out in order to get an insight into the grain boundary misorientation distributions as well as grain size analysis. Low angle boundaries were shown in blue and they were defined as having angles between 5 and 15°. High angle boundaries were depicted in red and the misorientation angle were defined as those above 15°. The grain size data obtained were used to enable a useful comparison with grain size measurements taken from SEM images.

Figure 6.2a shows a SEM image for 01-630Nb⁺VMo. The existence of some slightly elongated grains was observed and they resembled grains formed when steel is cold rolled. The EBSD maps in Figure 6.3a also confirmed their existence. Occasional pearlite, shown on the SEM image, was also observed randomly scattered throughout the sample. Features that looked like precipitate clusters were a common occurrence. The bimodality of the grains was clearly discernible on the SEM images and this was also confirmed through EBSD (see misorientation map in Figure 6.3b). However, the bimodality is not very clear in Figure 6.3a. Sub grain boundaries, not detected by SEM, but detected through EBSD might have existed in some of the coarse grain, indicating that some of the coarse grains might have been bainitic ferrite. The randomness of the crystal orientation in Figure 6.3a indicates that there was no preferred crystal orientation within the microstructure.

Figure 6.2b shows the grain boundary misorientation distribution for sample 01-630Nb⁺VMo. It is clear from Figure 6.3b that most of the boundaries were high angle grain boundaries. 87% of them were high angle grain boundaries compared to approximately 13% low angle boundaries. This is also in agreement with the SEM images in Figure 6.2a, which showed equiaxed grains. This formed positive confirmation that the microstructure was composed mainly of equiaxed grains.

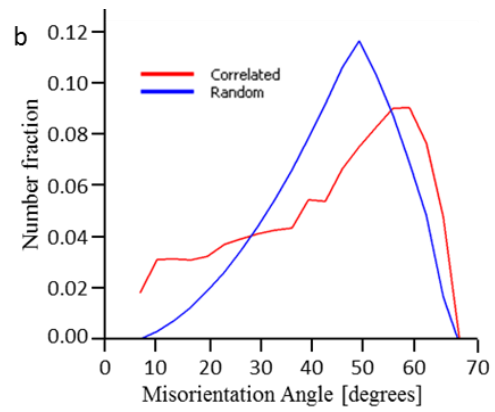
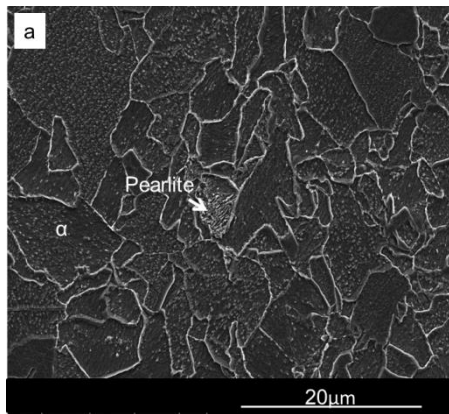


Figure 6.2 – a) SEM images showing the microstructures of samples 01-630Nb⁺VMo and b) grain boundary misorientation distribution for the same sample.

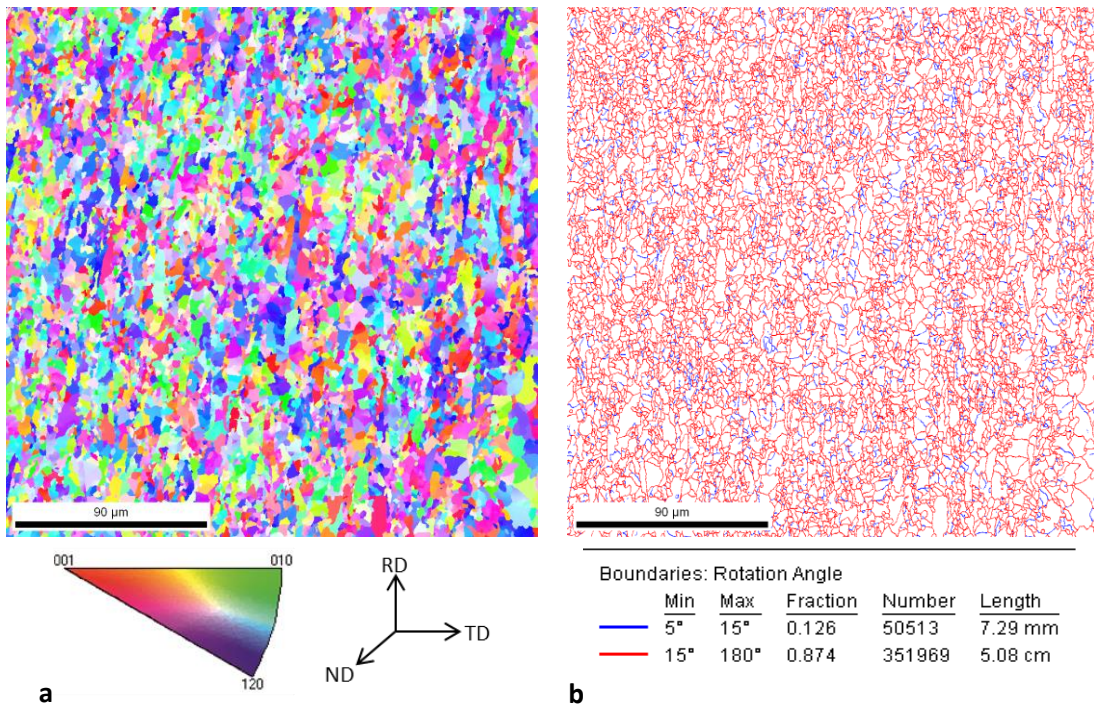


Figure 6.3 – EBSD maps for 01-630Nb⁺VMo showing a) texture of the grains and b) low angle boundaries in blue and high angle boundaries in red

The SEM image in Figure 6.4a shows the microstructure for sample 02-630Nb⁺VMo. Note that this sample was also coiled at 630°C just like 01-630Nb⁺VMo; the main difference between the two being the V and Mo content which were doubled in 02-630Nb⁺VMo as compared to 01-630Nb⁺VMo. Despite this difference in chemical composition, SEM showed similar microstructures with equiaxed ferrite dominating. The major difference between the two was the slightly elongated grain structure in 01-630Nb⁺VMo, which was not observed in the other. The few patches of pearlite shown in Figure 6.4a were also found randomly distributed throughout the microstructure. Features that looked like precipitates, though fewer than in 01-630Nb⁺VMo, were also quite common. The bimodality of the grains was quite evident in the SEM images and these were also confirmed by the misorientation map in Figure 6.5b. It was also evident that the bimodality was more pronounced in 02-630Nb⁺VMo as compared to 01-630Nb⁺VMo.

Figure 6.4b shows grain boundary misorientation distribution for 02-630Nb⁺VMo. The misorientations map in Figure 6.5a shows that 88% of the grain boundaries were high angle while 12% were low angle. These figures compare well with 01-630Nb⁺VMo. SEM also showed that the majority of the grains were equiaxed. The random orientation which was characteristic of 01-630Nb⁺VMo was also confirmed by the EBSD map in Figure 6.5a.

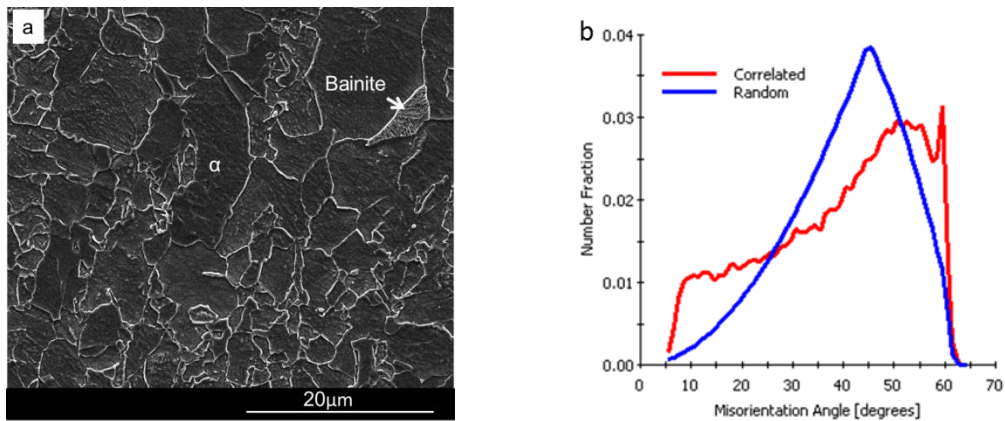


Figure 6.4 – a) SEM images showing the microstructures of samples 02-630Nb⁺VMo and b) grain boundary misorientation distribution for the same sample.

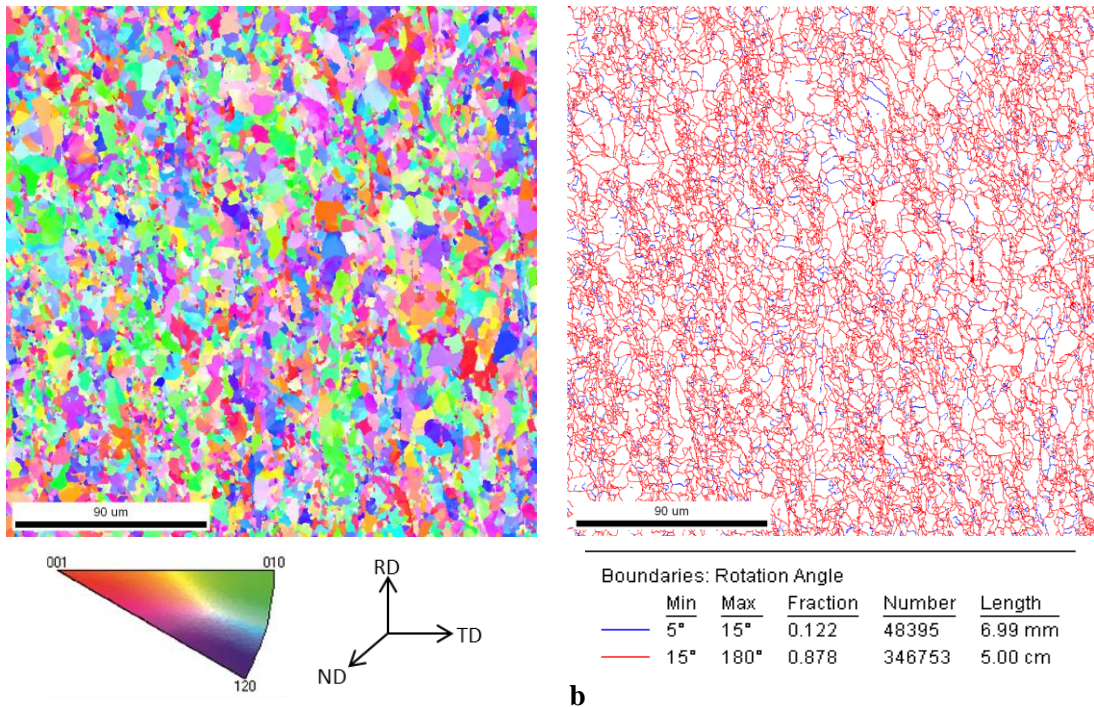


Figure 6.5 – EBSD maps for 02-630Nb⁺VMo showing a) texture of the grains and b) low angle boundaries in blue and high angle boundaries in red

The microstructure for 06-600Nb⁺VMo is shown on the SEM image in Figure 6.6a. Once again, this sample was quite similar in microstructure to 01-630Nb⁺VMo and 02-630Nb⁺VMo. Sparsely distributed pearlite was a common feature while equiaxed polygonal ferrite dominated the sample. A bimodal distribution of grains was observed on SEM images in Figure 6.6. EBSD and grain boundary misorientation distribution maps in Figure 6.7 also confirmed these.

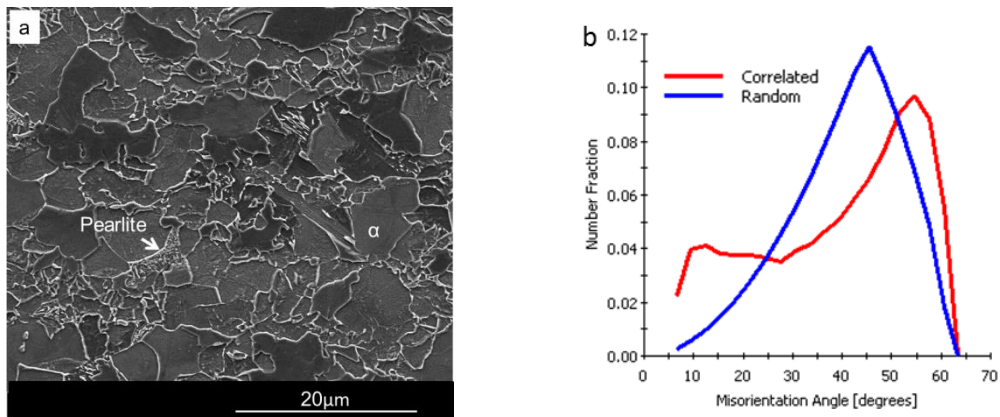


Figure 6.6 - a) SEM images showing the microstructures of samples 06-600Nb⁺VMo and b) grain boundary misorientation distribution for the same sample

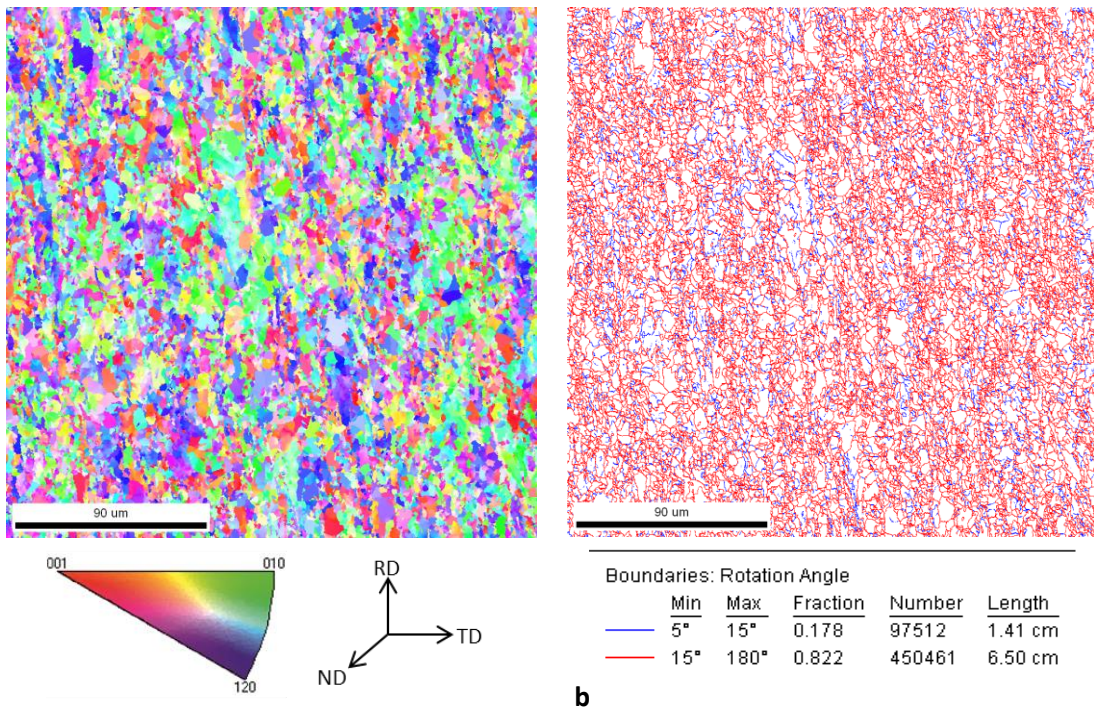


Figure 6.7 – EBSD maps for 06-600Nb⁺VMo showing a) texture of the grains and b) low angle boundaries in blue and high angle boundaries in red

High angle grain boundaries formed 82% of the overall boundaries and these were slightly less compared to 02-630Nb⁺VMo and 06-600Nb⁺VMo which averaged 87% and 88% respectively. The overall grain boundary misorientation distribution is shown in Figure 6.6b.

The SEM and EBSD maps and images for 07-630NbVMo were presented in Figure 6.8 and Figure 6.9. The major difference in chemical composition between 06-600Nb⁺VMo and 07-630NbVMo was the reduced Nb content in the later, which was half as much in 07-630NbVMo (0.027 wt.%) as compared to double the amount in 06-600Nb⁺VMo. The Mo content was also reduced to half in the same sample (see table 2.1 - table of chemical compositions). Equiaxed polygonal ferrite dominated the microstructure just like in the samples previously discussed. Pearlite, previously observed in the other samples, was also observed in this sample, though the occurrences were rare. The grains were also much finer and grain bimodality was not as prominent as in 02-600Nb⁺VMo. The grain boundary misorientation distribution is shown in Figure 6.8b, while the EBSD orientation and the grain boundary misorientation distribution maps are shown in Figure 6.9. The misorientation distribution map confirmed SEM results which showed equiaxed ferrite. High angle boundaries in this instances accounted for 82% of the grain boundaries as compared to 18% low angle boundaries and this was quite similar to 06-600Nb⁺VMo.

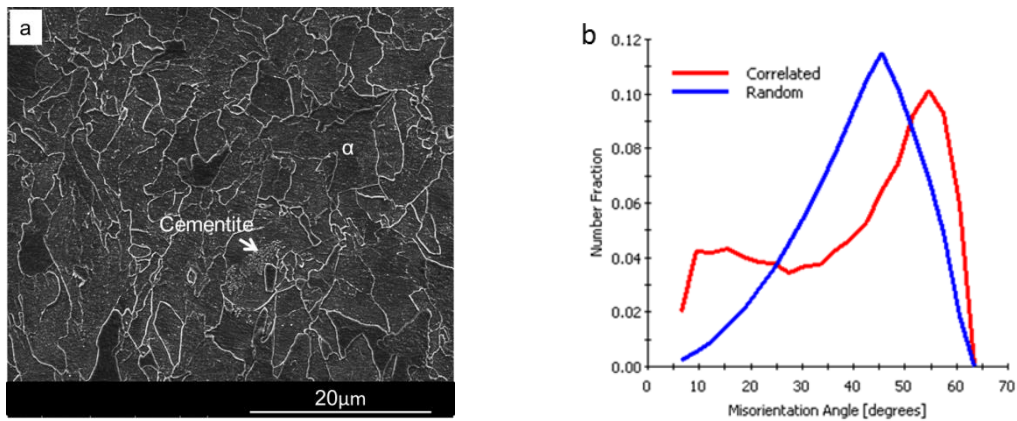


Figure 6.8 - a) SEM images showing the microstructures of samples 07-630NbVMo and b) grain boundary misorientation distribution for the same sample

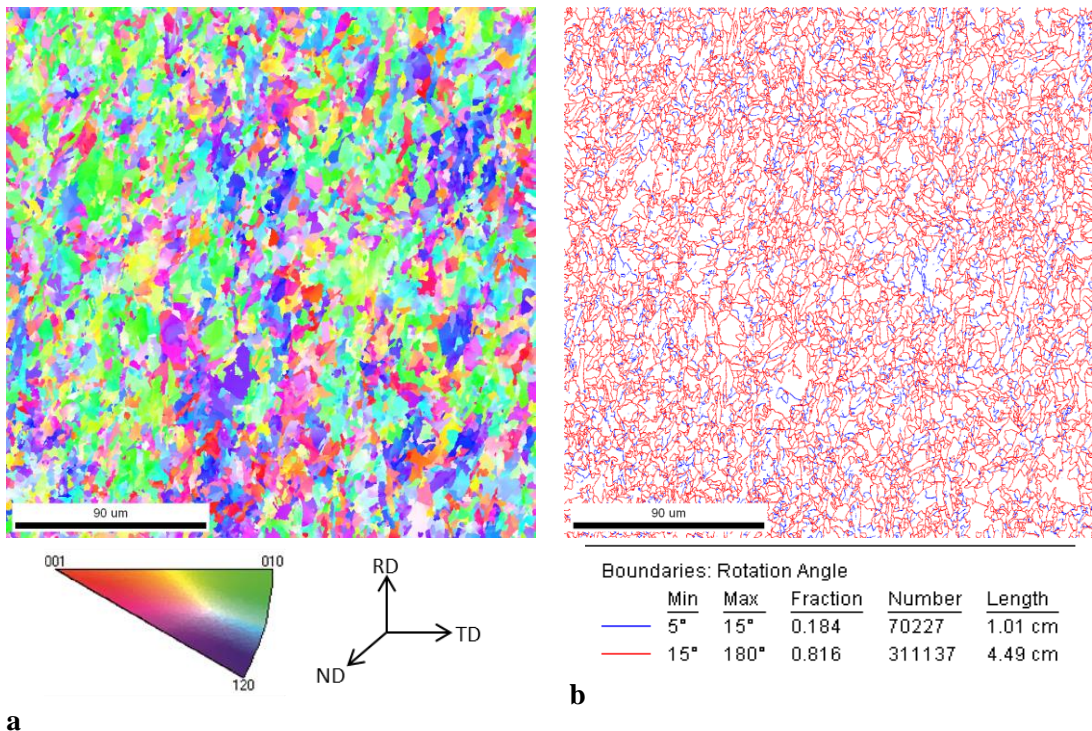


Figure 6.9 – EBSD maps for 07-630NbVMo showing a) texture of the grains and b) low angle boundaries in blue and high angle boundaries in red

Figure 6.10a is an SEM image for 10-630Nb⁺VMo. Similar to samples previously discussed was the existence of bands of coarse ferrite grains which were observed on both SEM images and EBSD misorientation map in Figure 6.11b. The randomness of the crystal pattern on the EBSD map in Figure 6.11a showed no preferred crystal orientation in this steel. SEM also showed the majority of the grains were equiaxed. This was also confirmed by EBSD. The misorientation map in Figure 6.11b showed that 87% of the grain boundaries were high angle. The grain boundary misorientation

distribution curve in Figure 6.10b also showed the highest numbers of grains at angles above 30°.

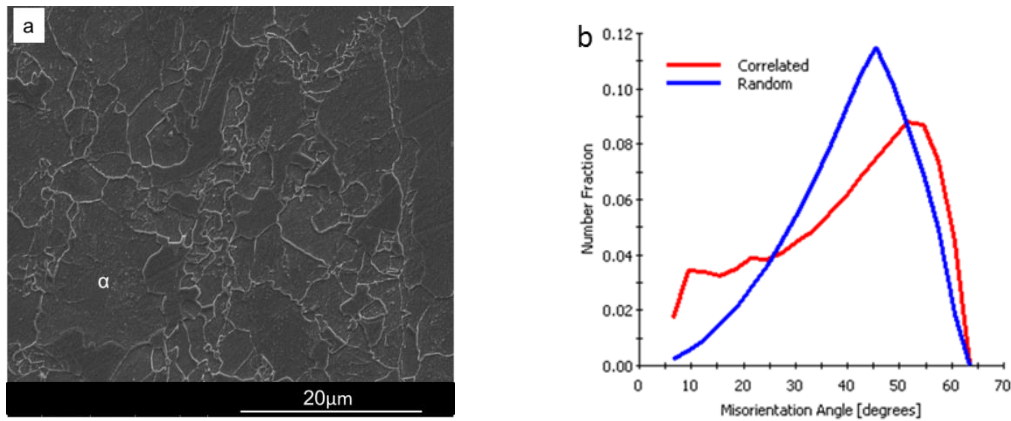


Figure 6.10 – a) SEM images showing the microstructures of samples 10-630Nb⁺VMo and b) grain boundary misorientation distribution for the same sample

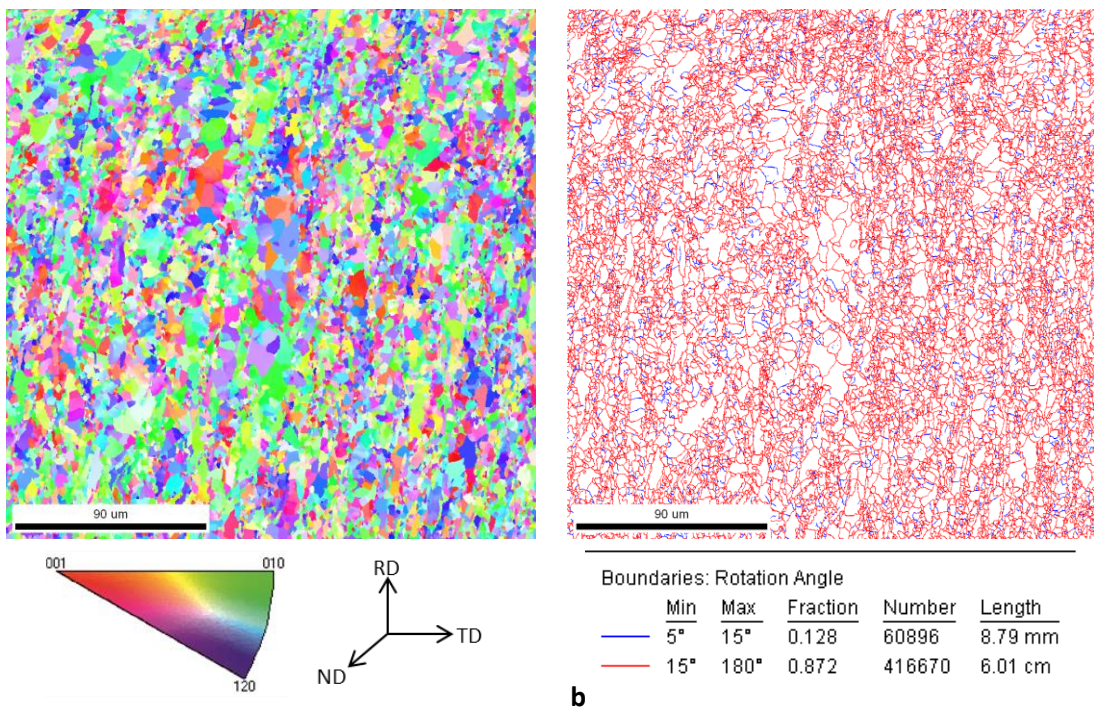


Figure 6.11 – EBSD maps for 10-630Nb⁺VMo showing a) texture of the grains and b) low angle boundaries in blue and high angle boundaries in red

The SEM image in Figure 6.12a shows the microstructure for 14-650Nb⁺VMo. Both SEM and the misorientation distribution map in Figure 6.13b showed the presence of bands of coarse ferrite grains. Equiaxed ferrite grains dominated the microstructure with occasional pearlite islands randomly distributed throughout the sample. The crystallographic orientation of the grains was quite random as shown on the EBSD

map in Figure 6.13a. Figure 6.12b shows the grain boundary misorientation distribution and it is clear that the majority of the grains were equiaxed. The misorientation map in Figure 6.13b confirmed that high angle grain boundaries accounted for 92% of the boundaries with only 8% of the boundaries being low angle.

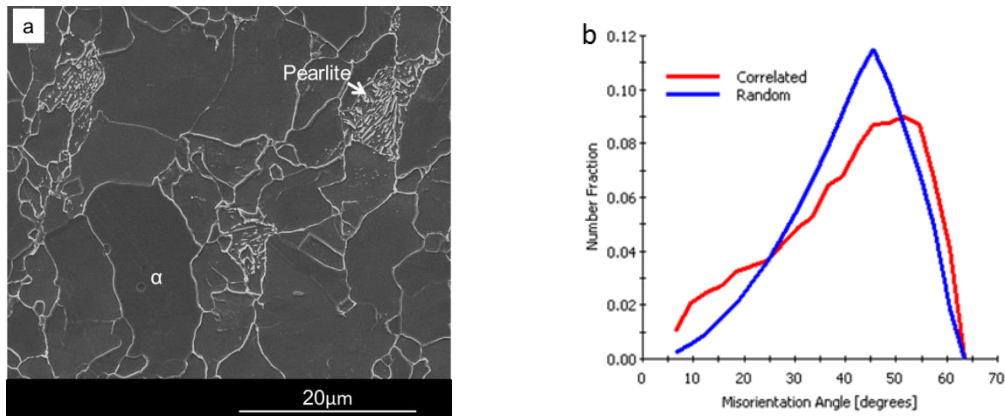


Figure 6.12– a) SEM images showing the microstructures of samples 14-630Nb⁺VMo and b) grain boundary misorientation distribution for the same sample

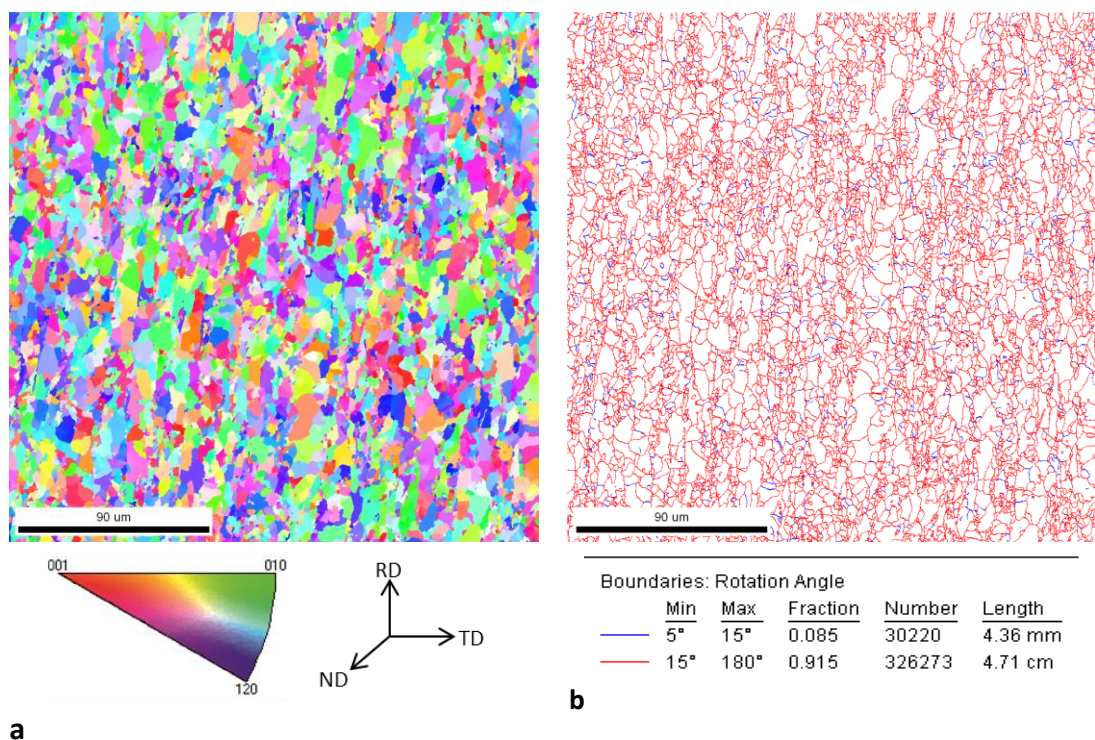
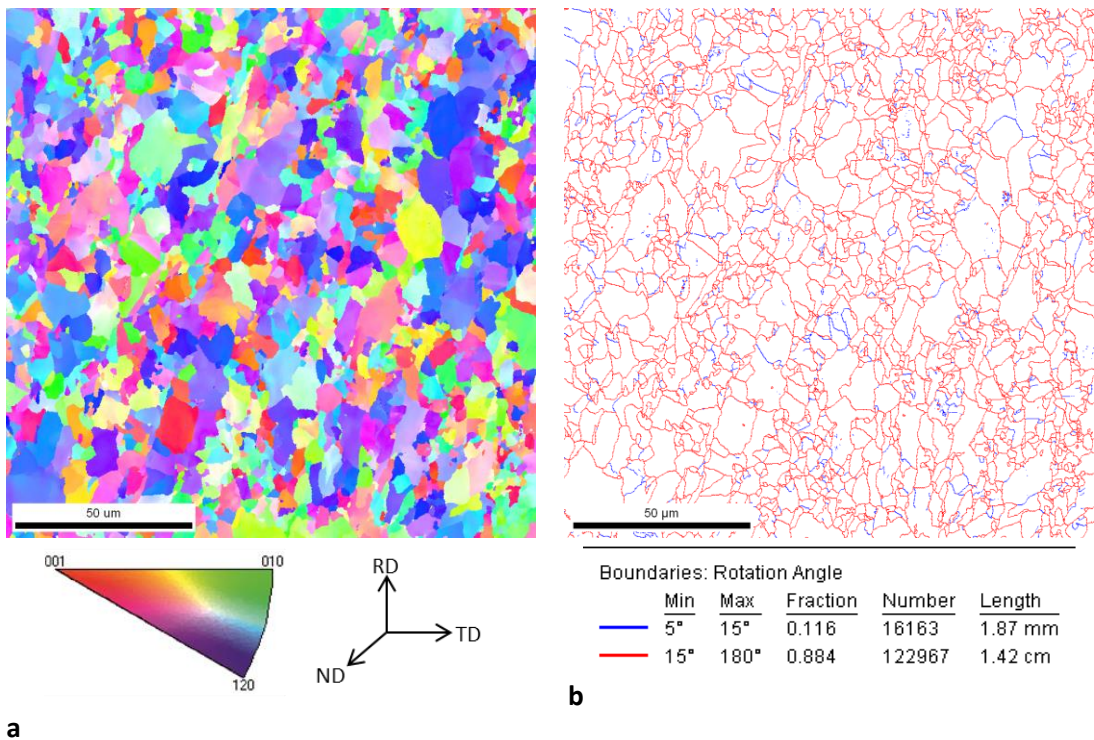
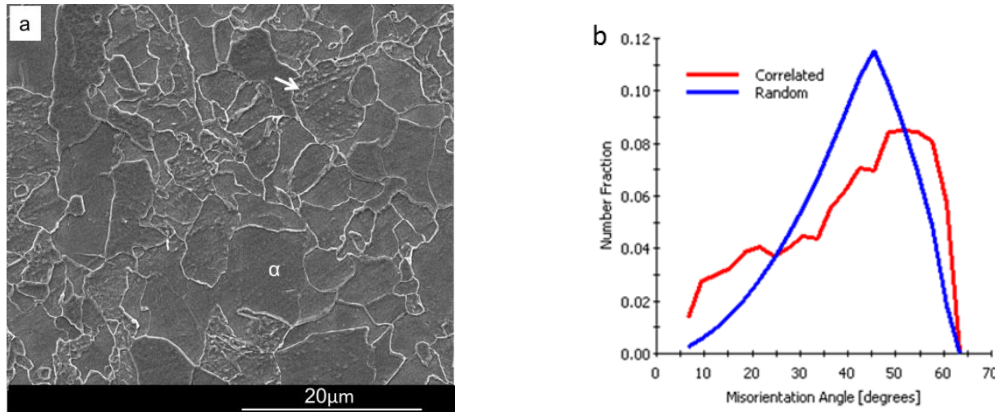


Figure 6.13 – EBSD maps for 14-630Nb⁺VMo showing a) texture of the grains and b) low angle boundaries in blue and high angle boundaries in red

Figure 6.14 and Figure 6.15 shows SEM images, EBSD maps and grain boundary misorientation distribution maps and curves for samples 15-650TiMo.



Large ferrite grains observed in SEM images were also confirmed by both the EBSD map and the grain boundary misorientation distribution maps in Figure 6.15. Banded ferrite revealed through SEM was one of the few features, which was unique to this sample. High angle grain boundaries accounted for 88% of the boundaries as shown

on the grain boundary misorientation distribution in Figure 6.14b and the map in Figure 6.15b. The fact that equiaxed ferrite dominated the SEM images was also confirmed through the grain boundary misorientation distribution which showed on 12% low angle boundaries.

The images in Figure 6.16 and Figure 6.17 are SEM images, EBSD maps and grain boundary misorientation distribution maps and curves for samples 16-650Ti.

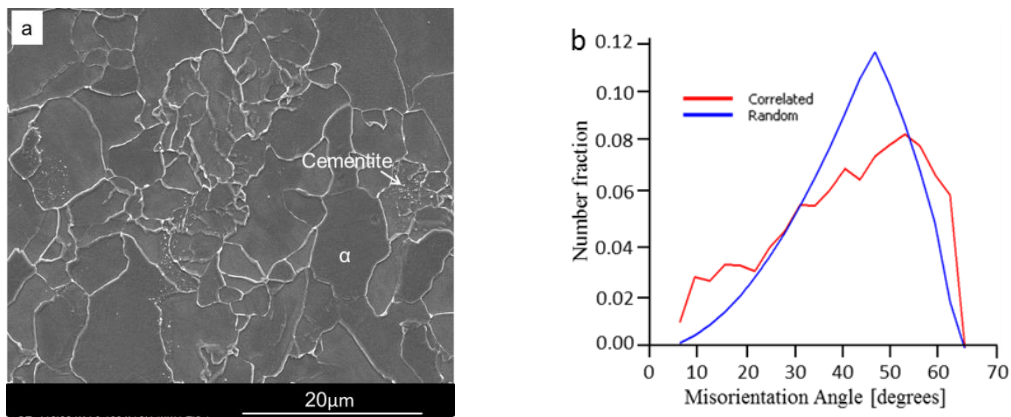


Figure 6.16 – a) SEM images showing the microstructures of samples 16-650Ti and b) grain boundary misorientation distribution curve for the same sample

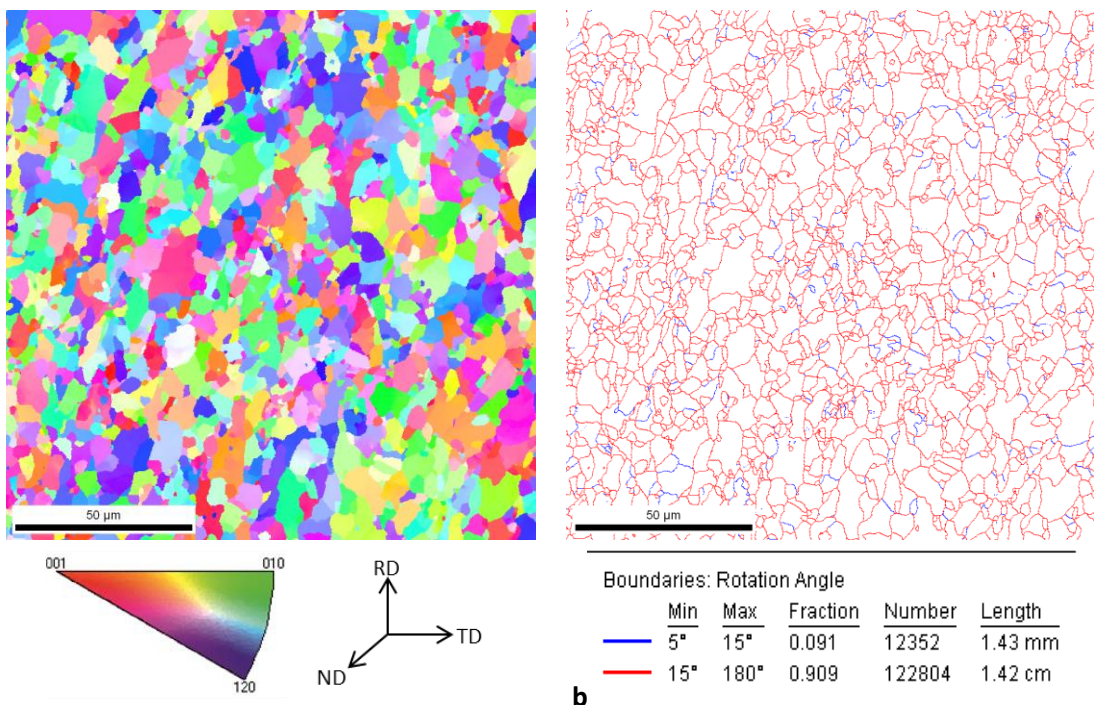


Figure 6.17 – EBSD maps for 16-650Ti showing a) texture of the grains and b) low angle boundaries in blue and high angle boundaries in red

This sample had many similarities with 15-650TiMo, apart from the banded structure in 15-650TiMo. Coarse polygonal ferrite dominated the microstructure while bainitic ferrite was also observed in other regions. The bimodality of the grains in both samples was also observed in both SEM images and misorientation maps. The other noticeable difference was the existence of particles of cementite within the ferrite in sample 16-650Ti. The randomness of the crystal orientation within the microstructure was observed through EBSD mapping in Figure 6.17a. Equiaxed grains dominated the microstructure as shown on the SEM image, with EBSD showing that high angle grain boundaries in Figure 6.17b accounted for 91% of the boundaries. The grain boundary misorientation distribution curve is also shown in Figure 6.16b.

Figure 6.18 shows the SEM images for sample 17-650VMo. The microstructure was composed mainly of coarse ferrite grains. Pearlite and cementite were also observed in some of the grains. The existence of coarse grains was also confirmed through EBSD mapping and grain boundary misorientation distribution map in Figure 6.19. The random crystal orientation patterns on the EBSD map in Figure 6.19a confirmed that there was no preferred crystal orientation within the microstructure. This was also confirmed through EBSD grain boundary misorientation distribution mapping in Figure 6.19b, which showed that high angle grain boundaries accounted for 92% of the microstructure as compared to only 8% low angle boundaries. The grain boundary misorientation distribution curve is also shown in Figure 6.20. Another common feature observed in SEM was the existence of pearlite. A higher resolution image in Figure 6.18b shows the blocky morphology of the pearlite as well as the presence of raised grain boundaries. The raised grain boundaries suggest they were possibly hardened by something within them; the highest probability being dislocations and discrete carbides and this will be further investigated later.

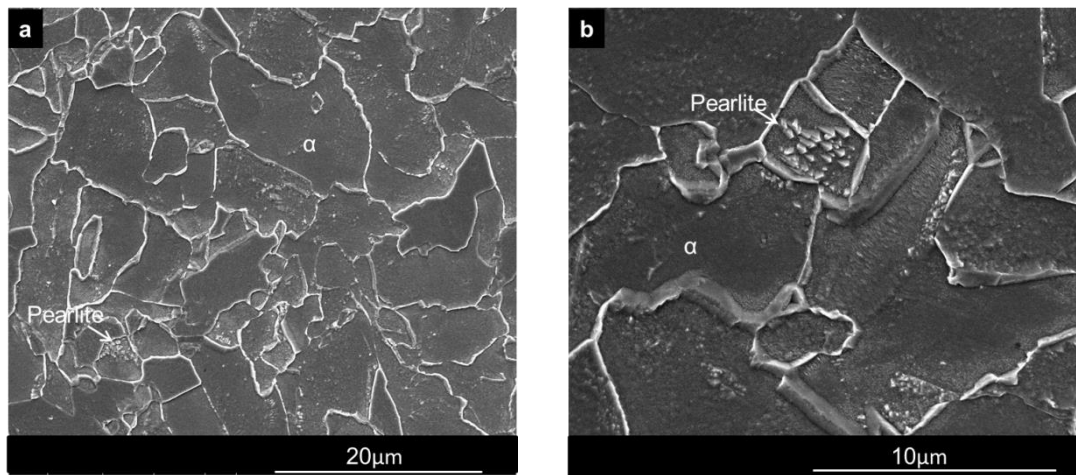
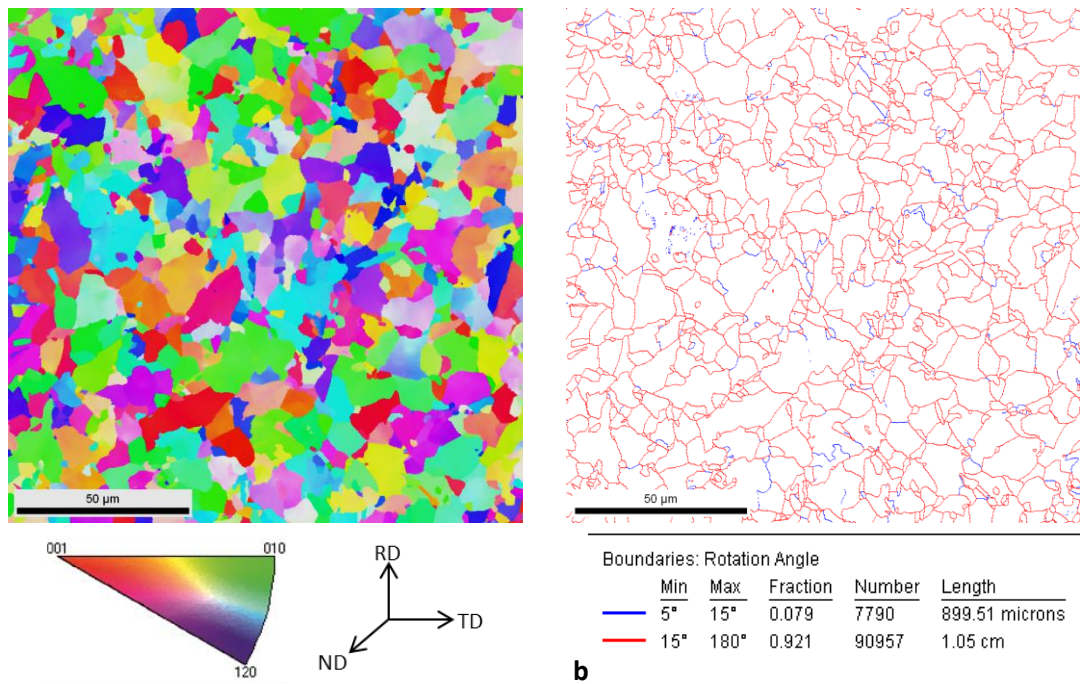


Figure 6.18 – SEM images for 17-650VMo showing a) the general microstructure and b) high resolution image showing to show the presents of pearlite within the grains.



a
Figure 6.19 – EBSD maps for 17-650NbMo showing a) texture of the grains and b) low angle boundaries in blue and high angle boundaries in red

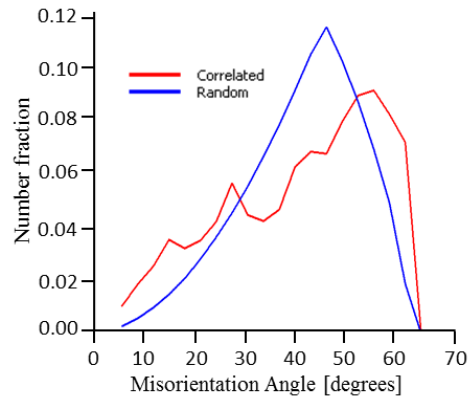


Figure 6.20 – Grain boundary misorientation distribution curve for 17-650VMo

Figure 6.21 and Figure 6.22 are SEM images, EBSD maps and grain boundary misorientation distribution maps and curves for samples 18-650V. The main chemical composition dissimilarity between 17-650VMo and 18-650V was the existence of Mo in 17-650VMo which was deliberately omitted in 18-650V.

SEM imaging showed that 18-650V had the coarsest grains as compared to any of the other samples. This was also observed on the EBSD maps in Figure 6.22. It is also important to note that the microstructures developed in these two samples were more homogenous. 18-650V had the most homogenous microstructure as compared to any of the other samples. The coarser banding previously observed in the other samples was no longer evident. The pearlite previously observed in 17-650VMo was also observed in this sample. The EBSD misorientation distribution map in Figure 6.22b showed that high angle grain boundaries accounted for 92% of the boundaries as compared to only 8% low angle boundaries. The grain boundary misorientation distribution curve is also shown in Figure 6.21b.

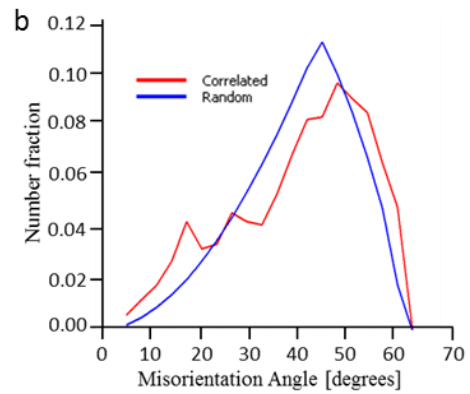
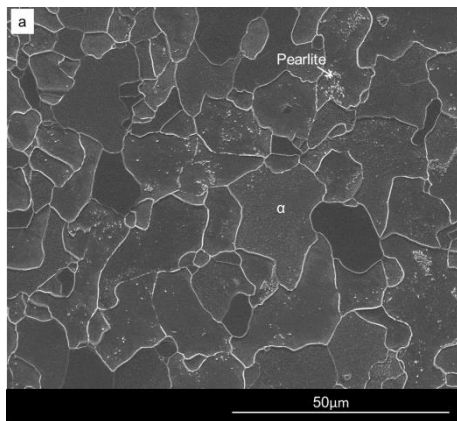
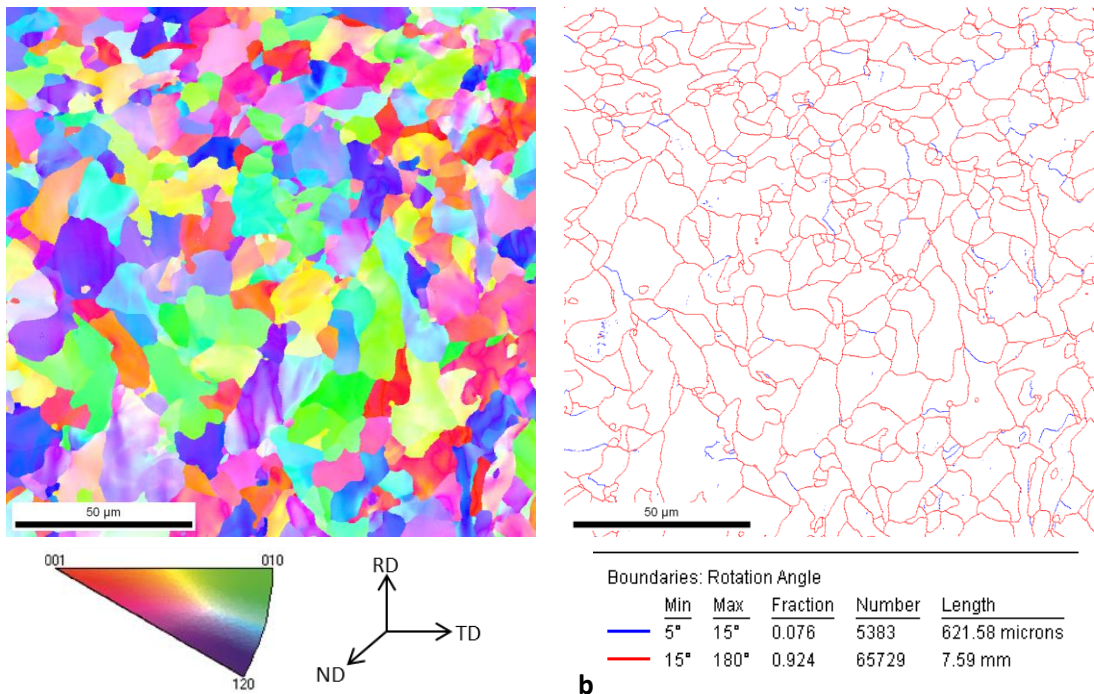


Figure 6.21– a) SEM images showing the microstructures of samples 18-650V and b) grain boundary misorientation distribution curve for the same sample



a) texture of the grains and b) low angle boundaries in blue and high angle boundaries in red

The SEM images, EBSD maps and grain boundary misorientation distribution maps and curves for samples 19-650NbMo are shown in Figure 6.23 and Figure 6.24.

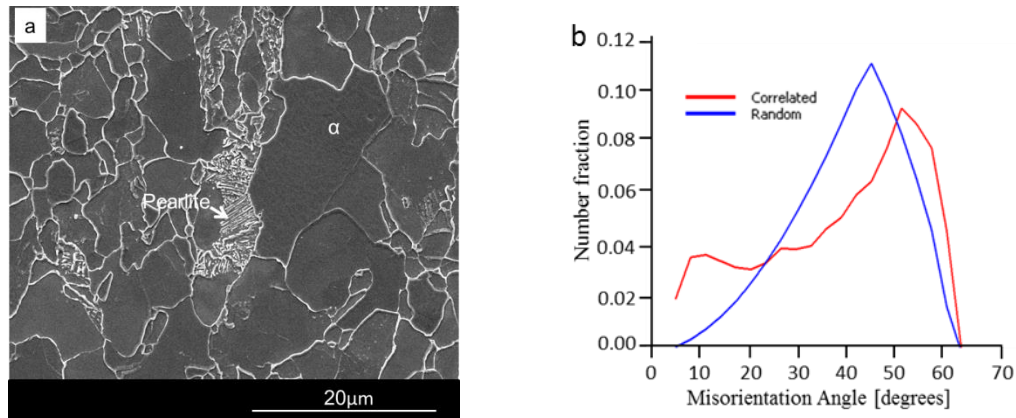


Figure 6.23 – a) SEM images showing the microstructures of samples 19-650NbMo and b) grain boundary misorientation distribution curve for the same sample

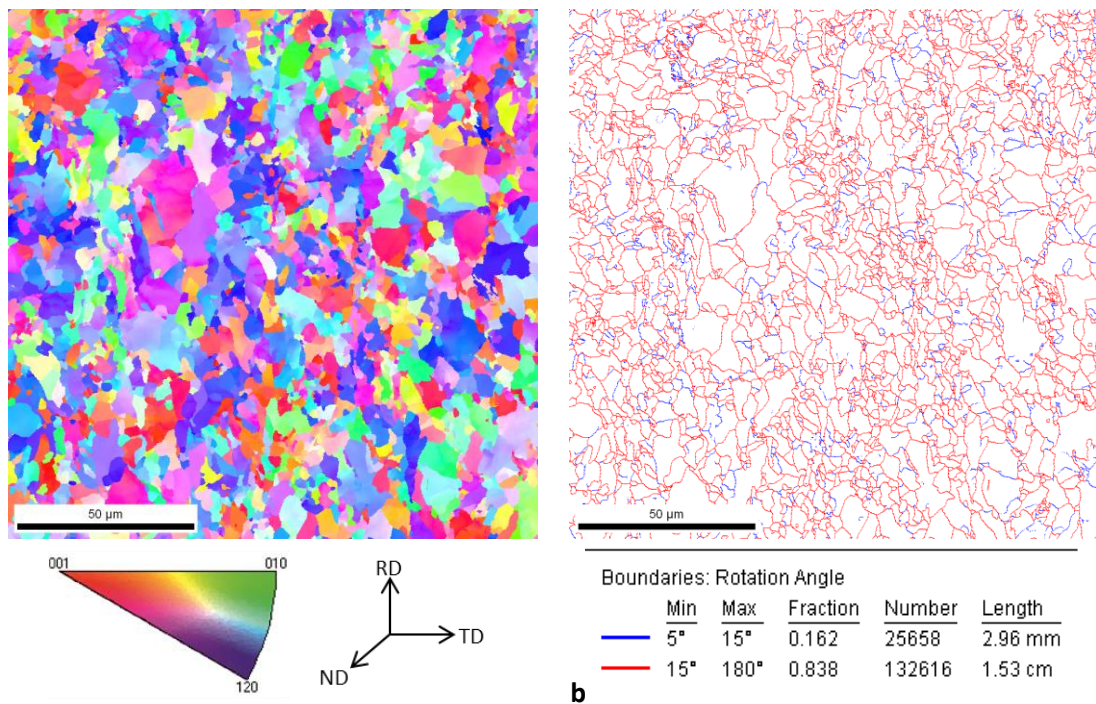


Figure 6.24 – EBSD maps for 19-650NbMo showing a) texture of the grains and b) low angle boundaries in blue and high angle boundaries in red

The microstructure observed in the SEM showed the existence of banded polygonal ferrite. Some elongated ferrite, possibly bainitic ferrite, was also observed. Lamellar pearlite that might have exhibited partial spheroidisation was also a common feature throughout the microstructure. EBSD mapping showed no preferential crystal orientation in this sample. The fact that most of the grains in SEM images were

equiaxed was also confirmed through the grain boundary misorientation mapping which showed that 84% of the boundaries were high angle grain boundaries with 16% being low angle. The grain boundary misorientation curve is shown in Figure 6.23b

Figure 6.25 and Figure 6.26 are the SEM image, EBSD map and grain boundary misorientation distribution map and curves for samples 20-650Nb. The major difference between 19-650NbMo and 20-650Nb was the existence of Mo in 19-650NbMo, which was deliberately omitted in the other. V and Ti were also omitted in both samples. Both SEM images and misorientation maps showed that grains in both samples were quite inhomogeneous. Bands of coarse grains were observed sandwiched between finer grains as previously observed in other samples (e.g. in 14-650Nb⁺VMo). Pearlite, though few and far between, was also found at random throughout the sample. The random texture of the microstructure showed no preferential crystal orientation. The EBSD grain boundary misorientation distribution map in Figure 6.26 showed that 90% of the grain boundaries were high angle as compared to 10% low angle. The grain boundary misorientation distribution curve is shown in Figure 6.25b.

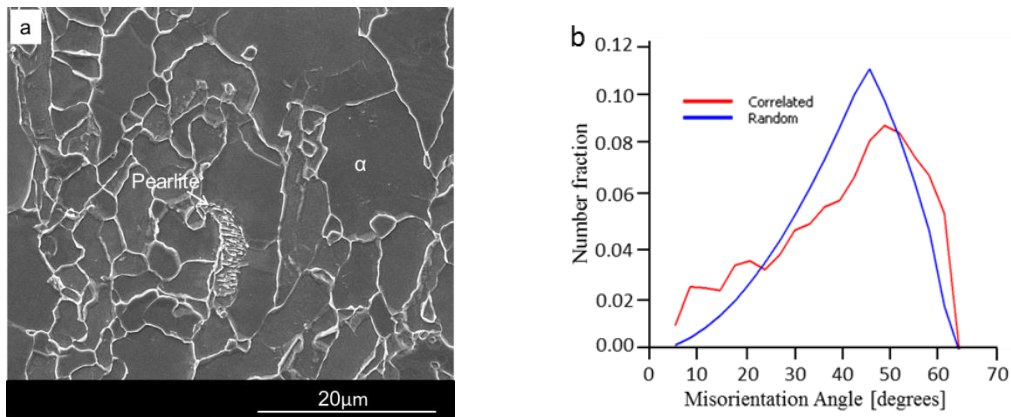


Figure 6.25 – a) SEM images showing the microstructures of samples 20-650Nb and b) grain boundary misorientation distribution curve for the same sample

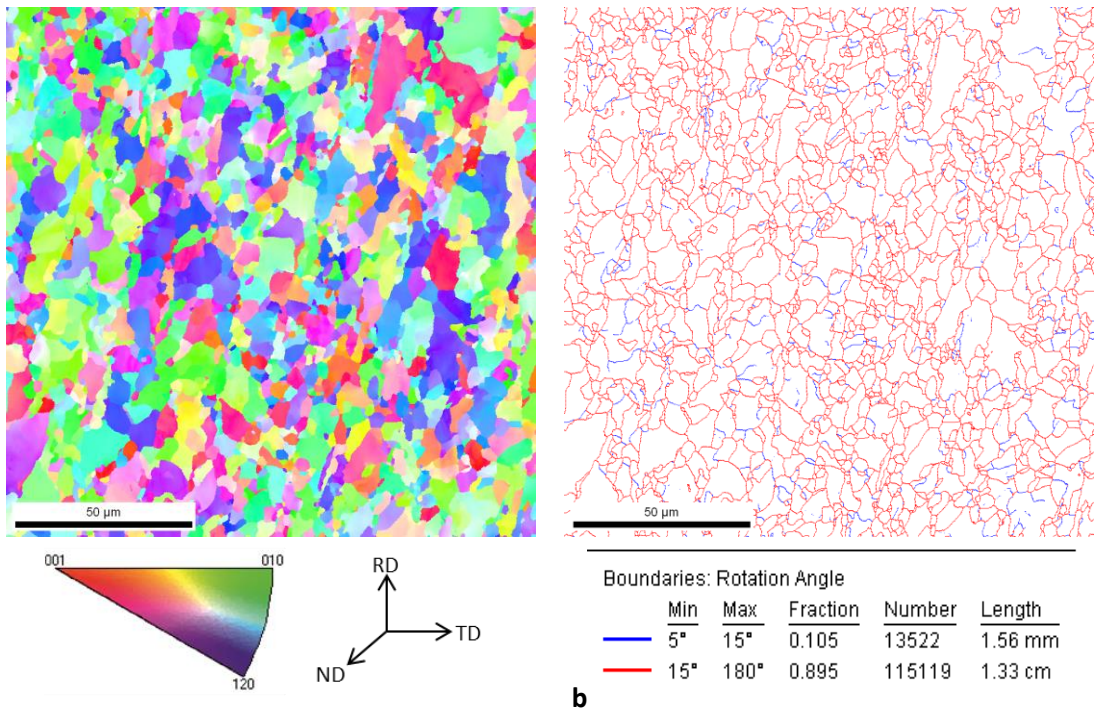


Figure 6.26– EBSD maps for 20-650Nb showing a) texture of the grains and b) low angle boundaries in blue and high angle boundaries in red

The SEM image, EBSD map and grain boundary misorientation distribution map and curve for sample 21-650TiMo are shown in Figure 6.27 and Figure 6.28. Even though coarser polygonal ferrite grains were expected due to the high coiling temperature of 650°C, SEM images showed that the microstructure was predominantly fine bainitic ferrite. EBSD mapping in Figure 6.28 also confirmed this observation. The random crystallographic orientation of the crystals was also

confirmed through EBSD. Fewer coarse grains were also observed on both SEM images and the grain boundary misorientation distribution map.

High angle grain boundaries were 85% of the microstructure as compared 15% low angle boundaries. The distribution curve for the grain boundary misorientation is shown in Figure 6.27b.

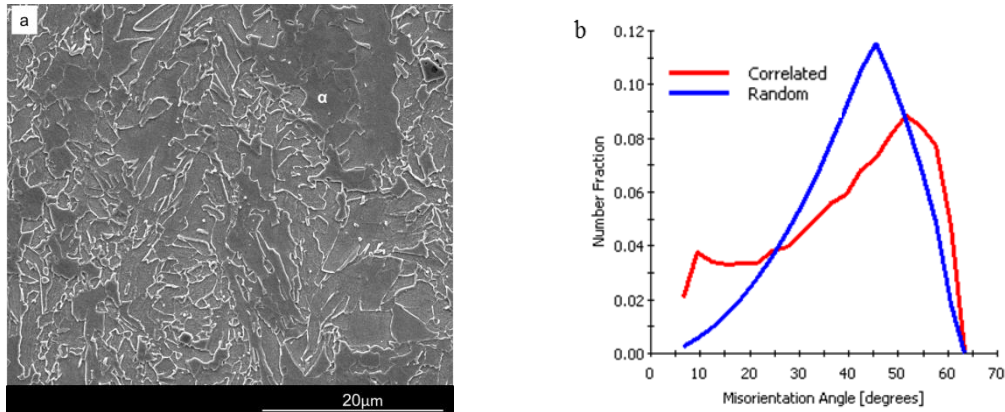


Figure 6.27 – a) SEM images showing the microstructures of samples 21-650TiMo and b) grain boundary misorientation distribution curve for the same sample

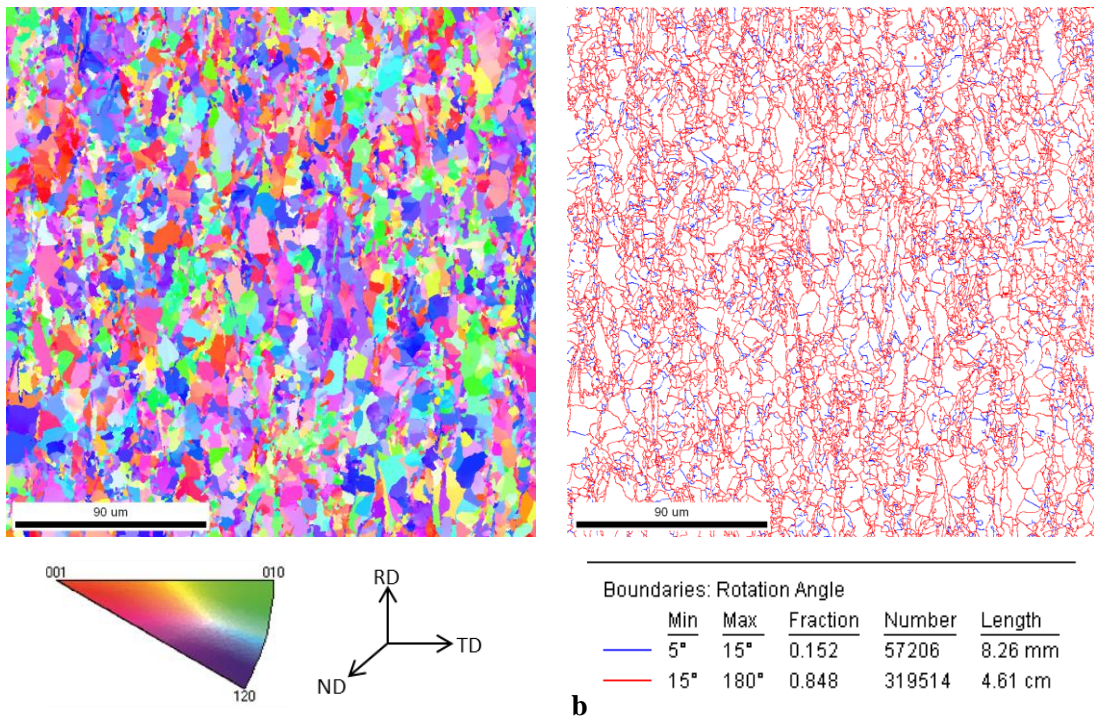


Figure 6.28 – EBSD maps for 21-650TiMo showing a) texture of the grains and b) low angle boundaries in blue and high angle boundaries in red

Figure 6.29 and Figure 6.30 are SEM images, EBSD map and grain boundary misorientation distribution map and curve for sample 22-630N⁺. The chemistry of this sample was unique in that it was the only one with more than double the nitrogen content as compared to any of the other samples. As expected, the grains were reasonably homogenous as shown on the SEM image in Figure 6.29a and this was also confirmed through EBSD mapping in Figure 6.30. The high N content was not expected to make any contribution to grain refinement, but rather on the precipitates formed. The MOD map in Figure 6.30b showed that 87% of the grain boundaries were high angle with only 12% of the boundaries being low angle. The distribution curve for the grain boundary misorientation is also presented in Figure 6.29b.

The summarised misorientation data for all the samples were tabulated in Table 6.2

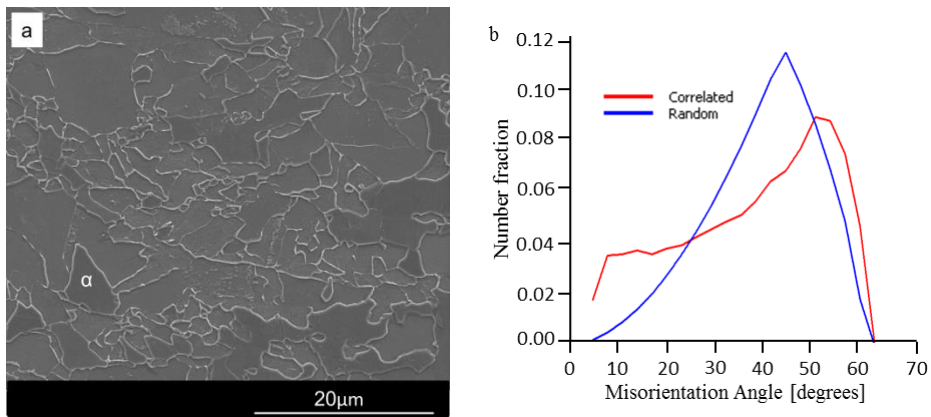


Figure 6.29 – a) SEM images showing the microstructures of samples 22-630N+ and b) grain boundary misorientation distribution curve for the same sample

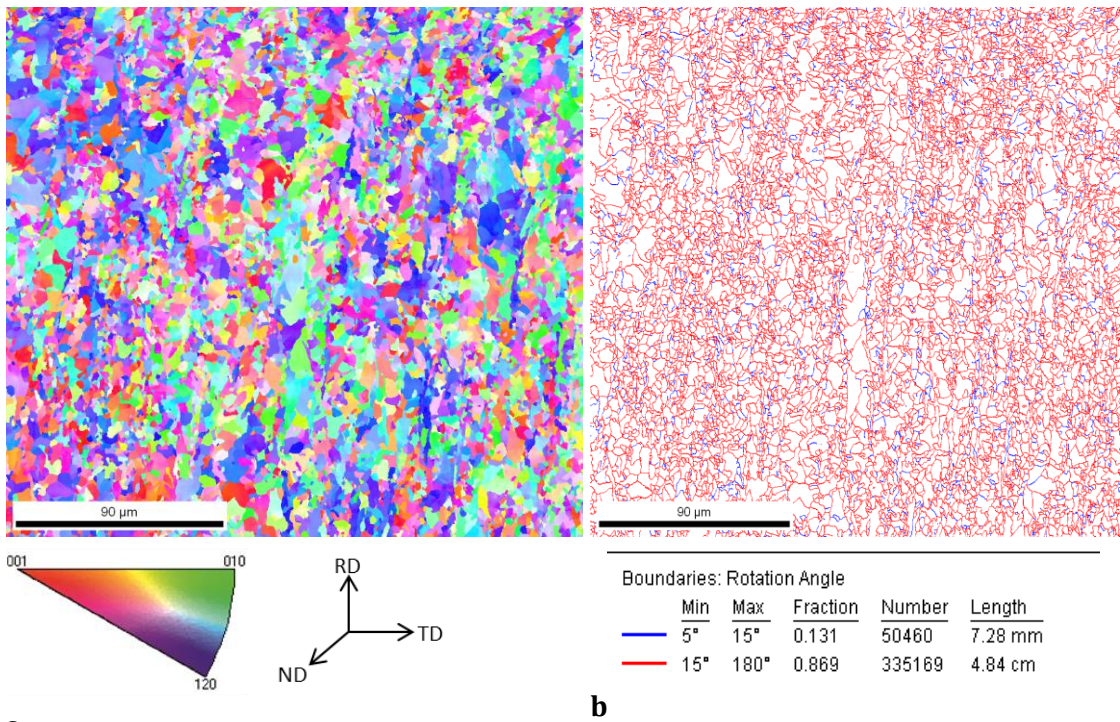


Figure 6.30 – EBSD maps for 22-630N+ showing a) texture of the grains and b) low angle boundaries in blue and high angle boundaries in red

6.4 Grain Sizes Distribution

In general, all the samples were dominated by ferrite. Occasional pearlite was also found scattered within all the samples examined. Using at least ten images per sample, over 300 grains per sample were measured using the linear intercept method. The average grain sizes for all the samples were tabulated in Table 6.2. Figure 6.31 compares the average grain sizes for all the samples.

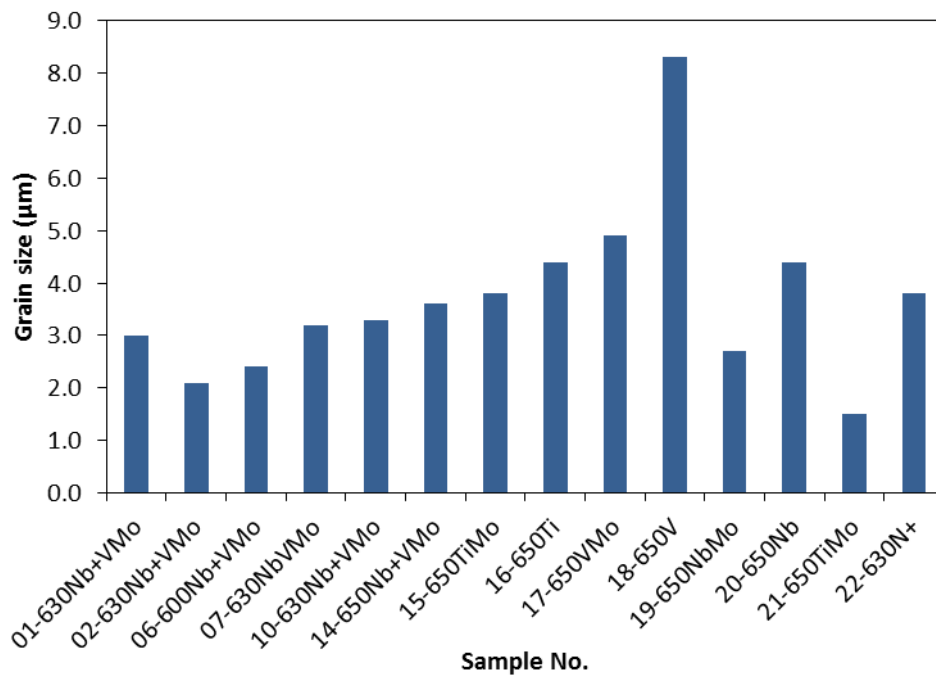


Figure 6.31 – Measured average grain sizes for all the samples

It is quite evident from Figure 6.31 that 18-650V had the largest average grain size of $8.3 \pm 0.6\mu\text{m}$ followed by 17-650VMo with $4.9 \pm 0.1\mu\text{m}$. 16-650Ti and 20-650Nb had $4.4 \pm 0.4\mu\text{m}$ and $4.4 \pm 0.3\mu\text{m}$ respectively. 02-630Nb⁺VMo and 06-600Nb⁺VMo were found to have smaller grain sizes of $2.1 \pm 0.2\mu\text{m}$, $2.4 \pm 0.2\mu\text{m}$ respectively. However, 21-650TiMo had the finest grains averaging $1.5 \pm 0.1\mu\text{m}$. The grain sizes distribution curves for all the samples are shown in Figure 6.32 and Figure 6.33

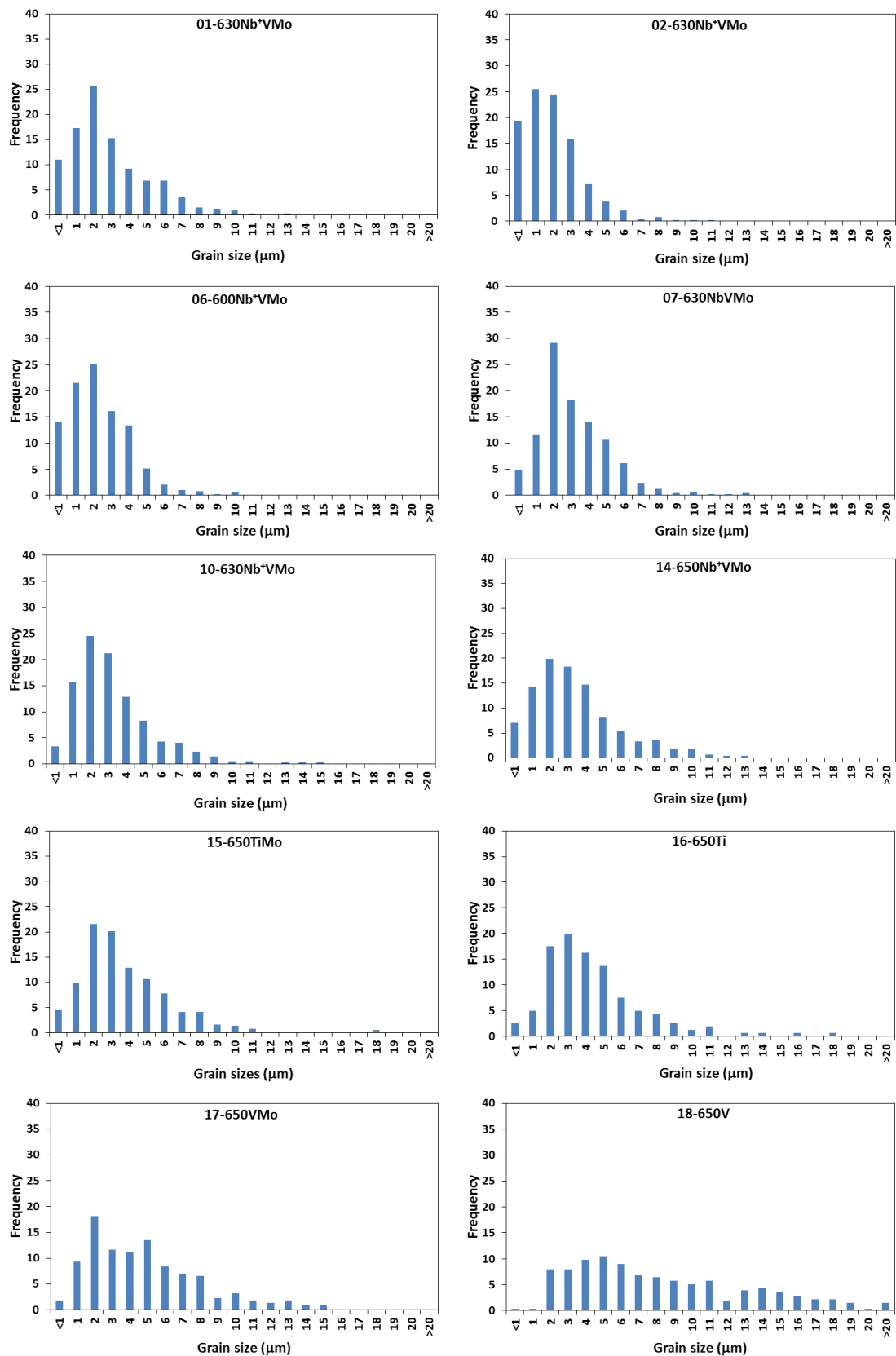


Figure 6.32 – Grain size distribution curves for samples 01-630Nb⁺VMo to 18-650V

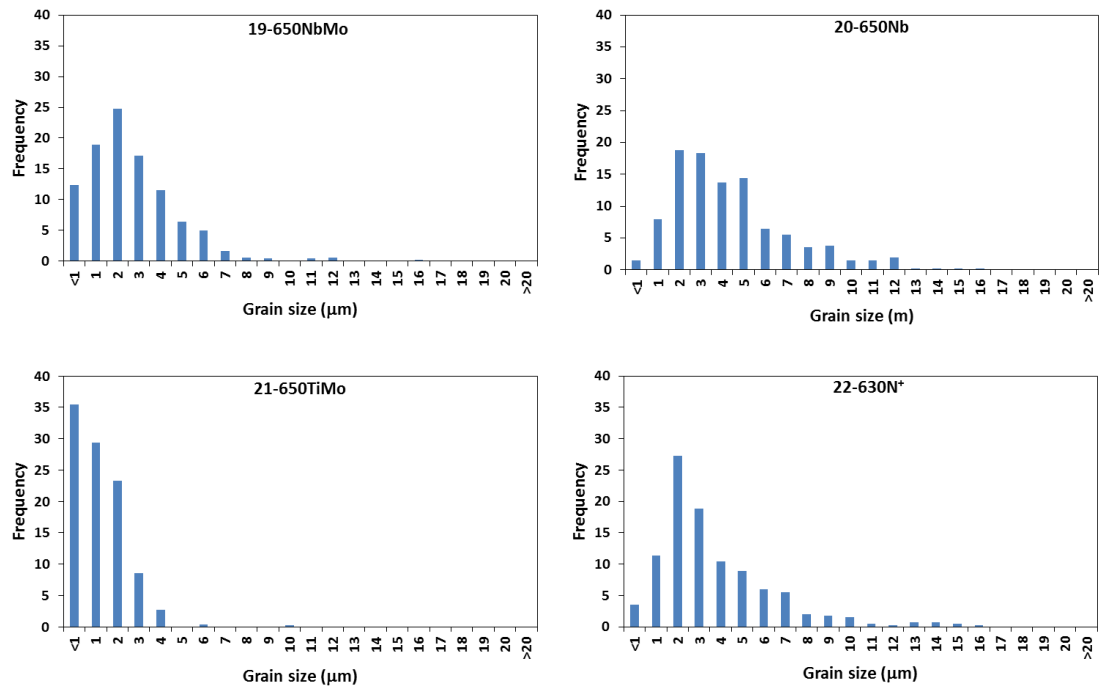


Figure 6.33– Grain size distribution curves for samples 19-650NbMo to 22-630N⁺

Table 6.2 – Summarised grain sizes and grain boundary misorientation data

Sample	Measured Grain Size (μm)	EBSD Grain Size (μm)	% Low angle boundaries [5 – 15°]	% High angle boundaries [15 – 180°]
01-630Nb ⁺ VMo	3.0 ± 0.2	2.9	13	87
02-630Nb ⁺ VMo	2.1 ± 0.2	2.6	12	88
06-600Nb ⁺ VMo	2.4 ± 0.2	2.2	18	82
07-630NbVMo	3.2 ± 0.2	3.3	18	82
10-630Nb ⁺ VMo	3.3 ± 0.2	2.3	13	87
14-650Nb ⁺ VMo	3.6 ± 0.2	2.8	8	92
15-650TiMo	3.8 ± 0.3	3.0	12	88
16-650Ti	4.4 ± 0.4	3.3	9	91
17-650VMo	4.9 ± 0.1	4.1	8	92
18-650V	8.3 ± 0.6	6.3	8	92
19-650NbMo	2.7 ± 0.2	2.9	16	84
20-650Nb	4.4 ± 0.3	3.3	10	90
21-650TiMo	1.5 ± 0.1	3.0	15	85
22-630N ⁺	3.8 ± 0.3	2.4	13	87

6.5 Precipitate Analysis

As previously stated, the major strengthening mechanisms in this study were mainly grain refinement, precipitate strengthening and solid solution strengthening. Precipitate strengthening formed the major part of this project and this was the main reason why carbon extraction replicas were prepared in order to analyse the precipitates alone without interference from the matrix. The major objectives for this exercise were mainly to:-

1. Establish the precipitate types and morphology
2. Establish the precipitate composition
3. Quantify the precipitates in terms of size and distribution
4. Use empirical formulas to estimate precipitate strengthening from the precipitate counts

For all the microalloyed steels examined, the precipitates could be imaged both in bright and dark field. A detailed description of precipitate size distribution will be presented and the actual precipitates analysed in this section. TEM thin foils were also produced in order to get a better insight into how the precipitates were distributed within the matrix. Energy Loss Spectroscopy (EELS) in conjunction with energy dispersive X-ray spectroscopy (EDX) were used in the TEM on carbon extraction replicas to determine the chemistry of the precipitates. EELS has been found to be the most appropriate technique due to its high sensitivity to light elements. However, for the heavier elements, EDX has been found to be the most appropriate and this was the major reason why both techniques were employed. Precipitate chemistry and morphology

Figure 6.34 shows TEM thin foil images while Figure 6.35 shows TEM carbon extraction replicas images for sample 01-630Nb⁺VMo. TEM thin foil images show the existence of high precipitate number densities. The fine precipitates were observed randomly distributed throughout the sample. Though most of the regions had randomly distributed precipitates, fewer regions showed signs of planar interphase precipitation (IP) as shown in Figure 6.34a. Due to the size, morphology and number densities of these precipitates, it was most likely that the random precipitates might have been formed at the interphase boundary during transformation from α to γ . Ricks and Howell described such random IP as having

been formed through the looping mechanism for interphase precipitation[145]. This will be discussed later in the discussion chapter.

The existence of these fine precipitates was confirmed through carbon extraction replica images in Figure 6.35. Precipitates observed in both thin foils and carbon extraction replicas were mostly spherical with a few rods and cube type precipitates. EELS were then used to identify the chemistry of the various particles. Figure 6.36 and Figure 6.37 shows the EELS spectrum for the particles identified. The majority of the finest particles were found to be vanadium carbides (VC) while some of them were found to be vanadium carbonitrides (VCN) as shown in Figure 6.37. The fact that no Ti was added to the alloy during casting tends to suggest the Ti peaks found in some of the precipitates were a result of contaminations from previous castings. Ti is such a strong carbide former to such an extent that all the Ti in the alloy forms carbides or carbonitrides no matter how little the quantities are. Therefore, it is concluded that the vast majority of fine precipitates were VC and VCN. Due to the similarities in chemical composition between the rod shaped and the spherical particles, it was possible that the particles that looked spherical might have been the same rod shaped precipitates, the difference being the orientation at which they were observed. The spherical precipitates could be rod shaped, but viewed along the long axis and end-on.

EDX analysis carried out on the particles showed spectra similar to those for 02-630Nb⁺VMo, shown in Figure 6.41. One interesting feature observed through EDX analysis was the existence of Mo in all the fine precipitates. Hence, the fine precipitates formed were V(Mo)C.

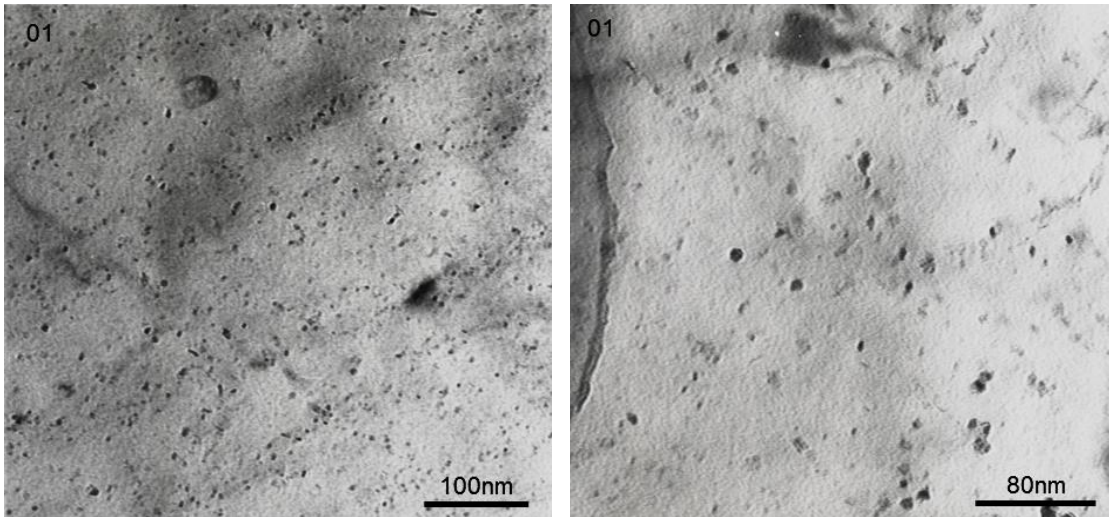


Figure 6.34 – TEM thin foil images for 01-630Nb⁺VMo showing the existence of fine precipitates; some in slightly ordered arrays and the majority randomly distributed

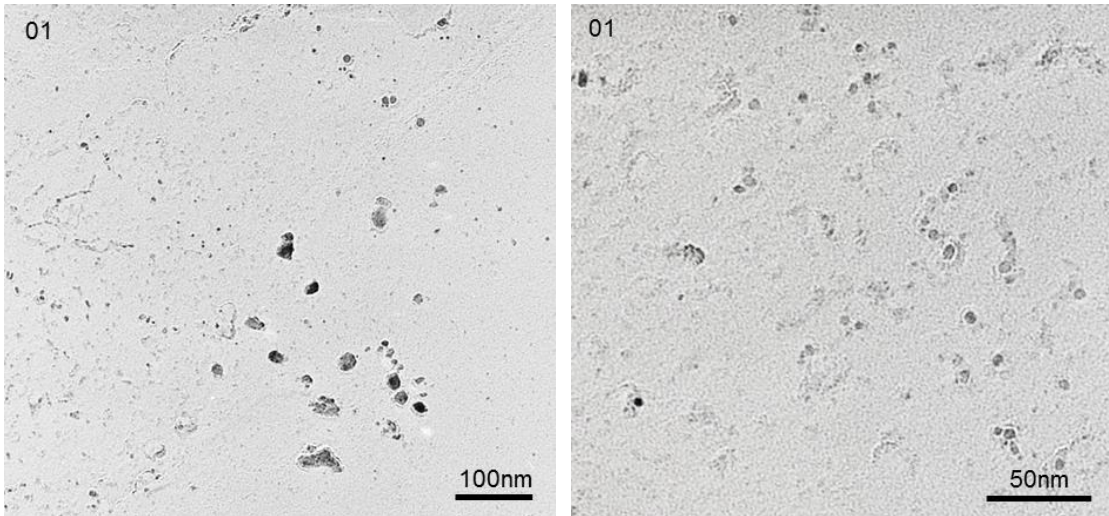


Figure 6.35 – TEM Carbon extraction replica images showing the existence fine precipitates in 01-630Nb⁺VMo

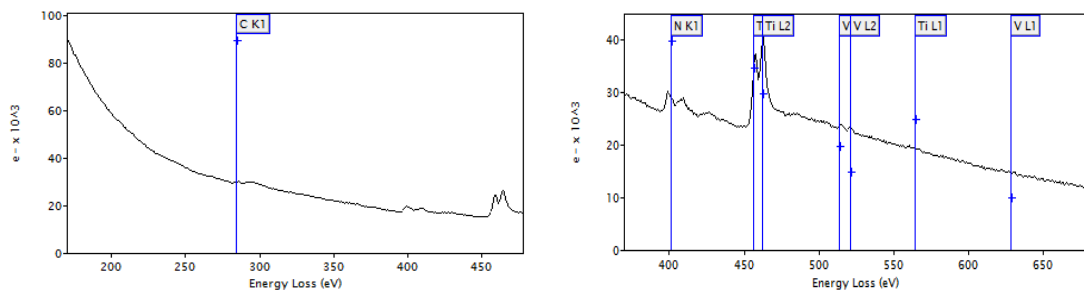


Figure 6.36 - EELS spectras for 01-630Nb⁺VMo showing that some of the Spheres, rods and cube type precipitates

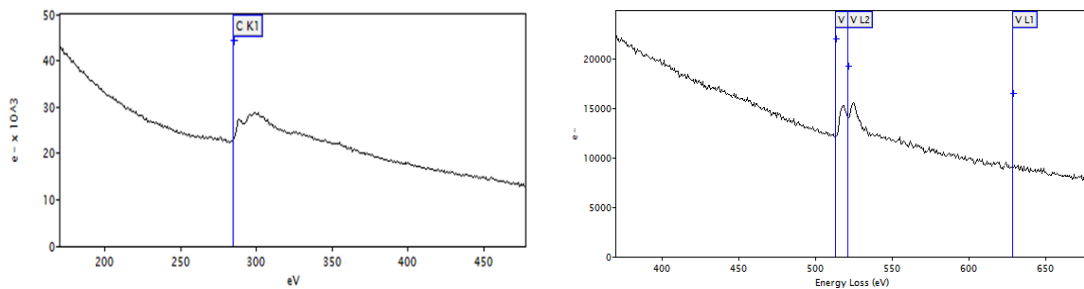


Figure 6.37 – EELS spectra for 01-630Nb⁺VMo showing that the fine sphere and rod shaped precipitates were mainly VC

The existence of arrays of precipitates in TEM thin foil images shown in Figure 6.38 confirms the presents of planar interphase precipitates in sample 02-630Nb⁺VMo. IP was very common in this sample and it was found randomly throughout most of the regions within the specimens. The high resolution images on carbon extraction replicas in Figure 6.39 shows the existence of very fine precipitates of very high number densities. Just like 01-630Nb⁺VMo, spherical precipitates dominated the sample followed by a few rod shaped ones. Cube shaped precipitates and stringers, though few and far between, were also found. However, the picture painted by thin foil images seemed to contradict that portrayed by the carbon extraction replica images. TEM thin foils images in Figure 6.38 suggests that the precipitates were mainly rod shaped while the carbon extraction replica images suggest that most of them were spherical. A detailed analysis of both rod and spherical precipitates revealed that they were mainly VC as shown on the EELS spectra in Figure 6.40. As a result of their similarity in chemical composition, it was also assumed that they were both the same and at different orientations, as previously observed in 01-630Nb⁺VMo. EDX analysis was also performed on the same particles and the spectrums are shown in Figure 6.41. The existence of Mo was also unique in the entire fine precipitates examined. Combining EELS and EDX data confirmed that

most of the particles were V(Mo)C just like in the 01-630Nb⁺VMo alloy. Due to their chemistry, rods and cube type precipitates were most likely to be the same, the difference being the direction in which the precipitates were orientated.

Finally, where IP was produced, the interparticle distances as well as the row spacings were measured. The average interparticle spacing was found to be 10 ± 2 nm while the row spacing was found to be 15 ± 2 nm.

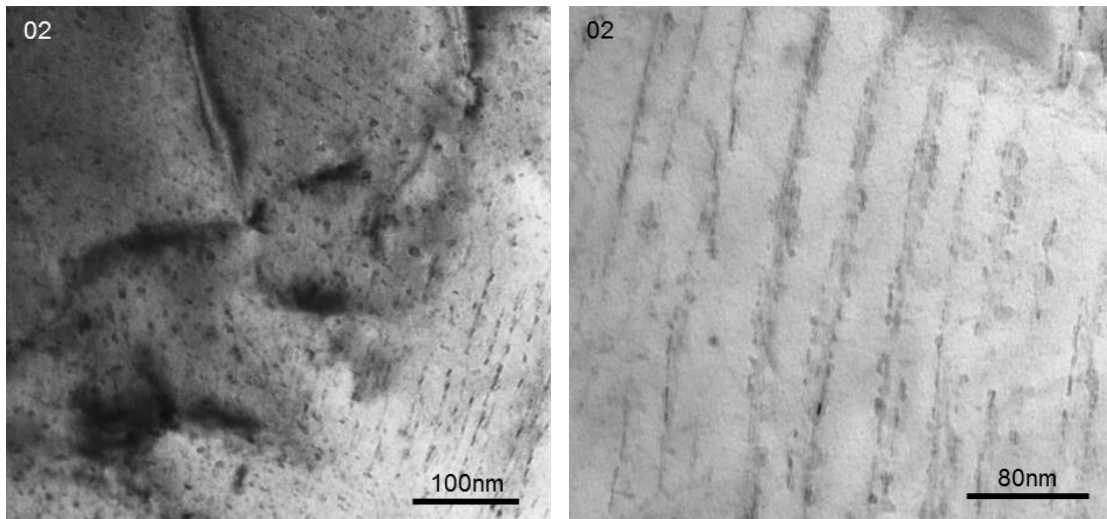


Figure 6.38 –TEM thin foil images showing the existence of planar IP in sample 02-630Nb⁺VMo

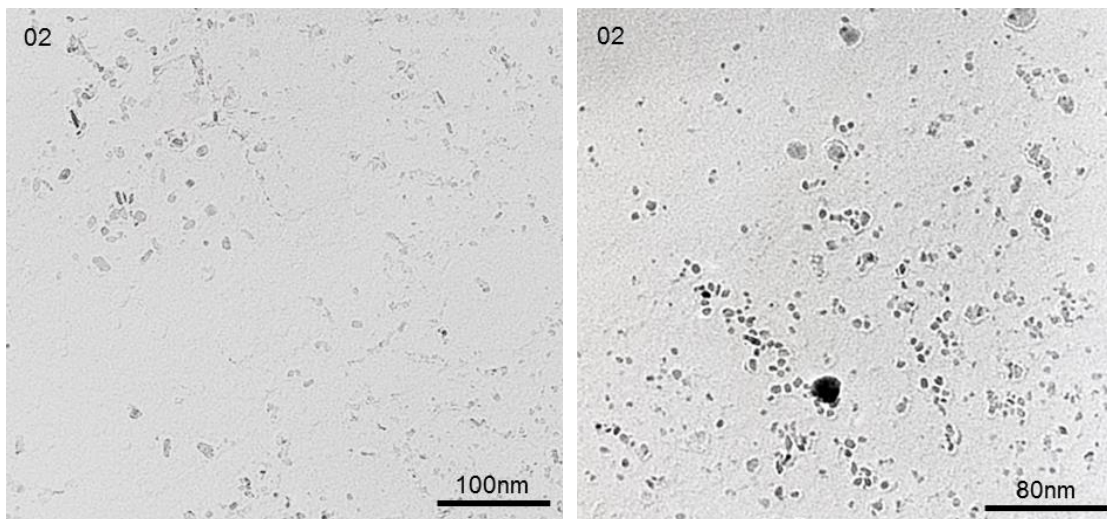


Figure 6.39 – TEM carbon extraction replica images showing the morphologies and relative sizes and distribution of the precipitates

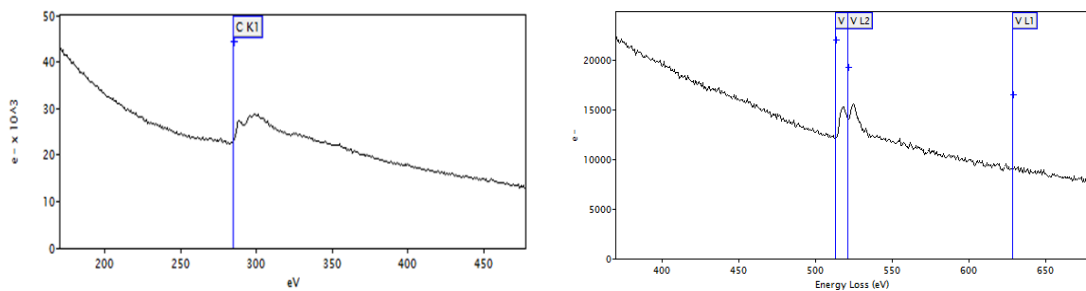


Figure 6.40 – EEL spectra for sample 02-630Nb⁺VMo showing that the rod and spherical precipitates were mainly VC

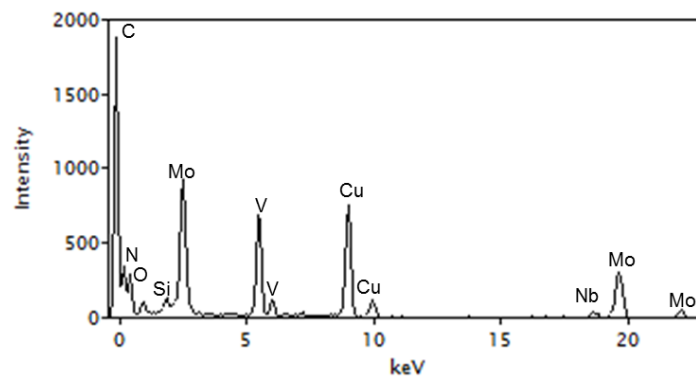


Figure 6.41 - EDX spectrum for spherical and rod shaped precipitates in samples 01-630Nb⁺VMo and 02-630Nb⁺VMo showing the presents of Mo in all fine precipitates

The images in Figure 6.42 are TEM thin foil micrographs for sample 06-600Nb⁺VMo. Fine precipitates were found randomly distributed throughout this sample. Interphase precipitates, though not very common, were occasionally found in some of the regions as depicted in Figure 6.42b. The same figure also shows the existence of coarse precipitates that were occasionally found in this sample.

Further studies were carried out on carbon extraction replicas and one of the images is shown in Figure 6.43. The images confirmed the presents of very fine precipitates which were previously observed on TEM thin foils. EEL spectroscopy was then carried out to analyse the precipitates found and the EELS spectra are shown in Figure 6.44 to Figure 6.46. EELS analysis showed that the majority of the precipitates were mainly VC and VCN. Even though Ti was not deliberately added Figure 6.46 showed its presence in some of the precipitates. Minute contaminations from previous castings are always detected. The strong peak detected can be attributed to the strong carbide forming tendency of Ti.

Once more, the rod and cube shaped precipitates had the same chemistry which suggests that they could be the same, just like in previous samples. Wherever fine precipitates were found, EDX analysis always revealed that Mo was always present and this sample was not an exception. EDX analysis showed the presence of both Mo and Nb in all the particles examined as shown in Figure 6.47.

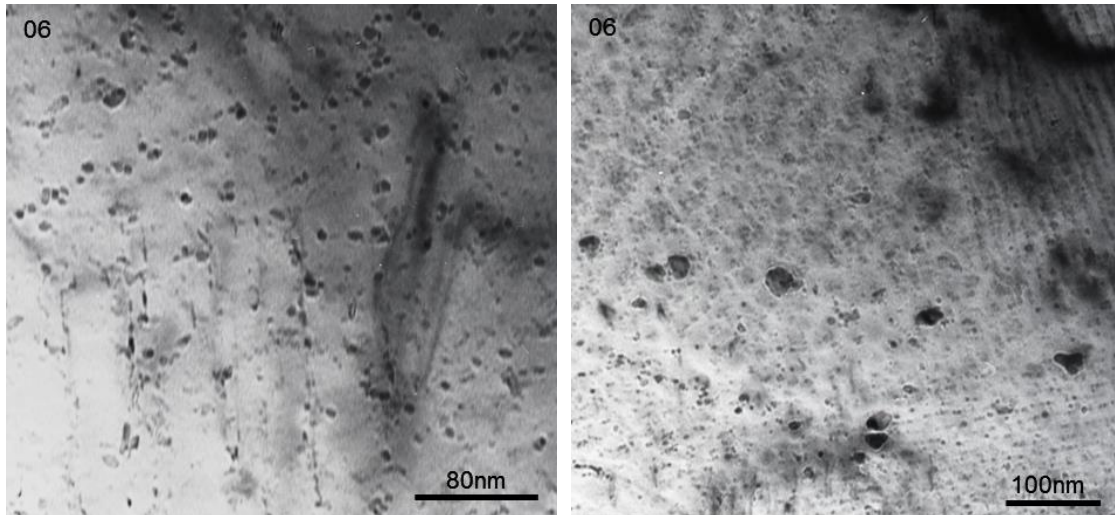


Figure 6.42 – TEM thin foil images for 06-600Nb⁺VMo showing regions with high precipitate number densities and some regions with planar IP

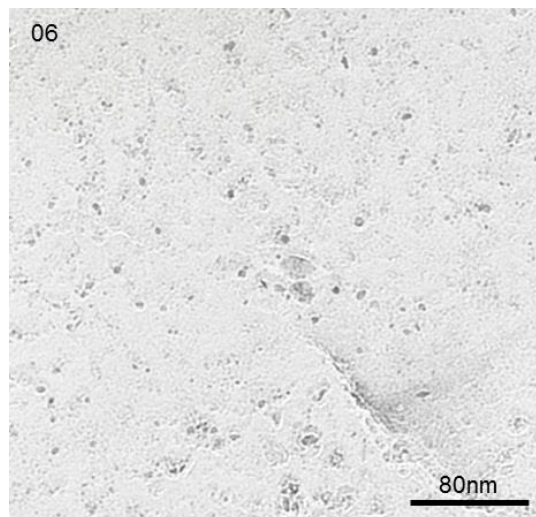


Figure 6.43- Carbon extraction replica image showing fine precipitates in a region of high precipitate density in 06-600Nb⁺VMo

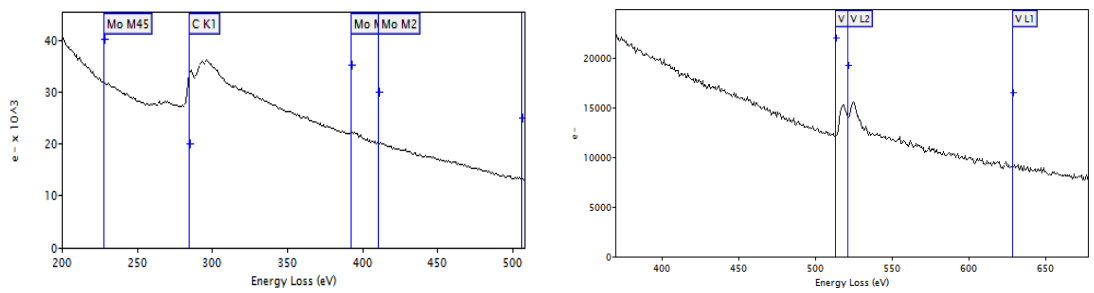


Figure 6.44 - EELS spectra showing V(Mo)C for the finest (~5nm) sphere and rod shaped precipitates in steel 06-600Nb⁺VMo

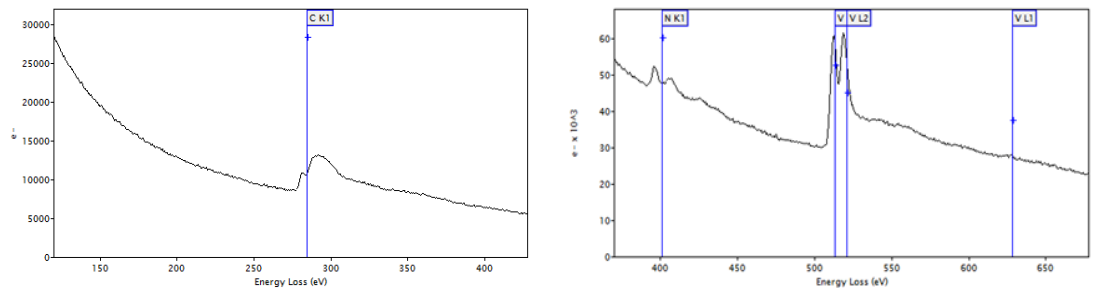


Figure 6.45 - EELS spectra showing VCN for (~10nm) sphere and rod shaped precipitates and stringers in steel 06-600Nb⁺VMo

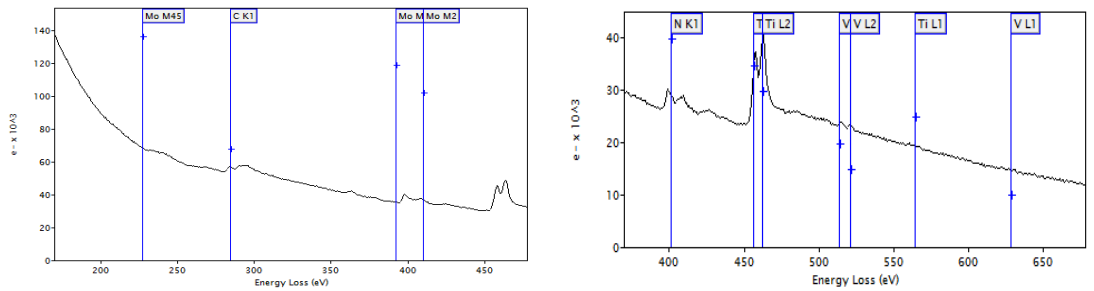


Figure 6.46 - EELS spectra showing the presence of Ti in some of the sphere and rod shaped precipitates, as well as stringers. This was common in coarser precipitates (>20nm)

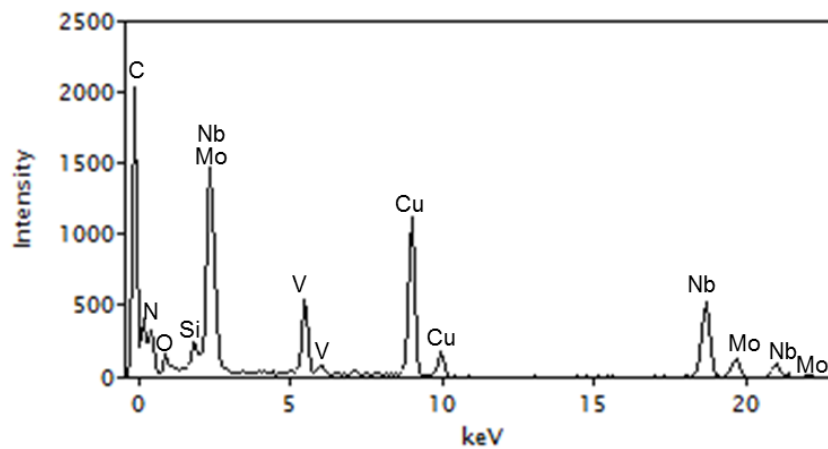


Figure 6.47 –EDX analysis revealed the presents of Mo and Nb in all precipitates analysed

The TEM carbon extraction replica images for sample 07-630NbVMo are shown in Figure 6.48. A mixture of coarse and fine precipitates were observed in Figure 6.48a while Figure 6.48b shows bands of precipitates that seemed to have been captured along a raised grain boundary. The majority of the precipitates were spherical, with a few rod, cube type and stringers. EEL spectroscopy in Figure 6.49 revealed that they were mainly VC while EDX analysis in Figure 6.50 showed high Mo peaks as well as the presents of Nb. Generally, the sensitivity of N in EELS is very high, resulting in very well defined peaks. The presence of N was not detected by EELS at this point; however the EDX spectrum in Figure 6.50 shows a small N peak.

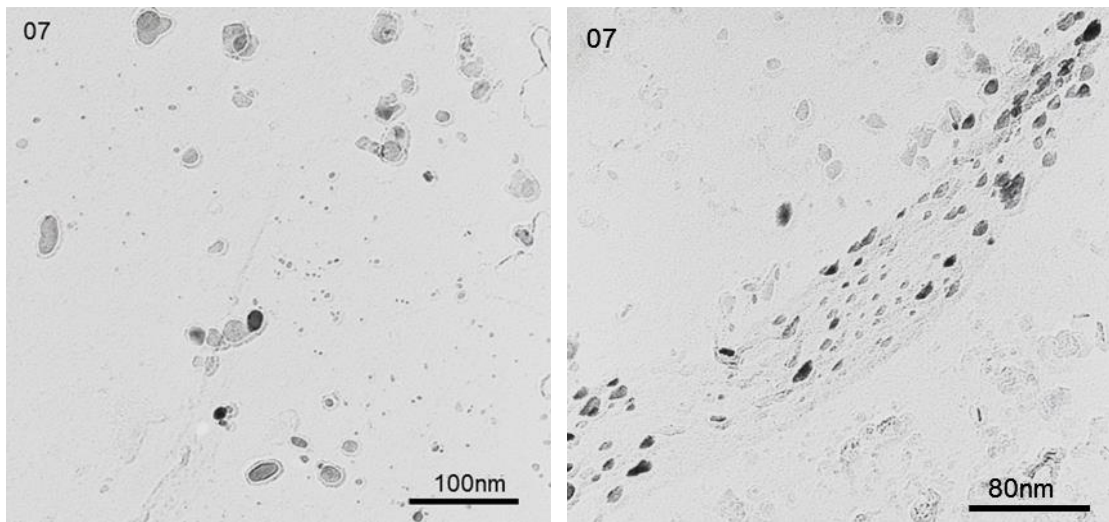


Figure 6.48 – TEM carbon extraction replica images for 07-630NbVMo showing a) a mixture of coarse and fine precipitates and b) precipitate bands which seemed to have been captured along raised grain boundaries.

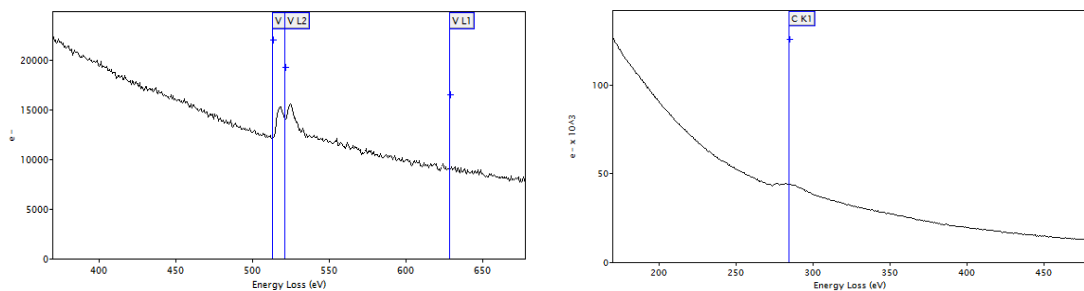


Figure 6.49 – EELS spectra for 07-630NbVMo confirming that the precipitates were vanadium carbides

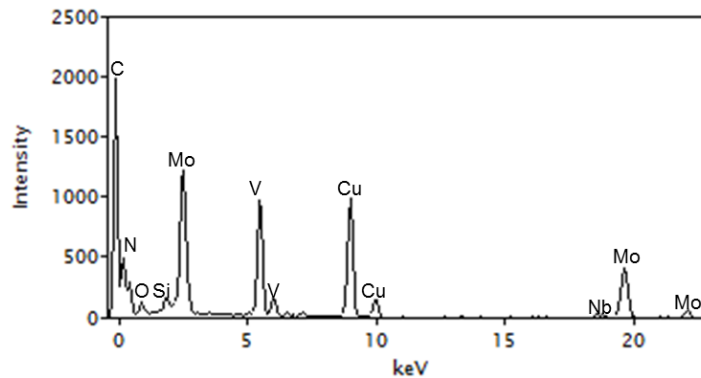


Figure 6.50 – EDX spectrum showing the presents of Mo in the fine precipitates

Figure 6.51 shows TEM thin foil images for 10-630Nb⁺VMo. Generally, IP was quite prevalent in this sample and where IP could not be established, high precipitate number densities were quite common. When performing TEM analysis, the sample should be carefully tilted to ensure that the precipitates are orientated in the right direction. Without proper tilting, precipitates can appear as random while in fact, they are planar interphase precipitates. The existence of such high number density of random precipitates like those shown in Figure 6.51a seems to imply that IP might have been present, but probably not at the correct orientation for imaging.

Generally, it is difficult to visualise IP in carbon extraction replicas. However, in this instance, distinct rows of precipitates were clearly observed as shown in Figure 6.52a; confirming planar IP previously identified though TEM thin foils. Similar to TEM thin foils analysis, carbon extraction replica samples also confirmed the dominance of fine precipitates of high number densities. The morphology for some of them can be envisaged on the high resolution image in Figure 6.52b. Spherical precipitates dominated the sample, while cube and rod type precipitates were also occasionally found. Most of the precipitates were VCN as confirmed by the EELS spectrum in Figure 6.53. Similar to all the previous samples discussed, EDX analysis shown in Figure 6.54 also confirmed the existence of Mo in the finest precipitates. Even though Nb was also present, the signal was quite weak.

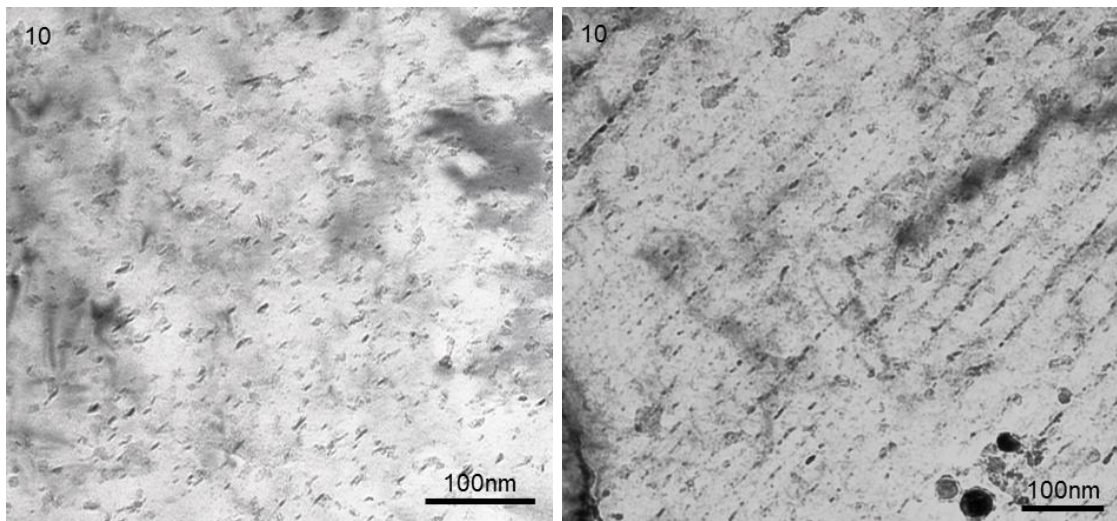


Figure 6.51 – TEM thin foil images for 10-630Nb⁺VMo showing a) random distribution of fine precipitates and b) rows of precipitates which confirms planar IP in this sample

Where IP was observed, the interparticle spacing was measured from the TEM thin foil images and this was found to be $8 \pm 2\text{nm}$ while the row spacing was found to be $22 \pm 3\text{nm}$.

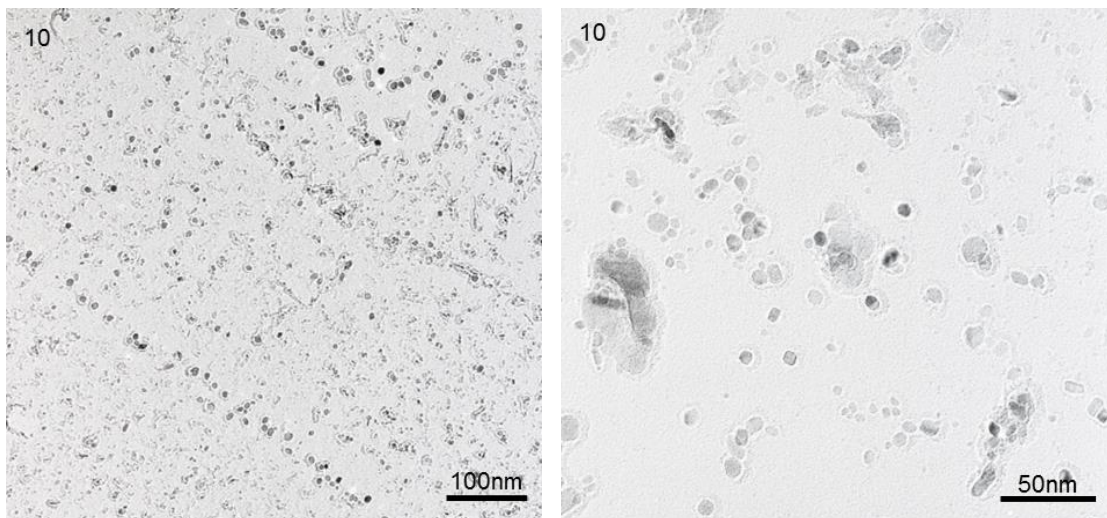


Figure 6.52 – Carbon extraction replica images for 10-630Nb⁺VMo showing a) region of planar IP and b) high resolution image showing the morphology of some of the precipitates

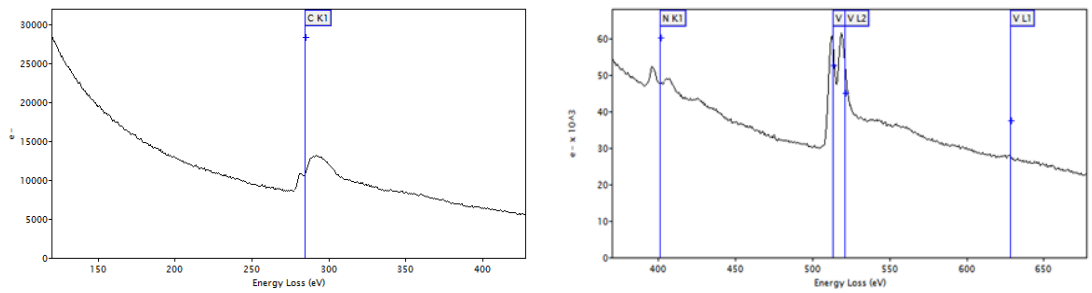


Figure 6.53 – EELS spectrum for spheres, strings, precipitate clusters, rods and cube type precipitates in 10-630Nb⁺VMo

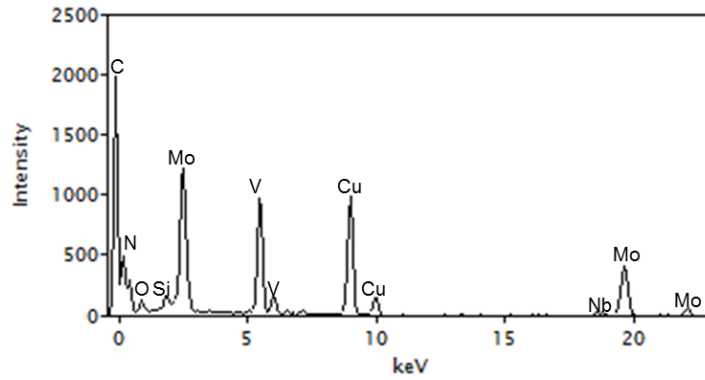


Figure 6.54 – EDX spectra for spheres, strings precipitate clusters, rods and cube type precipitates in 10-630Nb⁺VMo`

TEM thin foil images in Figure 6.55 show the morphology and distribution of precipitates in some of the regions of sample 14-650Nb⁺VMo. In general, three different regions were identified. The first region was dominated by IP as shown in Figure 6.55a while the second region had high precipitate number densities randomly distributed as shown in Figure 6.55b. The third region had fewer randomly distributed precipitates. TEM carbon extraction replicas shown in Figure 6.56 confirmed the same. Precipitate clusters were also a common occurrence as shown in carbon extraction replica images and some of these fine precipitates were less than 3nm in size. Due to the small size of these precipitates, it was quite difficult not only to capture them during the preparation of carbon extraction replicas, but also to count them. ImageJ software used to count the precipitates in this project sometimes finds it difficult to distinguish between dark contrast and the actual precipitates especially in instances where the precipitates are so fine. As a result, counting errors are a possibility. The precipitate count was likely to be underestimated, thereby understating the precipitate strengthening contribution to the yield strength.

Similar to the other samples, spherical particles formed the majority of the precipitates while a few of them were either rod or cube shaped. EELS analysis on the precipitates showed that the spherical and the rod shaped particles were mainly VCN. A few of them were identified as TiV(CN) while the cubic particles were identified as TiCN. EDX analysis in Figure 6.60 shows the existence of Nb and Mo in all the particles examined. Even though Ti was not deliberately added to this steel, the strong carbide (carbonitride) forming ability of Ti shows it was present probably as contamination from previous castings.

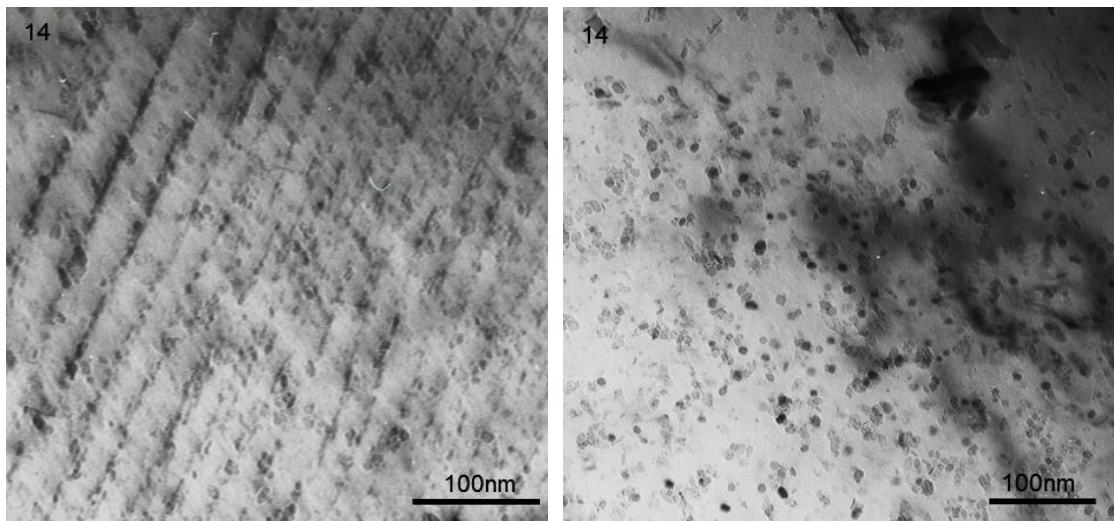


Figure 6.55 – TEM thin foil images for 14-650Nb⁺VMo showing a) region of IP and b) region of high precipitate numbers randomly distributed

The interparticle spacings were also measured in regions where IP was found and it was found to be approximately 11 ± 1 nm, while the row spacing was found to be approximately 30 ± 3 nm.

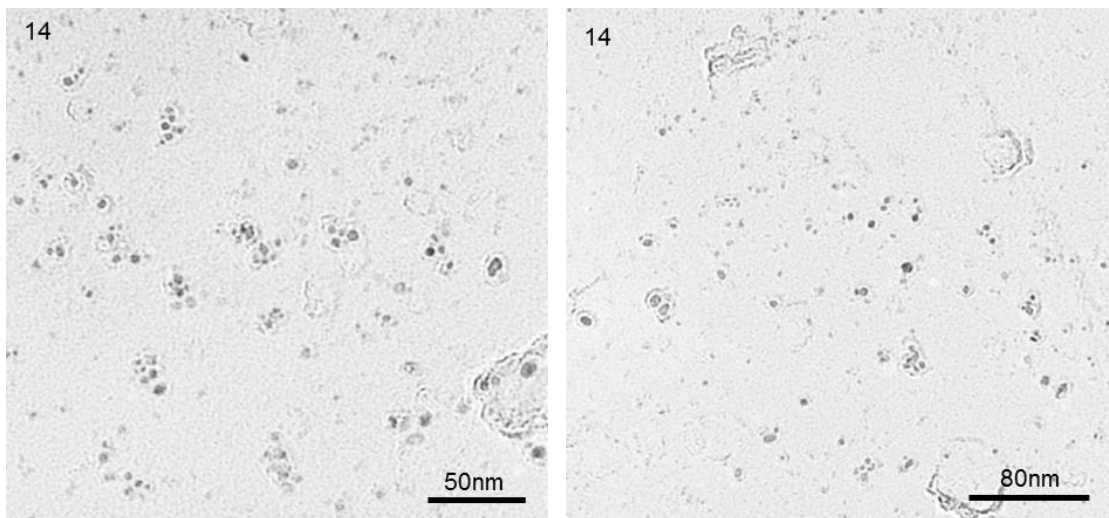


Figure 6.56 – TEM carbon extraction replica images showing fine precipitates, some of them in clusters, in sample 14-650Nb⁺VMo

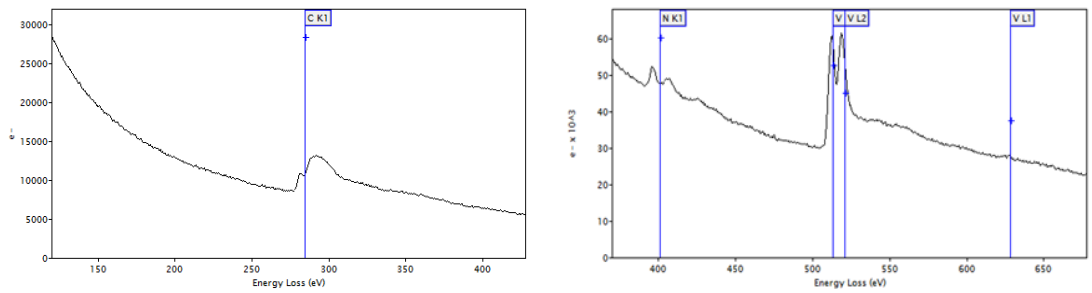


Figure 6.57 - EELS spectra for steel 14-650Nb⁺VMo showing VCN for the fine sphere and rod shaped precipitates

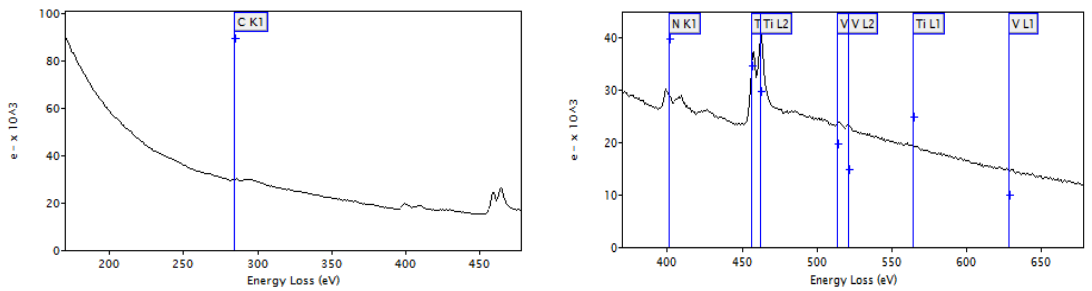


Figure 6.58 - EELS spectra for steel 14-650Nb⁺VMo showing Ti(V)CN in some stringers and cube type precipitates

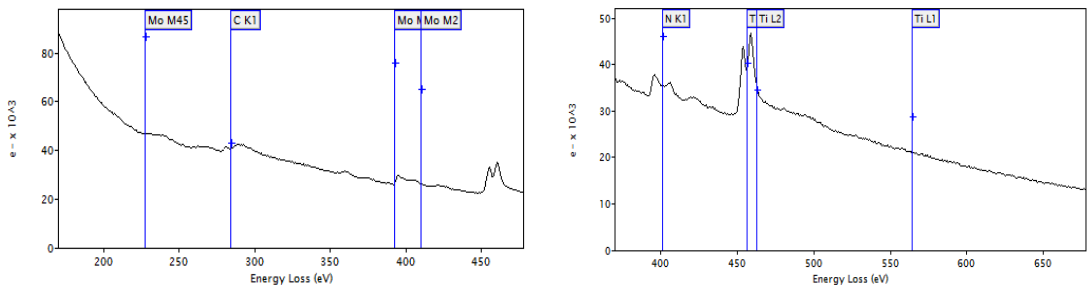


Figure 6.59 - EELS spectra for steel 14-650Nb⁺VMo showing TiCN mostly in cube type precipitates

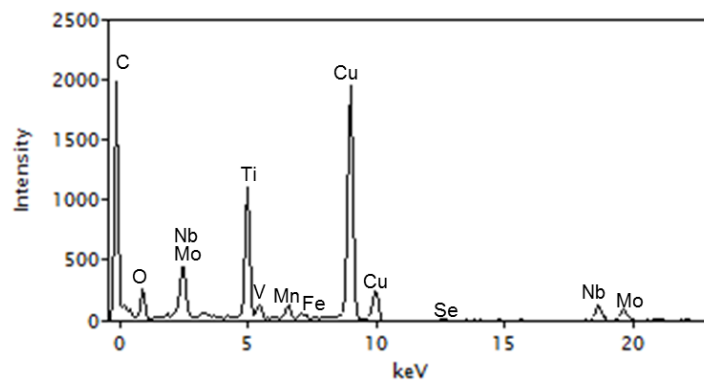


Figure 6.60– EDX spectrum showing the presents of Nb and Mo in sphere, rod, stringer and cube type precipitates in 14-650Nb⁺VMo

Figure 6.61 shows TEM thin foil images for sample 15-650TiMo. Figure 6.61a shows the existence of precipitates randomly distributed throughout the sample. The existence of two rows of precipitates on the edges of the grain boundary seems to suggest that they were not grain boundary precipitates, but interphase precipitates being viewed through the edge of the tilted grain boundary. Though not very distinct, the existence of IP is also confirmed by Figure 6.61b which shows arrays of precipitates especially when viewed from the bottom of the image. However, IP was not a regular occurrence in this sample. Generally, high precipitate number densities were only observed in some regions, while some of the regions had fewer precipitates. In most of these cases, the precipitates were randomly distributed. Carbon extraction replica images in Figure 6.62 confirm the observations from TEM thin foils. The images were taken in such a way that they could give a reflection of the majority of the regions within this sample. It is evident in both images that high precipitate number densities were located in half of the image while the other half had little or none at all. The precipitates found in this sample were mainly spheres, rods and cubes.

As expected, EEL spectroscopy in Figure 6.63 showed that most of the fine precipitates found were TiC. Even though V was not deliberately added to the alloy, EELS also confirmed the existence of VC and VCN as shown in Figure 6.64 and Figure 6.65 respectively. V might have been introduced through contamination from previous castings. EDX analysis in Figure 6.66 also confirmed the presents of Mo and Nb within all the precipitates analysed.

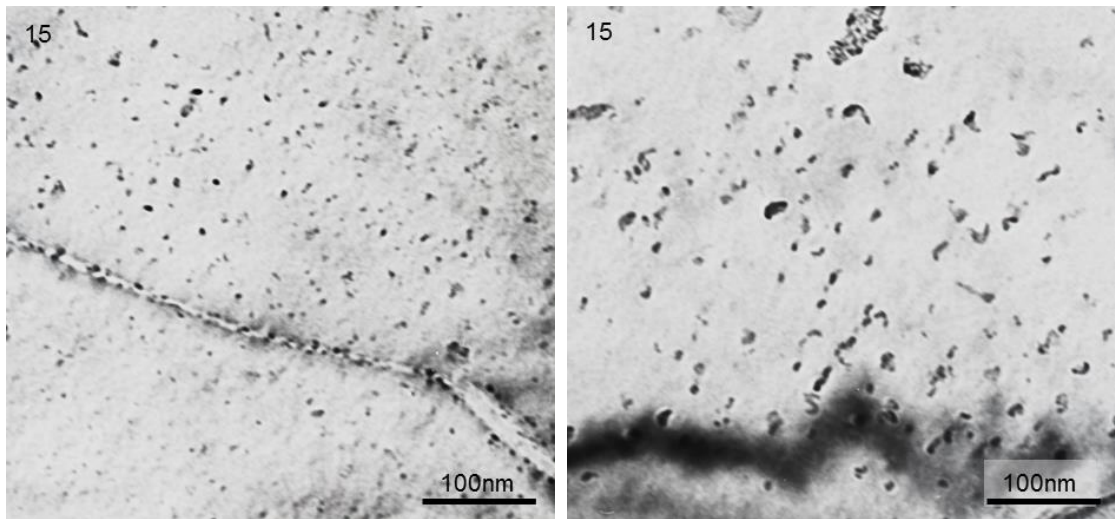


Figure 6.61 – TEM thin foil images for 15-650TiMo showing 15a) region of high precipitate number density as well as possible IP along a tilted grain boundary and 15b) region with possible IP

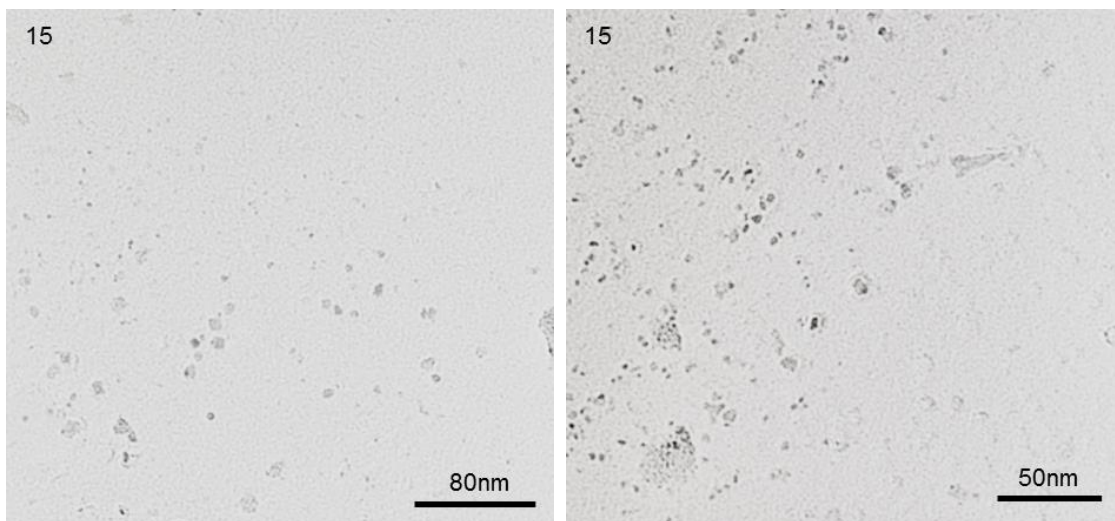


Figure 6.62 – TEM carbon extraction replica images showing the distribution of fine precipitates within the sample in 15-650TiMo

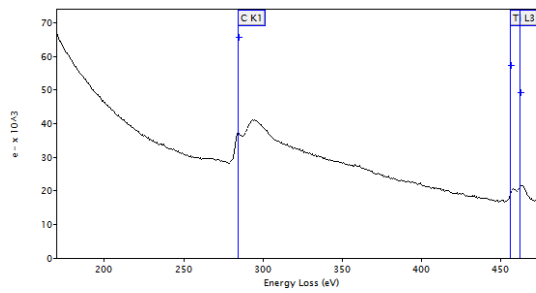


Figure 6.63 - EELS spectra for steel 15-650TiMo showing that the majority of the fine carbides were TiC

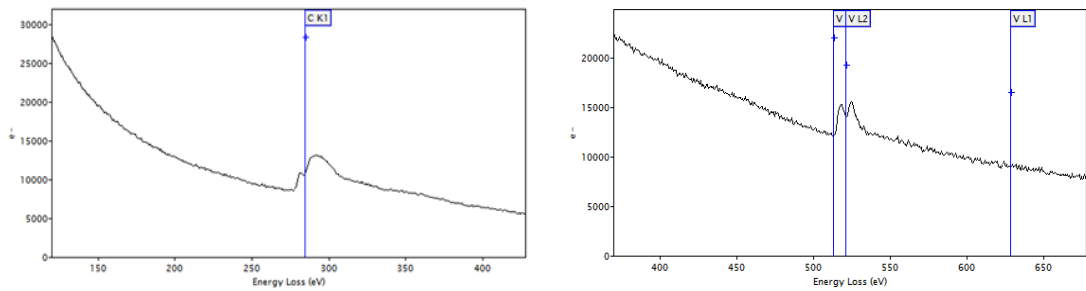


Figure 6.64 - EELS spectra for steel 15-650TiMo showing that some of the round and square precipitates were VC

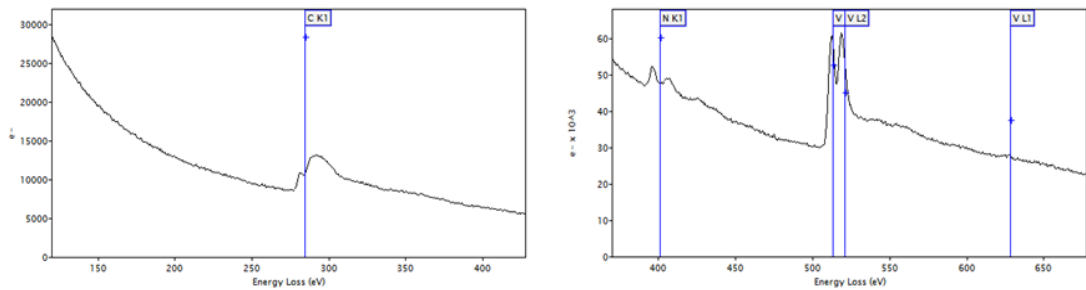


Figure 6.65 - EELS spectra for steel 15-650TiMo showing that some of the round and square precipitates were VC

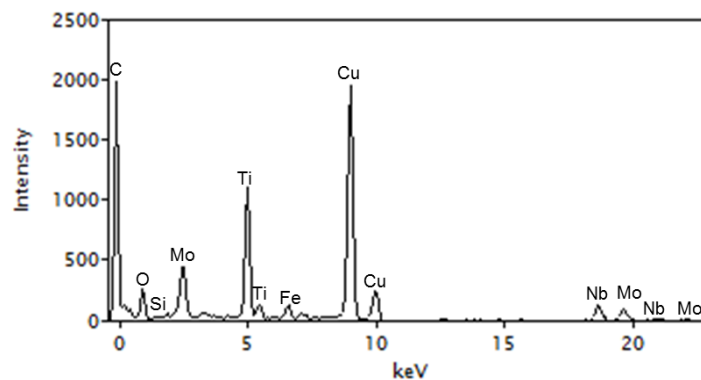


Figure 6.66 – EDX spectrum showing the presents of Mo and Nb in all precipitates analysed

The images in Figure 6.67 are carbon extraction replica micrographs for 16-650Ti. The major characteristic of this sample was the existence of fewer regions with high precipitate number densities. Most of the regions had a low number density of precipitates as shown in Figure 6.67. The sample was also dominated by spherical precipitates while rod and cubic shaped precipitates were scarcely distributed. EELS analysis in Figure 6.68 showed that these precipitates were TiC. EDX analysis in Figure 6.67 showed that Nb was also present within the precipitates.

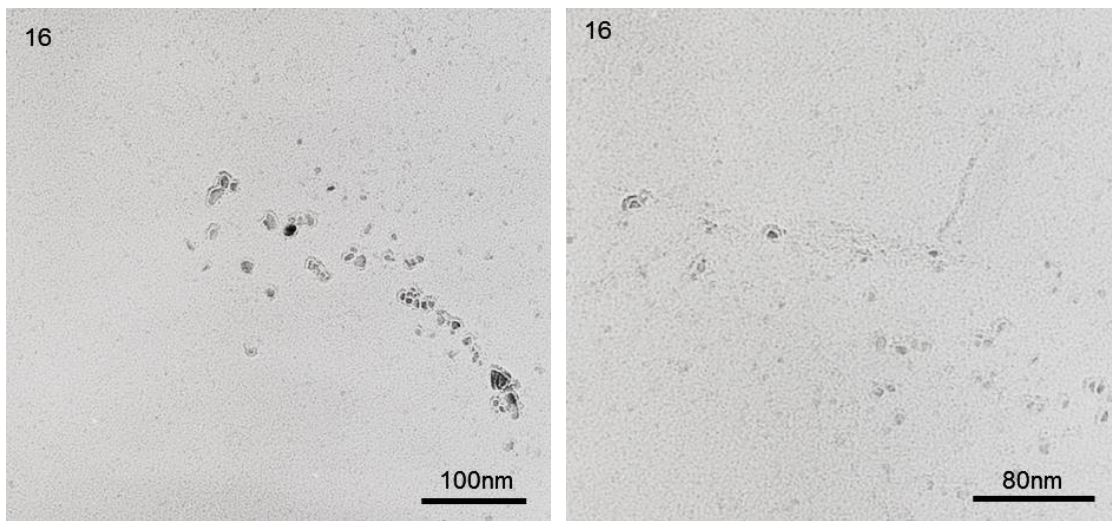


Figure 6.67 – TEM Carbon extraction replica images for spheres and stringers in sample 16-650Ti

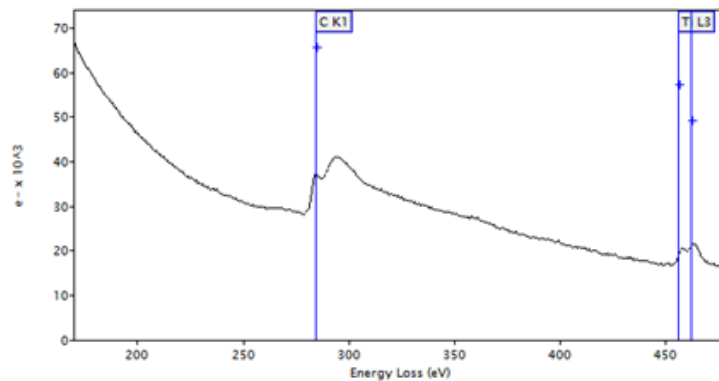


Figure 6.68 – EELS spectrum for spheres and stringers in sample 16-650Ti

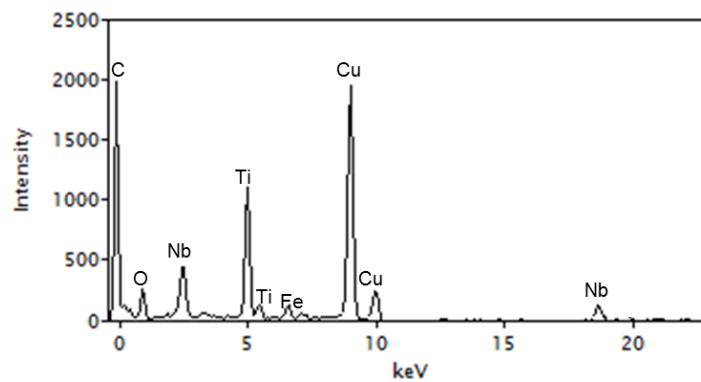


Figure 6.69 – EDX spectrum for spheres and stringers in sample 16-650Ti

Just like 16-650Ti, 17-650VMo had very few regions of high precipitate number densities. However, where precipitates could be found, they were in high number densities, mostly randomly distributed even though planar IP was also quite common. Figure 6.70 are TEM thin foil images showing a region of random high precipitation number densities and a region with planar IP. Figure 6.70a shows a region of high number density dominated by rod type precipitates while Figure 6.70b shows that where planar IP existed, the precipitates seemed to exist in pairs, the reason of which could not be established at this stage. Grain boundary carbides were also found in other regions as shown by the arrows in Figure 6.70b. TEM on carbon extraction replicas also confirmed the low precipitate counts in the sample as shown in Figure 6.71. Most of the regions had very few or no precipitates at all. As previously shown on TEM thin foil images, the precipitates found were mainly either spherical or rod shaped. The array of precipitates in Figure 6.71b seemed to have formed along the grain boundary, while there were no precipitates at all within the grains in this instance.

EELS analysis in Figure 6.72 on the precipitates showed that they were mainly VC with some VCN while EDX analysis in Figure 6.73 confirmed the existence of Mo in the fine VC. However, EDX analysis also showed the existence of Nb and Ti in these precipitates. The fact that Ti was not intentionally added suggests cross contamination probably from previous batches.

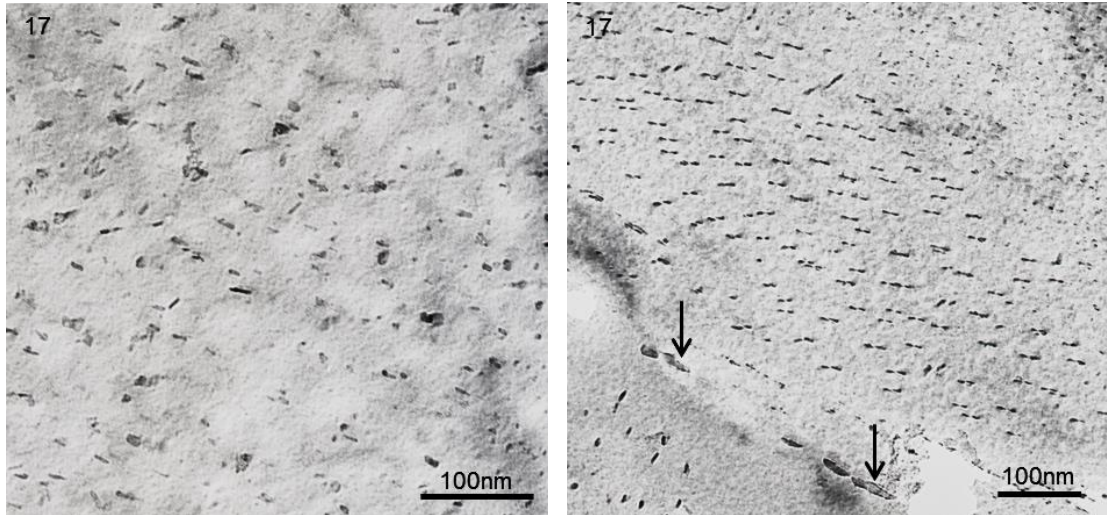


Figure 6.70 – TEM thin foil images for 17-650VMo showing a) region of high rod shaped precipitate number densities and b) region with IP and grain boundary carbides shown by the arrows

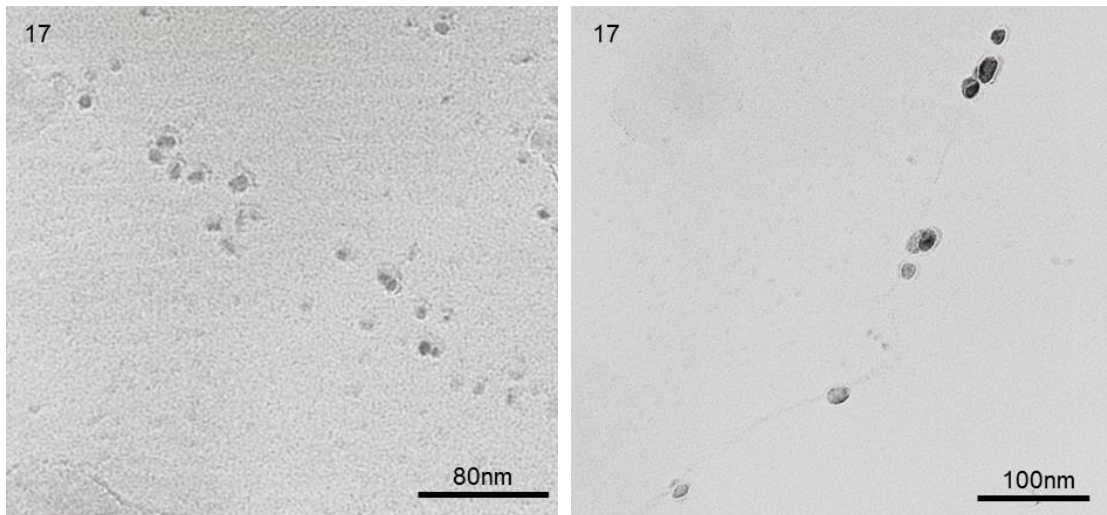


Figure 6.71 – TEM carbon extraction replica images showing the low precipitation counts within the 17-650VMo

a

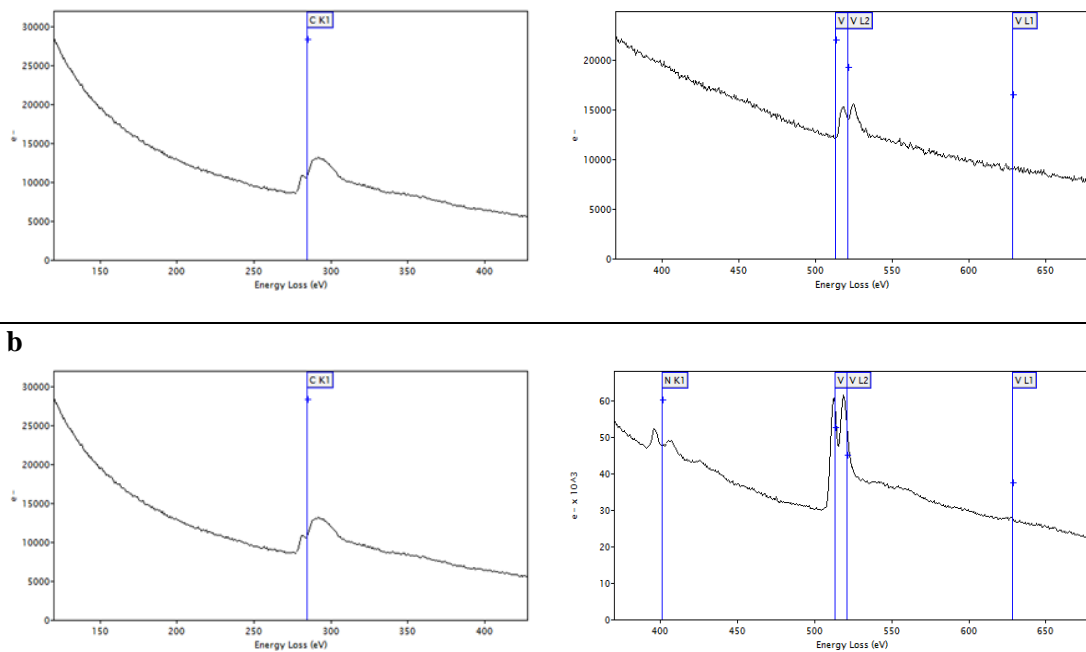


Figure 6.72 - EELS spectra for spherical, stringers and rod type precipitates in 17-650VMo

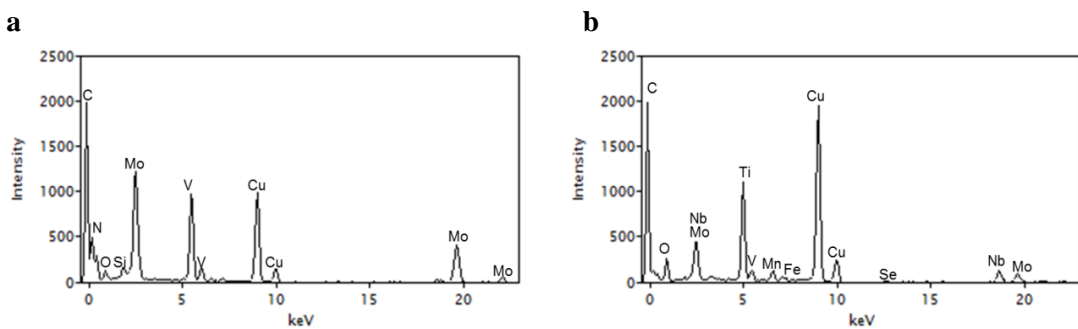


Figure 6.73 – EDX analysis for 17-650VMo showing spectrum for a) the majority of round, stringers and rod type precipitates and b) a few rod type precipitates

Figure 6.74 are carbon extraction replica images for sample 18-650V. The major similarity between this sample and 17-650VMo was the existence of regions free from precipitates as well as other regions with very few precipitates. This is clearly illustrated in Figure 6.74a where the bottom half has got very few precipitates while the top half has high precipitate number density. The same is also shown in Figure 6.74b. Coarse precipitates that seemed to have been formed along the grain boundary shown in Figure 6.74a were also seldom found in this sample. Spherical type precipitates dominated the sample while rod shaped precipitates were very few and far between. Both EELS analysis in Figure 6.75 and EDX analysis in Figure 6.76 confirmed that these precipitates were VC.

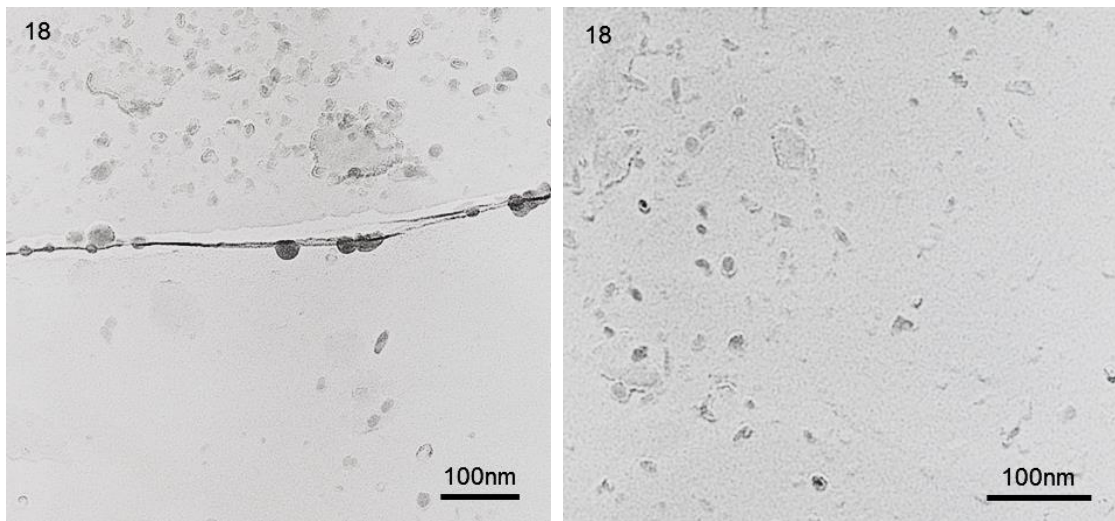


Figure 6.74 – Carbon extraction replica images showing regions of high and low precipitate number densities in 18-650V

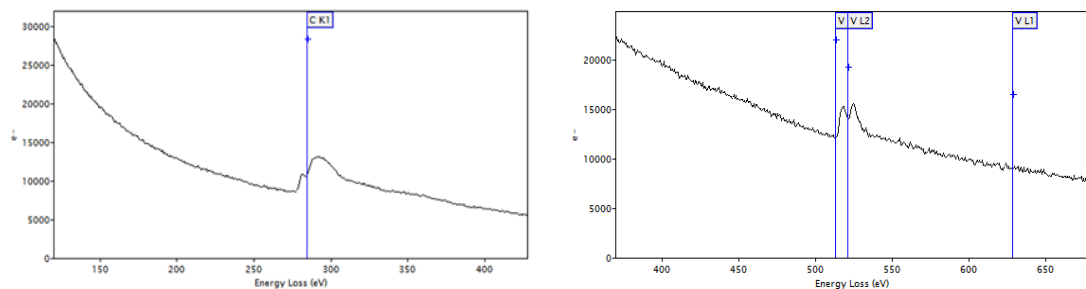


Figure 6.75 - EELS spectra for rod and sphere type precipitates in 18-650V

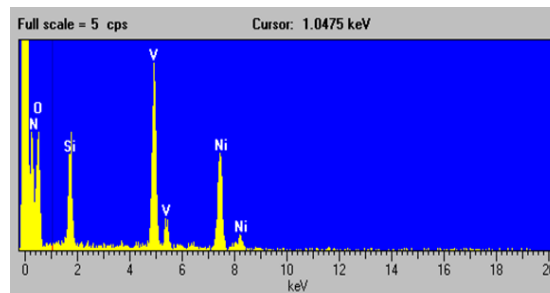


Figure 6.76 – EDX spectrum for rod shaped and spherical precipitates in 18-650V

Figure 6.77 shows TEM images from thin foil samples for sample 19-650NbMo. Some precipitates were found in the grain boundaries as shown in Figure 6.77a while the majority were found randomly distributed throughout the sample. Some appeared as stringers while others were spherical and rod shaped. The curved boundaries suggest pinning of the grain boundary by the precipitates.

The images in Figure 6.78 are TEM carbon extraction replica micrographs for the same sample. As in thin foils, the precipitate number densities were quite low. Fewer regions had average precipitate counts as shown in both thin foil and carbon

extraction replica images with most of the regions having few or no precipitates at all.

Due to the high sensitivity of the technique for Ti, the EELS spectra for 19-650NbMo in Figure 6.78 show that the precipitates found were mainly TiCN even though Ti was not purposefully added. Hence, the presence of Ti can only be due to contamination from previous castings. However, EDX analysis in Figure 6.80 shows the presence of Nb and Mo. It was concluded that the precipitates in this sample were mainly Nb(Mo)C.

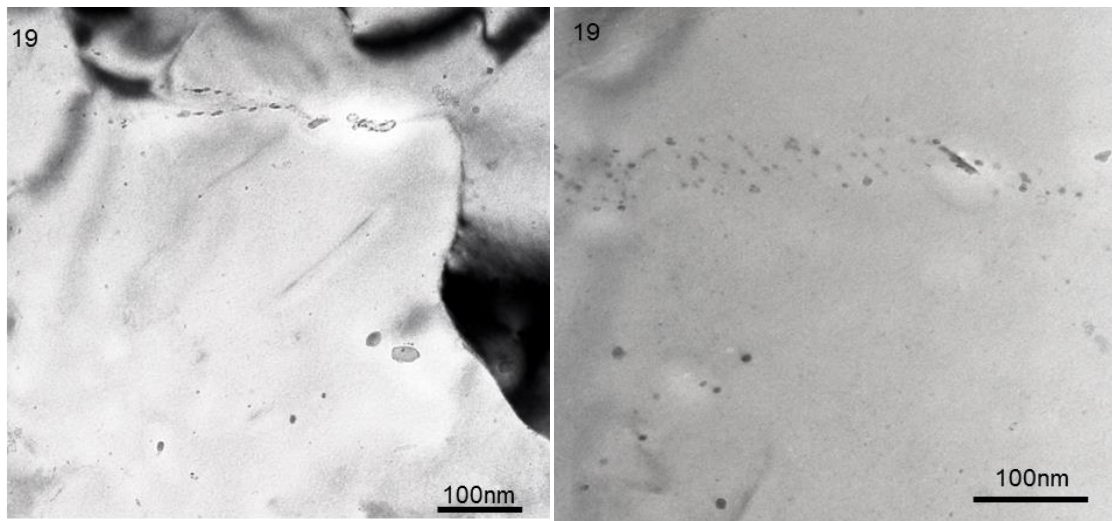


Figure 6.77 – TEM thin foil images showing the location and morphology of precipitates in 19-650NbMo

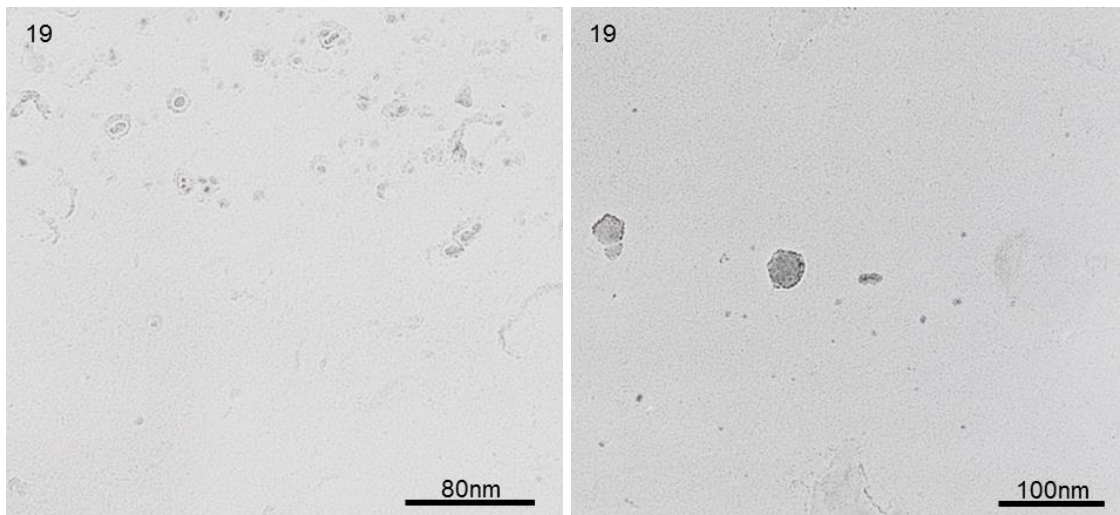


Figure 6.78 – TEM carbon extraction replica images precipitate distribution in 19-650NbMo

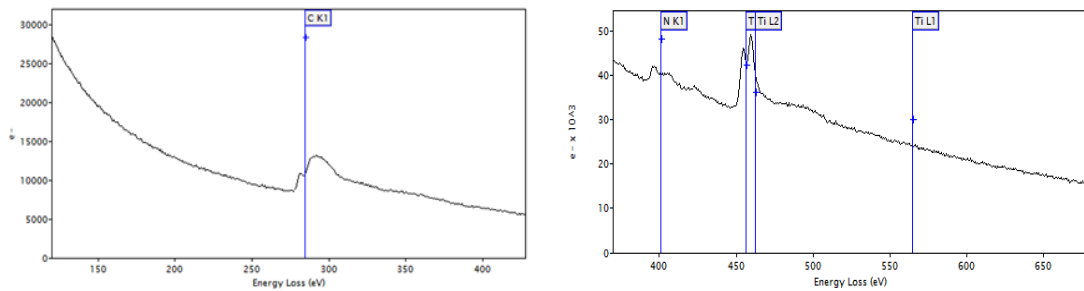


Figure 6.79 – EELS spectrum for the sphere and cube type precipitates in 19-650NbMo

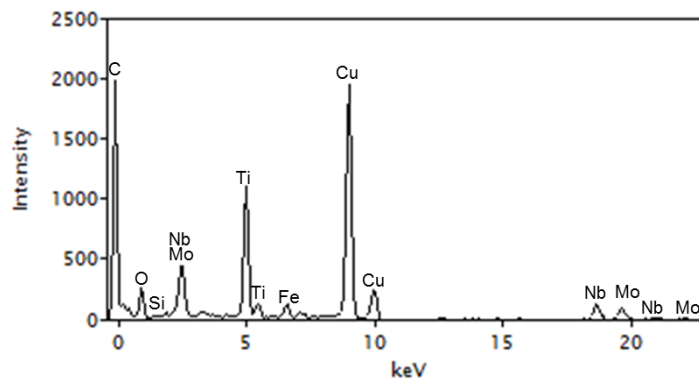


Figure 6.80 – EDX spectrum for the sphere and cube type precipitates in 19-650NbMo

TEM Carbon extraction replica images for sample 20-650Nb are shown in Figure 6.81. The distribution of the precipitates in this sample was quite similar to 19-650NbMo. Spherical particles formed the majority of the precipitates while a few cube shaped precipitates, though few, were also found haphazardly distributed throughout the sample. In general, some of the regions had very few or no precipitates at all while average precipitates counts could be found in other regions as presented in Figure 6.81.

A comprehensive analysis of the precipitates using EEL spectroscopy revealed that they were mainly Ti(Mo)CN even though Ti was not deliberately added. Again, the presents of Ti could be a result of contamination from previous castings. Figure 6.82 shows the EELS spectrum while Figure 6.83 shows the EDX analysis for 20-650Nb. EDX analysis shows a high Nb peak, which confirms that the precipitates found were Nb(Mo)C. The reason why Nb was not detected by EELS could be due its low sensitivity in EELS. Again, this is a good example where combining EELS and EDX can produce better results rather than using one technique.

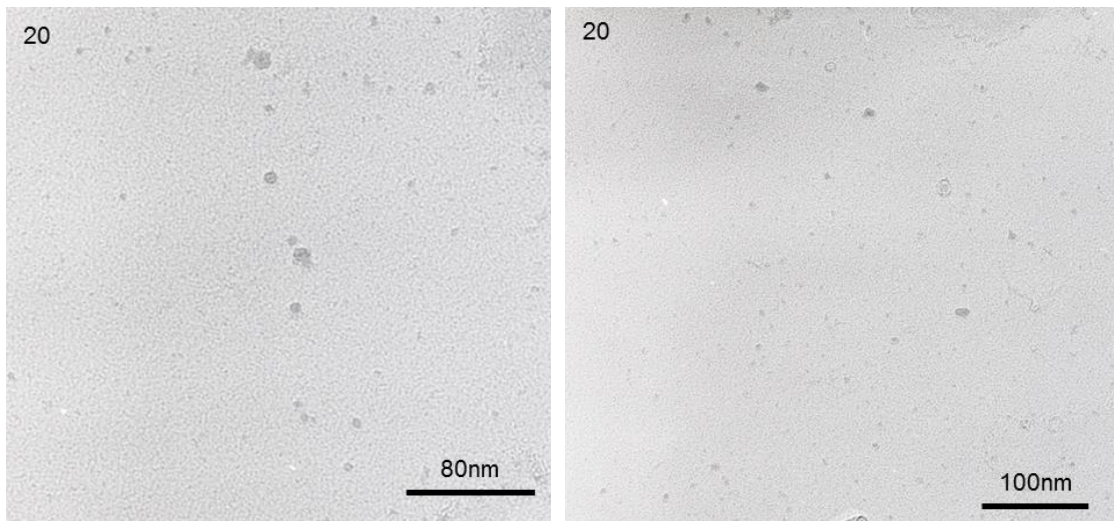


Figure 6.81 – TEM carbon extraction replica images showing the distribution of precipitates in 20-650Nb

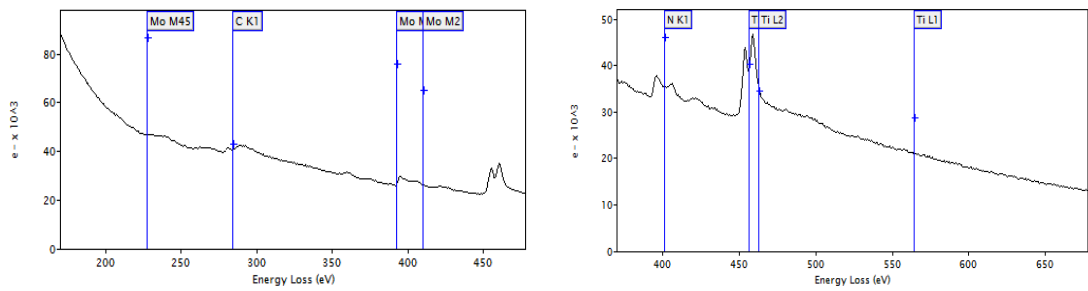


Figure 6.82 – EEL spectroscopy analysis showing the chemistry of the precipitates in 20-650Nb

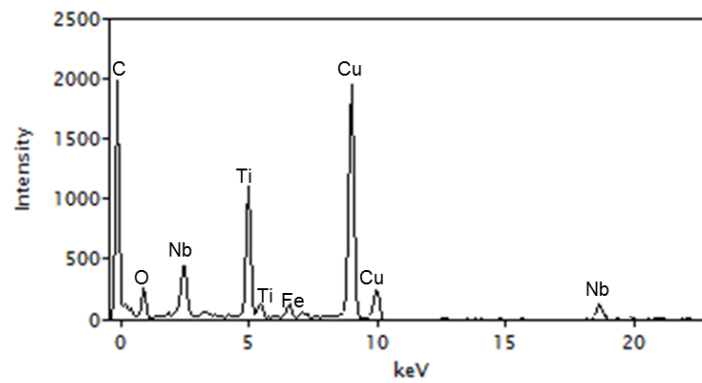


Figure 6.83 – EDX analysis showing the chemistry of the precipitates in 20-650Nb

Figure 6.84 shows TEM thin foil images for sample 21-650TiMo. One noticeable feature was the high number densities of precipitates homogeneously distributed throughout the sample. The precipitate density compared very well to samples 02-630Nb⁺VMo and 10-630Nb⁺VMo. However, unlike the other two, there was no clear evidence of IP in this sample. A close analysis of the microstructure of 21-650TiMo in Figure 6.25 shows that it was predominantly bainitic ferrite. This could be the reason why IP could not be produced. However, the high carbon content in the sample ensured that there was enough carbon to form high number densities of precipitates.

The precipitate morphology as well as their distribution can be clearly visualized in the images in Figure 6.84. It is clear that the sample also had superfine precipitates (<3nm) which can be seen in Figure 6.84a. Spherical precipitates dominated the sample, however, the finest precipitates appeared to be rod shaped. Cube type precipitates were also found, even though they were very few and far between. High resolution TEM carbon extraction replica images in Figure 6.85 confirmed the precipitate morphology and their distribution as previously revealed through TEM thin foils. Due to the precipitate high number densities, it was difficult to establish whether some of the dark contrasts were actual precipitates. As a result, dark field imaging was also used to verify that these were actual precipitates. Figure 6.85b is a dark field image confirming that the dark spots were actual precipitates. EELS analysis in Figure 6.86 endorses that the precipitates found were TiC. Since EELS is not sensitive enough to heavier elements, the EDX spectrum in Figure 6.87 confirmed the presence of Mo in the precipitates. It has already been reported in literature that Mo plays a role in slowing down the rate of coarsening in TiC[7, 10]. This is likely to be the major reason why such superfine precipitates were observed.

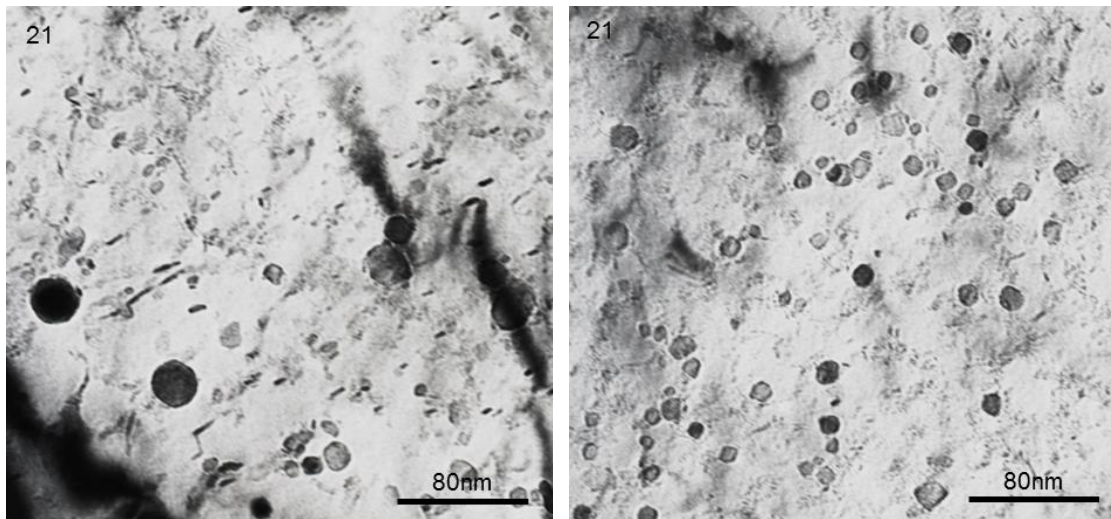


Figure 6.84 – TEM thin foil images for 21-650TiMo showing random distribution of fine precipitates within the sample

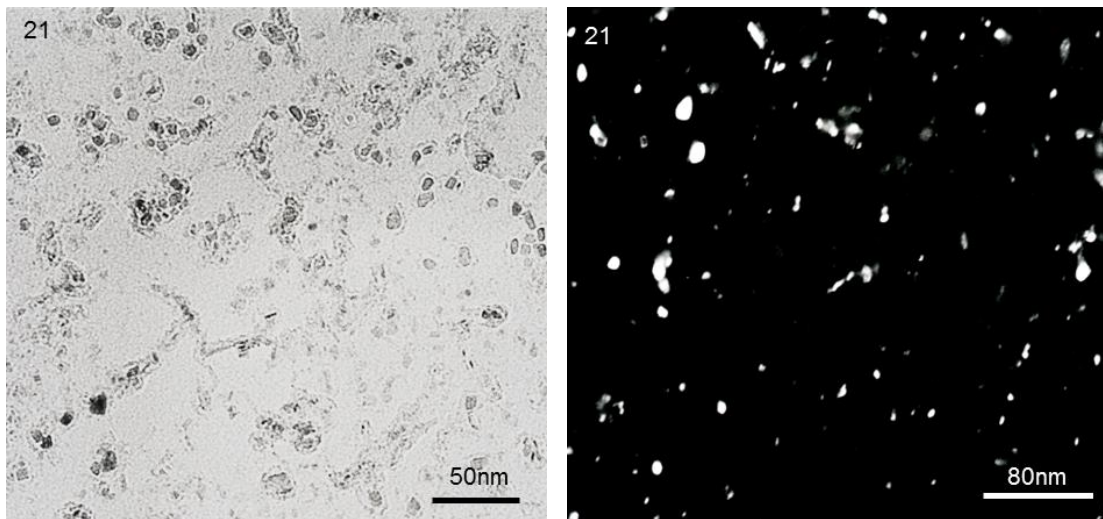


Figure 6.85 – TEM carbon extraction replica images for sample 21-650TiMo showing a) high resolution bright field image showing fine precipitates and b) dark field image confirming that the dark contrast were actual precipitates

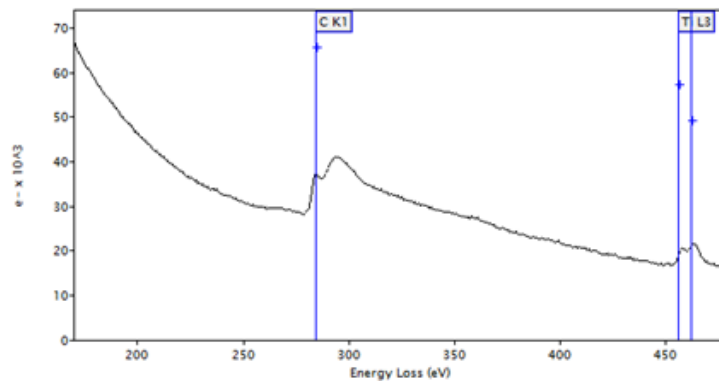


Figure 6.86 – EELS spectrum for 21-650TiMo showing that the fine precipitates were TiC

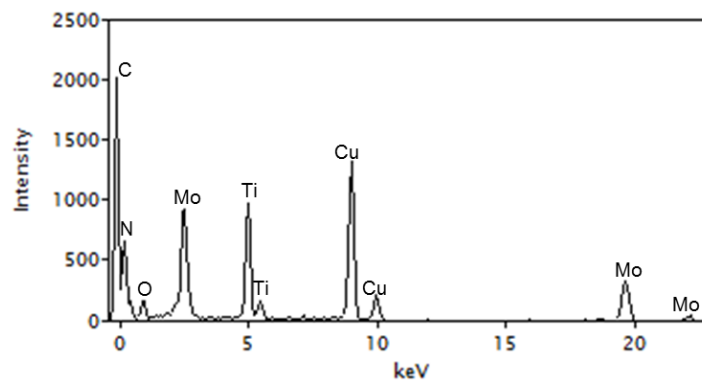


Figure 6.87 – EDX spectrum confirming the presents of Mo (Ti(Mo)C) in the fine precipitates in 21-650TiMo

Figure 6.88 are TEM thin foil micrographs for sample 22-630N⁺. The major difference between this sample and the others were the high N content which was more than double in this sample as compared to any of the other samples. Some regions had high precipitate number densities as well as evidence of IP while others had little or no precipitates at all. The existence of high precipitate density and possible IP can be seen in Figure 6.88b while Figure 6.88a shows a region with random precipitates surrounded by regions with few precipitates. Figure 6.89 are micrographs from carbon extraction replica showing the precipitation morphology and their distribution within the sample. Figure 6.89a show a region where a band of precipitates is sandwiched between regions with very few precipitates and this was quite a common occurrence within this sample. In some cases, precipitates were found in clusters, surrounded by regions with few or no precipitates at all as shown in Figure 6.89b. The majority of the precipitates were spherical, with a few rod, cube and some stringers scattered all over the sample. EELS analysis in Figure 6.90 confirmed that the precipitates were mainly VCN. Further EDX analysis in Figure

6.91 confirmed the presence of Mo and Nb in the precipitates. The presence of Mo under conditions of high N content confirms the fact that Mo also plays a role in retarding coarsening of precipitates wherever N is involved just as in C. The high N content was deliberately added in this sample in order to establish the effect of Mo when both C and N are introduced while Nb was limited to 0.008 in order to minimise the rolling forces.

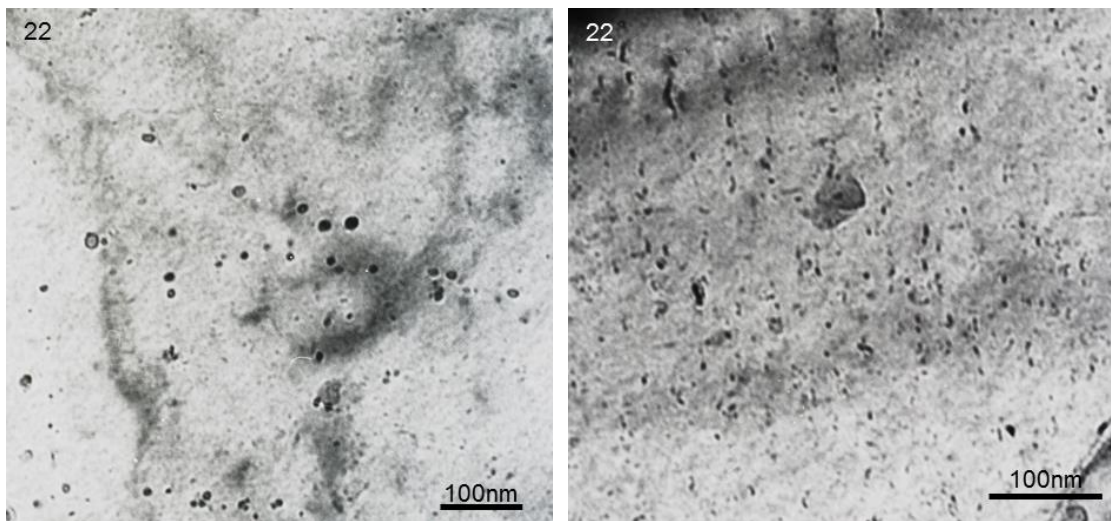


Figure 6.88 – TEM thin foils images for 22-630N⁺ showing a) random distribution of precipitates and b) Interphase precipitates in some regions

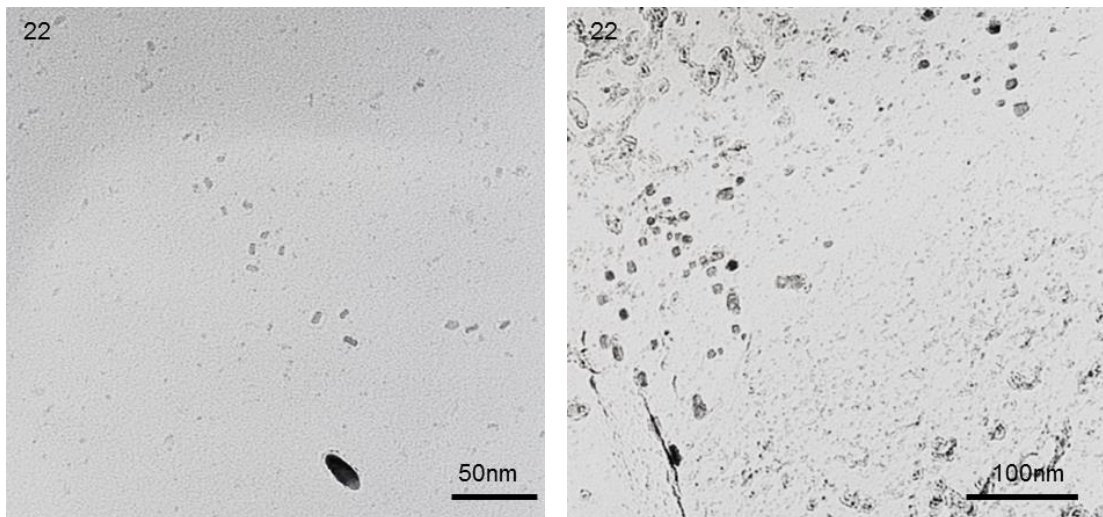


Figure 6.89 – TEM carbon extraction replica images for 22-630N⁺ showing a) region of low precipitation number densities and b) random distribution of precipitates in the sample

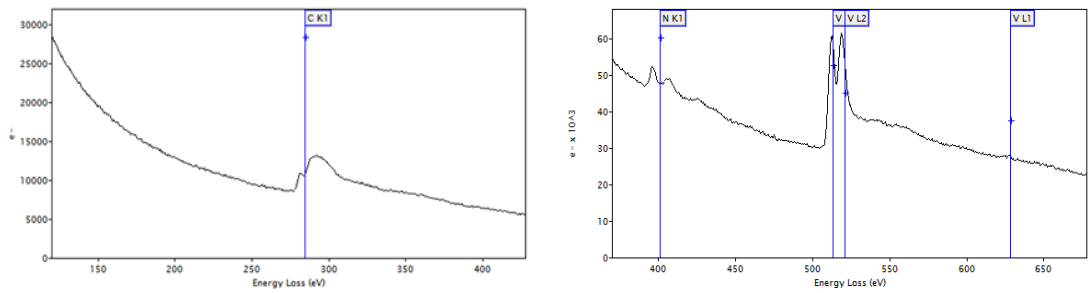


Figure 6.90 – EELS spectra showing that the spheres, rods and stringers in 22-630N⁺ were mainly VCN

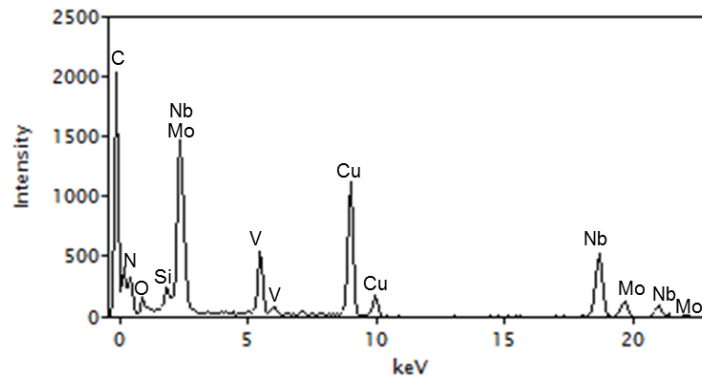


Figure 6.91 - EDX spectrum confirming the presents of Nb and Mo in the precipitates previously analysed by EELS above

6.5.1 Precipitate Size Distribution

Using at least ten TEM carbon extraction replica images per each sample, a total of up to 4000 precipitates were counted per sample. The precipitate counts are tabulated in Table 6.3.

Table 6.3 – Precipitate Counts Summary

Sample	Precipitates counts per μm^2	Average Precipitate Size (nm)
01-630 Nb ⁺ VMo	475	6.9 ± 0.1
02-630 Nb ⁺ VMo	1467	4.9 ± 0.1
06-600 Nb ⁺ VMo	747	4.0 ± 0.1
07-630NbVMo	316	8.6 ± 0.1
10-630Nb ⁺ VMo	1766	5.2 ± 0.1
14-650Nb ⁺ VMo	730	4.2 ± 0.1
15-650TiMo	610	7.2 ± 0.1
16-650Ti	180	8.2 ± 0.2
17-650VMo	157	10.8 ± 0.3
18-650V	194	12.9 ± 0.1
19-650NbMo	328	5.6 ± 0.1
20-650Nb	153	6.3 ± 0.2
21-650TiMo	1467	5.7 ± 0.1
22-630 N ⁺	311	6.9 ± 0.3

A comparison of precipitate counts converted to per μm^2 is shown Figure 6.92. It is apparent that 10-630Nb⁺VMo had the highest precipitate count of 1766 particles/ μm^2 . In the same category were 02-630Nb⁺VMo and 21-650TiMo with 1467 particles/ μm^2 per each of the samples. Samples with the lowest counts included 16-650Ti with 180 particles/ μm^2 , 17-650VMo with 157 particles/ μm^2 , 18-650V with 194 particles/ μm^2 and 20-650Nb with 153 particles/ μm^2 .

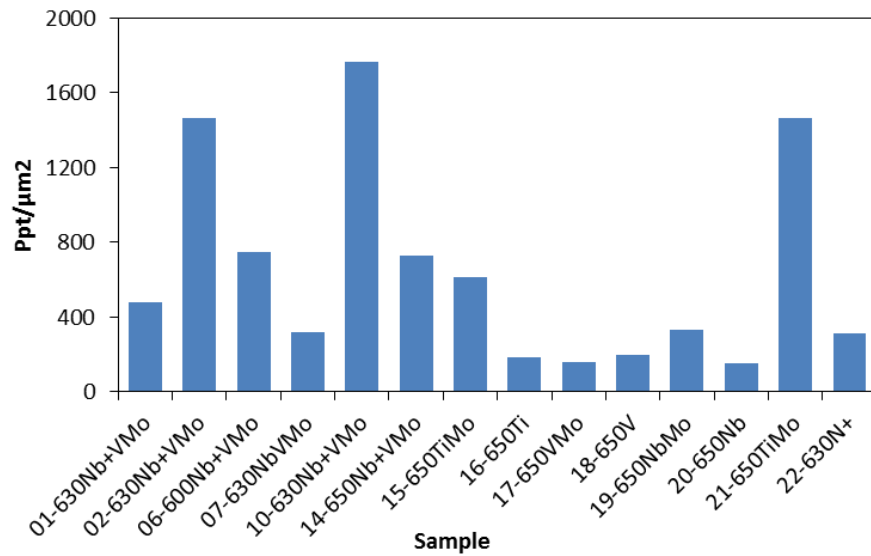


Figure 6.92 – Precipitates counted per μm^2 for the various samples

Figure 6.93 shows the average precipitate sizes for all the samples. 18-650V had coarsest precipitates with an average diameter of $12.9 \pm 0.1\text{nm}$ followed by 17-650VMo with average diameter of $10.8 \pm 0.3\text{nm}$. 07-630NbVMo and 16-650Ti had average precipitate sizes of $8.6 \pm 0.1\text{nm}$ and $8.2 \pm 0.2\text{nm}$ respectively while 06-630Nb⁺VMo, 14-650Nb⁺VMo and 02-630Nb⁺VMo had the lowest average precipitate sizes of $4.0 \pm 0.1\text{nm}$, $4.2 \pm 0.1\text{nm}$ and $4.9 \pm 0.1\text{nm}$ respectively.

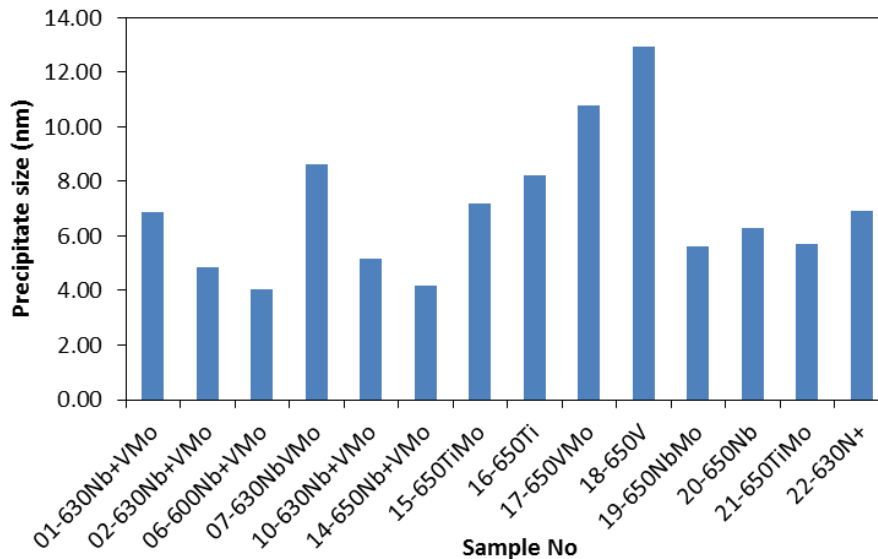


Figure 6.93 – Average precipitate sizes for all the samples

It is also evident that the samples that had the highest average grain sizes had wider distribution ranges. The precipitate distribution curves in Figure 6.94 and Figure 6.95 confirms that 18-650V and 17-650VMo had the widest size distribution ranging

from 6nm to 30nm and 3nm to 30nm respectively. Only 2% of the precipitates counted in 18-650V were less than 6nm whereas it was 25% in 17-650VMo. The samples with lower average precipitate sizes had corresponding low size distribution ranges as well. 93% of all the precipitates in samples 06-630Nb⁺VMo and 14-650Nb⁺VMo had precipitate sizes below 6nm while 86% were below 6nm in 02-630Nb⁺VMo. Of all the steels with Mo, the majority of the precipitates had sizes below 10nm except 17-650VMo. It was also noted that there was a strong correlation between the grain size distribution curves and the precipitate size distribution curves. A typical example is 17-650VMo; the grain size distribution was over a wide range with some of the grains being quite coarse (up to 20 μ m). The same applied to its precipitate size distribution which is also characterised by not only a wide precipitate size distribution, but also by coarse precipitates (>30nm).

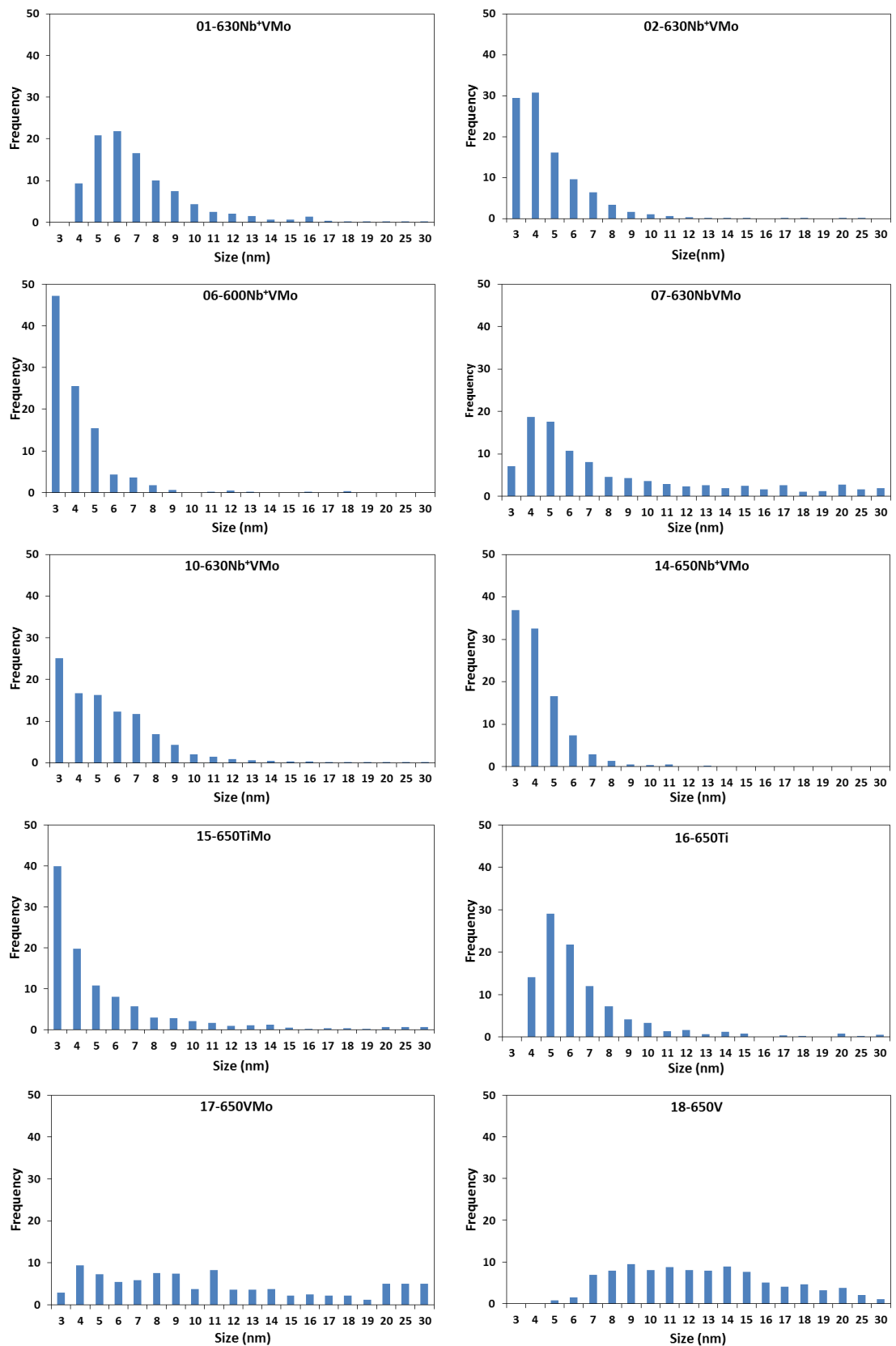


Figure 6.94 – Precipitate size distribution curves for samples 02-630Nb⁺VMo to 18-650V

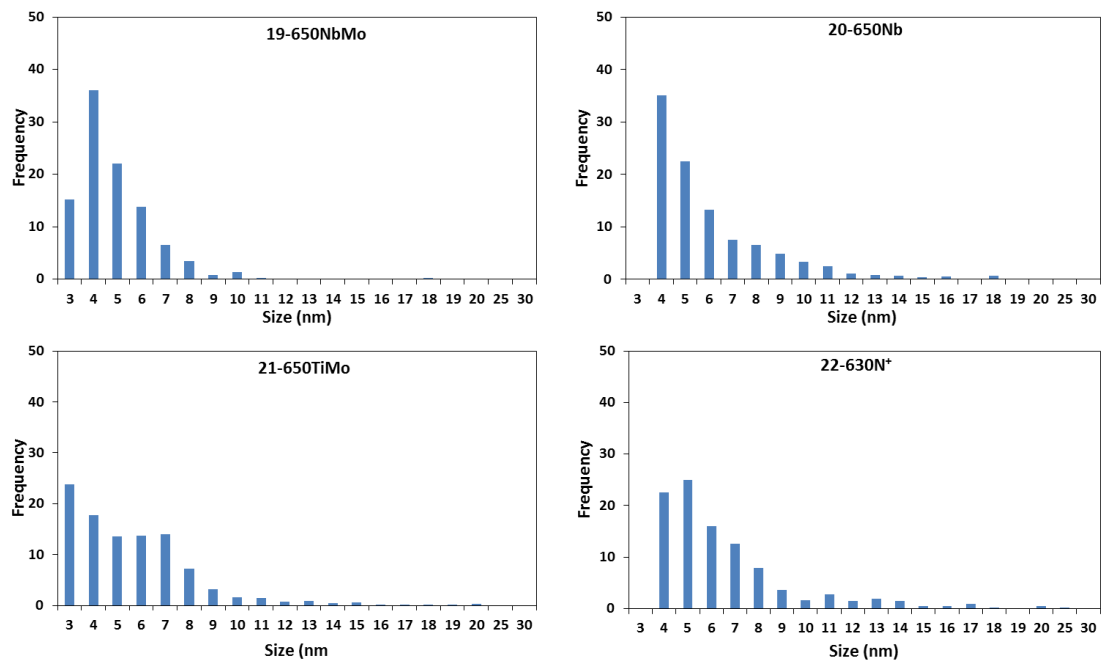


Figure 6.95 - Precipitate size distribution curves for samples 19-650NbMo to 22-630N⁺

6.6 Summary

The microstructure obtained in the majority of the samples was predominantly ferrite with occasional pearlite. The grain size distribution was generally within the range of 0.4 to 15 μm . The majority of the samples had more than 80% of the grains less than 6 μm with the exception of 17-650VMo that had 74% and 18-650V with 46%. The smallest grains were found in 21-650TiMo with an average grain size of $1.5 \pm 0.1 \mu\text{m}$ while 18-650V had the largest with $8.3 \pm 0.6 \mu\text{m}$. EBSD mapping for all the samples showed that there was no preferred crystal orientation in any of the microstructures. It was also confirmed that the high angle grain boundaries accounted for more than 80% of all the boundaries.

Generally, interphase precipitates were found in most of the samples even though some of the samples had much lower precipitate densities. Precipitate analysis on TEM carbon extraction replicas using both EELS and EDX analysis showed that in all the samples alloyed with both V and Mo, the chemistry of the finest precipitates were always found to be of the type V(Mo)C. 18-650V, which did not have Mo was found to have coarser precipitates with an average size of $12.9 \pm 0.1 \text{nm}$. Most of the precipitates found were mainly spheres, rod and cube types. However, in some cases, they were found in clusters and sometimes in form of stringers. Where rod shaped precipitates were found, it was also discovered that they had the same chemistry as their spherical counterparts, which led to the possible conclusion that they could have been one and the same, but probably oriented in different directions. It was also noted that the grain sizes distribution for each and every one of the samples had some form of correlation with the size distribution of its precipitates. As an example, where coarse grains were found, it was most likely that coarse precipitates would also be found.

CHAPTER 7: THE DISCUSSION

The necessity to reduce carbon emissions which causes global warming, partly a result of emissions from automotive vehicles, has resulted in governments and industry developing strategies to improve automotive materials for vehicle light-weighting. This has resulted in resources being made available for the development of steels with higher strength and ductility. This project's main objective was to develop an Ultra High Strength Steel (UHSS) with the ferrite strengthened by nanoprecipitates, formed by interphase precipitation during transformation from austenite to ferrite. The project was divided into three major parts.

Stage 1 - The first part studied three multiphase steels in order to determine which chemical composition was likely to produce the desired optimum mechanical properties.

Stage 2 - The second part was mainly to develop optimum thermal cycles in order to optimise the mechanical properties of V microalloyed steel.

Stage 3 - The third and last part of the project was to develop new steel compositions with a combination of high strength and high ductility.

The microstructures of the steels produced at each stage of the project were extensively studied and related to the mechanical properties.

7.1 Multiphase Steels with Ferrite Strengthened by Nanoprecipitates

The chemical composition of the first three steels were discussed in the experimental procedure section (chapter 5) and tabulated in table 5.1. TiAlMo was selected as the benchmark for making a comparison with the other two steels since it had already been shown to have good mechanical properties[13, 156]. It was subject to a patent by JFE Steels[13]. The V alloyed steel was chosen since VC can be formed through interphase precipitation, which plays a crucial role in precipitation strengthening. The Ti alloyed steel was selected as a suitable substitution for V since it is also known to play an important role in precipitation strengthening. For each of the three steels, two thermal cycles were developed. One of the samples was continuously cooled while the other was held for 4 seconds in the $\alpha + \gamma$ temperature region. The 4 second hold was intended to provide adequate time for the transformation from γ to α , thereby creating suitable conditions for interphase precipitation to occur.

7.1.1 Retained Austenite Content

The balance between strength and ductility can be enhanced through the presence of retained austenite (RA) in the steel, giving a TRIP effect, whereby the retained austenite transforms to martensite during straining. XRD was performed on all the steel samples to verify the existences of retained austenite and the results were tabulated in table 4.2. Even though the heat treatment cycles employed were not conducive for carbon partitioning into retained austenite, the two TiAlMo samples were found to have RA content of approximately 7% while it was not detected in any of the other samples. The major difference between the TiAlMo steel and the others was the high Al content (1.25%) in TiAlMo, which was not present in the others. Al is known to promote the formation of ferrite and the diffusion of carbon into austenite, which stabilizes the austenite, thereby allowing retained austenite which is stable at room temperature[13]. Al additions are also used in TRIP steels to suppress the formation of cementite, and therefore pearlite. Since the heat treatment sequence was similar for all the samples, the presence of Al in TiAlMo might have had an

influence on the partitioning of carbon into retained austenite as compared to Ti and V alloyed samples, which had no Al additions.

Even though isolated particles of retained austenite shown in figure 4.20 were observed through TEM in the V microalloyed steels, these were not detected through X-ray diffraction. The reason why it was not detected could be due to the low volume fraction which might have been below the threshold detected through XRD. ASTM standard E975-13 suggests 2% as being the minimum detectable retained austenite in a steel sample[152]

7.1.2 TiAlMo Microalloyed Steels

The best combination of both strength and ductility were obtained in TiAlMo steels. However, this steel was already subject to a patent by JFE Steels[13] and one of the reasons why it was studied was mainly to verify the claims made by JFE steels[13] and other authors[7, 10].

Optical microscopy showed the presence of a ferrite matrix and an unresolved second phase in both TiAlMo samples. Further high resolution imaging through both SEM and TEM confirmed that the second phase was comprised of bainite, martensite and retained austenite in both samples. The domination of ferrite is advantageous in obtaining high stretch flangeability and ductility. On the other hand, bainite is associated with high strength and in a single phase, it can also exhibit high stretch flangeability [13]. Retained austenite improves the work hardenability of the steel while martensite enhances the overall strength of the alloy.

The thermomechanical treatment process for the continuously cooled sample involved fast cooling from approximately 870°C to the bainitic transformation temperature of 450°C following rolling. Bearing in mind that there was no temperature hold in the $\alpha + \gamma$ region, the expected microstructure would have been bainitic to a large extent. Most of the austenite would have been expected to transform to bainite at the bainite transformation temperature after the quench. The remaining austenite would have been expected to transform to martensite at the M_s temperature. However, this was not the case; ferrite dominated the microstructure instead, with 7% of the microstructure being retained austenite. Possibly, the cooling

rate from the austenising temperature of 950°C to the bainitic temperature of 450°C might not have been high enough to suppress the transformation from γ to α .

As expected, the two steps cooled TiAlMo sample was composed of a ferrite matrix, some bainite, martensite and 7% retained austenite. The 4s temperature hold at 670°C was intended to allow some of the austenite to transform to ferrite. Quenching from the $\alpha + \gamma$ temperature of 670°C to 450°C ensured that the remaining austenite was transformed to bainite. The partitioning of C into retained austenite was also expected at this stage. Any remaining non-stabilized austenite was expected to transform to martensite at the M_s temperature during the slow cooling to room temperature. Si and Al additions to the TiAlMo steel promoted carbon partitioning into retained austenite while suppressing the formation of cementite. Microalloying with these two elements also ensured that the M_s temperature was above room temperature, which promoted the formation of martensite during cooling from 450°C.

TiAlMo-2S had UTS and total elongation of 780MPa and 19% respectively while TiAlMo-CC had 773MPa and 22% respectively. This result was in agreement with the reports by other authors [7, 10, 13]. The high strength in this steel was attributed to a good number of strengthening mechanisms. Si, Mo and Mn additions contributed towards solid solution strengthening while the various phases within the microstructure also made significant contributions towards the overall yield strength. The fine grained microstructure averaging 1.39 μ m and 1.56 μ m in TiAlMo-2S and TiAlMo-CC respectively suggests that fine carbides and carbonitrides effectively pinned the grain and sub-grain boundaries and dislocations, thereby limiting grain growth.

Strengthening the soft ferrite, which was the major phase, presented one of the major challenges. Multiphase microstructures comprising a complex mixture of ferrite and other phases can suffer cracking at the interphase boundaries attributed to the difference in hardness[13]. In order to lower the difference in strength between the ferrite and bainite, it has been claimed that the introduction of nanoprecipitates formed at the interphase boundary during the transformation from γ to α can improve the strength of the ferrite without lowering the ductility[10].

The addition of Mo has been known to enhance Ti precipitation as well as slowing down the migrating interphase boundaries[7]. It has also been claimed that it enhances resistance to coarsening, which is critical to the performance of the alloy, with the finest being TiAl(Mo)C precipitates without nitrogen[13, 75]. Nanoprecipitates formed at the interphase boundaries by combining Ti, Al, Mo and C to form complex carbides which strengthened the ferrite without compromising ductility, thereby reducing the differential strength between the ferrite and the other phases. TEM thin foils confirmed the existence of IP in TiAlMo-2S as shown in figure 4.9b. Yen et al.[159] showed the existence of IP on an isothermally treated steel alloy of almost similar chemical composition. High precipitate number densities were also confirmed through TEM extraction replica analysis shown in figure 4.12.

The slightly higher strength in TiAlMo-2S could be due to higher number densities of finely spaced precipitates and planar IP which was more noticeable in this steel. Mostly random precipitates were observed in TiAlMo-CC instead. The average grain size was also slightly lower, which will have contributed to a higher yield strength. Though most of the regions were dominated by random precipitates, the fine precipitate size as well the high number density suggests that they were likely to be random interphase precipitates similar to those observed by Ricks and Howell[144]. The slight decrease in total elongation in TiAlMo-2S as compared to TiAlMo-CC may have been a result of a small difference in phase constitution, since the finer grain size in TiAlMo-2S would be expected to give higher elongation, not lower. In comparison to the rest of the other samples in this batch, it was clear that alloying with Ti, Al and Mo had greater advantages in terms of optimising both strength and ductility.

7.1.3 Ti Microalloyed Steels

Even though fine microstructures were observed in both Ti-2S and Ti-CC, this was only as expected for the continuously cooled sample (Ti-CC). The quench from the final rolling temperature of 870°C to the bainite transformation temperature of 450°C was supposed to ensure transformation of the austenite started at the bainite transformation temperature without allowing the austenite to transform to ferrite in

the $\gamma + \alpha$ region. Any remaining austenite after bainite transformation was then expected to transform to martensite. On the other hand, the 4s hold in the two step cooled sample (Ti-2S) was expected to encourage the transformation from γ to α . However, this was not the case. Possibly the 4s hold was not long enough to allow sufficient transformation. As a result, both Ti-CC and Ti-2S were predominantly bainitic with occasional martensite also found within the microstructure, but no retained austenite.

The strength and ductility recorded for Ti-CC was 810MPa and 8% respectively while that for Ti-2S were 755MPa and 12% respectively. It is clear that Ti-CC recorded the highest strength and lowest ductility as compared to any of the other steel. TEM thin foil analysis showed regions with few precipitates while in some cases, none were observed at all. However, the presence of irregular grain boundaries shown in figure 4.16b suggest pinning of the grain boundary and therefore that some precipitation had occurred. Thus, it would appear that the high strength in both samples was a result of the fine bainitic microstructure, while the absence of ferrite was responsible for the low ductility. The higher dislocation density found in both the bainite and the few ferrite grains also made significant contribution to the high UTS and low ductility. Where precipitates were found, they were fairly coarse averaging 30nm and above.

7.1.4 V Microalloyed Steels

Of the V microalloyed steels, V-2S was mainly composed of ferrite which was most likely to have been formed during the 4s hold. A few martensite islands located along ferrite grain boundaries were also observed through SEM (figure 4.8). However, TEM imaging revealed the existence of pearlite as shown in figures 4.18 and 4.19, which suggested the cooling rate of 40°C/s was not fast enough to suppress this transformation.

The average grain size of $3.67 \pm 0.25\mu\text{m}$ was recorded for V-2S. This was markedly coarser than any of the other samples and could be the possible explanation why it had the lowest UTS of 623MPa and the highest uniform elongation of 21%. Since maximum precipitation hardening arises from a uniform distribution of finely spaced precipitates, the irregular distribution and locally wide spacing between precipitates

in the samples could have had a contribution towards the lower overall strength. The strength of the alloy was further lowered by carbon being tied up in pearlite rather than partitioning into retained austenite or forming VC precipitates. High ductility in V-2S was contributed by the sample being predominantly ferrite. The movement of the boundary during cooling might have caused the accumulation of the precipitates and dislocations in the low angle grain boundary as shown in figure 6.21b.

In contrast, V-CC was predominantly bainitic with a smaller fraction of ferrite than expected. The high cooling rate from the finish rolling temperature to the bainite transformation temperature ensured that most of the austenite was transformed to bainite. This resulted in a high UTS of 794MPa and a low total elongation of 9% being recorded for this steel. The steel also contained precipitates and dislocations randomly distributed within the few ferrite grains and at grain boundaries. Both the precipitates and the dislocations were most likely to have contributed towards the overall high strength of the steel. An irregular shape to the grain boundaries was also quite common and this was attributed to Zener pinning of the grain boundaries by precipitates. The ferrite often exhibited an elongated morphology, shown in figure 4.18, which may have been a result of a local breakdown in Zener pinning, allowing the grain boundary to bow out. Isolated particles of retained austenite shown in figure 4.20, though not detected by X-ray diffraction, were also found in the sample. The small volume fraction of retained austenite suggested that retained austenite did not play a significant role in the overall strength-ductility balance of the steel. Despite the heat treatment schedule, there was no evidence of interphase precipitation in either V-2S or V-CC.

7.1.5 Summary and Introduction to V Microalloyed Steels

A study of the initial three multiphase steels managed to achieve the set objectives. One of the objectives was to study and verify the claims made by Raabe et al.[10] and JFE Steels[13]. A detailed analysis of the TiAlMo steel revealed the high UTS of 780MPa and high uniform elongation of 21%, which was in agreement with the claims by JFE Steels. However, claims by Raabe et al. that over 1GPa UTS could be attained could not be verified. It was also confirmed that TiAlMo offered the best desired microstructure and mechanical properties. The combination of high strength and high ductility appears to have been a result of interphase precipitation giving a dispersion of fine precipitates in the ferrite, along with some retained austenite that might have provided a small TRIP effect. However, interphase precipitation was only observed in this steel, and not in the Ti and V alloyed steels.

Since the TiAlMo steel was subject to a patent, and the Ti and V alloyed steels had failed to produce the required combination of strength and ductility, the next stage of the project was aimed at optimizing the V microalloyed steel composition to find the correct conditions to produce IP and to provide a suitable alternative to TiAlMo for Tata Steel. The V alloyed steel composition was chosen since it is one of the most commercially viable options for Tata Steel. It was also observed that finding interphase precipitation was quite difficult even in TiAlMo-2S. Perhaps the short holding time of 4 seconds might have been inadequate to produce the desired results. Yen et al.[159] demonstrated that IP could be produced in steels of almost similar chemical composition when the temperature was held at 680°C for 20 minutes. As a result, trials with longer times formed part of the next stage of this study to optimise precipitation strengthening.

The dependency of the microstructure on the temperature, time and transformation were extensively studied. Mechanical testing was carried out on the samples in order to relate the microstructure obtained to the mechanical properties. The results obtained were used to make informed decisions on the development of the next generation of UHSS for Tata Steel and these forms the basis for discussions in the next section.

7.2 The Time/Temperature/Transformation behaviour of a Vanadium Microalloyed Steel

The chemical composition of the V microalloyed steel discussed in this section was listed in table 3.1. It was selected on the basis that V alloyed steels have always been known to produce interphase precipitates (IP)[11, 70]. The chemistry was similar for all the samples, with the only variable being the thermal cycle developed during heat treatment. The thermal cycles were also listed in table 3.2 while the thermomechanical processing stages were described in detailed in the experimental method section in chapter 3. The major issue was to optimise conditions to produce nanoprecipitation in multiphase microalloyed steel for improved mechanical properties as well as to understand the temperature/time/transformation behaviour of a V microalloyed steels.

7.2.1 Microstructural Development

As expected, X-ray diffraction analysis carried out on the samples revealed no evidence of retained austenite (RA) in any of the samples. This was also consistent with the V microalloyed steel examined to kick start the project (initial multiphase steels).

The microstructures for 950Q, 950-60Q and 950-120Q were presented in figures 5.3, 5.4, 5.5 and 5.6. Optical microscopy images for these three samples showed a fine microstructure consisting mainly of bainite, some ferrite and some unresolved regions. Further SEM analysis revealed that the microstructures were predominantly bainitic with a few ferrite grains and martensite sandwiched between the bainite. Note that these samples were all quenched from an austenising temperature of 950°C to the bainite transformation temperature of 450°C. The fast cooling from the austenising temperature to the bainite transformation temperature was fairly effective in preventing γ to α transformation even though some transformation to ferrite did occur. Following this, the steels were slowly cooled to room temperature, and the small fraction of remaining austenite apparently transformed to give a small amount

of martensite at the martensite start temperature (M_s). The only processing difference between these three steels was the holding time at the austenising temperature of 950°C, which might have affected the amount of VC(N) taken into solution, although this is a low temperature for dissolution of VN.

The microstructure for 750-60s was presented in figures 5.5 and 5.6 while that for 750-1800s and 725-1800s were presented in figures 5.7 and 5.8. It was clear that despite the short holding time of 60s at 750°C, ferrite grains had already started to develop. Increasing the holding time to 1800s resulted in the coarsening of the ferrite grains as shown in figure 5.8. The same argument could be applied to 725-1800s. Rapid cooling from the $\gamma + \alpha$ temperature of 750°C and 725°C to the bainite transformation temperature of 450°C ensured that the remaining austenite transformed to bainite. Further cooling resulted in any residual austenite transforming to martensite at the M_s temperature.

The microstructure developed in the 700-30s sample was predominantly ferrite with bainite and a few martensite islands located mainly along the grain boundaries as shown in figure 5.9 and 5.10. The lower transformation temperature of 700°C ensured that most of the austenite transformed to ferrite, with the remaining austenite transforming mostly to bainite after fast cooling to the bainite transformation temperature of 450°C. Further cooling resulted in the small volume fraction of austenite that remained transforming to martensite at the M_s temperature. The same microstructure was expected in the 700-1200s. Surprisingly, 700-1200s had a high volume fraction of martensite rather than the expected bainite. This suggests little diffusional transformation occurring during the 1200s hold.

The microstructure for 650-60s shown in figures 5.11 and 5.12 resembled that of 700-1200s. Even though ferrite dominated the microstructure, it was clear that martensite was formed following fast cooling. This was also quite surprising since bainite was the phase expected to form on cooling to 450°C. However, the microstructure was almost entirely ferritic and this might have been due to the lower transformation temperature of 650°C which favoured higher transformation kinetics from austenite to ferrite.

The microstructure for 625-300s was presented in figure 5.13. Although the microstructure predominantly comprised ferritic, pearlite was also found scattered throughout the sample, in contrast to the other steels that were composed mainly of ferrite, bainite and martensite.

7.2.2 Grain Sizes Analysis

Average grain sizes for some of the samples were recorded in table 5.2. However, the grain sizes for 950-Q, 950-60Q, 950-120Q and 750-60s could not be measured since the bainitic structure obscured the grain boundaries. As previously stated, these samples were predominantly bainitic and this accounted for the fine microstructure shown in figures 5.3 to 5.6.

As for the rest of the samples, the grain size decreased with decreasing transformation temperature as expected, as clearly shown in Figure 7.1. Lowering the transformation temperature from 750°C to 725°C for the same transformation time of 1800s resulted in the average grain size decreasing from 5.78µm to 4.75µm. The lower transformation temperature provided the required driving force for increased nucleation sites for ferrite to form, resulting in smaller grains being formed. The holding time at constant transformation temperature did not seem to have any significant influence on the grain size, implying that grain growth was not significant at these temperatures. A good example was the average grain sizes for samples transformed at 700°C; 700-30s had an average grain size of 3.80µm as compared to 700-1200s with 3.49µm. This suggests that Zener pinning by precipitates was effective at this stage. As expected, 650-60s had an average grain size of 2.58µm as compared to 650-600s with slightly coarser grains averaging 2.85µm. In this case, the slightly coarser grains could be attributed to the longer holding time.

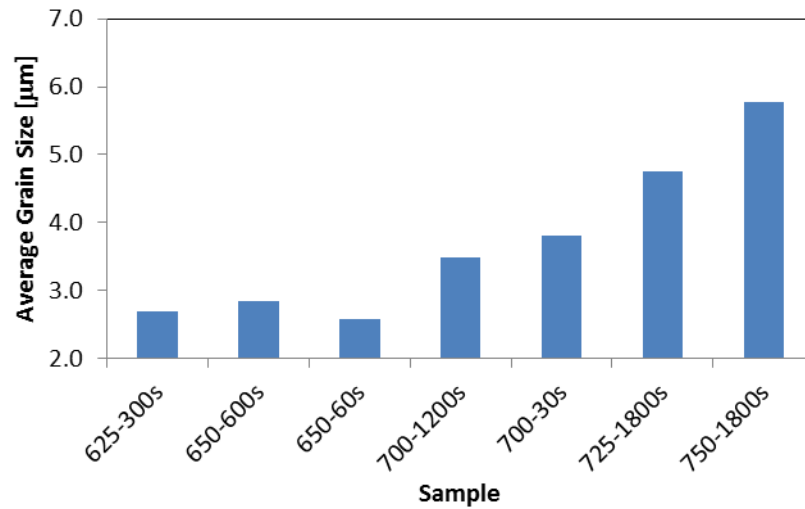


Figure 7.1 – Average grain sizes for the various samples

7.2.3 Phase Distribution

Where possible, the volume fraction of the second phases were quantified and recorded in table 5.2. For samples 950-Q, 950-60Q, 950-120Q and 750-60s the microstructure was predominantly bainite, with similar average grain size. The volume fraction of ferrite increased with decreasing transformation temperature as shown in Figure 7.2. Lowering the transformation temperature increased the driving force for transformation from austenite to ferrite. The low temperatures provided further nucleation sites for ferrite while suppressing grain growth, hence, the existence of finer grains.

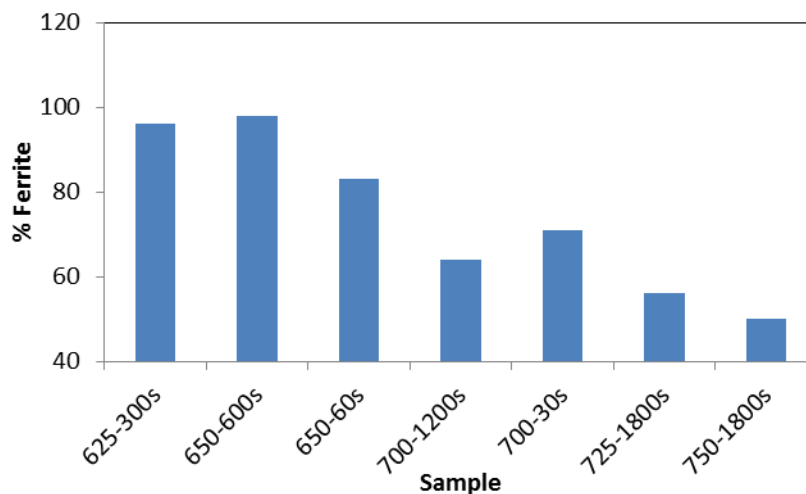


Figure 7.2 – Percentage ferrite in the various samples

Even though the phase diagram dictates that the volume fraction of each phase should be the same for the different holding times, it was evident that the volume fraction of ferrite was different for each of the holding times. Typical examples were 700-30s with 71% α as compared to 700-1200s with 64% α . Differences were also recorded in 650-60s and 650-600s, which had 83% and 98% α respectively. The differences in these cases could be due to experimental error as well as variability of material from point to point as a result of banding.

7.2.4 Precipitate Analysis

From the precipitate counts recorded in table 5.3, it was evident that most of the samples had low precipitate counts ranging from 20 to 60 particles/ μm^2 . However, considerably higher precipitate number densities were also observed in samples 700-1200s, 700-30s and 650-60s with 394, 194 and 174 particles/ μm^2 respectively. A comparison of the precipitate counts is shown in Figure 7.3.

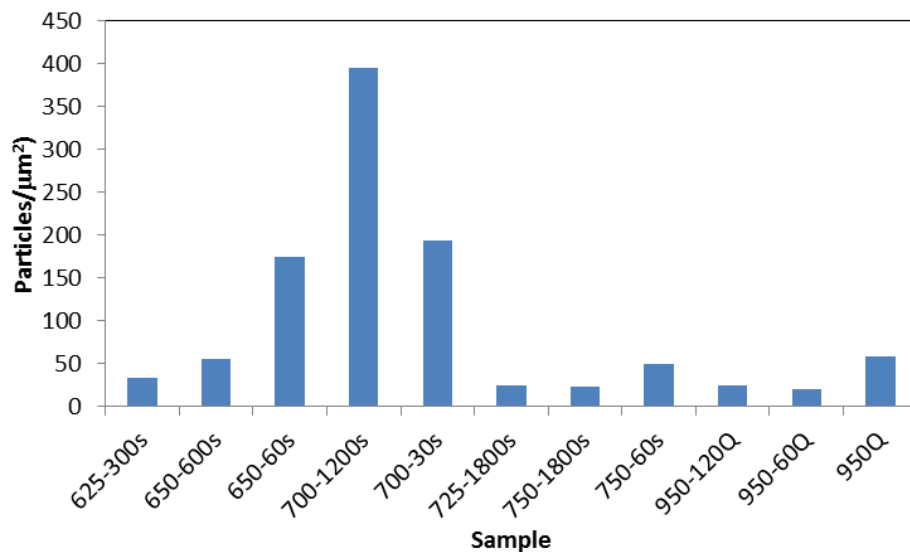


Figure 7.3 - Precipitate count comparisons for the various samples

Thermomechanical treatment of the samples included preheating to an austenising temperature of 950°C, followed by either fast cooling to the bainitic transformation temperature of 450°C or to an intermediate temperature in the $\alpha + \gamma$ temperature region. Thermodynamic calculations using Thermo-Calc showed that better dissolution of the carbides and carbonitrides would have been undertaken at 1050°C.

Hence, the austenising temperature of 950°C was inadequate to effectively dissolve the majority of carbides and carbonitrides in the steels.

Low precipitate counts were expected in 950Q, 950-60Q and 950-120Q. Fast cooling from the austenising temperature to the bainite transformation of 450°C ensured that austenite transformed to bainite. A fine dispersion of precipitates is normally expected to form at the interphase boundary during the transformation from austenite to ferrite. The absence of a temperature hold in the $\alpha + \gamma$ temperature zone minimised the possibilities of austenite transforming to ferrite, thereby minimizing chances for interphase precipitates to form.

The precipitate size distribution curves in figure 5.21 showed that precipitate diameters ranged from 4nm to 40nm in 950Q and 950-120Q. The existence of coarse precipitates suggests that the solution treatment temperature was not adequate to dissolve precipitates that had previously formed during coiling after hot rolling; especially Ti carbides and carbonitrides which tend to dissolve at higher temperatures. As a result, instead of dissolving all the carbides and carbonitrides, the solution temperature of 950°C might have encouraged coarsening of these carbides.

Steels 725-1800s and 750-1800s had low precipitate counts of 24 and 23 particles/ μm^2 and average precipitate sizes of 19.5nm and 13.5nm respectively. Residual carbon and vanadium dissolved in the austenite during solution treatment was expected to precipitate as carbides during the temperature holds. However, the long temperature hold of 1800s might have encouraged the vanadium carbides formed at this stage to coarsen. The Lifshitz-Wagner theory[70] suggests that high rates of coarsening are always associated with particles with higher solubilities. The solubility products in figure 2.12 show that vanadium carbides and carbonitrides fall into this category. The rate of coarsening is also dependent on the diffusivity of the solute molecules as well as well as the time. Hence, since all the samples had the same chemical composition, the diffusivities for all the samples were constant. Precipitate coarsening could have been reduced through optimisation of the holding time at the transformation temperature of 725°C and 750°C. When the transformation time was reduced to 60s in 750-60s, the precipitate count doubled to 50

particles/ μm^2 as compared to 23 particles/ μm^2 in 750-1800s. Similar observations were also made for samples 650-600s and 650-60s. The precipitate count trebled from 56 to 174 particles/ μm^2 when the transformation time was reduced from 600s to 60s. The average precipitate size was also reduced by approximately 50% from 15.3nm to 8.7nm in 650-60s.

The highest precipitate number densities in this batch were recorded when the steels were transformed at 700°C for 1200s. 700-1200s had the highest precipitate number density of 394 particles/ μm^2 followed by 700-30s and 650-60s. Even though the average precipitate size for this steel was found to be 14.1nm, it was noted that this was due to a few coarse precipitates averaging between 16nm and 40nm. 88% of the precipitates counted in 700-1200s averaged 4nm to 10nm with the highest frequency of 29% averaging 6nm. The same pattern was also observed in the other two samples with high precipitate counts. 90% of the precipitates in 700-30s were below 10nm while 81% were recorded in 650-60s. In terms of energy efficiency, it was in Tata's interests to verify whether solution treatment at lower austenising temperatures (950°C) could yield acceptable results. However, it is clear that precipitate number densities could have been boosted by austenisation at temperatures above the 1050°C threshold that had been predicted through thermodynamic calculations.

It can also be argued that even though planar interphase precipitates were not clearly visible, the random precipitates observed in some regions; due to their size, number densities and possible coherency, were likely to have been formed at the interphase boundary during transformation from austenite to ferrite. Ricks and Howell[145], working on 10Cr 0.2C steel observed that irregular arrays are sometimes observed within the same grains as planar arrays [142]. These are believed to nucleate at higher energy γ to α interphase boundaries that migrate without the step propagation. The interphase boundary is believed to bow around particles using a mechanism similar to Orowan looping mechanism of dislocations and precipitates.

The array of fine precipitates observed in 700-1200s (figure 7.29a) was also of great interest. This was the only case where such a feature was observed. Since they were present as a single array it was unlikely that they had been formed at the interphase boundary. The only planar feature that was likely to be present in this steel was

recrystallisation twins in the austenite. Thus, if these precipitates did form on a twin boundary, they were likely to have formed in the austenite prior to transformation. This raises the important question as to how much precipitation occurred in the austenite? If it had been extensive, then clearly the potential for interphase precipitation would have been much less.

As previously reported in the results section, planar interphase precipitation was not obvious in any of the samples. The high N and Ti contents in the steel studied might have had some influence on this. The solubilities of V, Nb and Ti in austenite have since been studied in detail and it has been established that V carbides have the highest solubility while Ti carbonitrides are the least soluble[160]. Nitrides are even more stable than carbides and their coarsening rate during isothermal holds are much lower. The presents of Ti and N in the precipitates were confirmed through electron energy loss spectra analysis (EELS) which confirmed that all of the finer precipitates were either nitrides or carbonitrides.

For the samples transformed at 750°C (750-60s and 750-1800s), the high transformation temperature favoured lower transformation kinetics from austenite to ferrite. The mechanism for IP is dependent on carbon diffusion at the transforming boundary being quick enough for precipitation to occur during transformation, which of course is dependent on the transformation temperature. The abrupt increase in precipitate number density at a lower transformation temperature of 700°C might have been due to a greater driving force for precipitation. Balliger and Honeycombe[129] showed that when IP is produced in V alloyed steels, the row spacing and interparticle distance tended to decrease with decreasing transformation temperature. The carbon concentration at the transformation front also affects the interparticle spacing[70]. However, the diffusion rate for carbon decreases with decreasing temperature. Hence, a relatively slow transformation front is required in order to account for the slow diffusion which is key to the transformation mechanism. Even though lowering the temperature can further increase the driving force (faster transformation boundary), this has the potential to create unfavourable conditions for IP due to the slower diffusion. Hence, there is the possibility that the optimum balance between the driving force and diffusion were attained at 700°C.

The observation that the highest precipitate number density was observed at the long hold of 1200s at 700°C suggests that the long hold provided adequate time for diffusion to occur, resulting in the highest number density of 394 precipitates / μm^2 . This observation seems to suggest that the precipitates might have been formed in the ferrite, possibly on dislocations, rather than on the interphase boundary. Decreasing the transformation temperature further to 650°C resulted in the precipitate number densities decreasing, confirming that the threshold might have been at 700°C.

Regions of high dislocation density and high precipitate density were also observed as shown in figure 7.25. The observation that precipitates were observed on dislocations prompts the question as to whether heterogeneous nucleation occurred on dislocations. The high cooling rates would have been expected to introduce high dislocation densities that could potentially act as nucleation sites for precipitates in the above mentioned three samples with high precipitate densities. However, dislocations would have been mobile at these temperatures and it would have been possible that the dislocations moved, as part of a recovery process, to the point where they were pinned by a precipitate that had been homogeneously nucleated in the ferrite.

7.2.5 Mechanical Properties - Estimated versus Measured

The stress-strain curves for 700-30s, 700-1200s, 650-60s and 650-600s were shown in figure 5.1a. Yield strengths were also estimated for the same samples using the precipitate counts and grain size measurements obtained through experimental results. The estimated and actual tensile results are given in Table 7.1.

Table 7.1– Estimated Yield Strength, UTS and Total Elongation

Sample	Estimated [MPa]			Actual		
	Base Strength (σ_b)	Precipitate Strength (δ)	YS	% Tot. Elong. ($\% \epsilon$)	YS (2%) [MPa]	UTS [MPa]
700-30s	352	199	551	32.5	534	618
700-1200s	363	270	633	30.8	562	627
650-60s	405	200	605	33.4	548	610
650-600s	390	132	522	32.0	533	585

As expected, 700-1200s had the highest yield strength while 650-600s had the lowest yield strength. The high yield strength in 700-1200s was mainly attributed to the high number density of fine precipitates, which made a significant contribution to the overall yield strength. The estimated yield strength for this sample was 270MPa and this compared very well to the 300MPa reported by Funakawa et al.[7].

Since the chemical composition of the steels examined were the same, the solid solution contributions to the base strength were assumed to be equal. The differences in base strength therefore only arose from differences in grain size. 650-60s had the finest grains averaging $2.58\mu\text{m}$, giving a base strength of 405MPa. 700-1200s, with an average grain size of $3.49\mu\text{m}$, had a lower base strength as compared to 650-60s and 650-600s. However, the low precipitate counts in 600-60s ensured that it had the lowest yield strength as compared to the other three samples.

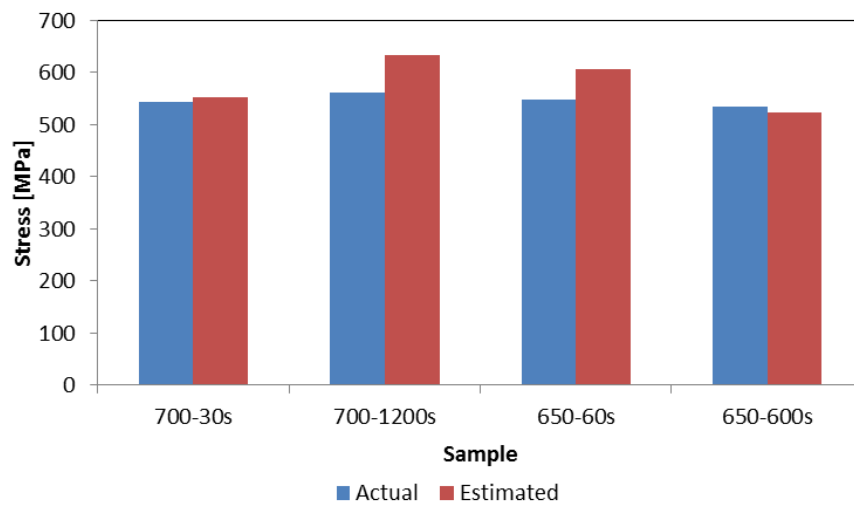


Figure 7.4 – Actual versus Estimated Yield Strength

Comparisons of the actual yield strength obtained through tensile testing and the estimated yield strength are shown in Figure 7.4 above. It is clear that there was a significant overestimation of yield strength in 700-1200s and 650-60s samples. 700-1200s was overestimated by 71MPa while 650-60s was overestimated by 57MPa. Systematic errors sometimes occur due to the selection of areas that might not be representative of the whole sample, particularly for precipitate size and number density measurements. Even though the specimens were supposed to be representative of the entire sample, this was not always the case taking into account

the high degree of inhomogeneity in the samples. Some of the regions had a high precipitate number density while others had little or no precipitates at all. The other source of error could have been the software packages used for precipitate counting. ImageJ software was used to count the precipitates and sometimes it was difficult to distinguish between dark contrast and the actual precipitates especially in regions with fine precipitates. This could have resulted in overestimation of the actual precipitates, which in turn contributed towards overestimation of the overall yield strength.

Even though the actual yield strength compared very well to the estimated yield strength, the Young's modulus of the four steels in figure 5.1 averaged way below the expected Young's modulus of steel which normally ranges above 200GPa. Young's modulus ranging between 3GPa and 5GPa were recorded. Significant errors normally arise from the deflection of the load frame rather than the specimen. The deflection of the specimen alone can be corrected by introducing an extensometer attached either directly to the specimen or using a non-contact system. In this instance, the tests were carried out without an extensometer.

Another factor which might have contributed towards the error was the condition of the tensile testing equipment. Slippage might have occurred as a result of worn out wedge grips at both ends of the specimen. Properly aligned of the grips to the specimen is also of paramount importance to reduce bending stresses. However, the highest contributory factor in this instance was likely to be the absence of the extensometer and this might have affected the Young modulus for all the samples tested.

7.2.6 Summary and Introduction to Ferritic Microalloyed Steels

Even though a high total elongation of 30.8% was recorded in the sample with the highest UTS of 627MPa (700-1200s), it is obvious that the UTS obtained was not adequate enough for the steel to be classified as UHSS. Within the current generation of automotive steels, steel grades such as TRIP 450/800 have better mechanical properties as compared to the V microalloyed steels in this study. The strengthening of ferrite by nanoprecipitation has since been reported [11, 70, 161]. The reason why the mechanical properties did not meet expectations could be attributed to inadequate precipitation, both in terms of precipitate sizes as well as the number densities. Hence, the question remains as to why planar interphase precipitation was not observed, when it has been widely reported in the literature. Was this caused by the high N and Ti contents in the steel or was it caused by the low austenising temperature of 950°C which failed to dissolve most of the precipitates to allow the formation of interphase precipitates during the temperature hold in the $\gamma + \alpha$ region? In reality it was probably a combination of the two factors. The formation of nitrides and carbonitrides meant that a higher solution treatment temperature was required than that used. Therefore, there was insufficient precipitation potential in these steels to allow interphase precipitation to occur.

In order to answer the above question, the next stage of this project involved the development of predominantly ferritic microalloyed steels strengthened by nanoprecipitates. It is well known that Mo additions enhances the formation of fine precipitates in Ti and Nb microalloyed steels [10, 75, 99, 137]. Precipitate coarsening is retarded by the presence of Mo in these alloys. However, there is a gap in the literature on whether Mo has similar effects in V microalloyed steels. For comparison purposes, most of the steels studied in the next section were microalloyed with Nb-V-Mo while some were Ti-Mo, Ti, V-Mo, V, Nb-Mo and Nb. In order to study the effects of N on the microalloyed steels, a high amount of N was deliberately added to one of the steels. This was done in order to verify whether the low precipitate count in the V microalloyed steels studied in this section were influenced by the high N content.

7.3 Ferritic V-Nb-Mo Microalloyed Steels Strengthened by Nanoprecipitates

The previous chapter looked at optimizing the mechanical properties of microalloyed multiphase steels with the ferrite strengthened by nanoprecipitates. That strategy had the advantage of benefits brought about by the existence of other phases such as bainite, martensite and retained austenite. The work discussed in this section was quite the opposite. The microstructure developed in this instance was purely ferritic, taking advantage of the ductility brought about by ferrite. The challenge was to optimise the strength without significant reduction in ductility. Nanoprecipitates have been known to be effective in this role. The strengthening mechanisms in this study were assumed to be mainly, grain refinement, solid solution strengthening and precipitation strengthening.

7.3.1 Yield Strength Estimation

As previously stated, the strength in microalloyed steels is a combination of several different mechanisms. As a result, estimating the contributions to yield strength can be quite difficult. The microstructure developed for most of the samples under current discussion were mostly ferritic with a few instances of pearlite or cementite. In this instance, it was assumed that precipitate strength (σ_{ppt}) and base strength (σ_b) were the major contributors to the yield strength (YS). The base strength calculation took into consideration both solid solution strengthening and grain refinement and it was defined as being the contribution to yield strength by solid solution strengthening (σ_{ss}) and grain refinement (σ_d).

Using empirical equations that take into account the grain size and the chemical composition, the base strength was calculated [67, 77, 78]. The calculated base strength for each of the samples was tabulated in Table 7.2. Since SEM showed that the microstructures for most of the samples were mainly ferrite with only a few examples of pearlite, it was assumed that the majority of the carbon was tied up in the form of precipitates. Based on this assumption, precipitation strengthening was

calculated using the Ashby Orowan equation [7, 102, 134]. The calculated results were also tabulated in Table 7.2.

Table 7.2 – Yield Strength Estimation

Sample	Estimated YS [MPa]		
	Base Strength (σ_b)	Precipitate Strength (σ_{ppt})	Yield Strength (YS)
01-630 Nb ⁺ VMo	399	310	709
02-630 Nb ⁺ VMo	442	488	930
06-600 Nb ⁺ VMo	421	326	747
07-630NbVMo	399	270	669
10-630Nb ⁺ VMo	363	546	910
14-650Nb ⁺ VMo	352	327	679
15-650TiMo	379	356	735
16-650Ti	357	201	558
17-650VMo	347	202	549
18-650V	291	236	527
19-650NbMo	428	242	670
20-650Nb	362	171	533
21-650TiMo	501	514	1016
22-630 N ⁺	374	251	626

It is clear from Figure 7.5 that precipitation strengthening made a significant contribution to strength in all the samples. It has been suggested that precipitates with sizes less than 20nm are more effective for precipitation strengthening [136, 137, 162]. In the present work, most of the precipitate studied averaged less than 10nm in diameter. It was observed that in all samples with yield strength above 800MPa, the greatest contribution to yield strength came from precipitation strengthening. The highest precipitation strength contributions were recorded in 10-630Nb⁺VMo with 546MPa, 21-650TiMo with 514MPa and 02-630Nb⁺VMo with 488MPa. The least contribution was in 20-650N⁺ with 171MPa. A comparison of the base strength to the precipitate strength was also presented in Figure 7.5.

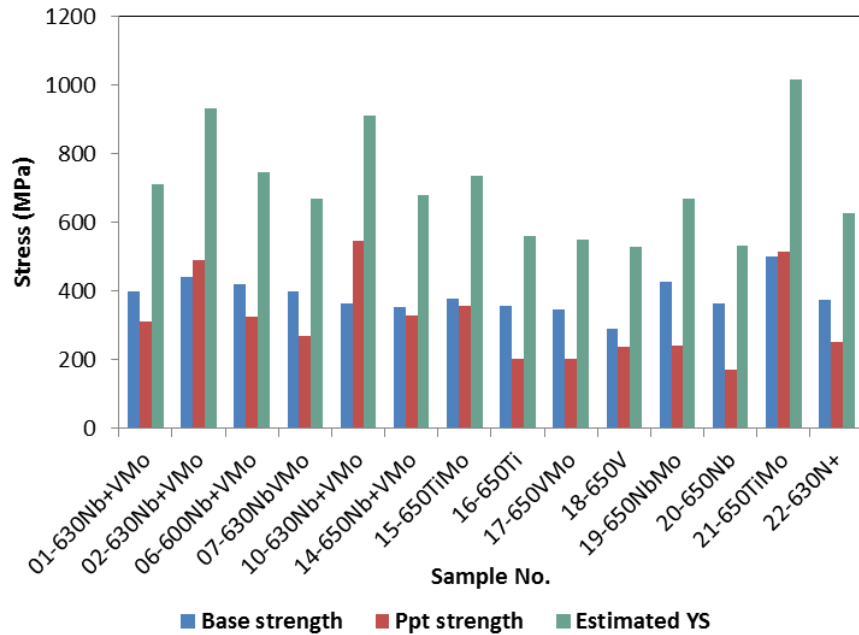


Figure 7.5 – Calculated base and precipitate strengths contributions to estimated yield strength

Mill trials by Funakawa et al.[7] estimated the contribution to yield strength by precipitation strengthening to be up to 300MPa which was an improvement from the 200MPa previously cited [163]. The contributions to yield strength by precipitation strengthening in this study surpassed those previously recorded by far.

In order to validate the estimated results, tensile tests were carried out at Tata Steel and the results were reported in table 6.1 and figure 6.1. Comparisons of the actual and estimated yield strength are shown in Figure 7.6. It is clear that in most of the cases, the actual results were a very good fit to the estimated values. Estimated yield strength versus actual yield strength were also plotted in Figure 7.7 and it was clear that most of the points lie close to the trend line $x = y$ with $R^2 = 1$, which is further evidence that estimation of yield strength through this method can be reasonably accurate.

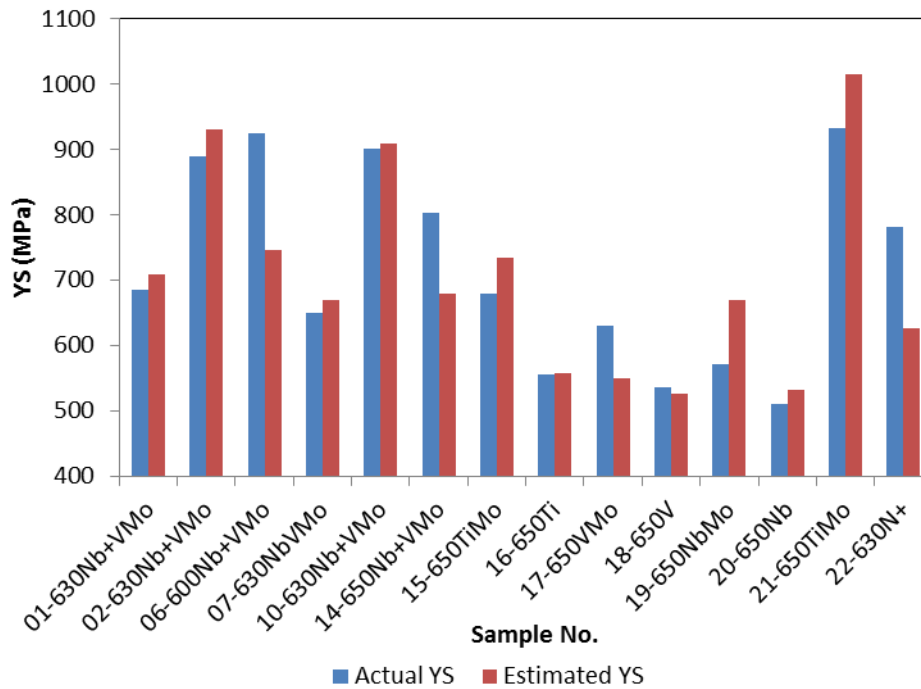


Figure 7.6 – Comparison of yield strength measured through tensile testing (Actual YS) and the estimated yield strength

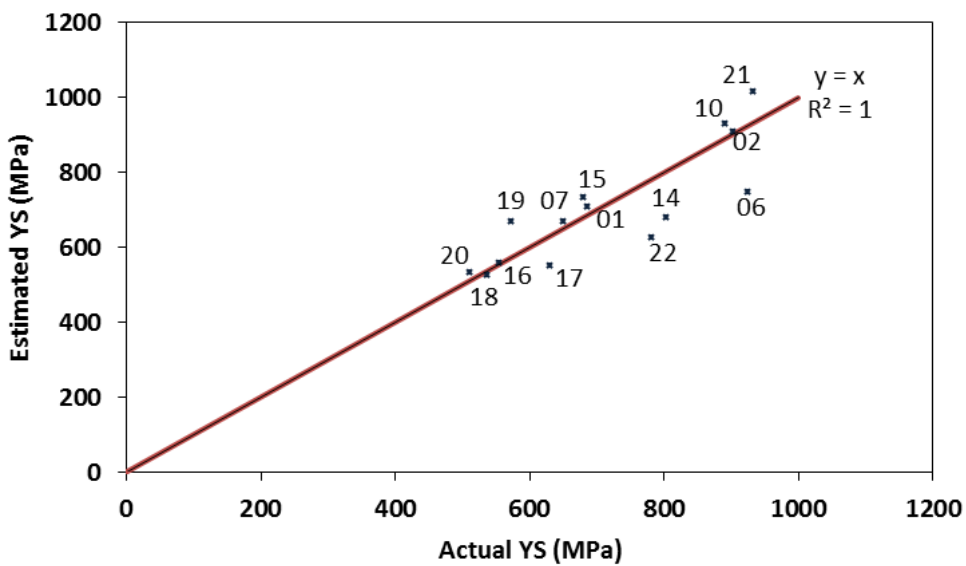


Figure 7.7 – Plot of estimated versus actual yield strengths showing that the two set of results were almost a perfect fit with most of the points on the trentline ($y = x$)

Steels 02-630Nb⁺VMo, 10-630Nb⁺VMo and 21-650TiMo had high yield strengths of 890MPa, 902MPa and 932MPa respectively. In addition to high yield strengths, the three steels also exhibited excellent uniform elongations of 18.9%, 18.2% and 17% which was just short of 20-650Nb which had the highest elongation of 25.2%, but the lowest yield strength of 510MPa. The excellent strength and ductility in these

steels could be attributed to adequate grain refinement and precipitation strengthening.

It has been established that ultra-fine grain size can produce the desired strength, without serious compromise of the ductility in microalloyed steels [12, 81, 82]. In this study, average grain sizes recorded for the highest strength steels were $2.1 \pm 0.2\mu\text{m}$, $3.3 \pm 0.2\mu\text{m}$ and $1.5 \pm 0.1\mu\text{m}$, which are larger than the $0.7\mu\text{m}$ average grain size reported for ultrafine grained steels[12, 81, 82].

7.3.2 Grain Refinement

As previously stated in the results section, at least 80% of the samples had grain sizes ranging between 0.4 and $6\mu\text{m}$ with the exception of 17-650VMo and 18-650V. The average grain sizes were below $4.5\mu\text{m}$ with the exception of these two that had $4.9 \pm 0.1\mu\text{m}$ and $8.3 \pm 0.6\mu\text{m}$ respectively.

It has already been shown that the mechanical properties of microalloyed steels are influenced by grain refinement to a large extent [12, 81, 82]. The Hall-Petch relationship confirms that the yield strength increases as the grain size decrease. It has also been suggested that a bimodal distribution is the best option to optimise both strength and ductility in low alloy steels[12]. A bimodal grain size distribution was observed in the majority of the samples with the exception of 18-650V. Before hot rolling, the samples were subjected to soaking at 1220°C for 45minutes followed by hot rolling to a finishing temperature of approximately 870°C . The roughing stage during hot rolling is supposed to make the steel more homogenous, however, segregation persists throughout the processing of the steel. Solute deficiency e.g. manganese poor regions, causes less solute drag resulting in coarser grains being formed. DeArdo[90] suggested that grains with sizes greater than $4/3$ of the average have the potential to grow. The result is the annihilation of smaller grains into neighbouring larger grains resulting in some grains being much coarser than the others. The fact that 18-650V was more homogenous suggests that solute distribution was better controlled in this sample as compared to the others.

7.3.3 Effects of Alloying Elements and Thermal History on Grain Coarsening

Figure 6.31 shows a comparison of average grain sizes for all the samples. 18-650V had the coarsest grains, followed by 17-650VMo. The absence of Nb and/or Ti could be one of the possible reasons why 18-650V had such grain morphology. Ti and Nb are the least soluble in austenite compared to V. VCN are mainly formed at lower temperatures especially during the transformation from austenite to ferrite, making them most suitable for precipitation strengthening rather than grain refinement. Ti and Nb carbides and carbonitrides that forms at higher temperatures are more suitable for pinning the grain boundaries after hot rolling, thereby reducing the rate of recrystallization and grain growth. To pin the austenite grain boundaries at high temperature, there should be a balance between the volume fraction of the pinning particles as well as the particle size and spacing, and this might have been lacking in 18-650V. Hence, the large grains could be partially attributed to insufficient particles to pin the austenite boundaries. The control of the coiling temperature after hot rolling also plays a crucial role to accomplish the preferred grain refinement[99-101]. Park et al.[76] demonstrated that lowering the coiling temperature promotes the formation of finer the grains. The higher coiling temperature of 650°C in this case might also have promoted grain growth.

The presence of Mo in 17-650VMo was most likely to have played a crucial role in the reduction of the average grain size to 4.9µm as compared to 8.3µm in 18-650V. Even though Mo is less soluble in austenite as compared to V, it is most likely that it was fully dissolved, hence, contributing less to Zener pinning. Gordon et al.[95] and Cuddy et al.[94] showed that the rate of boundary migration or grain growth can also be reduced by solute drag on the boundary. The presence of Mo was likely to have increased the drag on the austenite boundaries, resulting in smaller grains being formed as compared to 18-650V which had no Mo. The microstructure developed in these two steels was more homogenous with 18-650V having the most homogenous grains as compared to any of the other samples. SEM images for these two samples were shown in figures 6.18, 6.19, 6.21 and 6.22 and it was also noted that the coarser banding previously observed in the other samples was no longer evident.

The existence of Ti in 16-650Ti ensured that there were precipitates formed at high temperatures as well as strain induced precipitates to pin the grain boundaries preventing grain growth. Titanium nitrides can form in the liquid phase, but are too large to influence austenite recrystallization. Gladman et al[96] showed that grain growth can only be suppressed provided that the pinning particle radius is below the critical radius (r_c). They also demonstrated that effective pinning can only occur provided there are sufficient pinning particles of adequate size and spacing. Cuddy et al.[94] estimated this critical radius to range between 0.5 and 10nm. Strain induced precipitates formed during controlled hot rolling are known to be effective in pinning grain boundaries and these might have played an important role in controlling the final grain size. Whether the weight percentage of Ti in the steel was adequate to form enough precipitates to effectively pin the grain boundaries and produce the desired effect was one of the questions which remained unanswered. The coiling temperature of 650°C was also high, thereby promoting grain growth, resulting in this sample having the third highest average grain sizes and grain size distribution ranging from 0.4µm to 20µm. Differences in solute concentration in different regions might also have caused segregation, which resulted in banding in this sample.

The grain size distribution in 19-650NbMo and 20-650Nb was not as homogeneous as 18-650V. The existence of bands of coarse grains within finer grains suggests significant segregation similar to 650Nb⁺VMo. Ti was not deliberately added to this sample, hence, the Nb added might not have been adequate to form enough particles to influence recrystallization. This could be the reason why better grain refinement could not be achieved in these samples.

02-630Nb⁺VMo, 06-600Nb⁺VMo and 21-650TiMo had the finest average grain sizes of $2.1 \pm 0.2\mu\text{m}$, $2.4 \pm 0.2\mu\text{m}$ and $1.5 \pm 0.1\mu\text{m}$ respectively. The high Nb, Mo and C content in 02-630Nb⁺VMo and 06-630Nb⁺VMo ensured that there was adequate strain induced precipitates to pin the grain boundaries, thereby retarding grain growth. The lower coiling temperatures of 630°C and 600°C respectively also acted as a disincentive to grain growth. However, the reason why 21-650TiMo had the

smallest grain size could not be established; bearing in mind that it had a relatively high coiling temperature of 650°C.

7.3.4 Grain Size Estimation – SEM and EBSD

Using the linear intercept method, KS run 400 software was used to measure the grain sizes on SEM images. A minimum of ten images were analysed for each of the samples. Approximately 200 to 500 grains were measured for each of the samples and the grain size distributions were reported in figures 6.32 and 6.33. The average grain sizes were tabulated in table 6.2. In order to validate these results, Tata Steel carried out EBSD analysis on all the samples and the results were compared with data obtained through SEM analysis.

From EBSD analysis, grain boundary type proportions were calculated as the fraction of the total length. The red colour on the misorientation maps depicted high angle while blue indicated low angle grain boundaries. Orientation distribution curves were plotted from the EBSD misorientation results and it was quite clear that the majority of the recrystallized boundaries had misorientation angles ranging from 15 to 60°, consistent with the equiaxed structure resulting from comparatively slow transformation from austenite to ferrite. Grain size measurements from EBSD misorientation maps were also tabulated in table 6.2. A comparison of results for each of the samples is shown in Figure 7.8. While there is some difference between the two measurements, there is generally good agreement. Perhaps surprisingly, the greatest error was for 18-650, which had the coarsest grain size. EBSD tends to give a smaller measured grain size than SEM since EBSD will identify sub grain boundaries, which are probably not detectable in conventional SEM images. IN this respect, the sample preparation is crucial to the credibility of EBSD results. Plastic strains introduced during grinding and polishing can reduce the diffraction pattern quality [164]. Noise reduction or data clean up packages designed to enable the users to make adjustments to points “incorrectly” indexed can create rather than fix indexing errors[164, 165]. Data clean ups need to be performed more cautiously to avoid distortion of data. Subgrain boundaries can be indexed as grain boundaries when EBSD is used for grain size measurements. This can result in understating the average grain size and this together with some of the reasons mentioned above, could

be the possible reasons why the average grain size seemed lower in EBSD as compared to SEM in this study.

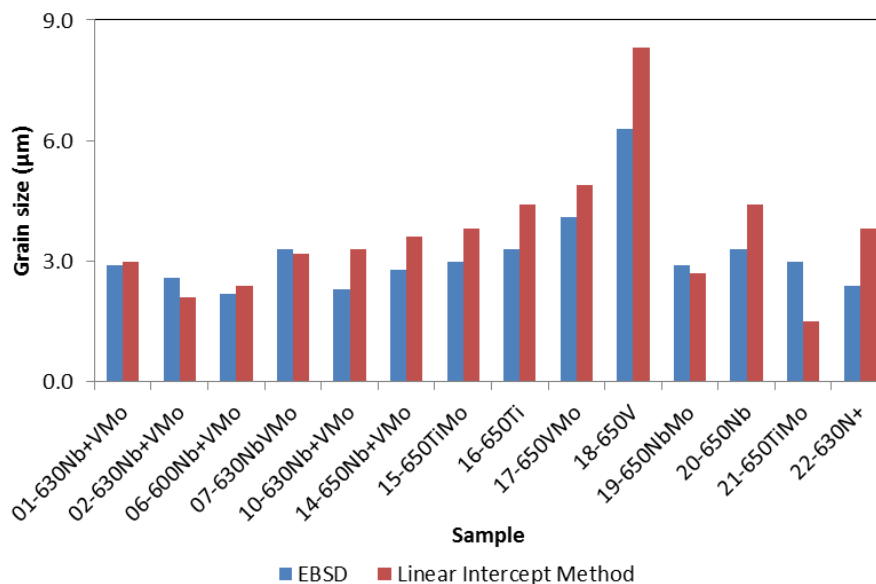


Figure 7.8 – Grain size comparisons for results obtained through EBSD and SEM

7.3.5 Precipitate Analysis

Due to the size, morphology and high number densities, the precipitates found in most of the samples investigated in this study were believed to be interphase precipitates (IP). Rows of planar IP were clearly observed in most of the samples. Even though planar IP was not clearly visible in 01-630Nb⁺VMo, the precipitates in figure 6.34 show a certain degree of orderliness which is only associated with IP. Ricks and Howell[145] showed that irregular arrays which are believed to nucleate at higher energy γ to α interphase boundaries that migrates without the step propagation are sometimes observed either independently or within the same grains as planar IP. The pinning process occurs in a disorderly manner, resulting in variable spacing, which leads to a more random distribution of precipitates. The mechanism for the formation of these precipitates is believed to be similar to Orowan looping, but without leaving loops on precipitates[142, 145]. This could be the reason why planar IP was not clearly evident in this sample.

The existence of arrays of precipitates in samples 02-630Nb⁺VMo, 06-630Nb⁺VMo, 10-630Nb⁺VMo, 14-630Nb⁺VMo, 15-650TiMo, 17-650VMo and 22-630N⁺ confirms that these precipitates were formed through interphase precipitation. Even

though 21-TiMo had a very high number density of fine precipitates it was not evident that they were formed by interphase precipitation. SEM imaging revealed that the microstructure for this sample was predominantly bainitic ferrite. This observation suggests that the transformation was too fast to allow interphase precipitation. Hence, the precipitates were likely to have been formed through other mechanisms, possibly on dislocations. The high carbon content coupled with a lower coiling temperature of 630°C created suitable conditions for high numbers of precipitate nucleation sites, resulting in high precipitate number densities in this sample.

TEM thin foil images in Figure 6.71 shows the existence of grain boundary carbides in 19-650NbMo. Curved boundaries were also a common feature, suggesting pinning of the grain boundaries possibly by strain induced precipitates. This was expected since Nb based carbide precipitation has been known to occur on dislocations and dislocation sub structures in the austenite[69]. They are normally formed at temperatures in the range of 850-950°C, e.g. during controlled rolling after solution treatment, and allowing times between deformation passes for precipitation to occur. In this case, the process route was not optimised for these precipitates to form, and evidently, they did not form via interphase precipitation, resulting in lower precipitate number densities.

7.3.6 Precipitate Morphology and Chemistry

TEM images on thin foils and on carbon extraction replicas showed that the majority of precipitates in all samples were spherical. However, rod shaped precipitates were also found. Cube shaped precipitates, though few and far between were also a common feature in all the samples. In some cases, the precipitates existed in the form of clusters while in other cases they existed as stringers.

Vanadium carbides, due to their high solubility in austenite, tend to form at much lower temperatures as compared to NbC and TiC[71, 127]. As a result, vanadium carbides play a more important role in precipitation strengthening as compared to the other two. Nb and Ti are more effective in grain refinement as compared to V. Alloying 01-630Nb⁺VMo 02-630Nb⁺VMo, 06-630Nb⁺VMo, 07-630NbVMo 10-

630Nb⁺VMo and 14-630Nb⁺VMo with vanadium was meant to bring about optimum precipitation strengthening since V has been well known to produce interphase precipitates[11, 70, 73].

The addition of Mo in Nb and Ti microalloyed steels is known to promote the formation of fine titanium and niobium carbides. Mo is known to retard precipitate growth in both Nb and Ti alloyed steels [10, 75, 99, 137]. This theory was also supported by the observation that fine precipitates containing Mo were detected by EELS and EDX analysis in samples 15-650TiMo and 19-650NbMo. The fine precipitates in 21-650TiMo were also found to be of similar chemical composition.

The effect of Mo on V microalloyed steel has not been studied so far. This study showed that Mo coexisted with V in all vanadium carbides in all the samples that were alloyed with both Mo and V. Energy dispersive X-ray spectroscopy (EDX) and Energy Loss Spectroscopy (EELS) on the fine spherical and rod shaped precipitates revealed that they were mostly V(Mo)C. Just like in Ti and Nb microalloyed steels, Mo is likely to slow down the migrating interphase boundary, thereby creating suitable conditions for interphase precipitates to form while at the same time providing the resistance to coarsening, which is critical for the performance of the alloy.

A high volume fraction of nitrogen was also deliberately added to sample 22-630N⁺ in order to study the effect of the high nitrogen content on a V-Mo-C microalloyed steel. Nb was limited to 0.008 wt.% to minimise the rolling forces. Just like the V microalloyed steels previously discussed, EELS spectroscopy revealed that the fine precipitates were mainly VCN. Further analysis using EDX showed the existence of Mo in all the VCN. This also confirmed that Mo plays a similar role in resisting precipitate coarsening as well as promoting IP by slowing down of the interphase boundary.

As expected titanium carbides formed the majority of the precipitates in 16-650Ti, while vanadium carbides formed the majority in 18-650V and niobium carbides formed the majority of the precipitates in 20-650Nb. Note that Ti was always detected even in samples where it was not deliberately added. The reason could be

due to the high sensitivity of Ti to EELS. Ti was detected in almost all the samples in this study suggesting possible contamination from previous castings in the refractory furnace.

Another important observation was that spherical and rod shaped precipitates were always of similar chemical composition. This implies that they might have been one and the same with the only difference being the orientation at which they were viewed. Hence, the spherical and rod shaped precipitates were the same; the rod shaped ones being viewed along the long axis and end-on. TEM thin foil analysis also showed that in regions dominated by IP, a substantial number of rod shaped precipitates always formed part of the IP, which seemed to support this conclusion.

7.3.7 Precipitate Size Distribution and Number Densities

It has been reported in literature that the concentration of alloying elements at the transformation front has a major effect on the interparticle distance[70]. Optimum solubility can only be attained through the addition of sufficient microalloying elements to get the right stoichiometric balance. The reason why high precipitate number densities were observed in 02-630Nb⁺VMo as compared to 01-630Nb⁺VMo could be due to the low percentage weight of V in 01-630Nb⁺VMo (0.10 wt.%) which was half as much as 02-630Nb⁺VMo (0.20 wt.%). The C content in 02-630Nb⁺VMo was also much higher, creating optimal conditions for solute diffusion at the transformation front to form precipitates. Hence, the C and V contents in 01-630Nb⁺VMo might have been below the threshold for optimum IP to occur.

The reason why 18-650V had the coarsest and also the widest size distribution could be attributed to the omission of Mo. This study suggests that Mo plays a similar role in V microalloyed steels as in Nb and Ti microalloyed steels. Mo seems to enhance V precipitation as well as slowing down the migrating interphase boundaries. It also enhances resistance to coarsening, which is critical to the performance of the alloy. The finest precipitates were V(Mo)C without nitrogen. The coiling temperature of 650°C was also adequately high enough to promote the coarsening of precipitates. Park et al.[76] studied the effects of coiling temperature on precipitate behaviour and their conclusion was that precipitate sizes tends to decrease with decreasing

coiling temperature. This was attributed to increased nucleation sites and reduced precipitate growth associated with supercoiling. The same could be said for 17-650VMo. The precipitates were slightly smaller in this instance and this could have been influenced by the presence of Mo in the steel. However, the observation that it had the second largest average precipitate size as well as size distribution suggests that the level of Mo in the steel might not have been adequate to have a significant influence on the coarsening rate. The right stoichiometric balance is always required for optimum precipitation strengthening. Lee et al.[137], working on a Nb microalloyed steel, concluded that the strength tends to improve with increasing Mo additions.

The existence of fine precipitates in most of the V microalloyed steels in the present study could therefore be credited to the presence of Mo in those steels.

7.3.8 Carbon Extraction Replicas – The Challenges

As previously mentioned, the preparation of TEM carbon extraction replicas was quite challenging. Initially, 5% nital solution was used to etch the samples before carbon coating. The same solution was then used to extract the replicas after carbon coating. However, instead of extracting the particles only, portions of the matrix were also extracted and this made it quite difficult to identify the actual precipitates. After trying several other etchants, Vilella's solution was found to deliver the best results. Vilella's solution was used to etch the samples both before carbon coating and after carbon coating. It was used to prepare the V microalloyed steels studied in the second part of this project and it was also most effective when it was used for the ferritic microalloyed steels which formed the last part of this project.

Extracting the actual particles also created another challenge. It was difficult to get good quality replicas from samples that later showed high precipitate number densities. The reason why this was the case could not be established at this point. Since extraction replicas are believed to reliably extract precipitates >5nm [69, 132], the fineness of the precipitates in this study means that not all the precipitates might not have been captured during the preparation of carbon extraction replicas. Counting the precipitates also presented another challenge; ImageJ software was

used for counting the precipitates. In some cases, the software found it difficult to distinguish between dark contrast and the actual precipitates especially in instances where the precipitates were so fine. Hence, precipitate number densities might have been underestimated in some cases while in others, they might have been overestimated.

7.4 Summary

As previously mentioned, vehicle light-weighting is one of the proven methods for reducing carbon emissions which causes global warming in automotive vehicles. As a result, the major objective of this study was to develop a microalloyed steel with the ferrite strengthened by nanoprecipitates. Interphase precipitates have been widely studied and they are known to strengthen the ferrite without affecting the ductility of the steel. The project was then divided into three major parts.

The first part of the project studied three multiphase steels to get an insight on which of the three chemical compositions was most likely to produce interphase precipitates, which are known to be crucial for precipitation strengthening. The first steel was the Ti-Al-Mo composition and had already been subjected to a patent by JFE Steels[13] and it was crucial to verify whether the claims made were true. It was also used as a suitable comparison to check whether the same mechanical properties could be obtained from the V and the Ti microalloyed steels which were studied at the same time. The initial results showed that the Ti-Al-Mo composition was superior to the other two and it was the only steel which showed signs of IP. High UTS of 780MPa and high uniform elongation of 21% was obtained in this steel. The good mechanical properties claimed by JFE steels were verified at this stage and the challenge was to check whether it was possible to get similar mechanical properties from either the Ti or the V microalloyed steel composition.

Following the initial studies on the three multiphase steels, the second stage of the project involved development of thermal cycles in order to study the time/temperature/transformation behaviour of V microalloyed steels. Thermal cycles were developed in order to optimise the mechanical properties. The microstructures developed were extensively studied and related to the mechanical properties. 700-1200s had the highest precipitate number densities. A high total elongation of 30.8% and UTS of 627MPa was observed for this steel. However, the YS and UTS obtained were not adequate enough to add value to the existing automotive steels. Questions were raised as to why IP was not observed. One of the possible reasons was the austenising temperature of 950°C which was believed to be too low to dissolve most

of the carbides in the alloy to promote IP during the temperature hold in the $\gamma + \alpha$ region. The high N content was also presented as being one of the possible reasons. However, this had to be verified and it became one of the objectives for the last stage of the project.

The last part of the project involved studying microalloyed Nb-V-Mo ferritic steel. Mo has been well known not only to enhance the formation of IP in Nb and Ti alloyed steels, but also to retard the rate of precipitate growth [10, 75, 99, 137]. However, little was known on the influence of Mo on V microalloyed steels. As a result, this was a good chance to fill the gap in literature on the influence of Mo on V microalloyed steels. For comparison purposes, the study also included Ti-Mo, Ti, V-Mo, V, Nb-Mo and Nb microalloyed steels. For most of the Nb-V-Mo microalloyed steels, IP was observed in the majority of the steels. The mechanical properties recorded were quite fascinating. Coiling the steel at 600°C resulted in a very high YS of 925MPa, UTS of 1023MPa and total elongation of 16.8%. The good mechanical properties were a credit to Mo additions, which were found to have a crucial influence on the formation of fine precipitates that strengthened the ferritic steels. It was concluded that Mo additions also plays a crucial role in retarding the rate of precipitate growth in V microalloyed steels. At this stage, it was also concluded that in the previous batch of V microalloyed steels, the high N content was not responsible for the low precipitate counts; it was probably the austenising temperature of 950°C which was not high enough to dissolve the carbides in the steel.

The objectives of the project were fulfilled by the end of the project. Tata Steel's commercial objective of creating viable steel with high strength and high ductility for automotive applications had also been fulfilled.

CHAPTER 8: FUTURE WORK

The current study revealed the presence of Mo in all the fine precipitates examined in all the V-Nb-Mo microalloyed steels in the last phase of this project. Studying these nanosized carbides is complicated by their mere sizes, however, further TEM work especially on carbon extraction replicas needs to be carried out in order to get EDX and X-ray spectrums as well as diffraction patterns. Quantitative EDX data could be analysed get the exact chemical composition of these precipitates while diffraction pattern analysis could be used to estimate the lattice parameters. This data could then be used to give a better description of the structure of the precipitates.

Atom Probe Tomography (APT) is known to be one of the most powerful tools for examining the location of atoms at the atomic scale[166]. This technique could also be used to determine the exact location of the Mo within the V(Mo)C and the V(Mo)CN. Using the same technique, the Guinier radius which is a representation of the precipitate's actual size could also be calculated. The results obtained would then be used as a suitable comparison with results obtained through TEM.

The steels studied in the final stage of the project had both high strength and high ductility. Further work is required to investigate the forming of these steels. In particular, focus should be on why these steels, with precipitates <10nm exhibited high ductility, while steels with a slightly larger precipitate size (>10nm) had lower ductility.

CHAPTER 9: CONCLUSIONS

The work presented in this thesis was broken down into three major stages with the overall objective being the development of ultra-high strength steel with the ferrite strengthened by nanoprecipitates for automotive applications. The conclusions from each part of the project will be presented.

9.1 Multiphase Steels with the Ferrite Strengthened by Nanoprecipitates

The first part of the project studied three multiphase steels to get an insight on which of the three chemical compositions was most likely to produce interphase precipitates, which are known to be crucial for precipitation strengthening. It was also intended to verify the exceptional mechanical properties claims by other authors on one Ti-Al-Mo steel. The following conclusions were noted.

1. The Ti-Al-Mo microalloyed steel had better mechanical properties as compared to the V and Ti microalloyed steels. High UTS of 780MPa and a total elongation of 21.8% were recorded and this was in agreement with claims by JFE Steels. However, claims by Raabe et al. of up to 1.5GPa could not be verified.
2. The 4s hold promoted the formation interphase precipitates, which were observed in TiAlMo-2S. The temperature hold allowed austenite to transform to ferrite. Interphase precipitates were then formed as a result of that transformation.
3. For the Ti microalloyed steels, high UTS of 755MPa and 810MPa were recorded in Ti-2S and TiCC respectively. However, this was at the expense of the total elongation, which was found to be low at 12.1% and 8.1% respectively. The bainitic microstructure in both steels might have contributed towards the high strength and low uniform elongation. The 4s hold in Ti-2S was not adequate to make a significant influence on the γ to α transformation, resulting in fine

grained microstructure as a result of the transformation from austenite to bainite after fast cooling to the bainite transformation temperature.

4. The existence of fully recrystallized grains in V-2S was a result of the 4s temperature hold which was adequate for the transformation from γ to α . The ferrite grains formed accounted for the high uniform elongation of 21% while the low UTS of 623MPa can be attribute to the low precipitate count. In V-CC, a high UTS of 794MPa and low total elongation of 9.0% were recorded and this was due to fast cooling from austenitic region to bainite transformation temperature which resulted in the transformation of all the austenite to bainite.
5. Retained austenite was not formed in any of the V and Ti microalloyed steels and this might have been due to the absence of Al. However, 7% RA was found in TiAlMo.

9.2 Time/Temperature/Transformation Behaviour of a Vanadium Microalloyed Steel

The dependency of the microstructure on the time/temperature/transformation behaviour of V microalloyed steels were studied as part of the second stage of this project and the following conclusions were made.

1. The average hardness decreased with decreasing transformation temperature. The samples that were quenched from the austenising temperature of 950°C were found to have the highest Vickers' hardness averaging 280HV10. However, the hardness decreased with decreasing temperature. The sample transformed at the lowest temperature of 625°C for 300s had the lowest Vickers hardness of 193.4HV10.
2. The volume fraction of ferrite increased with decreasing transformation temperature. Samples that were quenched from the austenising temperature of 950°C were either bainitic or a mixture of bainite, martensite and few ferrite grains. However, at the transformation temperature of 750°C, approximately 50% ferrite was recorded when the temperature was held for 1800s. At the transformation temperature of 625°C, the volume fraction of ferrite recorded was the highest at 98%.
3. The average grain size decreased with decreasing transformation temperature. Quenching from the austenising temperature of 950°C resulted in a fine microstructure comprising of bainite with martensite in some instances. When a temperature hold was introduced at 750°C, the average grain size recorded was 5.78µm and this decreased until a minimum of 2.69µm was recorded when the transformation temperature was at its lowest (625-300s).
4. Optimising the transformation temperature and time is key to the development of the desired microstructure for the best microstructure and subsequent mechanical properties. The optimum conditions for maximum

precipitation strengthening for this chemical composition was found to be the transformation at a temperature of 700°C coupled with a temperature hold for 1200s. The highest precipitate number densities were recorded under these conditions and it was also observed that a high uniform elongation of 30.8% and the highest yield strength of 562MPa were recorded under the same conditions.

5. The optimum precipitation strengthening can be achievable through a good balance between the precipitate sizes, how they are distributed within the microstructure, the degree of coherency and their number density. A high number density of precipitates with the smallest possible average separation distance can produce the greatest strengthening. 700-1200s had the highest precipitation count of 394 particles/ μm^2 with most of the particles averaging less than 10nm. It is clear from the estimated results that the highest contribution to yield strength through precipitation strengthening was recorded in this sample (270MPa).

6. Nanoprecipitates can boost the strength of microalloyed vanadium alloyed steels without significantly lowering the ductility. Despite 700-1200s having the highest yield strength of 562MPa, its uniform elongation of 30% was quite high and it compared very well with the other samples. As an example, the highest uniform elongation of 33.4% was recorded in 650-60s with 548MPa UTS.

9.3 Ferritic V-Nb-Mo Microalloyed Steels Strengthened by Nanoprecipitates

Based on the results in chapter 7 and the discussion in chapter 8, the following conclusions were made:-

1. Precipitation strengthening can significantly boost the yield strength without lowering the ductility in microalloyed steels. The highest contribution to yield strength from precipitation strengthening was recorded in 10-630Nb⁺VMo. An estimated total contribution of 546MPa was recorded and this boosted the yield strength to 902MPa.
2. Precipitation strengthening can boost the yield strength without compromising the ductility. Besides having the highest yield strength, 10-630Nb⁺VMo had a reasonably high uniform elongation of 18.2% as well.
3. Mo plays a crucial role in the nucleation of precipitates in V microalloyed steels. Mo was deliberately omitted from 18-650V and the precipitate count was 194 particle/ μm^2 . The 0.24wt.% Mo addition in 07-630NbVMo resulted in an abrupt jump in precipitate density to 316 particles/ μm^2 . Doubling the amount of Mo resulted in high precipitate counts being recorded. A good example was 10-630Nb+VMo with 1766 particles/ μm^2 .
4. Mo plays a crucial role in the retardation of precipitate growth in V microalloyed steels. 18-650V with no Mo additions had the widest precipitate size distribution as a result of precipitate coarsening. However, with Mo additions, over 80% of the precipitates counted were less than 10nm in size. This confirmed that Mo had a lot of influence on the rate of precipitate coarsening.
5. The presence of Mo in VCN [V(Mo)CN] and VN [V(Mo)N] under conditions of high N content confirms that Mo retards coarsening of VN and VCN in a similar way to VC. High amounts of N were deliberately added to 22-630N+ and fine precipitates averaging 7nm were observed.

-
6. Spherical and rod shaped precipitates had the same composition, suggesting that they were the same, but the rod shaped precipitates had been viewed along the long axis and end-on. Where IP was observed, rod shaped precipitates were sometimes observed even though carbon extraction replicas showed that most of the precipitates were spherical.

REFERENCES

- [1] National Statistics. (March, 2013). 2012 UK Greenhouse gas emissions, provisional figures and 2011 UK greenhouse gas emissions, final figures by fuel type and end user. *National Statistics: Department of Energy & Climate Change UK (Accessed 26/06/2013)*. Available: https://www.gov.uk/government/uploads/system/uploads/attachment_data/file/193414/280313_ghg_national_statistics_release_2012_provisional.pdf
- [2] H. Wallentowitz. (2003) Materials for future automotive body structures. *Business Briefing: Global Automotive Manufacturing & Technology (Accessed 18/02/2011)*. Available: http://www.touchbriefings.com/pdf/11/auto031_r_wallentowitz.pdf
- [3] "Toyota on a roll," *Nature*, vol. 435, pp. 1004-1004, 2005.
- [4] E. R. H. Fuchs, F. R. Field, R. Roth, and R. E. Kirchain, "Strategic materials selection in the automobile body: Economic opportunities for polymer composite design," *Composites Science and Technology*, vol. 68, pp. 1989-2002, 2008.
- [5] "Development of Ultra High Strength Steels for Reduced Carbon Emissions in Automotive Vehicles," in *Project Outlines*, ed. Sheffield: University of Sheffield and University of Manchester, 2010, p. 11.
- [6] K. Chung, K. Ahn, D.-H. Yoo, K.-H. Chung, M.-H. Seo, and S.-H. Park, "Formability of TWIP (twinning induced plasticity) automotive sheets," *International Journal of Plasticity*, vol. 27, pp. 52-81, 2011.
- [7] Y. Funakawa, T. Shiozaki, K. TOMITA, T. Yamamoto, and E. Maeda, "Development of High Strength Hot-rolled Sheet Steel Consisting of Ferrite and Nanometer-sized Carbides," *ISIJ International*, vol. 44 pp. 1945–1951, 2004.
- [8] T.-P. Wang, F.-H. Kao, S.-H. Wang, J.-R. Yang, C.-Y. Huang, and H.-R. Chen, "Isothermal treatment influence on nanometer-size carbide precipitation of titanium-bearing low carbon steel," *Materials Letters*, vol. 65, pp. 396-399, 2011.
- [9] M. A. Suarez, M. A. Alvarez-Pérez, O. Alvarez-Fregoso, and J. A. Juárez-Islas, "Effect of nanoprecipitates and grain size on the mechanical properties of advanced structural steels," *Materials Science and Engineering: A*, vol. 528, pp. 4924-4926, 2011.
- [10] D. Raabe, D. Ponge, O. Dmitrieva, and B. Sander, "Nanoprecipitate-hardened 1.5 GPa steels with unexpected high ductility," *Scripta Materialia*, vol. 60, pp. 1141-1144, 2009.

-
- [11] Bhadeshia H. K. D. H and Honeycombe R.W. K, "Steels Microstructure and Properties," E. publishing, Ed., 3rd ed Cambridge: Butterworth-Heinemann, 2006, pp. 88, 147, 148, 220 – 233.
- [12] T. S. Wang, Z. Li, B. Zhang, X. J. Zhang, J. M. Deng, and F. C. Zhang, "High tensile ductility and high strength in ultrafine-grained low-carbon steel," *Materials Science and Engineering: A*, vol. 527, pp. 2798-2801, 2010.
- [13] Yokota T, Kobayashi A, K. Seto, Hosoya Y, Heller T, Bode R, and Stich G, "A high strength steel excellent in uniform elongation properties and method of manufacturing the same," *European Patent 1 790 737 A1*, May 30, 2007.
- [14] SteelworksOnline. (June, 2013). Steel is the solution to achieve 54.5MPG by 2025. *American Iron and Steel Institute (Accessed - 05/06/2013)*. Available: http://www.steel.org/en/sitecore/content/Autosteel_org/Web%20Root/Research/Growth%20of%20AHSS.aspx
- [15] A. T. Mayyas, A. Qattawi, A. R. Mayyas, and M. Omar, "Quantifiable measures of sustainability: a case study of materials selection for eco-lightweight auto-bodies," *Journal of Cleaner Production*, vol. 40, pp. 177-189, 2013.
- [16] A. Mayyas, A. Qattawi, M. Omar, and D. Shan, "Design for sustainability in automotive industry: A comprehensive review," *Renewable and Sustainable Energy Reviews*, vol. 16, pp. 1845-1862, 2012.
- [17] ASMInternational. High Strength Low Alloy Steels. *Alloying: Understanding the basics (#06117G)*, 2001.
- [18] W. C. Leslie, "The physical metallurgy of steels," M.-H. B. Company, Ed., 3rd ed Washington, New York, London: Hemisphere Publishing Corporation, 1981, pp. 5,43-50, 142-210.
- [19] M. Kleiner, M. Geiger, and A. Klaus, "Manufacturing of lightweight components by metal forming," *CIRP Annals - Manufacturing Technology*, vol. 52, pp. 521-542, 2003.
- [20] M. Kleiner, S. Chatti, and A. Klaus, "Metal forming techniques for lightweight construction," *Journal of Materials Processing Technology*, vol. 177, pp. 2-7, 2006.
- [21] R. Neugebauer, T. Altan, M. Geiger, M. Kleiner, and A. Sterzing, "Sheet metal forming at elevated temperatures," *CIRP Annals - Manufacturing Technology*, vol. 55, pp. 793-816, 2006.
- [22] ULSAB-AVC. Body Structure Materials. *Technical Transfer Dispatch No. 6, 2001*.

-
- [23] WorldAutoSteel. Advanced High Strength Steel (AHSS) - Application Guidelines. *Version 4.1, June 2009 (Accessed 12/09/2013)*. Available: <http://www.worldautosteel.org/projects/ahss-guidelines/>
- [24] F. Ozturk, A. Polat, S. Toros, and R. C. Picu, "Strain Hardening and Strain Rate Sensitivity Behaviors of Advanced High Strength Steels," *Journal of Iron and Steel Research, International*, vol. 20, pp. 68-74, 2013.
- [25] D. J. Schaeffler. (2004, Accessed: 07/08/2013). Introduction to advanced high strength steels Part I : Grade overview. Available: <http://www.thefabricator.com/article/metalsmaterials/introduction-to-advanced-high-strength-steels---part-i>
- [26] N. D. Beynon, T. B. Jones, and G. Fournalis, "Effect of high strain rate deformation on microstructure of strip steels tested under dynamic tensile conditions," *Materials Science and Technology*, vol. 21, pp. 103-112, 2005.
- [27] S. S. Hansen and R. R. Pradhan, "Structure – properties relationships and continuous yielding behaviour in Dual Phase steels," in *Conference and Proceedings of the Fundamentals of Dual – Phase Steels*, 1981, pp. 113-114.
- [28] S. Oliver, T. B. Jones, and G. Fournalis, "Dual phase versus TRIP strip steels: Microstructural changes as a consequence of quasi-static and dynamic tensile testing," *Materials Characterization*, vol. 58, pp. 390-400, 2007.
- [29] G. Thomas, "New Cold formable Fe/Al/C Dual Phase steels," in *Proceedings of an International Conference on HSLA Steels, Metallurgy and Applications*, 1985, pp. 801-808.
- [30] M. R. Akbarpour and A. Ekrami, "Effect of ferrite volume fraction on work hardening behavior of high bainite dual phase (DP) steels," *Materials Science and Engineering A*, vol. 477, pp. 306-310, 2008.
- [31] A. Kumar, S. B. Singh, and K. K. Ray, "Influence of bainite/martensite-content on the tensile properties of low carbon dual-phase steels," *Materials Science and Engineering A*, vol. 474, pp. 270-282, 2008.
- [32] F. M. Al-Abbasi and J. A. Nemes, "Characterizing DP-steels using micromechanical modeling of cells," *Computational Materials Science*, vol. 39, pp. 402-415, 2007.
- [33] N. Saeidi and A. Ekrami, "Comparison of mechanical properties of martensite/ferrite and bainite/ferrite dual phase 4340 steels," *Materials Science and Engineering A*, vol. 523, pp. 125-129, 2009.
- [34] G. Dini, A. Najafizadeh, R. Ueji, and S. M. Monir-Vaghefi, "Improved tensile properties of partially recrystallized submicron grained TWIP steel," *Materials Letters*, vol. 64, pp. 15-18, 2010.

-
- [35] T. B. Jones and C. Europea, *Optimisation of both steel properties and autobody structural designs for axial, side and off set impact loading*: Office for Official Publications of the European Communities, 2002.
- [36] A. K. Srivastava, D. Bhattacharjee, G. Jha, N. Gope, and S. B. Singh, "Microstructural and mechanical characterization of C–Mn–Al–Si cold-rolled TRIP-aided steel," *Materials Science and Engineering: A*, vol. 445–446, pp. 549-557, 2007.
- [37] H. Huh, S. B. Kim, J. H. Song, and J. H. Lim, "Dynamic tensile characteristics of TRIP-type and DP-type steel sheets for an auto-body," *International Journal of Mechanical Sciences*, vol. 50, pp. 918-931, 2008.
- [38] O. Matsumura, Y. Sakuma, and H. Takechi, "Trip and its kinetic aspects in austempered 0.4C-1.5Si-0.8Mn steel," *Scripta Metallurgica*, vol. 21, pp. 1301-1306, 1987.
- [39] O. Matsumura, Y. Sakuma, and H. Takechi, "Enhancement of Elongation by Retained Austenite in Intercritical Annealed 0.4C-1.5Si-O.8Mn Steel," *Transactions of the Iron and Steel Institute of Japan*, vol. 27, pp. 570-579, 1987.
- [40] B. C. De Cooman, "Structure-properties relationship in TRIP steels containing carbide-free bainite," *Current Opinion in Solid State and Materials Science*, vol. 8, pp. 285-303, 2004.
- [41] H. C. Chen, H. Era, and M. Shimizu, "Effect of phosphorus on the formation of retained austenite and mechanical properties in Si-containing low-carbon steel sheet," *Metallurgical Transactions A*, vol. 20, pp. 437-445, 1989/03/01 1989.
- [42] W. C. Jeong, D. K. Matlock, and G. Krauss, "Effects of tensile-testing temperature on deformation and transformation behavior of retained austenite in a 0.14C-1.2Si-1.5Mn steel with ferrite-bainite-austenite structure," *Materials Science and Engineering A*, vol. 165, pp. 9-18, 1993.
- [43] A. Itami, M. Takahashi, and K. Ushioda, "Cold-Rolled High-Strength TRIP Sheet Steels and Plastic Stability of Their Retained Austenite," *Proc. High-Strength Steels for Automotive Symposium*, p. 245, 1994.
- [44] K. Sugimoto, N. Usui, M. Kobayashi, and S. Hashimoto, "Effects of Volume Fraction and Stability of Retained Austenite on Ductility of TRIP-aided Dual-phase Steels," *The Iron and Steel Institute of Japan*, vol. 32, pp. 1311-1318, 1992.
- [45] H. K. D. H. Bhadeshia, "TRIP-Assisted Steels?," *ISIJ International*, vol. 42, pp. 1059-1060, 2002.

-
- [46] J. P.J, "Transformation-induced plasticity for high strength formable steels," *Current Opinion in Solid State and Materials Science*, vol. 8, pp. 259-265, 2004.
- [47] D. Barbier, N. Gey, S. Allain, N. Bozzolo, and M. Humbert, "Analysis of the tensile behavior of a TWIP steel based on the texture and microstructure evolutions," *Materials Science and Engineering: A*, vol. 500, pp. 196-206, 2009.
- [48] O. Grässel, L. Krüger, G. Frommeyer, and L. W. Meyer, "High strength Fe-Mn-(Al, Si) TRIP/TWIP steels development -- properties -- application," *International Journal of Plasticity*, vol. 16, pp. 1391-1409, 2000.
- [49] O. Bouaziz, S. Allain, and Y. Estrin, "Effect of pre-strain at elevated temperature on strain hardening of twinning-induced plasticity steels," *Scripta Materialia*, vol. 62, pp. 713-715, 2010.
- [50] A. Grajcar, R. Kuziak, and W. Zalecki, "Third generation of AHSS with increased fraction of retained austenite for the automotive industry," *Archives of Civil and Mechanical Engineering*, vol. 12, pp. 334-341, 2012.
- [51] G. Krauss, "Martensite in steel: Strength and structure," *Materials Science and Engineering A*, vol. 273-275, pp. 40-57, 1999.
- [52] D. H. Ping, M. Ohnuma, Y. Hirakawa, Y. Kadoya, and K. Hono, "Microstructural evolution in 13Cr-8Ni-2.5Mo-2Al martensitic precipitation-hardened stainless steel," *Materials Science and Engineering A*, vol. 394, pp. 285-295, 2005.
- [53] A. Ghosh, S. Das, and S. Chatterjee, "Ultrahigh strength hot rolled microalloyed steel: Microstructure and properties," *Materials Science and Technology*, vol. 21, pp. 325-333, 2005.
- [54] R. L. Klueh, N. Hashimoto, and P. J. Maziasz, "Development of new nano-particle-strengthened martensitic steels," *Scripta Materialia*, vol. 53, pp. 275-280, 2005.
- [55] Z. Guo, W. Sha, and D. Vaumousse, "Microstructural evolution in a PH13-8 stainless steel after ageing," *Acta Materialia*, vol. 51, pp. 101-116, 2003.
- [56] J. Speer, D. K. Matlock, B. C. De Cooman, and J. G. Schroth, "Carbon partitioning into austenite after martensite transformation," *Acta Materialia*, vol. 51, pp. 2611-2622, 2003.
- [57] J. G. Speer, A. M. Streicher, D. K. Matlock, F. C. Rizzo, and G. Krauss, "Austenite formation and decomposition " *Warrendale, PA, USA, TMS/ISS*, pp. 505 - 522, 2003.
- [58] A. J. Clarke, J. G. Speer, M. K. Miller, R. E. Hackenberg, D. V. Edmonds, D. K. Matlock, F. C. Rizzo, K. D. Clarke, and E. De Moor, "Carbon partitioning

-
- to austenite from martensite or bainite during the quench and partition (Q&P) process: A critical assessment," *Acta Materialia*, vol. 56, pp. 16-22, 2008.
- [59] D. V. Edmonds, K. He, F. C. Rizzo, B. C. De Cooman, D. K. Matlock, and J. G. Speer, "Quenching and partitioning martensite--A novel steel heat treatment," *Materials Science and Engineering: A*, vol. 438-440, pp. 25-34, 2006.
- [60] S. Zajac, V. Schwinn, and K. H. Tackle, "Characterization and quantification of complex bainitic microstructure in high and ultra-high strength linepipe steel," in *International Symposium -aS'05*, San Sebastian, 2005.
- [61] ASTM., "Electron microstructure of bainite in Steels," in *2nd Progress report by subcommittee XI of committee E-4*, ed: American Society for Testing and Materials, 1952, p. 543.
- [62] F. B. Pickering, "The Structure and Properties of Bainite in Steels," presented at the Transformation and Hardenability in Steels. , Michigan, 1967.
- [63] T. Gladman, I. D. McIvor, and F. B. Pickering, "Some Aspects of the Structure-Property Relationship in High Carbon Ferrite-Pearlite Steels," *Journal of Iron and Steel Institute*, vol. 210, pp. 916-930, 1972.
- [64] W. Heller, "Rail Steels," vol. STP 644, ed. Philadelphia: American Society for Testing and Materials, 1978, p. 162.
- [65] A. Saha Podder and H. K. D. H. Bhadeshia, "Thermal stability of austenite retained in bainitic steels," *Materials Science and Engineering: A*, vol. 527, pp. 2121-2128, 2010.
- [66] B. Mintz, "Hot dip galvanising of transformation induced plasticity and another intercritically annealed steel," *International Materials Reviews*, vol. 46, pp. 169-197, 2001.
- [67] R. D. K. Misra, H. Nathani, J. E. Hartmann, and F. Siciliano, "Microstructural evolution in a new 770 MPa hot rolled Nb-Ti microalloyed steel," *Materials Science and Engineering: A*, vol. 394, pp. 339-352, 2005.
- [68] F. A. Khalid, "Precipitation and compositional changes in the structural phases of microalloyed automotive steels," *Materials Science and Engineering A*, vol. 325, pp. 281-285, 2002.
- [69] W. M. Rainforth, M. P. Black, R. L. Higginson, E. J. Palmiere, C. M. Sellars, I. Prabst, P. Warbichler, and F. Hofer, "Precipitation of NbC in a model austenitic steel," *Acta Materialia*, vol. 50, pp. 735-747, 2002.
- [70] R. W. K. Honeycombe, "Fundamental Aspects of Precipitation in Microalloyed Steels," in *Proceedings of International Conference on HSLA Steels: Metallurgy and Applications*, Beijing, 1985, pp. 243-250.

-
- [71] K. Narita, *J. Iron. Steel Res. Int. Jpn.*, vol. 15, p. 147, 1975.
- [72] E. J. Drewes and E. F. Walker, "Niobium bearing steels in the automotive Industry," in *Proceedings of the International Symposium on Niobium TMS*, Warrendale, PA., 2001, pp. 873 - 888.
- [73] D. P. Dunne, "Review: Interaction of precipitation with recrystallisation and phase transformation in low alloy steels," *Materials Science and Technology*, vol. 26, pp. 410-420, 2010.
- [74] E. Girault, A. Mertens, P. Jacques, Y. Houbaert, B. Verlinden, and J. Van Humbeeck, "Comparison of the effects of silicon and aluminium on the tensile behaviour of multiphase TRIP-assisted steels," *Scripta Materialia*, vol. 44, pp. 885-892, 2001.
- [75] I. B. Timokhina, P. D. Hodgson, S. P. Ringer, R. K. Zheng, and E. V. Pereloma, "Precipitate characterisation of an advanced high-strength low-alloy (HSLA) steel using atom probe tomography," *Scripta Materialia*, vol. 56, pp. 601-604, 2007.
- [76] D.-B. Park, M.-Y. Huh, J.-H. Shim, J.-Y. Suh, K.-H. Lee, and W.-S. Jung, "Strengthening mechanism of hot rolled Ti and Nb microalloyed HSLA steels containing Mo and W with various coiling temperature," *Materials Science and Engineering: A*, vol. 560, pp. 528-534, 2013.
- [77] P. Chouquet, P. Fabregue, J. Giusti, B. Chamont, J. N. Pezant, F. Blanchet, and S. Yue, "Mathematical Modelling of Hot Rolling of Steels, ," in *The Metallurgical Society of CIM*, ed Montreal, 1990, p. 34.
- [78] M. Charleux, W. Poole, M. Militzer, and A. Deschamps, "Precipitation behavior and its effect on strengthening of an HSLA-Nb/Ti steel," *Metallurgical and Materials Transactions A*, vol. 32, pp. 1635-1647, 2001.
- [79] Y. M. Wang and E. Ma, "Three strategies to achieve uniform tensile deformation in a nanostructured metal," *Acta Materialia*, vol. 52, pp. 1699-1709, 2004.
- [80] W. D. Callister, "Material Science and Engineering: An Introduction," 7th ed New York: John Wiley & Sons Inc, 2007, pp. 174 - 201, 402 - 407.
- [81] H. Azizi-Alizamini, M. Militzer, and W. J. Poole, "A novel technique for developing bimodal grain size distributions in low carbon steels," *Scripta Materialia*, vol. 57, pp. 1065-1068, 2007.
- [82] Y. Okitsu, N. Takata, and N. Tsuji, "Mechanical properties of ultrafine grained ferritic steel sheets fabricated by rolling and annealing of duplex microstructure," *Journal of Materials Science*, vol. 43, pp. 7391-7396, 2008/12/01 2008.

-
- [83] R. Song, D. Ponge, D. Raabe, J. G. Speer, and D. K. Matlock, "Overview of processing, microstructure and mechanical properties of ultrafine grained bcc steels," *Materials Science and Engineering: A*, vol. 441, pp. 1-17, 2006.
- [84] R. Z. Valiev, A. V. Sergueeva, and A. K. Mukherjee, "The effect of annealing on tensile deformation behavior of nanostructured SPD titanium," *Scripta Materialia*, vol. 49, pp. 669-674, 2003.
- [85] I. V. Alexandrov and R. Z. Valiev, "Developing of SPD processing and enhanced properties in bulk nanostructured metals," *Scripta Materialia*, vol. 44, pp. 1605-1608, 2001.
- [86] V. V. Stolyarov, Y. T. Zhu, T. C. Lowe, R. K. Islamgaliev, and R. Z. Valiev, "Two step SPD processing of ultrafine-grained titanium," *Nanostructured Materials*, vol. 11, pp. 947-954, 1999.
- [87] L. Meyer, F. Heisterkamp, and W. Mueschenborn, "Microalloying 75," ed New York: Union Carbide Corp., 1976, p. 153.
- [88] T. Gladman, in *Recrystallization and grain growth of multiphase and particle containing materials*, Roskilde, Riso National Laboratories, 1980, pp. 183-192.
- [89] T. Gladman, in *HSLA Steels*, Warrendale, PA, TMS, 1992, pp. 3-14.
- [90] A. J. deArdo, "Metallurgical basis for thermomechanical processing of microalloyed steels," *Ironmaking & Steelmaking*, vol. 28, pp. 138-144, 2001.
- [91] I. Weiss and J. J. Jonas, "Dynamic precipitation and coarsening of niobium carbonitrides during the hot compression of HSLA steels," *Metallurgical Transactions A*, vol. 11, pp. 403-410, 1980.
- [92] S. Yamamoto, C. Ouchi, and T. Osuka, "Effect of microalloying elements on the recovery and recrystallization in deformed austenite," 1982, pp. 613-639.
- [93] T. Gladman, "On the theory of the effect of precipitate particles on grain growth in metals," *Proc Roy Soc Lon Ser. A Math Phys Sci, Lon*, pp. 298-309, 1966.
- [94] L. J. Cuddy, "Effect of microalloy concentration on the recrystallization of austenite during hot deformation," 1982, pp. 129-140.
- [95] P. Gordon and R. A. Vandermeer, in *Recrystallization, grain growth and textures*, Metals Park, OH, ASM, 1966, p. 205.
- [96] T. Gladman, "The physical metallurgy of microalloyed steels ", ed London: Maney Publishing for the Institute of Materials, 1997, pp. 298-303.
- [97] F. J. Humphreys and M. Hatherfly, in *Recrystallisation and related annealing phenomena*, ed Oxford: Pergamon, 1996, p. 114.

-
- [98] K. Lucke and H. P. Stuwe, in *Recovery and Recrystallization in Metals*, L.Himmel, Ed., ed New York: Interscience, 1963, p. 171.
- [99] W. B. Lee, S. G. Hong, C. G. Park, and S. H. Park, "Carbide precipitation and high-temperature strength of hot-rolled high-strength, low-alloy steels containing Nb and Mo," *Metallurgical and Materials Transactions A: Physical Metallurgy and Materials Science*, vol. 33, pp. 1689-1698, 2002.
- [100] B. Debray, P. Teracher, and J. J. Jonas, "Simulation of the hot rolling and accelerated cooling of a C-Mn ferrite-bainite strip steel," *Metallurgical and Materials Transactions A*, vol. 26, pp. 99-111, 1995.
- [101] R. Riva, C. Mapelli, and R. Venturini, "Effect of coiling temperature on formability and mechanical properties of mild low carbon and HSLA steels processed by thin slab casting and direct rolling," *ISIJ International*, vol. 47, pp. 1204-1213, 2007.
- [102] G. E. Dieter, in *Mechanical Metallurgy*, SI Metric ed. London: McGraw-Hill, 1988, pp. 26-33.
- [103] S. Gündüz and R. C. Cochrane, "Influence of cooling rate and tempering on precipitation and hardness of vanadium microalloyed steel," *Materials & Design*, vol. 26, pp. 486-492, 2005.
- [104] S. Suzuki, G. C. Weatherly, and D. C. Houghton, "The response of carbonitride particles in hsla steels to weld thermal cycles," *Acta Metallurgica*, vol. 35, pp. 341-352, 1987.
- [105] D. C. Houghton, G. C. Weatherly, and J. D. Embury, "Thermomechanical Processing of Microalloyed austenite," *Metallurgical Society of AIME*, pp. 267-72, 1982.
- [106] J. M. Gray, D. Webster, and J. H. Woodhead, "Precipitation in Mild Steels Containing Small Editions of Niobium," *Journal of Iron and Steel Institute*, pp. 203: 812-18, 1965.
- [107] A. Lebon, J. Rofes-Vernis, and C. Rossard, *Recrystallization and Precipitation during hot working of a Nb-bearing HSLA Steel*, pp. 9:36-40, 1975.
- [108] M. G. Akben, T. Chandra, P. Plassiard, and J. J. Jonas, "Dynamic precipitation and solute hardening in a titanium microalloyed steel containing three levels of manganese," *Acta Metallurgica*, vol. 32, pp. 591-601, 1984.
- [109] W. J. Liu and J. J. Jonas, "A stress relaxation method for following carbonitride precipitation in austenite at hot working temperatures," *Metallurgical Transactions A*, vol. 19, pp. 1403-1413, 1988.

-
- [110] W. J. Liu and J. J. Jonas, "Ti(CN) precipitation in microalloyed austenite during stress relaxation," *Metallurgical Transactions A*, vol. 19, pp. 1415-1424, 1988.
- [111] H. Yu, Y. Kang, K. Wang, J. Fu, Z. Wang, and D. Liu, "Study of mechanism on microstructure refinement during compact strip production process," *Materials Science and Engineering: A*, vol. 363, pp. 86-92, 2003.
- [112] C. P. Reip, S. Shanmugam, and R. D. K. Misra, "High strength microalloyed CMn(V-Nb-Ti) and CMn(V-Nb) pipeline steels processed through CSP thin-slab technology: Microstructure, precipitation and mechanical properties," *Materials Science and Engineering A*, vol. 424, pp. 307-317, 2006.
- [113] S. G. Hong, K. B. Kang, and C. G. Park, "Strain-induced precipitation of NbC in Nb and Nb-Ti microalloyed HSLA steels," *Scripta Materialia*, vol. 46, pp. 163-168, 2002.
- [114] K. B. Kang, O. Kwon, W. B. Lee, and C. G. Park, "Effect of precipitation on the recrystallization behavior of a Nb containing steel," *Scripta Materialia*, vol. 36, pp. 1303-1308, 1997.
- [115] M. Arribas, B. López, and J. M. Rodríguez-Ibabe, "Additional grain refinement in recrystallization controlled rolling of Ti-microalloyed steels processed by near-net-shape casting technology," *Materials Science and Engineering A*, vol. 485, pp. 383-394, 2008.
- [116] Z. Wang, X. Mao, Z. Yang, X. Sun, Q. Yong, Z. Li, and Y. Weng, "Strain-induced precipitation in a Ti micro-alloyed HSLA steel," *Materials Science and Engineering: A*, vol. 529, pp. 459-467, 2011.
- [117] M. D. C. Sobral, P. R. Mei, and H. J. Kestenbach, "Effect of carbonitride particles formed in austenite on the strength of microalloyed steels," *Materials Science and Engineering: A*, vol. 367, pp. 317-321, 2004.
- [118] J. W. Gibbs, "The Scientific Papers of J.W. Gibbs." vol. 1, ed New York: Longmans, Green & Co, 1906, p. 252.
- [119] M. Kahlweit, "Progress in Solid State Chemistry." vol. 2, H. Reiss, Ed., ed Oxford: Pergamon Press, 1965, p. 134.
- [120] G. M. Smith and R. W. K. Honeycombe, in *International Conference on Strength of Metals and Alloys*, Melbourne, 1982, p. 407.
- [121] K. C. Russel, "Nucleation in Solid: The induction and steady state effects," *Advanced Colloid Interphase Science*, vol. 13, p. 205, 1980.
- [122] J. W. Cahn, "Nucleation on Dislocations," *Acta Metallurgica*, vol. 5, p. 169, 1957.

-
- [123] R. Gómez-Ramírez and G. M. Pound, "Nucleation of a second solid phase along dislocations," *Metallurgical Transactions*, vol. 4, pp. 1563-1570, 1973/06/01 1973.
- [124] A. Kelly and R. B. Nicholson., "Precipitation hardening ", ed Oxford: Pergamon Press, 1963, p. 149.
- [125] G. W. Lorimer and R. B. Nicholson, "The Mechanism of Phase Transformations in Crystal Solids," *The Inst. Met* p. 36, 1969.
- [126] W. C. Johnson, C. L. White, P. E. Marth, P. K. Ruf, S. M. Tuominen, K. D. Wade, K. C. Russell, and H. I. Aaronson, "Influence of crystallography on aspects of solid-solid nucleation theory," *Metallurgical Transactions A*, vol. 6, pp. 911-919, 1975/04/01 1975.
- [127] H. Nordberg and B. Aronsson, "Solubility of niobium carbide in austenite," *Journal of the Iron and Steel Institute of Japan*, vol. 206, pp. 1263-1266, 1968.
- [128] I. M. Lifshitz and V. V. Slyozov, "The kinetics of precipitation from supersaturated solid solutions," *Journal of Physics and Chemistry of Solids*, vol. 19, pp. 35-50, 1961.
- [129] N. K. Balliger and R. W. K. Honeycombe, "Coarsening of Vanadium Carbide, carbonitride and Nitride in Low Alloy Steels," *Metal Science*, vol. 14, pp. 121-133, 1980.
- [130] G. L. Dunlop and R. W. K. Honeycombe:, "Ferrite morphologies and carbide precipitation in a Cr–Mo–V creep-resisting steel," *Met. Sci.*, vol. 10, pp. 124-132, 1976.
- [131] W. Xu, P. E. J. Rivera-Díaz-del-Castillo, and S. van der Zwaag, "Designing nanoprecipitation strengthened UHS stainless steels combining genetic algorithms and thermodynamics," *Computational Materials Science*, vol. 44, pp. 678-689, 2008.
- [132] B. Dutta and C. M. Sellars, "Effect of composition and process variables on Nb(C,N) precipitation in niobium microalloyed austenite," *Materials Science and Technology*, vol. 3, pp. 197-206, 1987.
- [133] M. Militzer, E. B. Hawbolt, and T. R. Meadowcroft, "Microstructural model for hot strip rolling of high-strength low-alloy steels," *Metallurgical and Materials Transactions A: Physical Metallurgy and Materials Science*, vol. 31, pp. 1247-1259, 2000.
- [134] D. P. Koistinen and R. E. Marburger, "A general equation prescribing the extent of the austenite-martensite transformation in pure iron-carbon alloys and plain carbon steels," *Acta Metallurgica*, vol. 7, pp. 59-60, 1959.

-
- [135] T. Gladman, "Precipitation hardening in metals," *Materials Science and Technology*, vol. 15, pp. 30-36, 1999.
- [136] S. Tang, Z. Y. Liu, G. D. Wang, and R. D. K. Misra, "Microstructural evolution and mechanical properties of high strength microalloyed steels: Ultra Fast Cooling (UFC) versus Accelerated Cooling (ACC)," *Materials Science and Engineering: A*, vol. 580, pp. 257-265, 2013.
- [137] W. B. Lee, S. G. Hong, C. G. Park, K. H. Kim, and S. H. Park, "Influence of Mo on precipitation hardening in hot rolled HSLA steels containing Nb," *Scripta Materialia*, vol. 43, pp. 319-324, 2000.
- [138] H. J. Kestenbach, "Dispersion hardening by niobium carbonitride precipitation in ferrite," *Materials Science and Technology*, vol. 13, pp. 731-739, 1997.
- [139] A. Itman, K. R. Cardoso, and H. J. Kestenbach, "Quantitative study of carbonitride precipitation in niobium and titanium microalloyed hot strip steel," *Mater. Sci. Technol*, vol. 13, pp. 49-55, 1997.
- [140] J. M. Gray and R. B. G. Yeo, "Niobium carbonitride precipitation in low-alloy steels with particular emphasis on precipitate-row formation " *Trans. ASM*, vol. 61, pp. 255-269., 1968.
- [141] A. T. Davenport and R. W. K. Honeycombe, "Precipitation of carbides at γ - α boundaries in alloy steels," *Proceedings of the Royal Society of London. Series A, Mathematical and Physical Sciences*, pp. 191-205, 1971.
- [142] K. Campbell and R. W. K. Honeycombe, "The Isothermal Decomposition of Austenite in Simple Chromium Steels," *Metal Science*, vol. 8, pp. 197-203, 1974.
- [143] A. D. Batte and R. W. K. Honeycombe, "Strengthening of Ferrite by Vanadium Carbide Precipitation," *Metal Science*, vol. 7, pp. 160-168, 1973.
- [144] R. A. Ricks and P. R. Howell, "The formation of discrete precipitate dispersions on mobile interphase boundaries in iron-base alloys," *Acta Metallurgica*, vol. 31, pp. 853-861, 1983.
- [145] R. A. Ricks and P. R. Howell, "Bowling mechanism for interphase boundary migration in alloy steels," *Metal Science*, vol. 16, pp. 317-322, 1982.
- [146] A. T. Davenport, F. G. Berry, and R. W. K. Honeycombe, "Interphase Precipitation in Iron Alloys," *Metal Science*, vol. 2, pp. 104-106, 1968.
- [147] A. J. Lacey, M. S. Loveday, G. J. Mahon, B. Roebuck, C. M. Sellars, and M. R. v. d. Windem, "Measuring Flow Stress in Hot Plane Strain Compression Tests," *Measuring good practice guide* vol. 12, 2002.

-
- [148] ASTM., "Standard Test Methods for Tension Testing of Metallic Materials," in *ASTM Standard vol. E8/E8M*, ed: American Society for Testing and Materials, 2009.
- [149] T. S. Hajime KITAGAWA, "An X-ray Diffraction Method for Quantitative Determination of Retained Austenite in the Production Line of Metastable Austenitic Stainless Steel," *ISIJ*, vol. (544) Transactions ISIJ, Vol. 23, , 1983.
- [150] X. Sauvage, J. M. Le Breton, A. Guillet, A. Meyer, and J. Teillet, "Phase transformations in surface layers of machined steels investigated by X-ray diffraction and Mössbauer spectrometry," *Materials Science and Engineering A*, vol. 362, pp. 181-186, 2003.
- [151] L. Technologies. (2006, 27/09/2010). Determination of Volume Percent Retained Austenite by X-Ray Diffraction. *Diffraction Notes No. 33, Fall 2006* 1 - 3. Available:
http://www.lambdatechs.com/html/resources/dn_33.pdf
- [152] ASTM, "Standard Practice for X-ray Determination of Retained Austenite in Steel with near random crystallographic orientation," in *ASTM Standard vol. E975-03.01*, ed: American Society for Testing and Materials, 2008.
- [153] C. F. Jaczak, "Retained Austenite and its measurement by X-ray Diffraction " *SAE Special publication* vol. 453, 1980.
- [154] D. B. Williams and C. B. Carter, *Transmission Electron Microscopy: A textbook for Material Science* vol. 1. New York: Springer Science and Business Media, Inc, 1996.
- [155] J. Zuno-Silva, "Microstructural Evolution of a Multiphase Steel Microalloyed with Vanadium," Doctor of Philosophy PhD, Department of Material Science and Engineering, University of Sheffield, PhD Thesis.
- [156] A. Bastos, S. Zaefferer, D. Raabe, and C. Schuh, "Characterization of the microstructure and texture of nanostructured electrodeposited NiCo using electron backscatter diffraction (EBSD)," *Acta Materialia*, vol. 54, pp. 2451-2462, 2006.
- [157] V. Randle, G. S. Rohrer, H. M. Miller, M. Coleman, and G. T. Owen, "Five-parameter grain boundary distribution of commercially grain boundary engineered nickel and copper," *Acta Materialia*, vol. 56, pp. 2363-2373, 2008.
- [158] A. F. Gourgues-Lorenzon, "Application of electron backscatter diffraction to the study of phase transformations," *International Materials Reviews*, vol. 52, pp. 65-128, 2007.

-
- [159] H.-W. Yen, C.-Y. Huang, and J.-R. Yang, "Characterization of interphase-precipitated nanometer-sized carbides in a Ti-Mo-bearing steel," *Scripta Materialia*, vol. 61, pp. 616-619, 2009.
- [160] R. W. K. Honeycombe, "Fundamental aspects of precipitation in microalloyed steels," in *HSLA Steels - metallurgy and Applications; Proc. Int. Conf. HSLA Steels '85*, Beijing, ASTM International, 1986.
- [161] A.T. Davenport, F.G. Berry, and R.W.K. Honeycombe, "Interphase Precipitation in Iron Alloys," *Metal Science*, vol. 2, pp. 17-31, 104-106, 1968.
- [162] R. D. K. Misra, K. K. Tenneti, G. C. Weatherly, and G. Tither, "Microstructure and texture of hot-rolled Cb-Ti and V-Cb microalloyed steels with differences in formability and toughness," *Metallurgical and Materials Transactions A: Physical Metallurgy and Materials Science*, vol. 34 A, pp. 2341-2351, 2003.
- [163] F. B. Pickering, "Physical Metallurgy and the design of steels," ed London: Applied Science Publishers Ltd, 1978, p. 50.
- [164] V. Randle, "Electron backscatter diffraction: Strategies for reliable data acquisition and processing," *Materials Characterization*, vol. 60, pp. 913-922, 2009.
- [165] F. J. Humphreys, "Characterisation of fine-scale microstructures by electron backscatter diffraction (EBSD)," *Scripta Materialia*, vol. 51, pp. 771-776, 2004.
- [166] Y. Toji, H. Matsuda, M. Herbig, P.-P. Choi, and D. Raabe, "Atomic-scale analysis of carbon partitioning between martensite and austenite by atom probe tomography and correlative transmission electron microscopy," *Acta Materialia*, vol. 65, pp. 215-228, 2014.